ANALOGUE MODELLING OF STRIKE-SLIP SURFACE RUPTURES: IMPLICATIONS FOR GREENDALE FAULT MECHANICS AND PALEOSEISMOLOGY

BY PERI JORDAN SASNETT

A thesis submitted in partial fulfilment of the requirements for the degree of Master in Science of Geology at the University of Canterbury

2013

ABSTRACT

Analogue modelling of strike-slip faulting provides insight into the development and behaviour of surface ruptures with accumulated slip, with relevance for understanding how information recorded in paleoseismic trenches relates to the earthquake behaviour of active faults. Patterns of surface deformation were investigated in analogue experiments using cohesive and non-cohesive granular materials above planar strike-slip basement faults. Surface deformation during the experiments was monitored by 3D PIV (particle image velocimetry) and 2D time lapse photography. Analysis focused on fault zone morphology and development, as well as the relationship of the models to surface deformation observed at the Greendale Fault that resulted from the 2010 Darfield earthquake.

Complex rupture patterns with similar characteristics to the Greendale Fault (e.g. en echelon fractures, Riedel shears, pop-up structures, etc.) can be generated by a simple fault plane of uniform dip, slip, and frictional properties. The specific structures and the style of their development are determined by the properties of the overburden and the nature of the material surface. The width of the zone of distributed deformation correlates closely with sediment thickness, while the width of discrete fracturing is controlled by the material properties as well as the thickness of the overburden. The overall deformation zone width increases with the growth of initial, oblique fractures and subsequently narrows with time as strain localizes onto discrete fractures parallel to the underlying basement fault.

Mapping the evolution of fracture patterns with progressive strain reveals that Riedel shears, striking at 90-120° (underlying fault strike = 90°) are more frequently reactivated during multiple earthquake cycles, and are thus most likely to provide reliable paleoseismic records.

This will help identify suitable locations for paleoseismic trenches and interpret trench records on the Greendale Fault and other active, strike-slip faults in analogous geologic settings. These results also highlight the tendency of trenching studies on faults of this type to underestimate the number and displacement of previous ruptures, which potentially leads to an underestimate of the magnitude potential and recurrence interval of paleoearthquakes.

ACKNOWLEDGEMENTS

So many people have combined to help this thesis come together, and first and foremost among them are my supervisors. Mark, I'm so glad you agreed to take me on as a student and make this opportunity possible. You've made a lot of time for me at a point when you didn't have much to spare, and I appreciate it. Sandy and David, you both looked after me so well in Australia. Having minimal experience with analogue modelling, I was reliant on you to figure out how to make my grand ideas into an actual model, and you totally came through. Pilar, you are the best brainstorming partner ever. The days you spent with me talking through my thesis and outlining the final version have made these few months of writing infinitely easier, and I am very grateful. Also, thanks for teaching me to make mole!

The Fulbright US Student Program made it possible for me to come back to New Zealand for postgraduate study. Fulbright New Zealand, specifically, did a wonderful job welcoming me and the other grantees to the country and supporting us during our time here. I also feel very lucky to have such awesome fellow Fulbrighters—you guys are the best, and I can't wait to see you all back in the States.

I'm also grateful to the University of Canterbury geology community that adopted me so effortlessly. Darren, Sam, and Anekant: Frontiers was the perfect re-introduction to New Zealand, both geologically and otherwise. Thanks to the staff as well—you have all been inexplicably eager to help me solve any problem, from the initial last minute decision to do a Masters, to constant requests for plane tickets a week in advance (sorry!). To the other UC postgrads, you have all been a great source of support and fun, from field work to conferences to

evenings (or afternoons…) at the Shilling Club. Also, a big shout out goes to the UC wiffleball team—let me know when it's time to organize an international tour.

Last but certainly not least, thanks to my friends, flatmates, and family. Past and present Peer Streeters—and honorary ones, you know who you are—there's no way I would have gotten this far without your constant, loving harassment. Kat, Kate, Kate, Courtney, and Louise, thanks for all the fun times, great chats, and many (many) wines. Mom and Dad—you guys get all the credit for gently suggesting I come back to New Zealand, and even more credit for actually letting me go abroad for so long. I'm so grateful for your support and encouragement, and your many postcards and excessively hyperlinked emails have made me feel not so far from home.

TABLE OF CONTENTS

LIST OF FIGURES

LIST OF TABLES

1. INTRODUCTION AND REVIEW OF CURRENT KNOWLEDGE

1.1 Introduction

Paleoseismic trenching studies are an important part of earthquake hazard analysis, because they make it possible to establish the rupture history of active faults, calculate slip rates, and estimate recurrence intervals, parameters which are used to assess the seismic hazard of a region. The principle of trenching is based on a theoretical model in which a fault's surface expression is confined to one or a few main traces, and the trench is placed across a segment that has ruptured in all or nearly all previous ruptures (e.g. Sieh and Jahns, 1984; Yetton, 1998). Many fast slipping, mature faults are likely to rupture in this manner, on confined fault traces (e.g. the San Andreas fault, Sieh et al., 1989; the Wellington Fault, Little et al., 2010; and the Denali fault, Haeussler et al., 2004), but slower-moving faults with longer recurrence intervals may result in complex rupture patterns that are more complicated to interpret (e.g. the Darfield earthquake, Quigley et al., 2012; the El Asman earthquake, Philip and Meghraoui, 1983; the Dasht-e-Bayaz earthquake, Tchalenko and Ambraseys, 1970).

On faults that generate distributed surface deformation (e.g. the Dasht-e-Bayaz Fault, Tchalenko and Ambraseys, 1970; the Greendale Fault, Quigley et al., 2010), it is much more challenging to identify a "main fault trace" on which paleoseismic studies should be focused. If some paleoruptures are not identified, or not even visible in trenches, or if only a fraction of the offset is measurable, the results of these studies could lead to significant underestimates of future earthquake hazard. A deeper understanding of the behaviour and development of strike-slip faults is necessary to avoid these pitfalls.

Analogue modelling has frequently been used to study strike-slip faulting, specifically the development of deformational features (e.g. Riedel, 1929; Tchalenko, 1970; Naylor et al., 1986; Schreurs, 1994; Richard et al., 1995), or basin formation and potential resource trapping structures (e.g. Wilcox et al., 1973; McClay and Dooley, 1995; Rahe et al., 1998), but the use of analogue models to inform paleoseismic interpretations of active faults has not been previously considered to the best of my knowledge.

The Greendale Fault rupture extends for ~30 km across the Quaternary surface of the Canterbury Plains, with a deformation zone that ranges from 30-300 m wide consisting of both concentrated fracturing and distributed shear (Figure 1.1; see section 1.2.2 for details; Quigley et

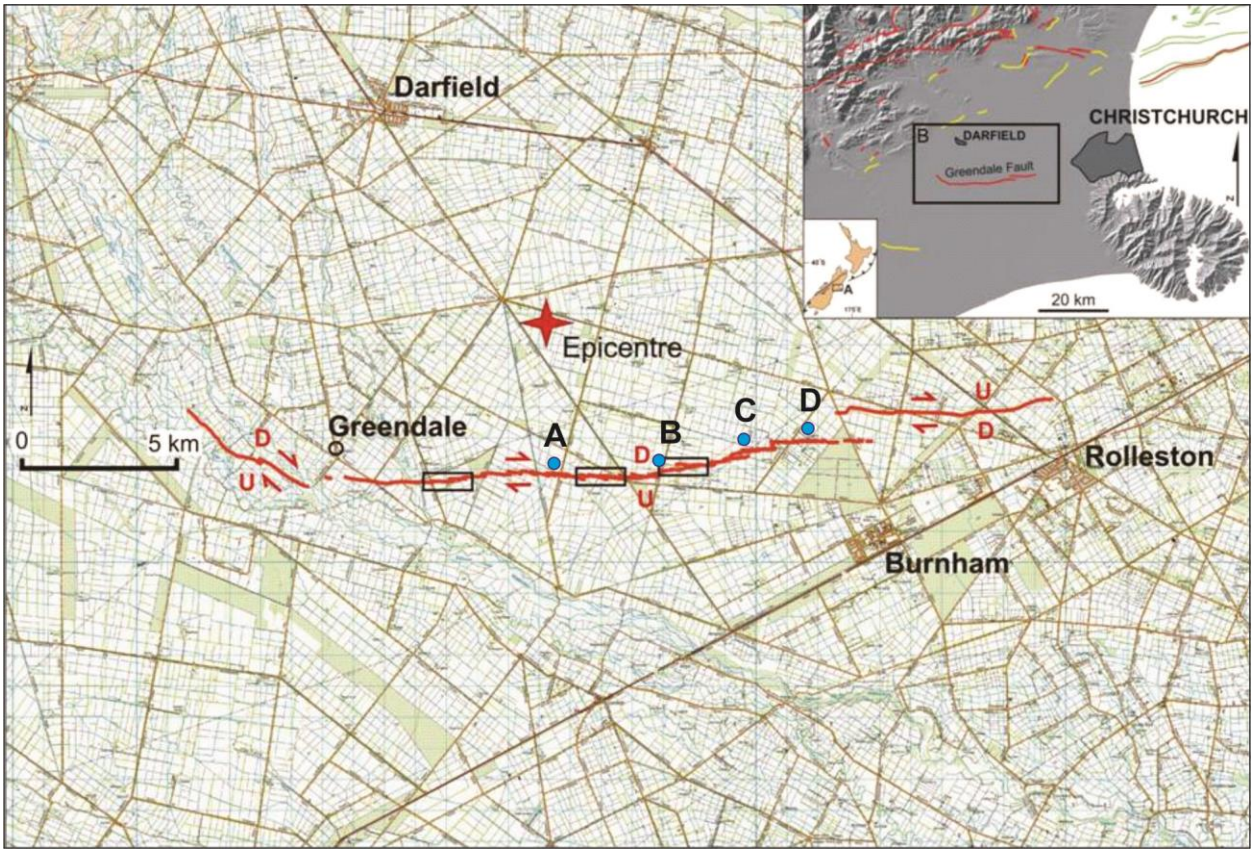

Figure 1.1. Map showing Greendale Fault trace across the Canterbury Plains and Darfield earthquake epicentre. Arrows show lateral sense of motion, while letters indicate vertical displacement (D = down, U = up). Blue dots mark locations of aerial photos referred to throughout the text: A) 1208, B) 1151, C) 1102, 1107, 1110, 1120, D) 1098, 1101. Inset shows location of fault west of Christchurch on Canterbury regional DEM (after Quigley et al., 2010).

al., 2012). The diffuse character of this deformation—where even the most focused rupture area is distributed over tens of meters and hundreds of small-scale fractures—has complicated efforts to situate paleoseismic trenches in ideal locations to study the earthquake history of the fault. Even with an unusually detailed rupture map to guide paleoseismic studies, there is no guarantee that recent high-displacement structures are the same ones that have been previously active or that will be in the future.

This investigation uses simple analogue experiments to gain further insight into the behaviour of strike-slip faults rupturing through granular, cohesive materials. The models were adjusted to test the effect on surface morphology of parameters such as sediment thickness, sediment type, cohesiveness, and interseismic sedimentation and erosion, and the resulting surface fractures were mapped and analysed at various strain increments.

This information was used to address questions about the Greendale Fault rupture relating to the appearance of surface deformation and its relationship to past events, and how this knowledge can help constrain paleoseismic studies. Specifically, why was the deformation zone so wide (up to 300 m; Van Dissen et al., 2011) and what controls the relationship between distributed deformation and discrete fracturing? Is this type of surface deformation a function of near-surface material properties or fault geometry at depth? What do the fracture patterns reveal about the fault's development and slip history? In such a complex network of fractures, how can one identify the fractures that persist through repeated ruptures and therefore provide the best targets for paleoseismic studies?

1.2 Regional geology

1.2.1 Regional Tectonic Context

The South Island of New Zealand straddles the boundary between the Pacific and Australian plates, which converge obliquely at 39-50 mm/yr (Demets et al., 2010). Approximately 70-75% of plate boundary motion is taken up along the Alpine Fault, a right-lateral transpressive fault that bisects the South Island (Figure 1.2; Norris and Cooper, 2001).

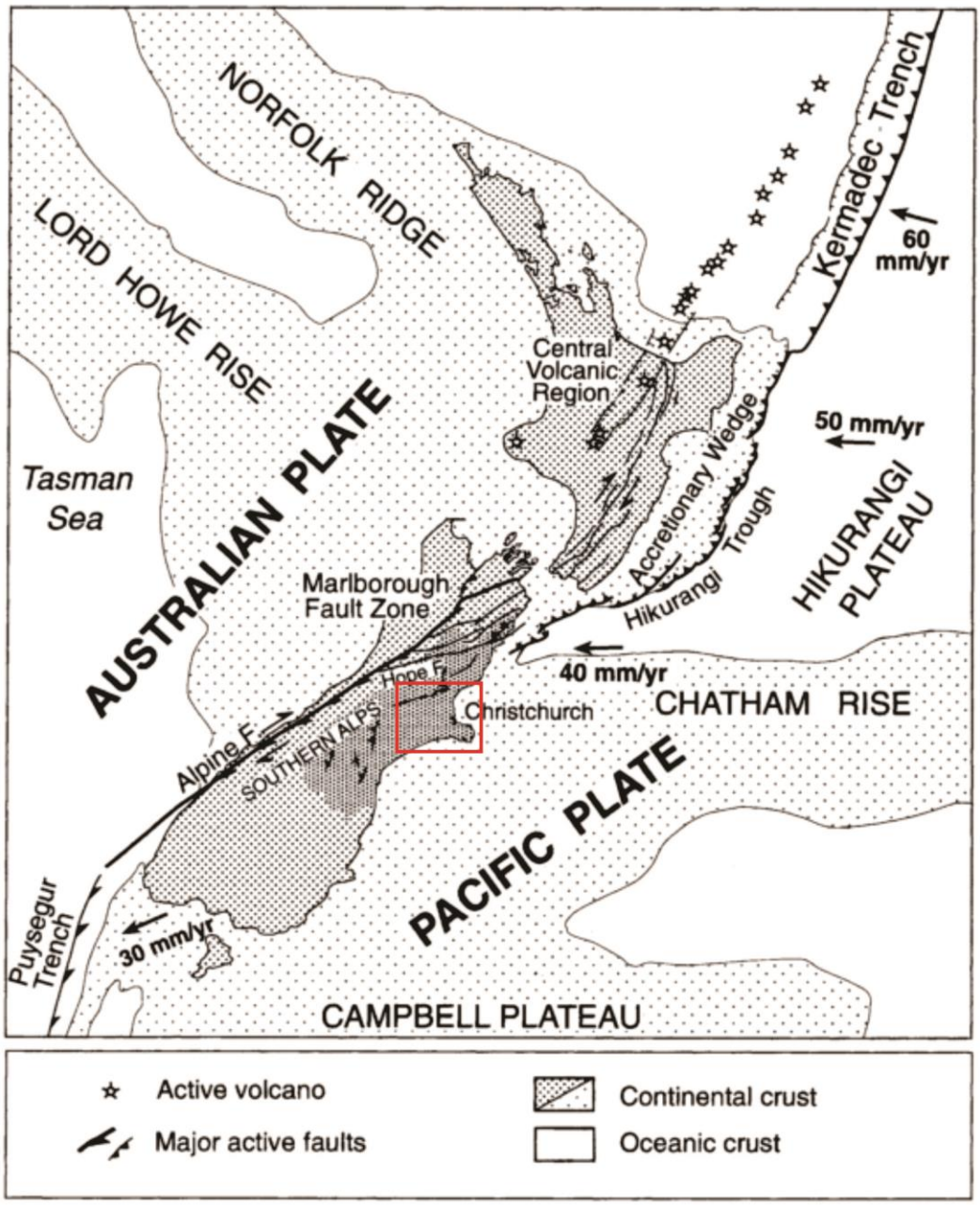

Figure 1.2. Regional tectonic map of New Zealand, showing plate boundary faults and other major structures, relative plate motion, and larger continental area. Red box shows location of Figure 1.1 inset (after Pettinga et al., 2001).

The remainder of this deformation is distributed eastward along faults within the Southern Alps and beneath the Canterbury Plains (Pettinga et al., 2001). In the Canterbury region, many of these faults are east-west oriented faults that initiated as steeply-dipping normal faults during late Cretaceous to Eocene extension (Ghisetti and Sibson, 2012). These faults are reactivated as dextral strike-slip within the contemporary stress field with maximum compressive stress (σ_1) oriented at 115±5° (Sibson et al., 2011; 2012). Examples include the Greendale Fault, the Springbank Fault, and the Ashley Fault (Jongens et al., 2012).

1.2.2 Greendale Fault and Canterbury Plains Stratigraphy

The Greendale Fault ruptured in the September 4, 2010 Darfield earthquake, with its epicentre located ~44km west of Christchurch, New Zealand. It was followed by an energetic aftershock sequence, including three damaging events of $M_W > 6.0$. However, the Darfield earthquake was the only one that generated a surface rupture. The flat, agricultural landscape of the Canterbury Plains, and the abundance of linear markers such as roads, fences, and shelter belts, facilitated detailed mapping of the rupture, producing a dataset that provides opportunities to study earthquake-induced surface deformation in high resolution (e.g. Quigley et al. 2012; Duffy et al., 2013).

The Greendale Fault rupture trace was 29.5±0.5 km in length, with an average right lateral displacement of 2.5±0.1 m (maximum 5.2±0.2 m) and vertical displacement generally less than 0.75 m (maximum 1.45±0.2) (Quigley et al., 2012). The surface rupture is made up of two main segments (eastern and central) that generally strike east-west and a western segment that strikes northwest (Figure 1.1). The fault zone consists of a wide zone of deformation (30-300 m) with both concentrated fracturing in en echelon, left-stepping segments separated by push-up

structures, as well as distributed shearing (Van Dissen et al, 2011; Quigley et al., 2012). Each of those en echelon segments consists of a complex pattern of synthetic and antithetic Riedel shears, tension fractures, and other subsidiary structures (Figure 1.3).

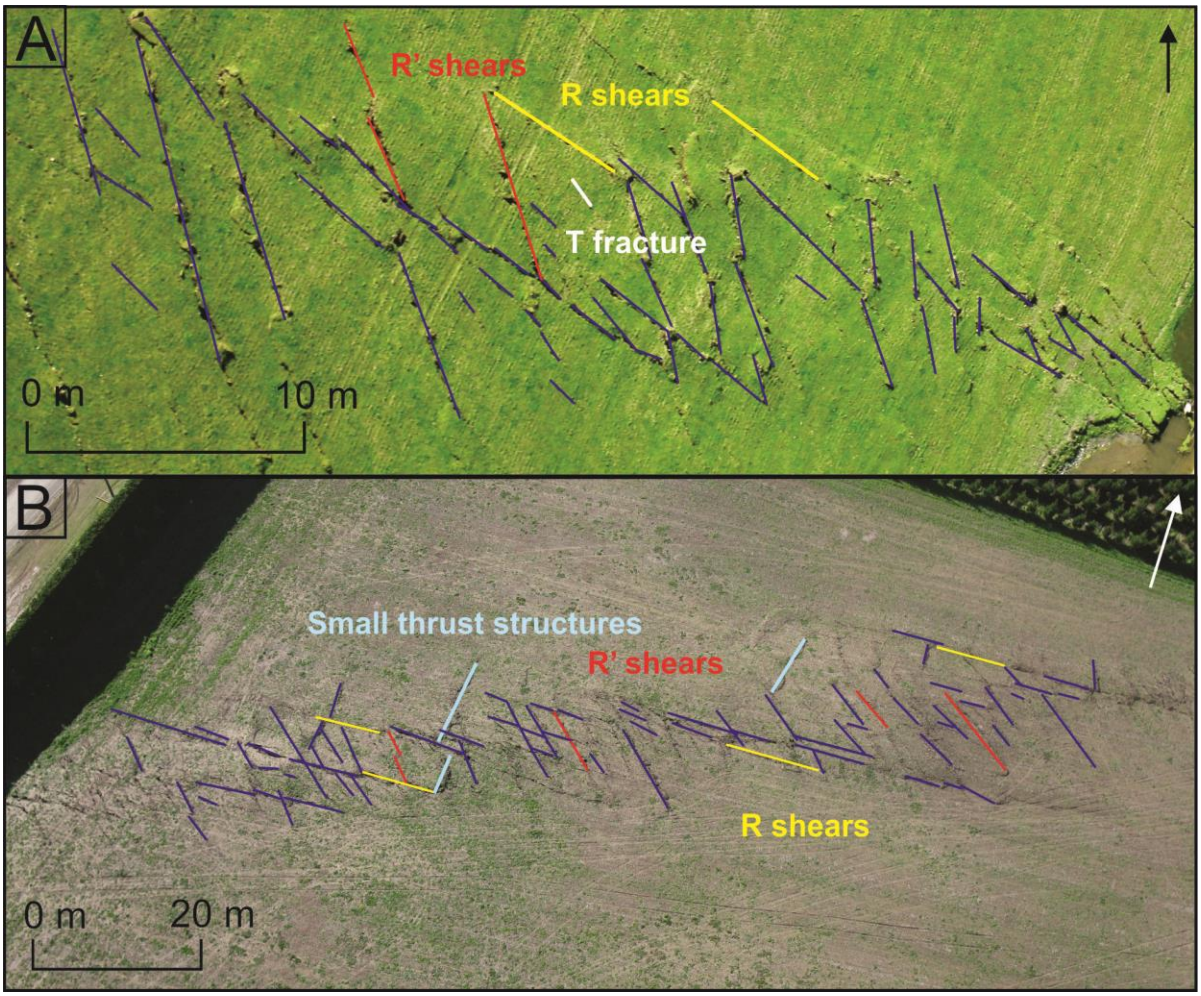

Figure 1.3. Aerial photos of Greendale Fault surface trace: 1120 (A) and 1151 (B), see Figure 1.1 for locations. Fractures are mapped in purple, with R shears highlighted in yellow, R' shears in red, tension fractures in white, and small thrust structures in blue. (Images courtesy of Mark Quigley.) Arrow indicates north.

The Darfield earthquake is thought to have been the product of near-simultaneous motion on multiple faults, in addition to the Greendale Fault surface rupture. The initial event occurred on the Charing Cross fault, a steeply southeast-dipping, blind reverse fault, which triggered the main oblique strike-slip Greendale fault rupture and multiple other blind thrust faults, most

notably one to the southwest of the Greendale fault trace (Gledhill et al., 2011). GPS and InSAR inversion data suggest motion on a blind reverse fault near the major stepover in the Greendale fault as well (Figures 1.4, 1.5 (next page); Holden et al., 2011).

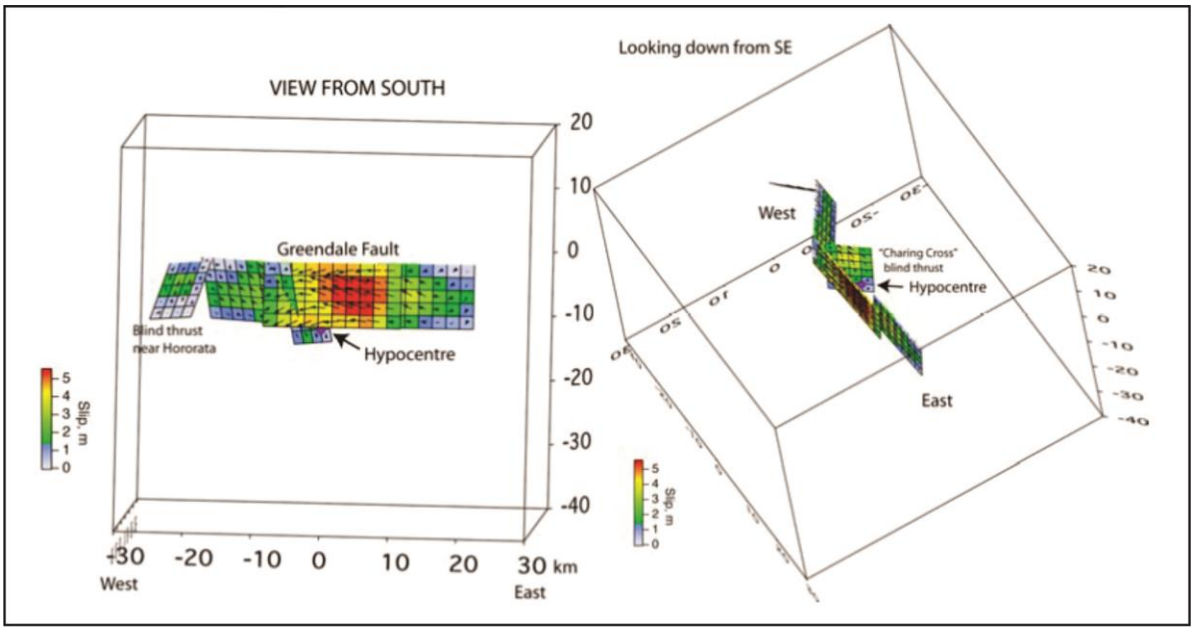

Figure 1.4. Model of Greendale Fault subsurface geometry by Holden et al. (2011). Note the presence of blind thrust faults, in addition to the main Greendale Fault plane.

The fault cuts across the Canterbury Plains, which consist of alluvial gravels of late Pleistocene age (Forsyth et al., 2008). Only the surface and upper few meters of the stratigraphy beneath the fault have been directly observed, which are made up of fluvial gravels with loess caps in places. These gravels are moderately indurated to a visible depth of 7 m, as observed in a quarry on Grange Road, >200 m from the central Greendale Fault. This level of induration is likely due to weak cementing by pedogenic silica. The Leeston-1 petroleum exploration well from 1969 is ~10 km south of the central-eastern part of the fault, and it provides the best estimate of the lower stratigraphy of the Canterbury Plains gravels. The well log shows ~400 meters of Pliocene to Quaternary gravels which are mostly fluvial or glaciofluvial in nature, with

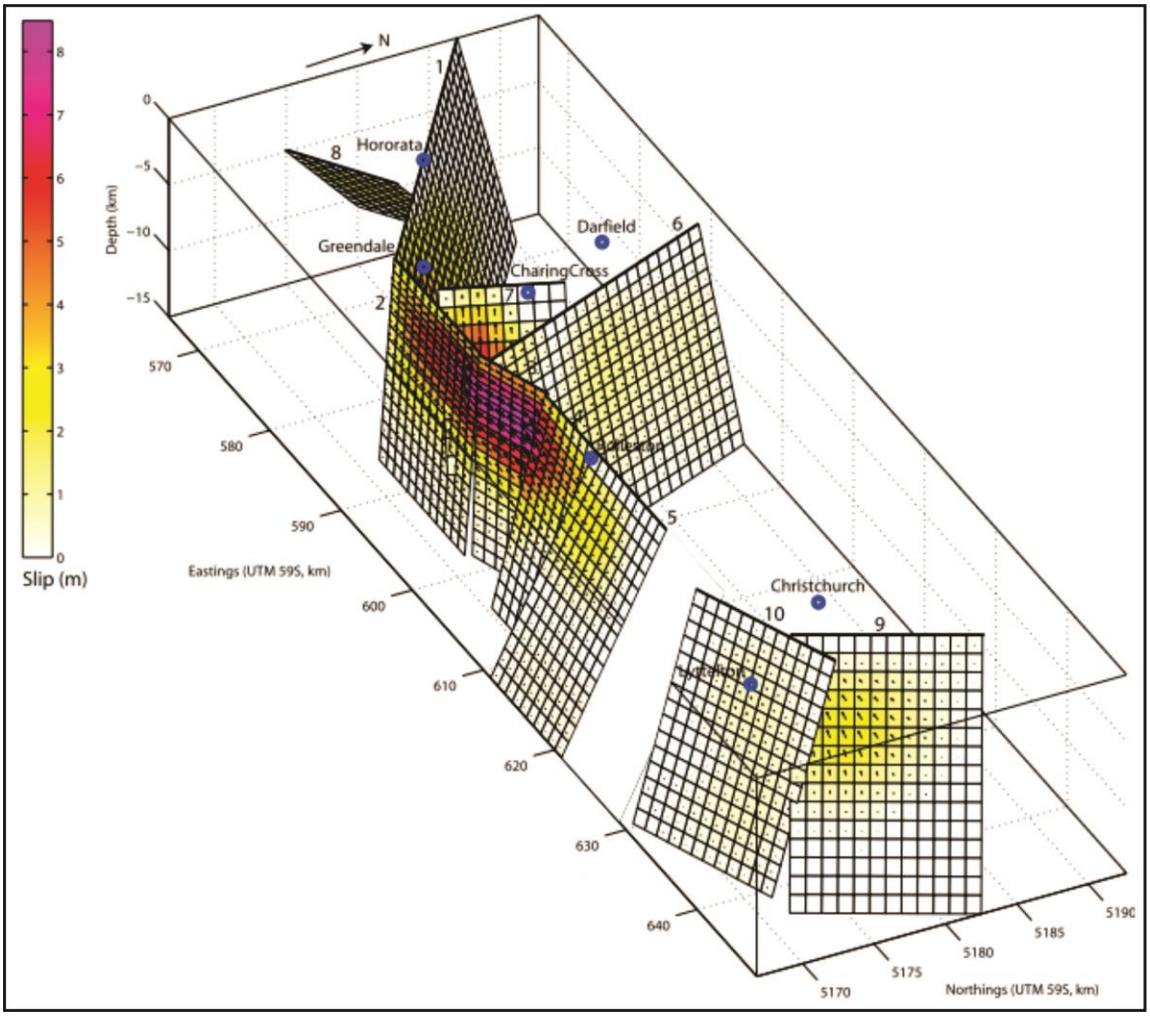

Figure 1.5. Model of Greendale Fault subsurface geometry by Elliott et al. (2012). These authors model the Greendale Fault as separate segments with variable strikes and dips. Note the presence of additional blind thrust faults that are not modelled by Holden et al. (2011). Fault planes shown near Christchurch city are from the February 22, 2011 earthquake and were not involved in the initial 2010 Greendale Fault rupture.

some marine input toward the bottom of the section (Wood et al., 1989). Beneath this is ~750 meters of more competent rock, including Miocene (Lyttelton Group) and Eocene (View Hill) volcanics, Cretaceous to Paleocene sedimentary rocks, and the Torlesse basement (Andrews et al., 1987). However, this stratigraphic section is based on a single well log, so it is not necessarily representative of the regional stratigraphy. Jongens et al. (2012) provides a regional

estimate for the depth to basement rock in the central Canterbury Plains of ~750±250 m, which is in general agreement with the Leeston-1 well log.

1.3 Previous Studies of Strike-Slip Deformation

1.3.1 Field Observations

Strike-slip fault ruptures have been frequently recognized and mapped around the world, and the geometry and displacements they display at the surface are dependent upon factors like the material properties of the rocks or sediments that the fault ruptures through, the thickness of the cover sequence, the topography at the surface, and the maturity of the fault zone, including frictional properties and fluid pressure of fault rocks, and fracture geometry.

This study specifically focuses on strike-slip ruptures that are expressed in young cover sequences, which tend to share some common features, particularly en echelon fractures, Riedel shears, and other associated structures. These classic shear deformation patterns have also been described in analogue modelling experiments (see section 1.3.2).

Similar experiments have found that the width (perpendicular to fault strike) of the surface deformation zone is proportional to the thickness of the cover sequence (Naylor et al., 1986; Atmaoui et al., 2005). The 2001 Kunlun earthquake provides a field example of this principle because it ruptures through exposed basement rock as well as thick alluvial cover sequences at different points along strike. In the alluvial deposits, a wide (up to 500 m) shear zone with frequent R shears was observed, while in the basement rocks, the fault zone was much narrower (5-50 m wide) and less complex, as predicted by analogue experiments (Lin and Nishikawa, 2011). Again, this refers only to the zone of discrete fracturing; the zone of broader distributed deformation is not always visible in the field.

Strike-slip fault traces tend to manifest as several interacting en echelon segments connected by stepovers, which can occur on scales from a few meters to a few kilometers (Wesnousky, 2008). Depending on the geometry of the stepover, related tensile or compressional stresses in the region between the two fault segments can cause the development of pop-up structures or pull-apart basins. The Greendale Fault rupture is dominated by left-stepping en echelon segments with pop-up structures in the restraining stepover areas. These stepovers are observed on multiple scales, both larger structures between major, ≥400 m segments of the fault, and smaller structures between ≤200 m fracture zones (Figure 1.6). This "Riedel within Riedel" pattern (sometimes called a double en echelon pattern) was first observed by Tchalenko (1970)

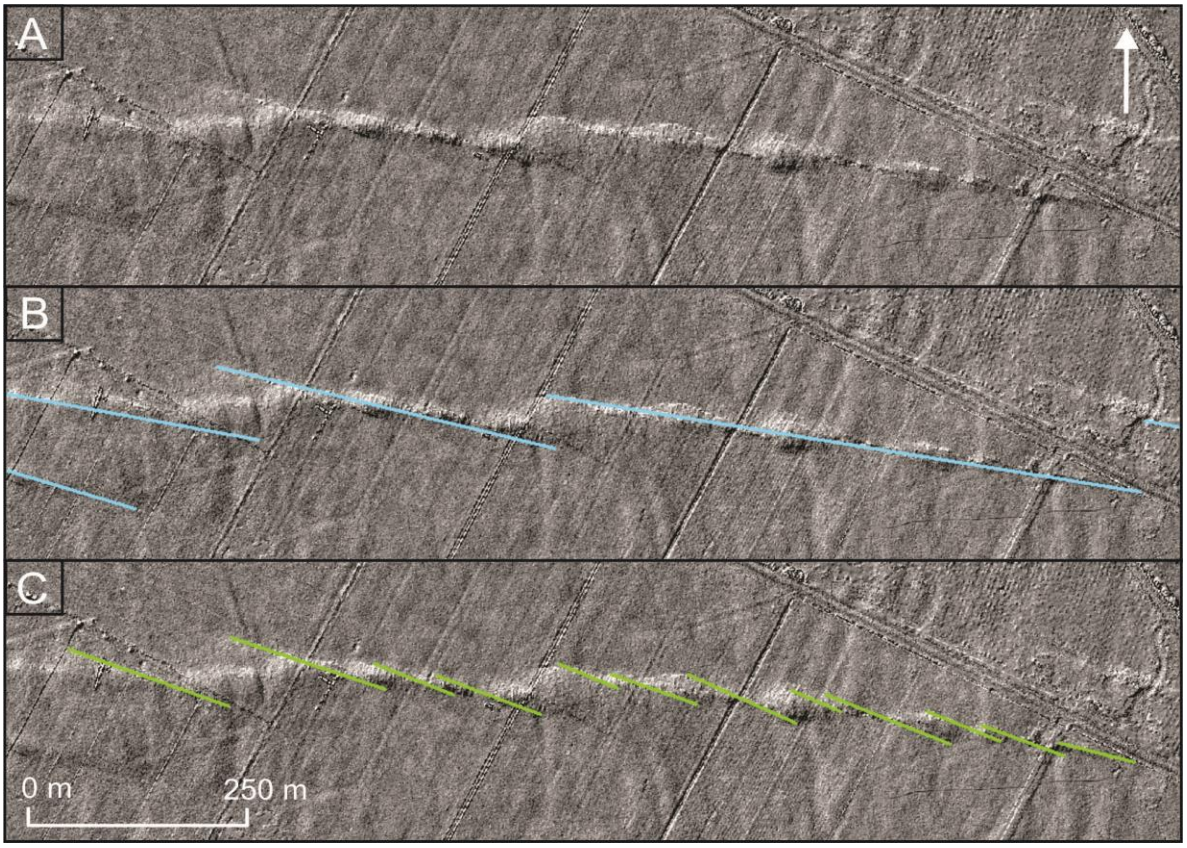

Figure 1.6. Different scales of en echelon segments and associated stepovers are present at a single ~1 km section of the Greendale Fault, generating a "Riedel within Riedel" pattern. A) LiDAR data shows the fault surface morphology, B) "macro" stepovers (traced in blue) are separated by 400-800 m fault segments, C) "micro" stepovers (traced in green) are separated by ≤200 m fault segments.

in analogue studies, and has since been frequently noted in strike-slip faulting environments with a cover sequence above bedrock (e.g. Bjarnason et al., 1993; Clifton and Einarsson, 2005; Carne and Little, 2012; see Figure 1.7 for a schematic representation). It is not always clear in the field how different stepover segments relate to one another at depth, whether they are separate segments (e.g. Elliott et al., 2012; Figure 1.5) or whether they branch from a single fault at depth (e.g. Carne and Little, 2012; Figure 1.8).

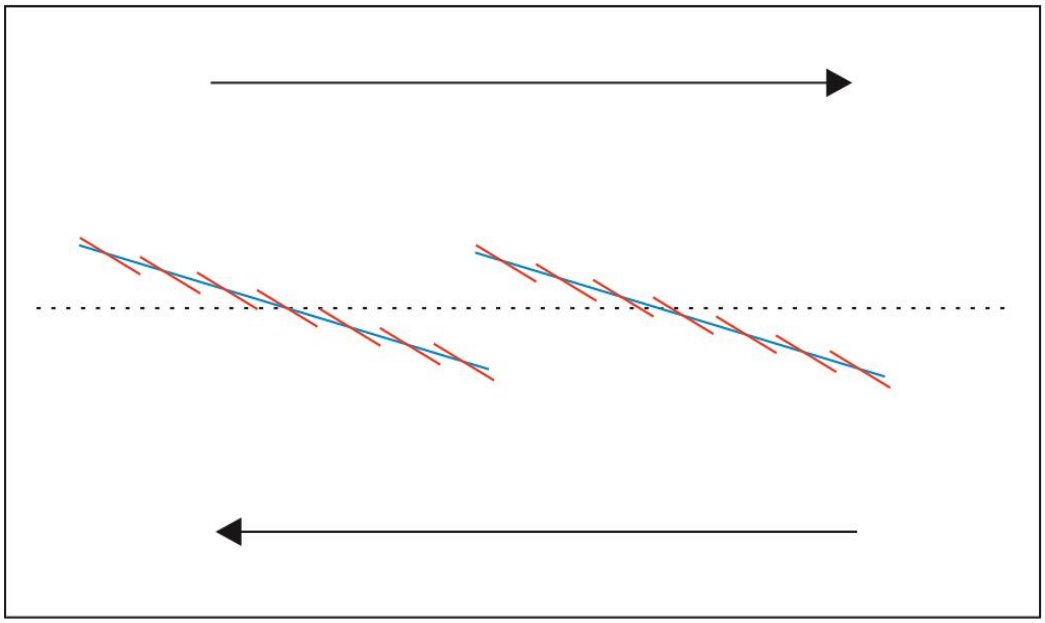

Figure 1.7. Model fault zone showing schematic "Riedel within Riedel" geometry. The blue fractures are classic Riedel shears oriented at 15° clockwise from the principal slip zone (PSZ), while the red structures are equivalent shears made up of an en echelon array of smaller shears oriented at 30° to the PSZ (15° clockwise from the larger scale, blue Riedel shear). Fractures at both these scales can be present simultaneously.

Shear deformation features are rarely as well-expressed in the field as they are in experiments, but the Greendale Fault is one of few historic ruptures that has generated en echelon structures and R and R' patterns in such complexity and so extensively along the rupture length (Figure 1.3). Its 30-300 m wide deformation zone is also unusual. These characteristics are partially due to the fault trace's location in a flat, agricultural landscape with linear markers which allowed this deformation to be observed and mapped in such detail. However, this level of

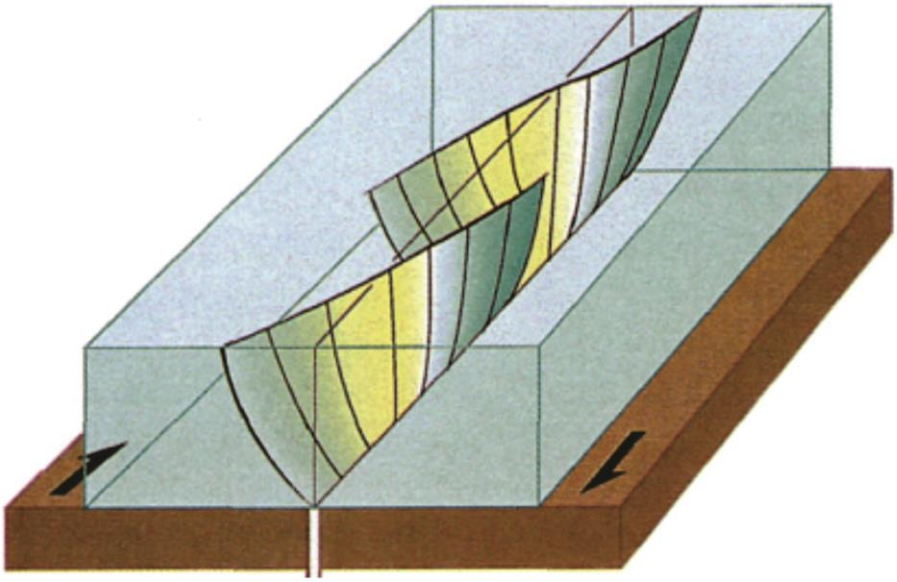

Figure 1.8. Block diagram showing three dimensional helicoidal geometry of Riedel shears that branch from a single, linear basement fault. (After Richard et al., 1995.)

complexity is also likely related to the material properties of the near-surface gravels or the circumstances of the fault rupture itself.

The Dasht-e-Bayaz rupture in Iran is relatively similar to the Greendale Fault in terms of the morphology of the fault trace and the types of structures it displays, particularly R and R' shears, P shears, and stepovers in a zone of dense fracturing (Tchalenko and Ambraseys, 1970; Figure 1.9). However, the overall complexity and the diversity of structures seen at Darfield and in Iran (R, R', P, etc.) is not always present in other historic ruptures, although similar patterns have been observed in geomorphic studies of prehistoric deformation (e.g. Keller et al., 1982; Erdlac and Anderson, 1982).

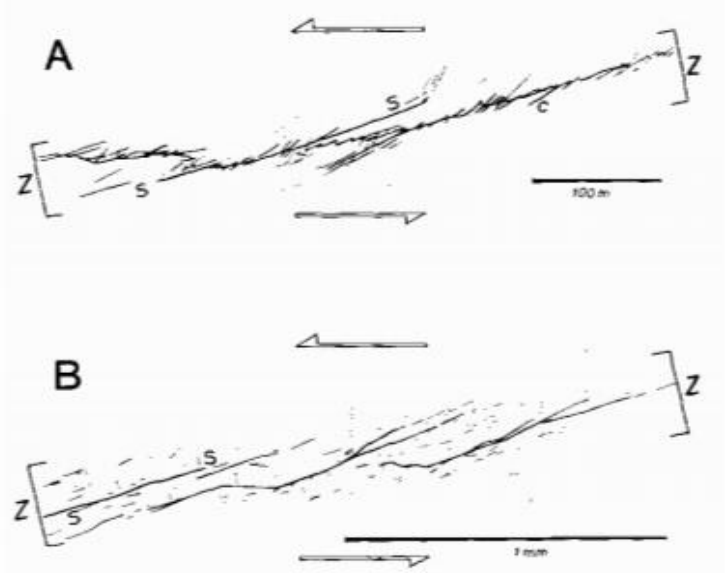

Figure 1.9. "Riedel within Riedel" patterns, as seen in A) a field example from the Dasht-e Bayaz earthquake and B) an analogue model of Morgenstern and Tchalenko (1967). Arrows show sense of motion and larger fault trend (Tchalenko, 1970).

Several recent events (e.g. 2003 Bam, Iran earthquake, Hessami et al., 2005; 1990 Rudbar, Iran earthquake, Berberian and Walker, 2010; 2010 El Mayor-Cucapah earthquake, Oskin et al., 2012; 2010 Yushu earthquake, Li et al., 2012) have much narrower and simpler shear zones, which are often confined to a single or a few main strands; en echelon fractures are observed sporadically, but the levels of complexity do not approach that of the Greendale Fault, even on faults in similar geological environments. It should also be noted that in these cases, only discrete surface fracturing was measurable, as previously linear markers were not present to record more subtle distributed deformation. These ruptures occurred in Quaternary sequences over bedrock, as did the Greendale and Dasht-e-Bayaz ruptures, so it is possible that controls on fault morphology in these cases are related to surficial factors, such as the material properties of the Quaternary deposits or the local topography, although fault maturity and other factors discussed earlier in this section could also be responsible for these differences.

1.3.2 Analogue Modelling Studies

The pattern of en echelon fractures in clay slabs undergoing simple shear deformation was first observed and described by Cloos (1928) and Riedel (1929). These oblique shear fractures include synthetic "Riedel shears" (R shears) that form at acute angles (90° + φ/2, where φ is the angle of internal friction and the underlying fault plane strikes at 90°, measured from north at 0°) to the principal slip zone (PSZ) and antithetic R' shears that form at angles more oblique to the PSZ (180° – φ/2; see Figure 1.10). Depending on the materials, tensile cracks (T fractures) can form parallel to the direction of shortening (σ_1, which typically is 45° from the PSZ), opening in the extension direction (σ_3). P shears can also form at a mirror image to R shears (90° – φ/2), and Y shears are parallel to the underlying fault plane (Figure 1.10).

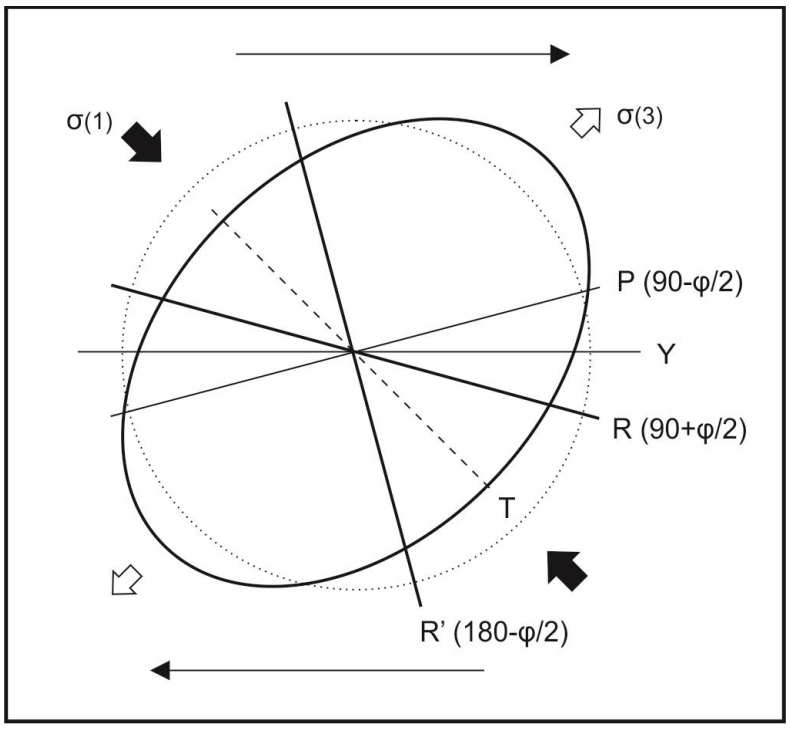

Figure 1.10. Strain ellipsoid for right lateral simple shear, showing the orientations of maximum compressive stress (σ_1) and extension direction (σ_3), and the resulting expected angles for synthetic and antithetic Riedel shears (R and R'), tension fractures (T), P shears, and the Y shear plane, which is the same plane as the PSZ.

It is important to note that these fracture orientations are calculated using the Coulomb fracture criterion, which is based on the frictional properties of the material being deformed. This gives only one set of orientations for a given material, regardless of its thickness, initial stress state, the stage of deformation, etc., all of which can result in deviations from the angles described in Figure 1.10 (e.g. Dresen, 1991; Ueta et al., 2000). A particularly important factor in these experiments is the three dimensional, helicoidal geometry that Riedel shears develop in unconsolidated sediments—the thicker the overburden is, the more space there is for the Riedel shear plane to rotate away from the underlying fault zone, generating fractures that are more oblique to the PSZ and a wider overall deformation zone (Ueta et al., 2000; Figure 1.8). These additional controls on the formation of Riedel shears and other fractures can account for a large amount of variation from the orientations expected based on frictional properties.

Many authors have studied the role that Riedel shears play in the initiation of fault zones and their development into continuous, throughgoing faults (e.g. Naylor et al., 1986; Schreurs, 1994; Richard et al., 1995). In these analogue experiments on previously undeformed materials, en echelon sets of R shears generally form first, relatively soon after initial displacement on the fault at depth. Depending on the specific properties of the model, these can be followed by R' shears, splay faults, P shears, and other structures that link the initial R shears together into a single anastomosing fault zone.

The particular conditions of the shear zone are especially important for the formation of R versus R' shears. Antithetic R' shears are much more common when materials are deformed by a zone of distributed shear, where they sometimes become the dominant structures (e.g. Hoeppener et al., 1969; Freund, 1974; Schreurs, 1994; An and Sammis, 1996). They are much less common in models with a single "basement fault", where they either do not form at all (e.g.

Richard et al., 1995; Dauteuil and Mart, 1998) or accumulate very little displacement compared to other structures (e.g. Wilcox et al., 1973; Naylor et al., 1986).

As mentioned previously, analogue modelling studies have shown that for a given stress state and set of material properties, the width of a fault rupture's surface deformation zone is directly related to the total overburden thickness (Naylor et al., 1986; Atmaoui et al., 2005). If one considers the subsurface branching geometry of Riedel shears, it is clear that if all other factors are the same, the deeper the "branching point" of the structures, the wider the zone of deformation will be when they reach the surface (Figure 1.8). To the best of my knowledge, only a few other analogue modelling studies have focused on the development of surface deformation zone width with progressive strain (e.g. Atamoui et al., 2005; Schrank et al., 2008).

Analogue modelling of pop-up structures, found at compressional stepovers (i.e. a left step on a right-lateral fault) has demonstrated that their morphology is mainly controlled by a few geometric variables: the degree of overlap of the fault segments, the width of the stepover with respect to the overall fault displacement, and the thickness of the overlying sediments (McClay and Bonora, 2001). Pull-apart basins are the analogous structure at releasing stepovers. They demonstrate similar geometric controls, and are often characterized by a cross-basin fault zone connecting the two fault segments (McClay and Dooley, 1995). Additionally, Schrank and Cruden (2010) found that dilational effects alone can result in positive and negative topography changes, depending on the initial compaction of the material.

1.4 Research Questions and Objectives

Existing literature shows how analogue modelling can be of use in understanding the development and behaviour of active faults. This study uses a series of experiments to

investigate strike-slip faulting in granular materials, in order to better understand the controls on surface rupture morphology and how it develops with continuing fault displacement. These findings can then be used to inform how the earthquake history of faults is studied.

In particular, I want to understand whether complex surface deformation is controlled by the conditions of the fault at depth (i.e. complex fault geometry, rupture dynamics, etc.) or whether the properties of the overburden and ground surface are more a more important factor. Similarly, what factors influence the characteristics and width of surface deformation, in terms of both distributed shear strain and discrete fracturing? I also wanted to explore how fractures form and propagate in cohesive granular materials.

The goal of this study is to provide insights on the mechanics of the central Greendale Fault rupture using simple analogue experiments in which the material properties of the overburden and the finite shear strain are varied. The results of these models can be used to help understand how faults develop through time, and how earthquake rupture morphology will change through multiple events. Chapter 4 applies this knowledge to constrain the best locations for paleoseismic trenches on these types of faults and better interpret the structures exposed in them. Likewise, the results can help identify structures or phenomena that may be misinterpreted in trenching studies, which would lead to over- or underestimates of earthquake activity on a given fault.

2. METHODS

2.1 Experimental Setup

Analogue experiments were carried out on a shear table that was divided so that one side could be offset right laterally relative to the other by an electronic actuator at a minimum rate of 1 mm/second. The table was 1 meter long (parallel to the basal velocity discontinuity) and ~40 cm wide. The experiments reported here used roughly half the available area of the shear table (Figure 2.1). This setup models a planar, vertical strike-slip basement fault at depth, above which various materials were layered to represent Quaternary cover sediments. The experiments were recorded with high-resolution time lapse photography and a Particle Imaging Velocimetry (PIV) system.

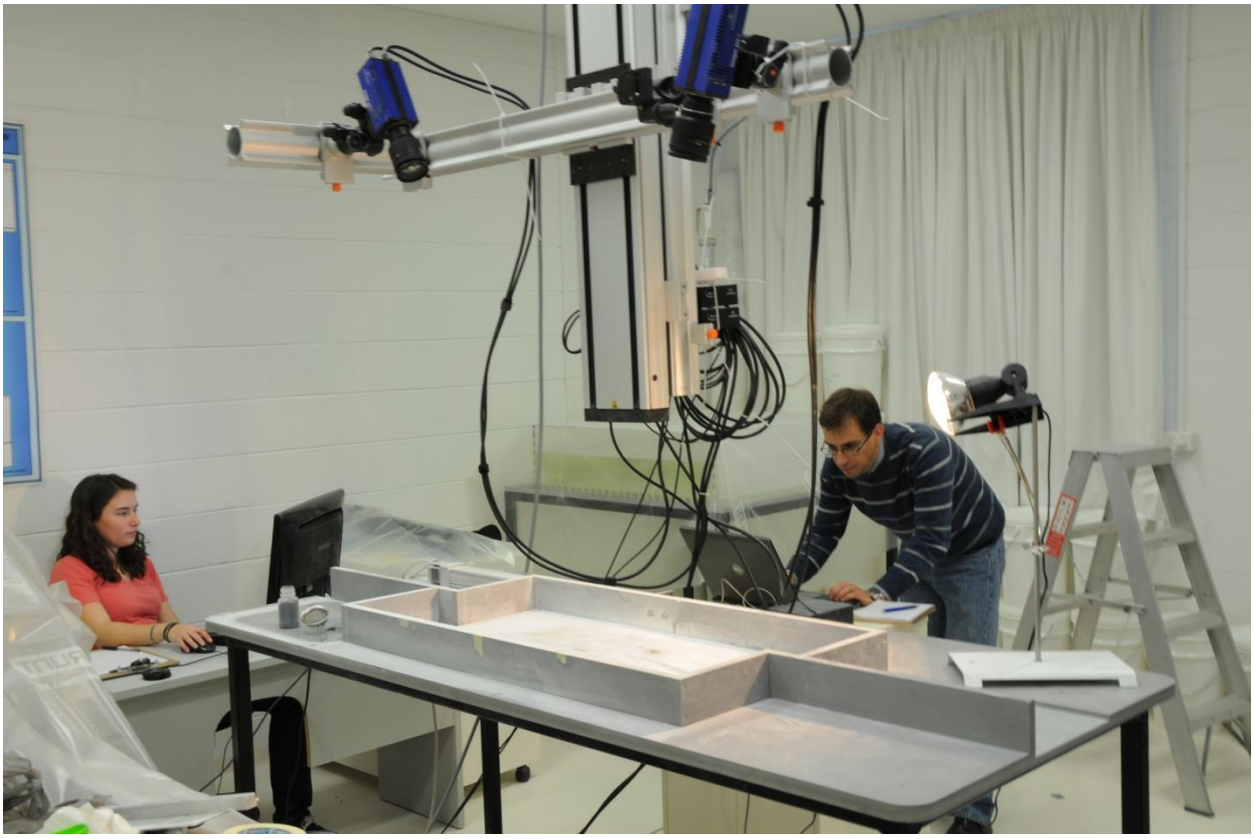

Figure 2.1. Experimental setup, with shear table at center and PIV cameras mounted above.

2.2 PIV setup

PIV is an electro-optical technique that was originally developed for measuring fluid flow, but has since been adapted for measuring the surface deformation of analogue models (e.g. Adam et al., 2005; Boutelier et al., 2008; Schrank et al., 2008; Schrank and Cruden, 2010). Two inclined cameras are set up to record the movement of particles on the surface of the model. Application of optical cross-correlation algorithms to the resulting images allows the system to calculate measurements of the instantaneous and cumulative distribution of 2D displacements, velocity fields, pure and shear strains and strain rates, and 3D topography, as well as other parameters. The cameras record five 2,048 x 2,048 pixel images per second, with a resolution of ~4 px/mm, so the model development was recorded in great spatial and temporal detail. The software used for these experiments was DaVis v.8 from LaVision GmBh.

2.3 Materials Tested

Initial tests were performed on a coarse sand to assess its suitability for modelling surface rupture above the Greendale fault. Dry sand is commonly used for crustal-scale analogue modelling because it deforms according to the same Coulomb-Navier failure criterion that governs brittle rock and soil mechanics (e.g. Horsefield, 1977; Naylor et al., 1986; Schreurs, 1994; McClay and Dooley, 1995). These preliminary experiments generated faults with small, low-angle Riedel shears and a quickly-localizing central shear zone (Figure 2.2), but there was no evidence of the complex structures that developed during the September 4, 2010 Darfield rupture, such as R' shears and tension cracks. The deformation localized quickly onto the Y shear plane in the coarse sand, and few structures developed other than incipient Riedel shears. Additionally, because dry sand has negligible cohesion, it cannot develop features like the open

tensile cracks that were ubiquitous at the Greendale Fault. While dry sand may be useful for larger scale experiments, this study is concerned with surface deformation of cemented gravels with loess caps in places. For these reasons, it was concluded that a cohesive material would be a more suitable analogue for the type of deformation observed along the Greendale Fault.

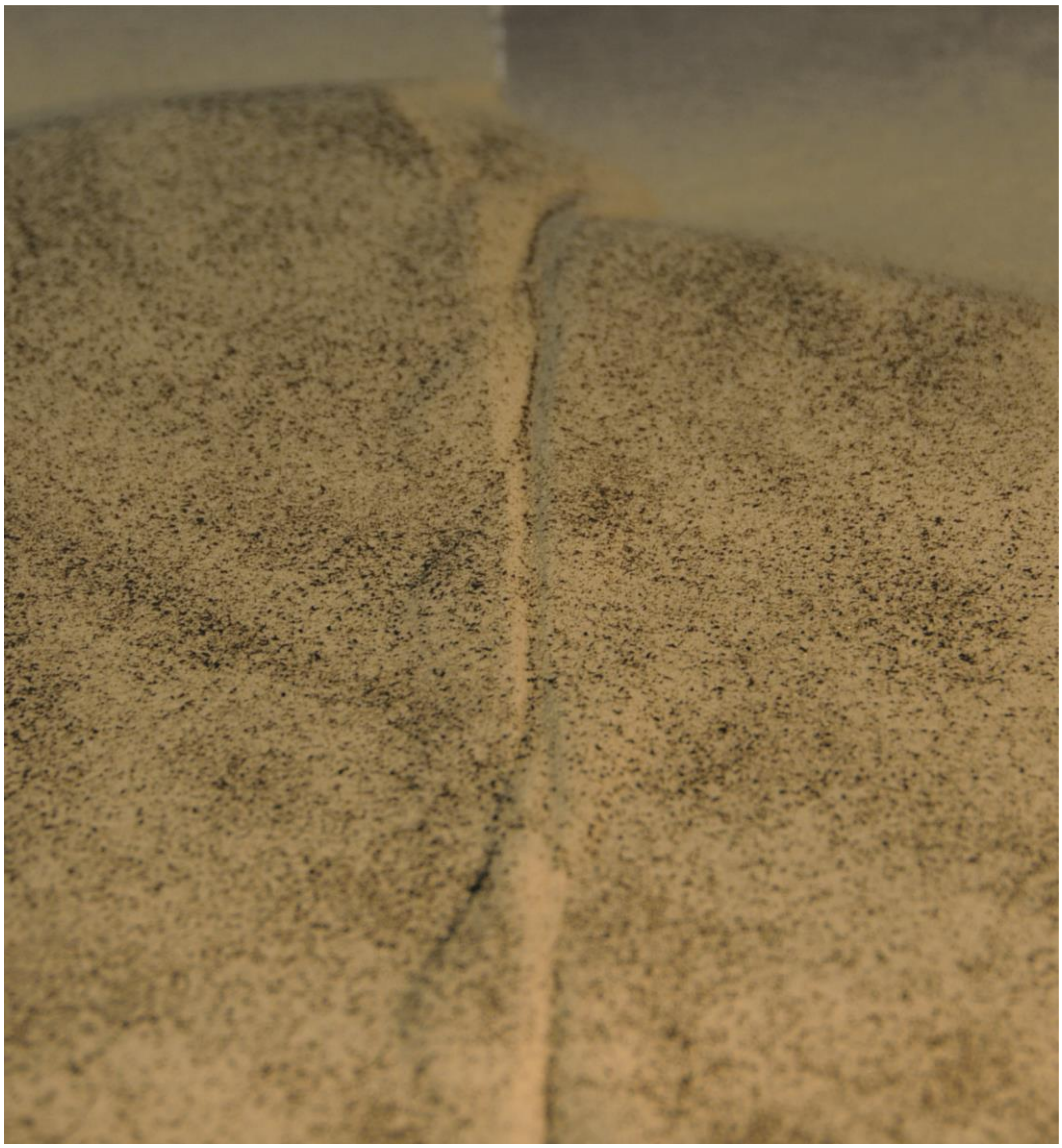

Figure 2.2. Oblique view of SAND experiment (a 3.5 cm thick layer of sand) after 30 mm displacement. Y shear is dominant, with inactive Riedel shears present at acute angles to the PSZ. The surface was scraped smooth before displacement began, and black particles were sprinkled on the surface to improve visibility.

The powders that were tested varied widely in cohesiveness, and included gypsum powder (also known as hemihydrate, or plaster of Paris), kaolin, and talc. Of these, gypsum powder and kaolin were the most cohesive, but qualitatively too much so. While tension fractures and Riedel shears did form in these materials with initial displacement, the powders were so cohesive that instead of developing and linking together, these fractures simply opened further and further in the σ_3 direction, and a throughgoing fault zone never developed (Figures 2.3, 2.4). Likewise, some sections of the material behaved as large coherent blocks, rotating and sliding over the rigid basement instead of deforming internally. Additionally, the internal cohesion of the powders was greater than the friction between the bottom surface of the material and the table, so at times a basal detachment developed between the powder and the moving shear table.

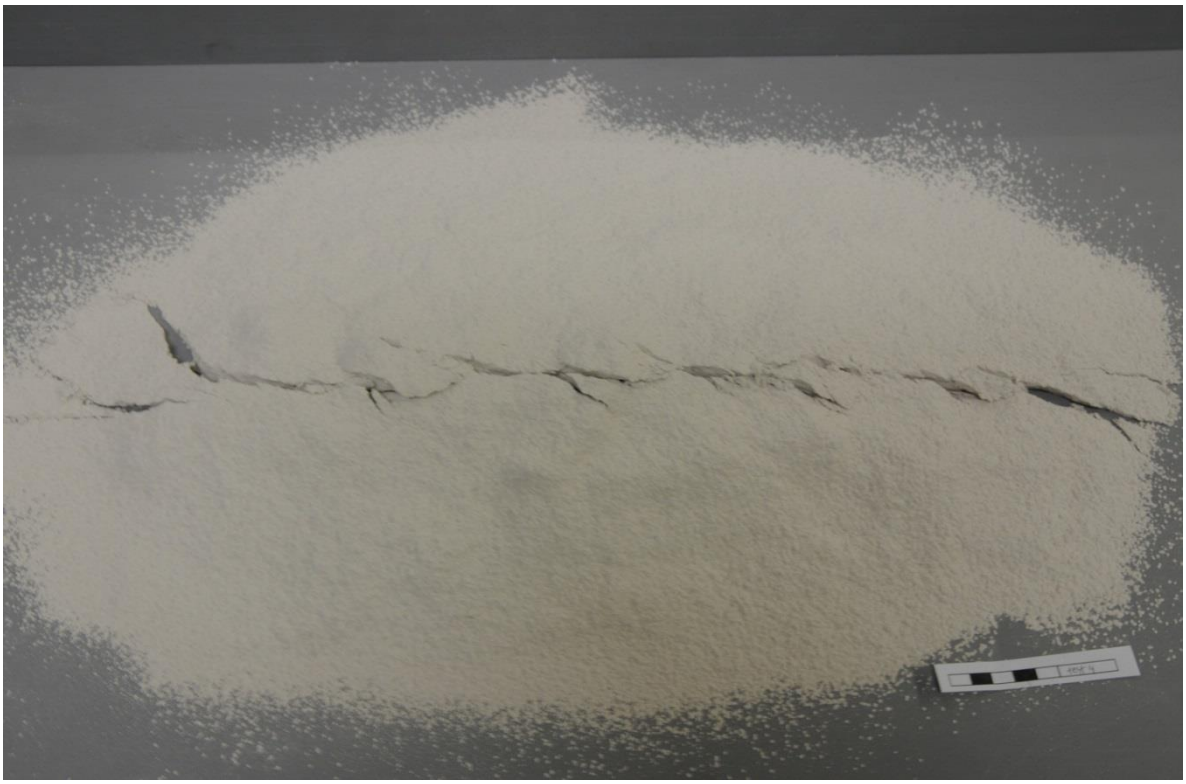

Figure 2.3. Preliminary test #4 with gypsum powder, sieved to a thickness of 3 cm and displaced 20 mm. Note undeformed blocks of material rotating within shear zone at center-left. 5 cm scale bar is visible at the bottom right.

Figure 2.4. Preliminary test #7 with kaolin powder, sieved to 1.5 cm thickness and scraped smooth. Note opening of major tensile cracks, as well as deformation of the surface due to the scraping process. Scale bar visible at the bottom right.

Dry talc powder was found to be cohesive enough to develop tensile cracks and Riedel shears, but it wasn't so cohesive that it never developed an anastomosing, throughgoing fault zone, like kaolin and gypsym powder (see above; Figure 2.5). It also generated the very fine-scale features that are the focus of this study, which were absent in tests with other materials. The fracture patterns observed in talc powder under shear strain were by far the best morphological match for the surface deformation features observed at the Greendale Fault, showing recognizable patterns of tension cracks, en echelon fractures, stepover areas with pop-up structures, and eventual development of a single throughgoing fault zone. Other authors have found dry talc powder suitable to model brittle deformation, particularly faulting and tension gashes (e.g. Deramond et al., 1983; Soula et al., 1984).

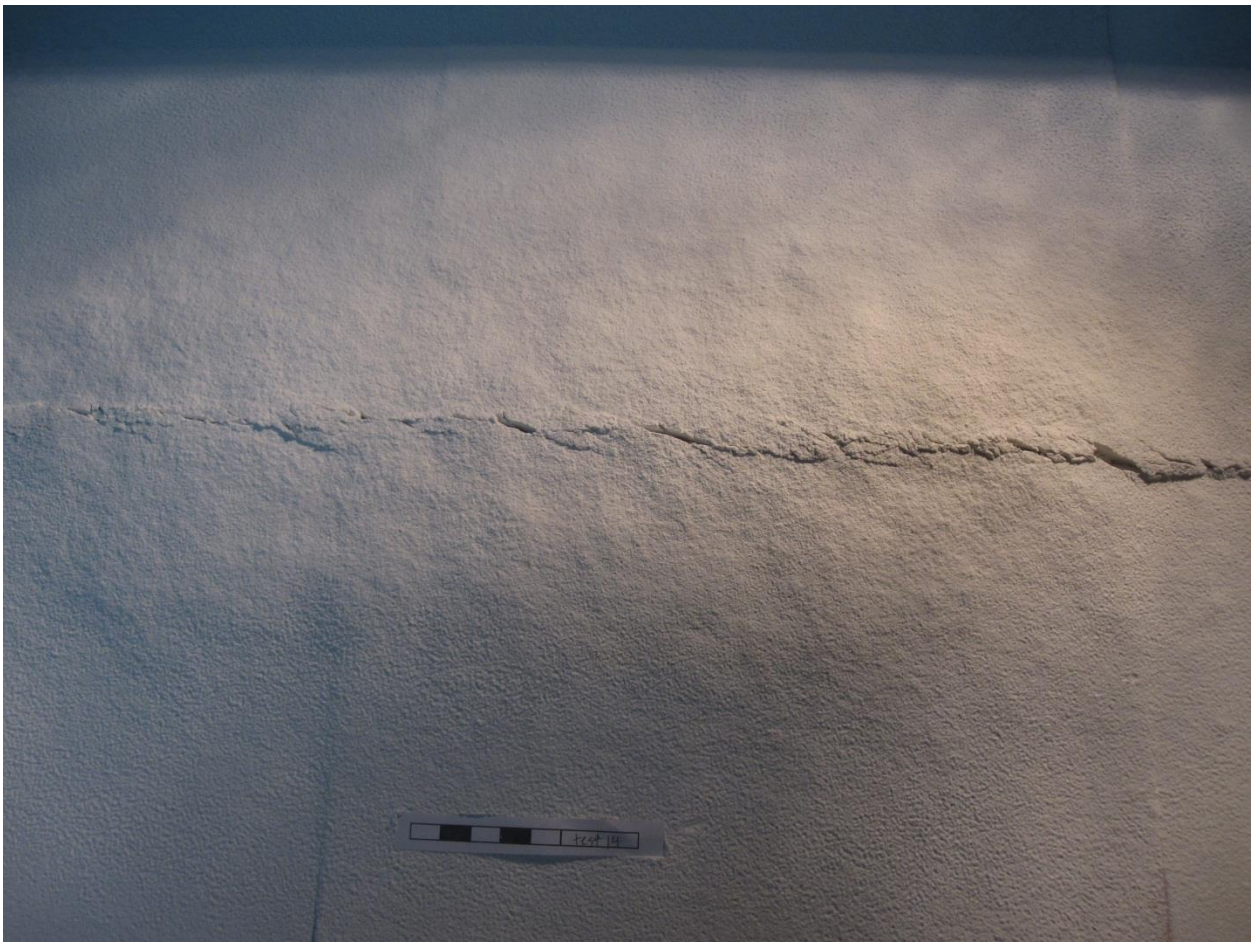

Figure 2.5. Preliminary test #14 using ~1.5 cm thick layer of talc powder after 15 mm displacement. Riedel shears and other fractures have developed in the early stages of deformation, and a single anastomosing fault zone is already visible in some places.

The best method for emplacing the talc powder into the deformation apparatus was found to be shaking it through a sieve, which produced a homogenous texture and smooth surface. Van Gent et al. (2010) did extensive work with gypsum powder and determined that sieving the powder from a height of ≥30 cm produced the least density variation throughout the model. Due to the relatively similar properties of gypsum powder and talc, this sieving height was adopted for these experiments. The sieve used was 710 μm mesh, because it was fine enough to result in a homogenous texture, but large enough to allow the powder through quickly.

Several tests were also performed to determine the thickness of sieved talc powder that best modelled the patterns I was interested in. When the material was too thin (<1 cm) the deformation localized very quickly, within the first 5-10 mm of displacement, so that any structures were either too small or too short-lived to be useful for our study (Figure 2.6). Conversely, when the talc powder approached 3 cm thickness, the material deposited on the model surface began to reach a steady state with the compaction of the powder beneath. This meant that any experiment with such a large thickness took an impractically long time to set up, as well as changing the material properties of the talc at the base of the model. In light of these factors, 2 cm was determined to be an ideal thickness to satisfy the desired requirements.

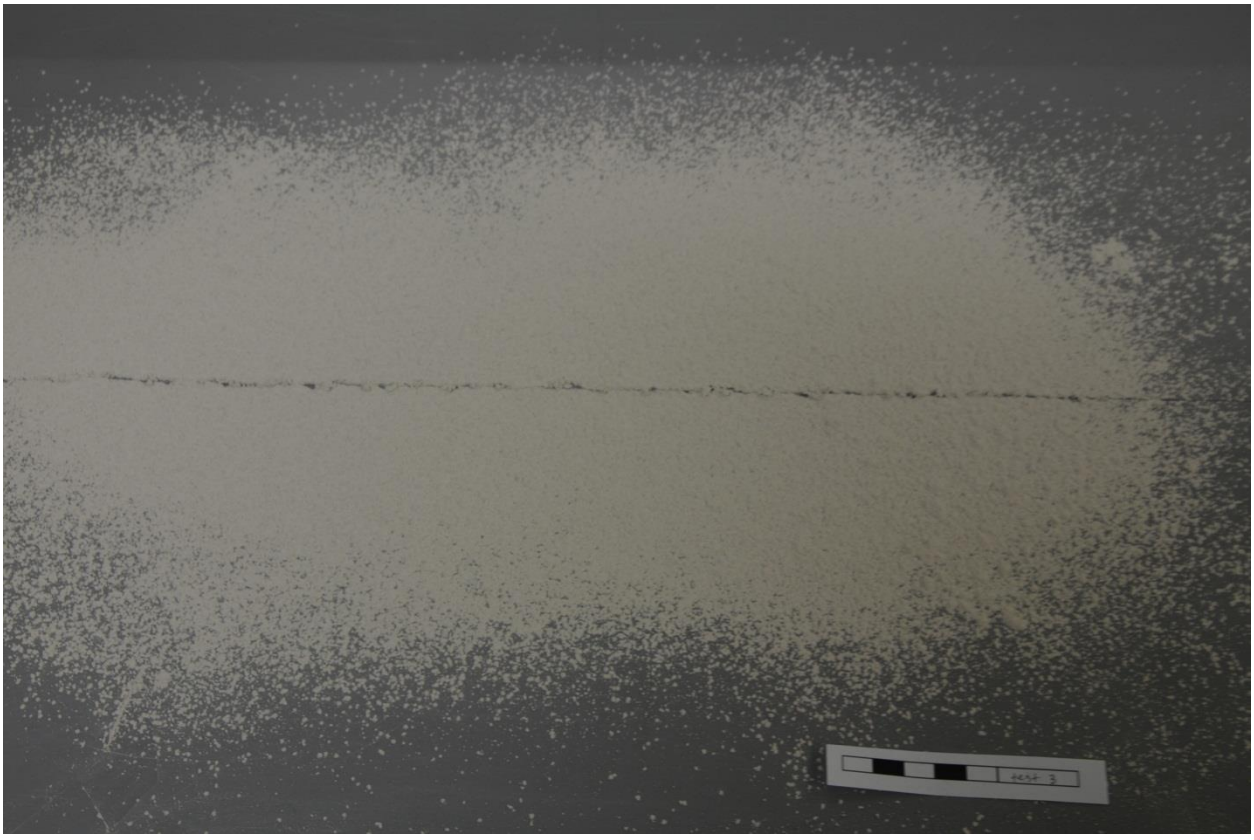

Figure 2.6. Preliminary test #3 using gypsum powder, sieved to a thickness of ~2-3 mm, after 10 mm displacement. The fault is already throughgoing, and any Riedel shears or other structures are too small to be studied in detail.

2.4 Material Properties

Standard tests were performed using a shear wagon as described by Hubbert (1951) to characterize the properties of the granular materials used in the experiments (talc powder and fine sand), specifically the constants describing internal friction in the Coulomb failure criterion:

$$\sigma_{xy} = C + \mu \cdot \sigma$$

where σ_{xy} represents the shear stress at failure, C is the cohesion of the material, μ is the coefficient of internal friction, and σ is the normal stress. The angle of internal friction (φ) can be derived from μ by the relationship tan(φ)=μ.

σ_{xy} and σ can be calculated based on the shear wagon data, and then plotted to give C and μ values. $\sigma_{xy} = \frac{F}{S}$, where F is estimated based on the force data produced during the tests (Figures 2.7, 2.8), and S is the measured surface area of the shear wagon base. Estimating F is nontrivial because of both noise in the force data and an element of personal judgment in where to estimate peaks or yielding points, as described below, which introduces an error of ±1 N.

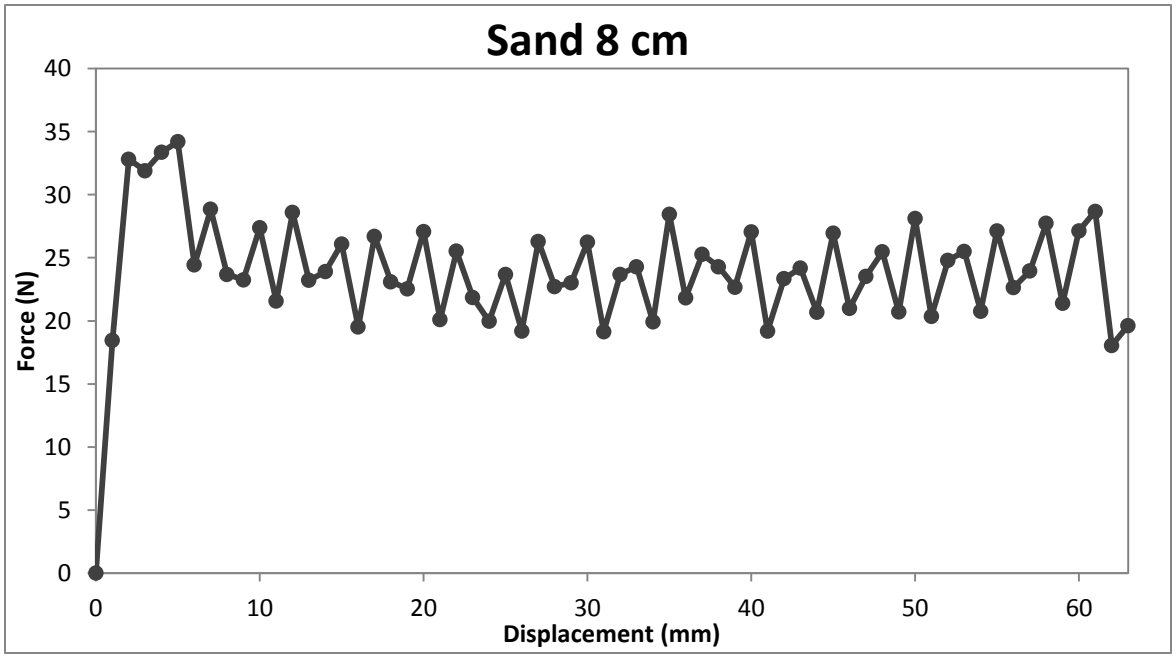

Figure 2.7. Example plot of shear wagon data for fine sand (8 cm thick), which shows an initial peak in force, then stable sliding. The noticeable noise in the data introduces some error into these calculations.

Likewise, the apparatus had its own internal friction for which a correction was made, but which may still contribute to higher shear strain and C values than would be expected. $\sigma = h \cdot g \cdot \rho$, where h is the height of material in the shear wagon apparatus, g is gravity, and ρ is the material density. ρ was calculated by emplacing each material as it was in the experiments into a container of known volume, which was then weighed. Based on multiple repetitions of these measurements, the volumes are accurate to within ~5 cm^3, while the sand masses have an error of ±15 gm and the talc masses have an error of ±1 gm. An additional source of error may be present if there were differences in how the materials were emplaced in the container versus how they were emplaced in the experiments, despite efforts to the contrary. The height of the material in the shear wagon (h) also has an error of ±1 cm because it was difficult to produce a flat, planar surface within the apparatus.

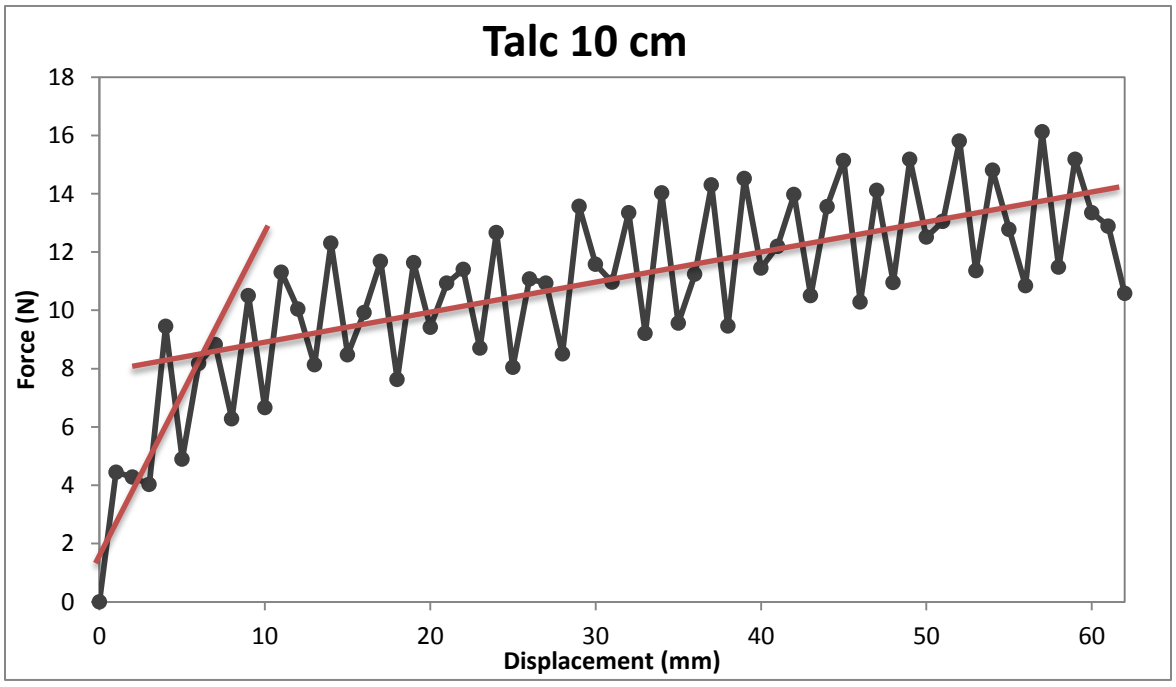

Figure 2.8. Example plot showing shear wagon data for talc (10 cm thick). Visually fitted trendlines indicate an initially rapid increase in force, followed by a later slow, steady increase in force after the "point of yielding", defined here as the intersection between the two trendlines.

C and μ (and, in turn, φ) can be calculated by plotting shear stress versus normal stress for multiple shear wagon tests with different material heights, which gives a linear relationship where the line's slope is μ and its intercept is C (e.g. Figures 2.9, 2.10; Table 2.1). For fine sand, they are calculated for peak and stable strength (Figure 2.7; see Appendix B for data from all individual tests). Talc did not demonstrate the same type of peak and stable behaviour. Instead, the force initially increased steeply, then transitioned to increasing more slowly with displacement, never reaching a stable value within the parameters of our experiment (Figure 2.8). For these data, a "point of yielding" was defined as the intersection between a trendline matching the steep initial increase of force and a trendline matching the later, slowly increasing force (noted on Figure 2.8). φ, C, and μ were also determined at 10, 20, and 30 mm displacement of the shear wagon to quantify how these parameters change with continuing displacement.

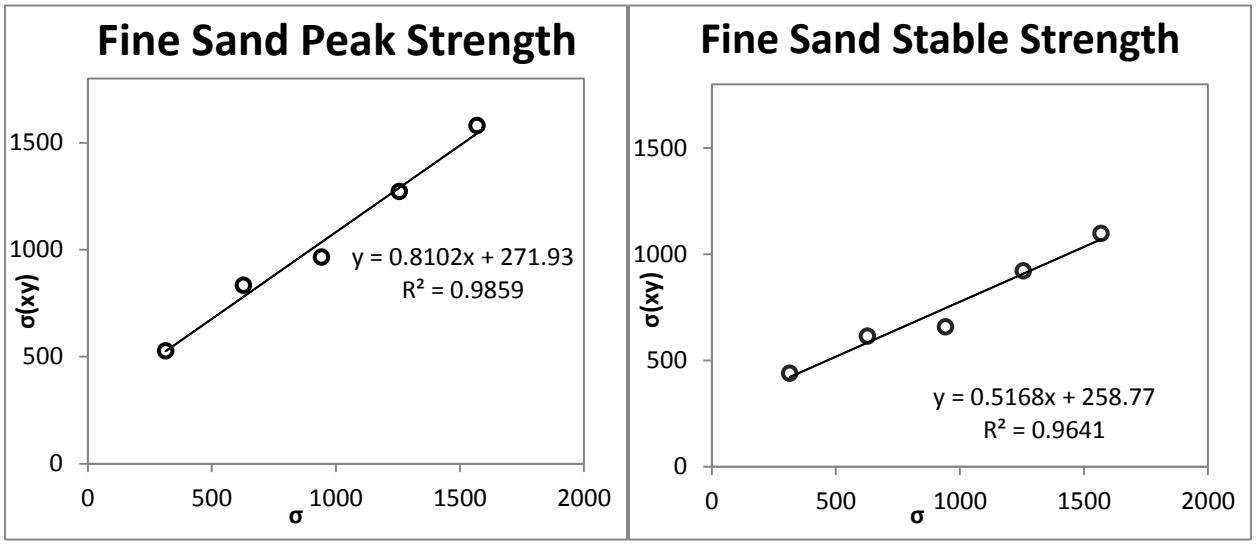

Figure 2.9. Plots of σ_{XY} vs. σ for fine sand at stable strength and peak strength.

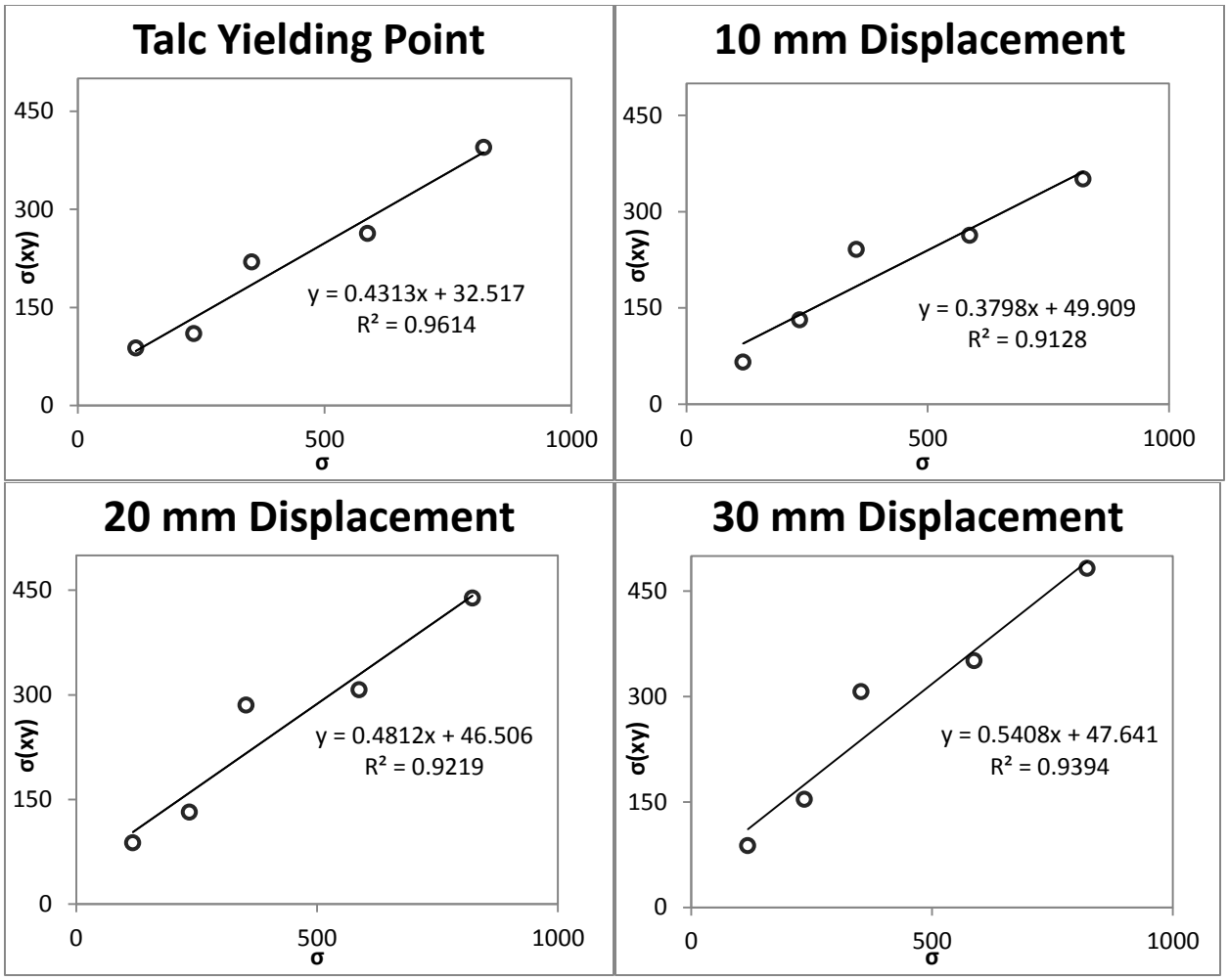

Figure 2.10. Plots of σ_{XY} vs. σ for talc powder at the point of yielding, and after 10, 20, and 30 mm displacement of the shear wagon.

	φ	C	μ [=tan(φ)]
Dry Fine Sand (peak)	39.0°	272	0.81
Dry Fine Sand (stable)	27.3°	259	0.52
Talc (yielding point)	23.3°	33	0.43
Talc (10 mm disp.)	20.8°	50	0.38
Talc (20 mm disp.)	25.7°	47	0.48
Talc (30 mm disp.)	28.4°	48	0.54

Table 2.1. Values describing internal friction measured in shear wagon tests (see Figures 2.9 and 2.10 for graphs used to calculate these values).

For dry fine sand, φ decreases significantly between the peak and stable values, while cohesion remains roughly the same. This behaviour of φ matches values described in the

literature for peak strength (30-40°) and stable strength (25-30°; Dooley and Schreurs, 2012 and references therein) and is consistent with the well-known strain softening behaviour of sifted dry sand. Many literature values for cohesion are closer to 25-100 (Dooley and Schreurs, 2012), although much higher values have been reported (e.g. Rossi and Storti, 2003). Conversely, some authors argue that dry sand has no cohesion (Schellart, 2000). Most likely, the abnormally high cohesion is due to friction in the shear wagon setup, which should be as close to frictionless as possible.

The talc values for φ decrease slightly from the point of yielding, but then increase with continuing displacement, which I suspect is due to increasing compaction of the powder. Cohesion remains roughly stable after the point of yielding, although like sand, these values may be artificially high due to excessive friction in the shear wagon. The literature is very limited regarding the material properties of talc powder and its use in analogue modelling (e.g. Deramond et al., 1983; Soula, 1984; Soula et al., 1988). Soula et al. (1988) only makes passing reference to the material properties of talc, estimating a "shear strength" (which itself depends on cohesion, friction angle, and normal stress) of 10-100 Pa.

Experiments have been performed using other cohesive powders, particularly hemihydrate powder (e.g. Van Gent, 2005; Holland et al., 2006; Van Gent et al., 2010), which was found to be too cohesive for this study. These authors also used a different setup for material characterisation, but their values can provide a point of reference for the material properties of cohesive powders like talc. Van Gent (2005) measured cohesion values for hemihydrate powder of 40-65 Pa and values for the coefficient of friction of ~0.45-0.75. However, in their tests, the cohesion and tensile strength were dependent on compaction, while the coefficient of friction remained constant (Van Gent et al., 2010). Either this is a characteristic specific to hemihydrate

powder, as opposed to a shared characteristic of cohesive powders, or the discrepancies could be caused by the different methods used to measure these properties.

2.5 Scaling

Ideally, scaling relationships between an analogue model and the real world would fulfil several parameters, the first of which is that the angle of internal friction within each system should be the same (Hubbert, 1937). The internal friction of most granular materials, including sand and talc (Table 2.1), fall between 20° and 40°, which is the same range as most brittle upper crustal materials (Dooley and Schreurs, 2012). Second, the ratios of cohesion, density, gravity, and length should satisfy the following relationship:

$$\frac{C_m}{C_n} = \frac{\rho_m}{\rho_n} * \frac{g_m}{g_n} * \frac{L_m}{L_n}$$

where *m* and *n* denote the model and the natural systems, respectively (see section 3.3 for application of these parameters within this study). Here, $\frac{g_m}{g_n} = 1$, and for talc in our experiments, $\frac{\rho_m}{\rho_n} = 0.27$ (for sand this ratio is 0.73). The equation simplifies to $\frac{C_m}{C_n} = 0.27 * \frac{L_m}{L_n}$, so if a reasonable length ratio for our experiments is taken to be ~10^{-4}, i.e. 1 cm = 100 m, then $\frac{C_m}{C_n} = 2.7x10^{-5}$. Essentially, the model material's cohesion would need to be very small compared to the real-world system to satisfy this equation. If $C_m \approx 50\ Pa$ (for talc; Table 2.1), and $C_n \approx 150\ kPa$ based on values for weakly cemented gravels (Fakher et al., 2007), then $\frac{C_m}{C_n} = 3x10^{-4}$, which is within one order of magnitude of the value calculated above ($2.7x10^{-5}$).

While sand is frequently used to model geological phenomena, it is not ideal for all scenarios. In this case, it is particularly unsuitable for modelling the brittle deformation features

this study is concerned with—because sand is effectively cohesionless, it cannot generate sustained fractures and open tension gashes (see section 2.3).

The other parameters that are often included in scaled models are time and strain rate. However, these only need to be addressed for viscous materials, like wet clay or silicone, whose behaviour is dependent on deformation rate. Dry sand and dry talc powder are rate independent materials, so time and strain rate are not relevant for scaling experiments involving these materials. Even so, the deformation rate in all the experiments and materials tests in this study was kept at 1 mm per second.

Beyond the parameters outlined above, many other complexities of the natural world are difficult to include in an analogue model, such as pore pressure, geothermal gradient, and other geological heterogeneities, while some parameters are simply unknown. Despite these limitations, the literature clearly shows that partially scaled experiments provide abundant and useful information about the systems they model (see Dooley and Schreurs, 2012 for a review of analogue modelling studies).

The scaling parameters in this experiment satisfy the relationships defined by Hubbard (1937) within an order of magnitude (Table 2.2). While it might be possible to find a material that is a more exact match, talc powder was additionally a very good morphological match with the deformation observed at the Greendale Fault.

	Model System	Natural System
Internal Friction Angle	20-40°	20-40°
Density	600-1600 kg/m^3	2200 kg/m^3
Gravity	9.8 m/s^2	9.8 m/s^2
Length	(see section 3.3.1.4)	29 ± 0.5 km
Cohesion	25-275 Pa	40-150 kPa

Table 2.2. Scalable parameters based on Hubbert (1937), listed for the model and natural (real world) systems, which should be scaled based on the relationships discussed at the beginning of this section.

It is also possible to consider the scaling of several different length parameters (i.e. fault segment length, overburden thickness, deformation zone width, displacement, etc.) between the models and the natural system. See section 3.3 for more specifics on these scaling parameters.

2.6 Experiments

After carrying out preliminary tests, 13 experiments were performed as part of this study, and 7 of those are examined in detail in this thesis. The experiments can be divided into four main groups: baseline, interseismic and surface effects, macro stepovers, and layered models (Table 2.3). The baseline experiments were the simplest models, providing a point of comparison for the more complicated models constructed later. TALC and TALC_PIV are experiments that consist of 2 cm of talc sieved above the basement fault (Figure 2.11) and are a major focus of this thesis.

Experiment #	Description	Recording Method
TALC	**Baseline: 2 cm of talc**	**Photography**
TALC_PIV	**Baseline: 2 cm of talc**	**PIV**
TALC_ER	**Interseismic erosion: surface scraped smooth at 5 mm intervals**	**Photography**
TALC_SED	**Interseismic sedimentation: talc sieved onto surface at 5 mm intervals**	**Photography**
TALC_SAND	**Layered: 2 cm of talc above 3.5 cm of sand**	**Photography**
TALC_SAND_PIV	**Layered: 2 cm of talc above 3.5 cm of sand**	**PIV**
SAND_PIV	**Layered: 3.5 cm of sand**	**PIV**
STEP3	Stepover: 3 cm width	Photography
STEP3_PIV	Stepover: 3 cm width	PIV
STEP1.5	Stepover: 1.5 cm width	Photography
STEP1.5_PIV	Stepover: 1.5 cm width	PIV

Table 2.3. Experiment numbers, descriptions, and recording methods. Experiments in bold are explored in detail in this thesis.

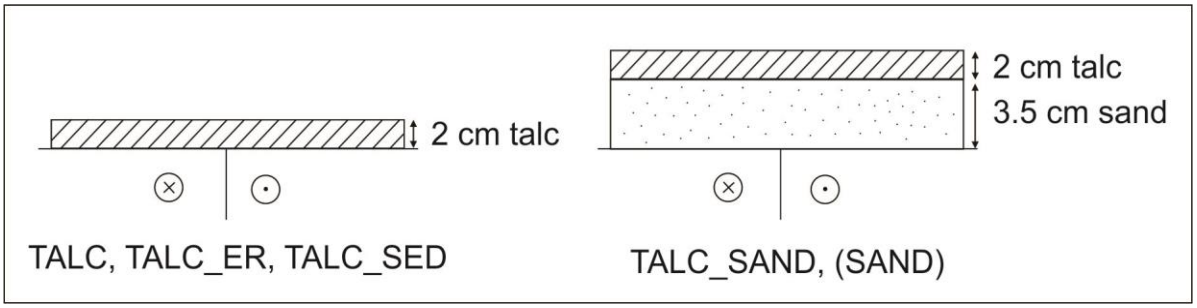

Figure 2.11. Schematic cross sections of model setups. TALC, TALC_ER, and TALC_SED all consist of a 2 cm thickness of talc (shown at left). The setup at the right shows TALC_SAND, while SAND consists of only the lower 3.5 cm layer of sand, without the talc.

The macro stepover group was designed to look closely at the behaviour of individual pop-up structures with different dimensions in STEP3 and STEP1.5, and they were recorded using the PIV system in STEP3_PIV and STEP1.5_PIV. However, for the purposes of this thesis I decided to focus on more basic questions addressed in the other models and did not pursue further analysis of these experiments. Further detail and data for these experiments are available in Appendices A and C, in text and on a data supplement disc.

The experiments studying interseismic and surface effects include TALC_ER and TALC_SED, which were designed to model interseismic erosion and sedimentation, respectively. In TALC_ER, a 2 cm thick layer of talc was sieved above the basement fault (Figure 2.11), and the surface was scraped smooth from left to right with a uniform metal scraper before displacement began, and it was subsequently scraped smooth after sequential 5 mm increments of displacement. This process mimics erosion or agricultural processes that would obscure a fault trace between earthquakes. For TALC_SED, the initial setup was the same as that of TALC (2 cm thickness of talc; Figure 2.11), but after every 5 mm increment of displacement, the motor was paused while a thin layer (1-2 mm) of talc was sifted onto the surface of the model to obscure surface evidence of earlier deformation, modelling a scenario in which significant sedimentation obscures the fault trace between seismic events.

The last group of experiments was an attempt to test the effect of multi-layered materials on the surface expression of the model fault. The experiments consisted of talc layered above fine sand, in an attempt to study the effects of combining cohesive and non-cohesive granular materials. These are TALC_SAND (2 cm of talc above 3.5 cm of fine sand; see Figure 2.11) and TALC_SAND_PIV (the same model recorded by PIV). SAND was a related experiment which was simply the 3.5 cm thick bottom layer of TALC_SAND, without the upper talc layer.

2.7 Greendale Fault Datasets

Several existing datasets were used to map the surface deformation resulting from the Darfield Earthquake. In the days following the September 4th 2010 rupture, LiDAR data was obtained along the fault trace, which has been processed at spatial resolutions of 0.5 and 0.25 m. From these measurements, a Digital Elevation Model (DEM) was produced of the fault zone, as well as slope and aspect maps that highlight different features of the ground deformation (see Figure 2.12 for examples). These data were provided courtesy of ECAN and GNS; please refer to Villamor et al. (2011) for specifics of data collection and processing.

Detailed field mapping was performed after the 2010 earthquake, using real time kinematic (RTK) GPS, differential GPS, and compasses and tape measures (Quigley et al., 2010; Van Dissen et al., 2011; Barrell et al., 2011). Individual structures were mapped, and linear, man-made features such as roads, fences, and hedgerows were used to measure displacements across the fault zone. The detailed methodology used for the collection of these datasets can be found in Villamor et al. (2011).

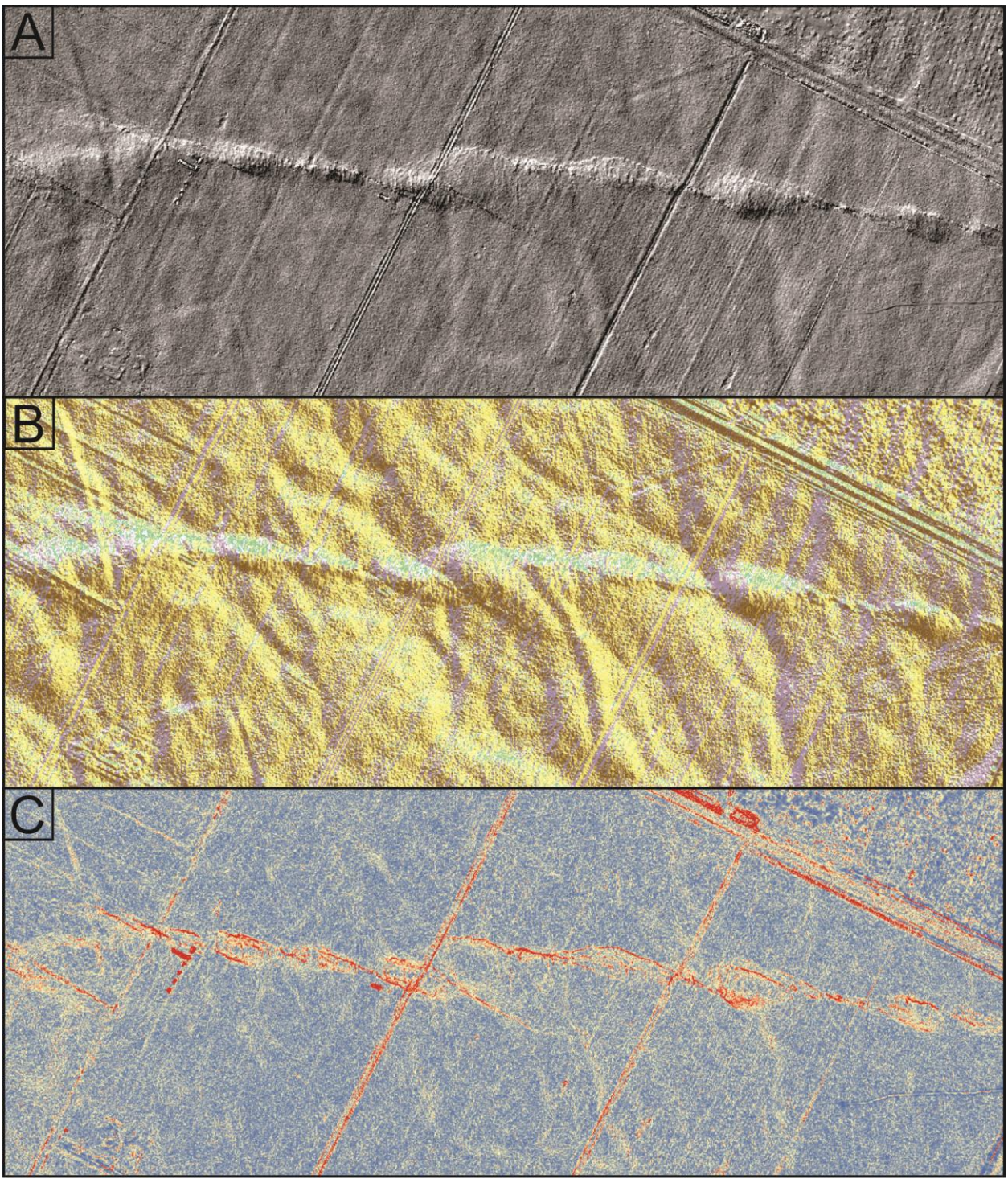

Figure 2.12. Examples of Greendale Fault datasets: A) Hillshade map shows illumination of land surface from the north, B) Aspect map shows downslope direction (0-360°) of the terrain, C) Slope map shows steepness of terrain, highlighting individual fractures. Combining these layers facilitates detailed and accurate mapping of the deformation generated by the fault rupture.

Hundreds of digital aerial photos of the fault trace were taken following the earthquake (photos included in this thesis courtesy of Mark Quigley). These are not oriented exactly orthogonal to the ground surface, which skews the angles of the fractures, making accurate measurements difficult. However, they have been very useful for characterising the small-scale surface structures generated by the fault rupture.

These datasets were all used to produce detailed digital maps of the deformation along the central segment of the fault, which had the highest displacement and the most visible surface deformation. This study incorporates my own maps of the fault zone, which focus on mapping fracture sets in detail and stepovers at multiple scales. A more comprehensive map of the fault's central segment was produced in ARC-GIS by Pilar Villamor and Monica Cabeza, highlighting individual fractures, push-up structures, and broad fault scarps, which has been useful for this study. I also used aerial photos to create maps of individual, meter-scale structures.

2.8 Analysis of Analogue Models and Greendale Fault Data

The data from the analogue experiments is in the form of high-resolution, time-lapse, digital photographs as well as exports from the PIV software. Surface fracture patterns visible in the photos were traced individually using CorelDraw, then exported to ARC-GIS to measure the length and azimuth of each segment, using a toolbar called XTools Pro 9. The program measures the straight-line length between two endpoints, irrespective of curvature; while most structures were not completely linear, they are close enough to linear that this method gives a suitable length measurement within the error of the mapping technique. Azimuths were also adjusted for local fault strike, splitting the central section into four segments with different general trends. ARC-GIS maps of the Greendale Fault surface deformation were analysed using the same

method to produce length and azimuth data, and deformation maps of aerial photos were also processed in the same manner.

Fault zone width was measured on both the still photographs and the PIV data, which produces two different datasets: the still photographs give the width of the zone of discrete fracturing, while the PIV data gives the width of distributed incremental and cumulative shear strain (see section 3.2 for examples of these data). Each of these quantities was measured with minimum and maximum values, to take into account the significant variation along the fault zone between areas where deformation was localized on a single shear versus where it was spread over several oblique fractures.

3. FAULT ZONE DEVELOPMENT AND CONTROLS ON SURFACE MORPHOLOGY FROM ANALOGUE EXPERIMENTS

3.1 INTRODUCTION

The goal of this chapter is to document the analogue modelling study, identify the experiments that best fit the features observed at the Greendale Fault, and assess the implications of the results for understanding deformation associated with the Greendale Fault surface rupture. A series of experimental fault zones were compared both quantitatively and qualitatively with the Greendale Fault deformation to identify the closest matches. Some of these experiments consider the influence of interseismic activity on the development of the fault zone. These results have implications for future paleoseismic studies of the Greendale Fault, and consequently for understanding the future hazard posed by the fault, which is addressed further in Chapter 4. This analysis can be more broadly applied to the study of any strike-slip fault zone developing in granular materials.

3.2 DATA AND RESULTS

3.2.1 Experimental Results

3.2.1.1 TALC and TALC_PIV

TALC and TALC_PIV are the simplest experiments in this study, and they are intended as a baseline with which to compare the other, more complex models. They consist of a 2 cm thick layer of talc sieved above the model's "basement fault", which was displaced at 1 mm/second for ~50 mm. The same experiment was performed twice, once recorded with time-lapse photography (TALC) and once with the PIV system (TALC_PIV).

After 3-5 mm displacement, the first Riedel (R) shears initiate, which are oriented at 110-115° (measured clockwise from 0° as north, with the underlying fault striking 90°; see Figures 3.1, 3.2**).** At 10 mm displacement, lower angle Riedel shears (~105°, noted by Naylor et al., 1986, and identified here as R_L shears following the terminology of Schreurs, 1994) start to develop in limited areas, linking the initial fractures. By 20 mm, R_L structures are widespread throughout the fault zone, and P shears (85-95°) have begun to develop (Figure 3.1). Longer fractures also develop, particularly in the 90-120° range (Figure 3.3). At this point, displacement is partially occurring on Y shears, and by 30 mm displacement the fault is fully throughgoing, though some inactive, more oblique structures are still visible (Figure 3.1). The longest fractures (>2.5 cm) occur at these later strain intervals and all strike 90-100°, showing the progression from oblique structures toward a single, throughgoing Y shear (Figure 3.3).

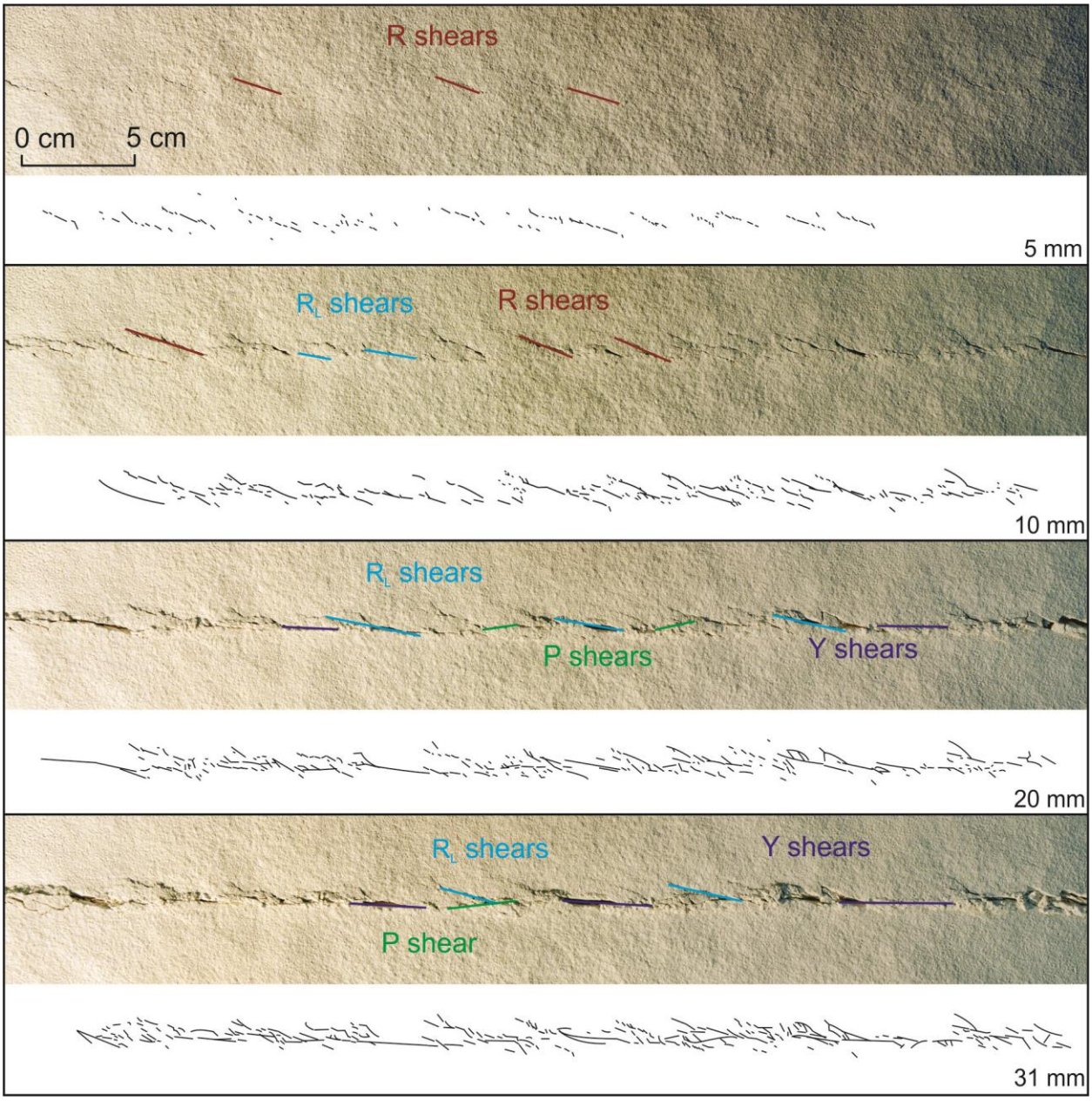

Figure 3.1. Images of TALC model at successive strain increments with corresponding fracture maps. Examples of R, R_L, P, and Y shears are highlighted. Note progression from oblique structures to more fault-parallel structures, although inactive, oblique fractures are still present at later strain intervals. All experiment images are available in Appendix C (data supplement disc).

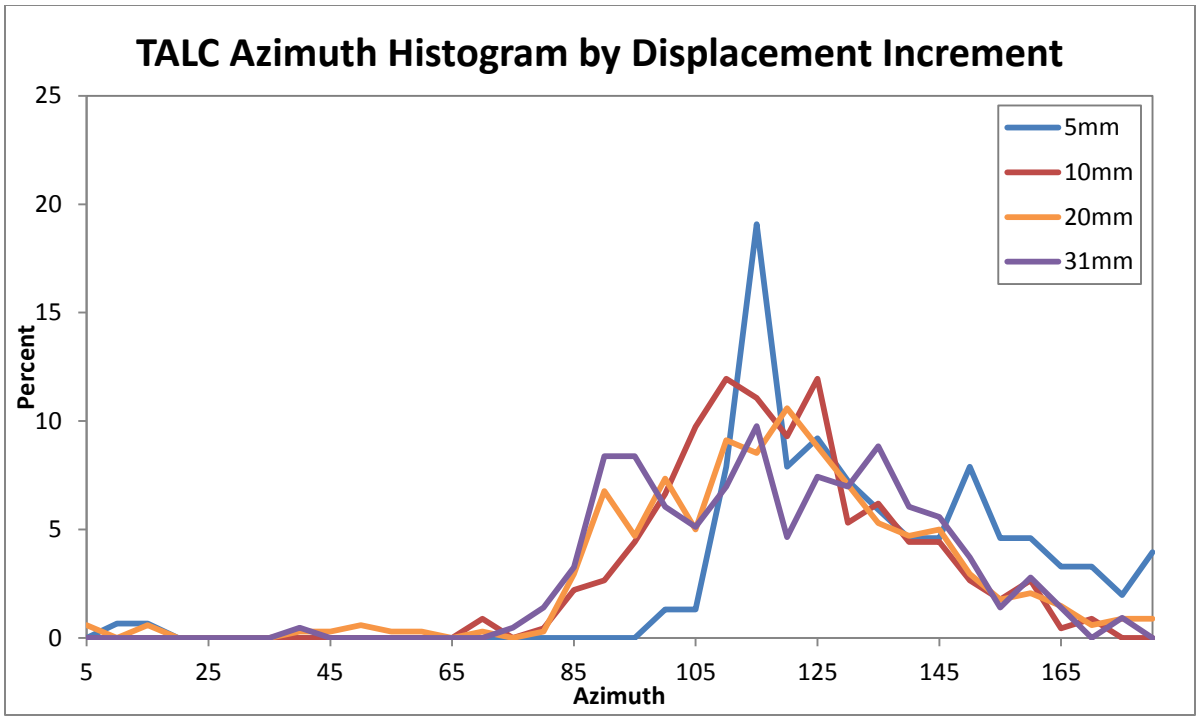

Figure 3.2. Distribution of fracture azimuths in TALC at progressive strain intervals. Initial fractures (5 mm displacement) are noticeably more oblique than later-developing structures.

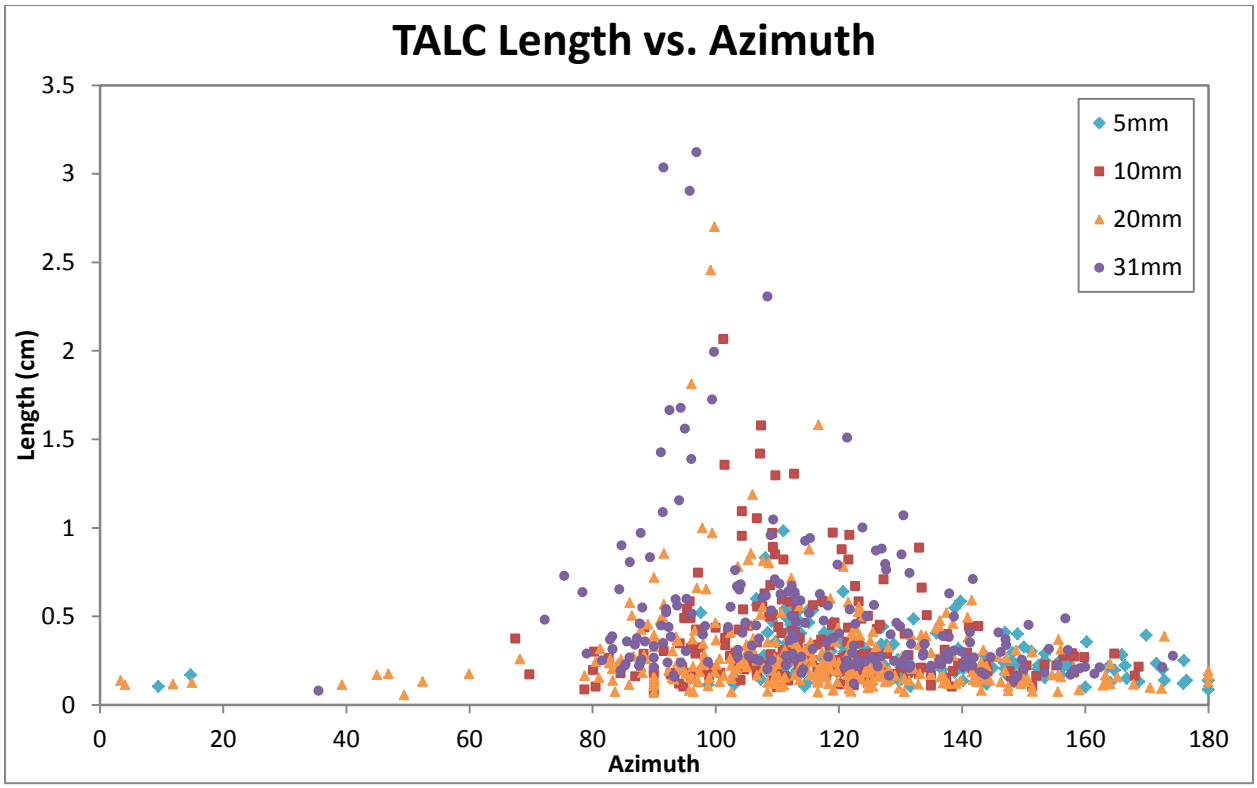

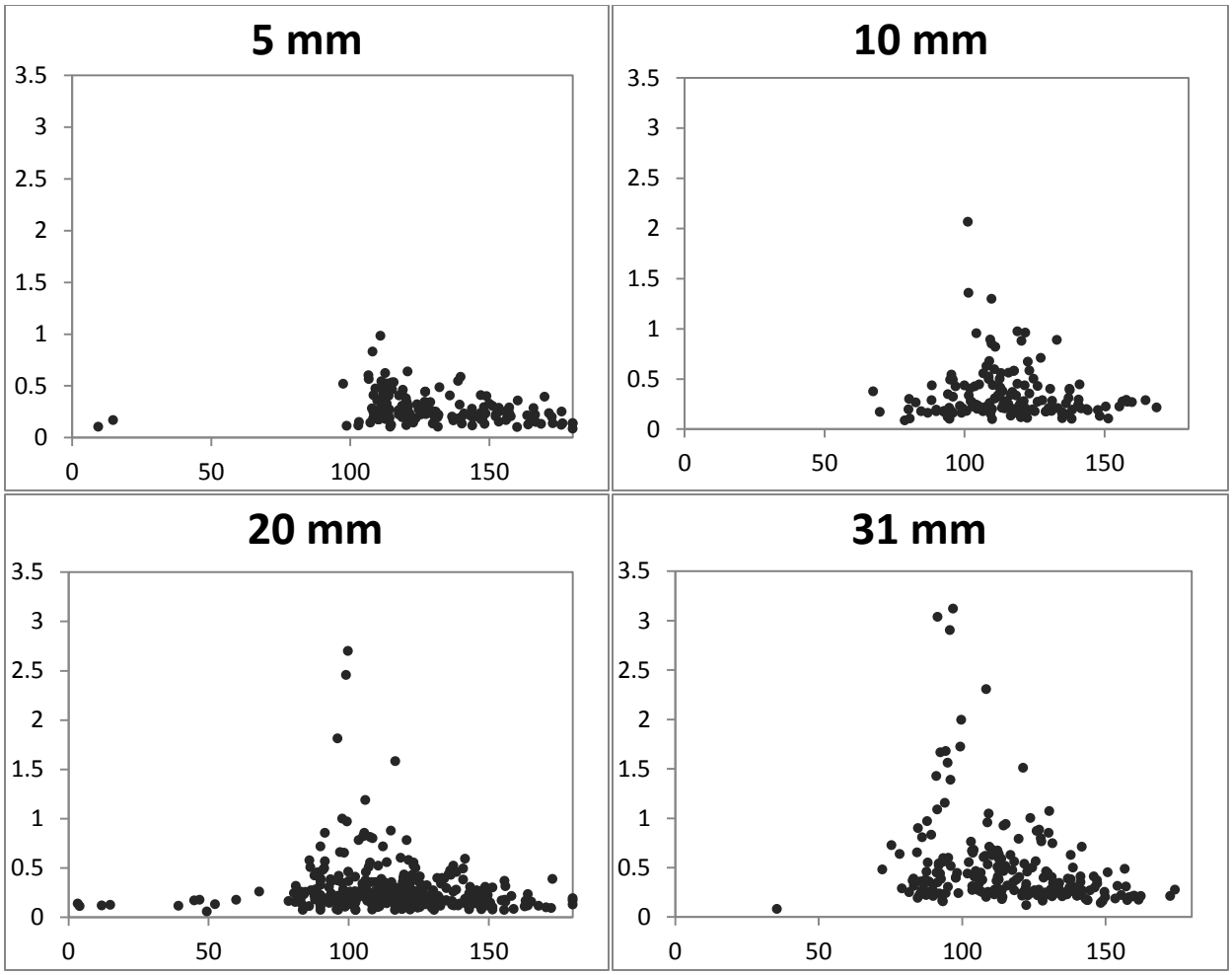

Figure 3.3. TALC fracture length plotted versus fracture azimuth. All displacement increments are plotted together (top), with individual increments shown below. With increasing strain, structures grow in length and become more parallel to the underlying fault. The longest structures are all in the ~90-120° range.

The zone of discrete fracturing in this experiment quickly grows in width with the initiation of surface fractures from ~5 mm displacement, then subsequently peaks when the highest angle fractures (R shears) are at their peak length (Figure 3.4). As lower angle fractures become dominant with increasing displacement, the deformation zone width gradually narrows.

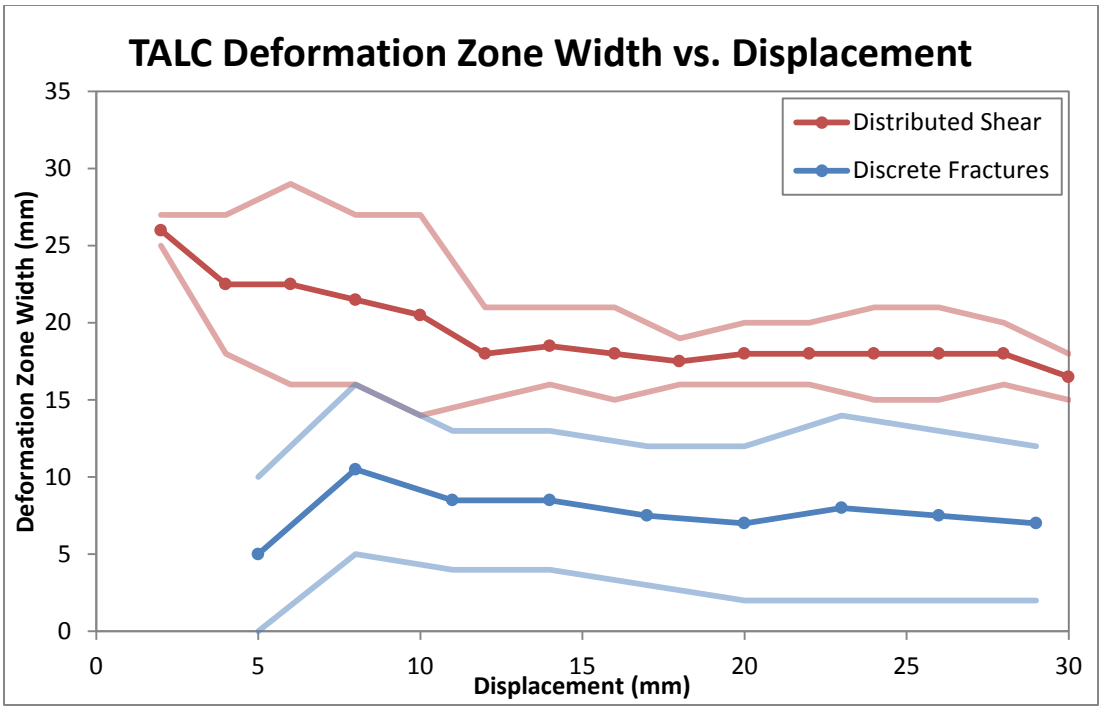

Figure 3.4. Plot showing development of TALC deformation zone widths (both discrete fracturing and distributed shear) with continuing displacement. The mean width is highlighted, while minimum and maximum values are shown in lighter colours.

The PIV data from this experiment (TALC_PIV) shows the shear strain distribution with continuing fault displacement, which is markedly different to the deformation that manifests as discrete fractures. The zone of distributed shear is initially quite wide, measuring 20-30 mm across, perpendicular to the underlying fault strike (Figure 3.5, 0-4 mm). This zone quickly narrows as shear strain begins to localize around several oblique, linear fractures. The deformation zone widens briefly as these shears lengthen (Figure 3.5, 4-6 mm), then narrows as these structures link together and shearing starts to localize on the Y shear (Figure 3.5, 6-12 mm). After ~15 mm displacement, the deformation zone stabilizes at 15-20 mm wide (Figure 3.5, 14-30 mm). See Figure 3.4 for a comparison of the distributed shear zone width and the width of discrete fracturing through time.

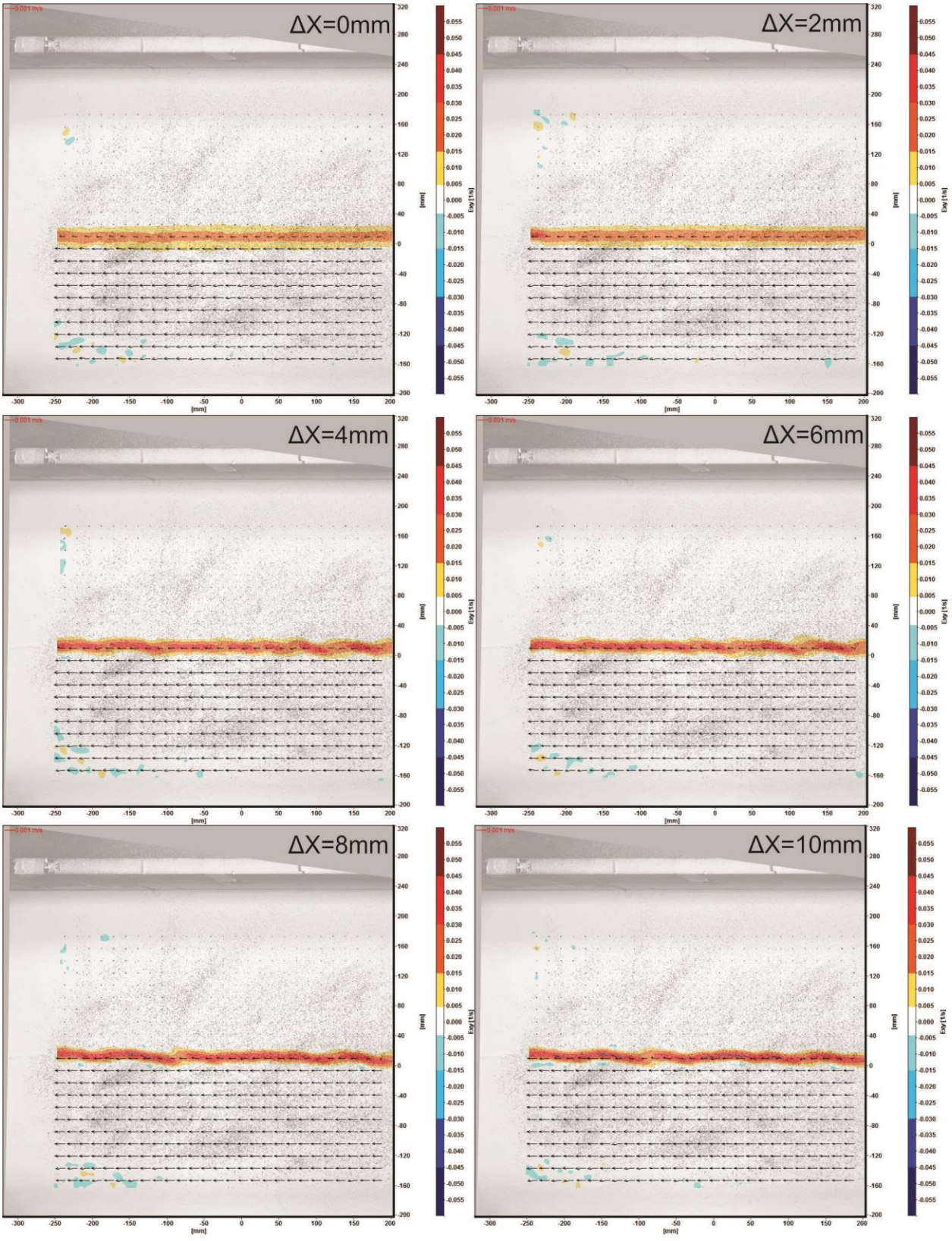
ΔX=0mm
ΔX=2mm
ΔX=4mm
ΔX=6mm
ΔX=8mm
ΔX=10mm
[mm]
Exy [1/s]

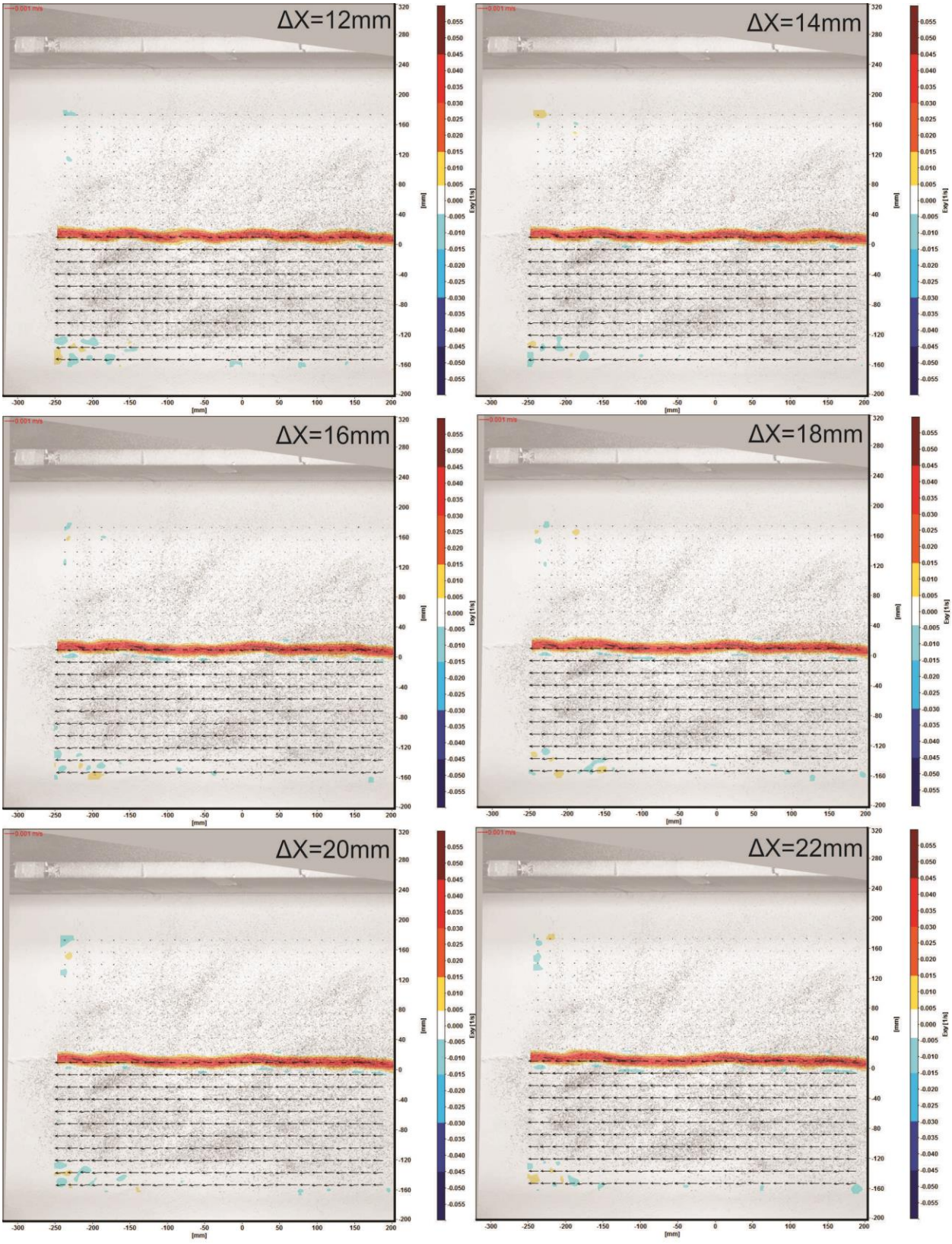
ΔX=12mm
ΔX=14mm
ΔX=16mm
ΔX=18mm
ΔX=20mm
ΔX=22mm
[mm]
Exy [1/s]

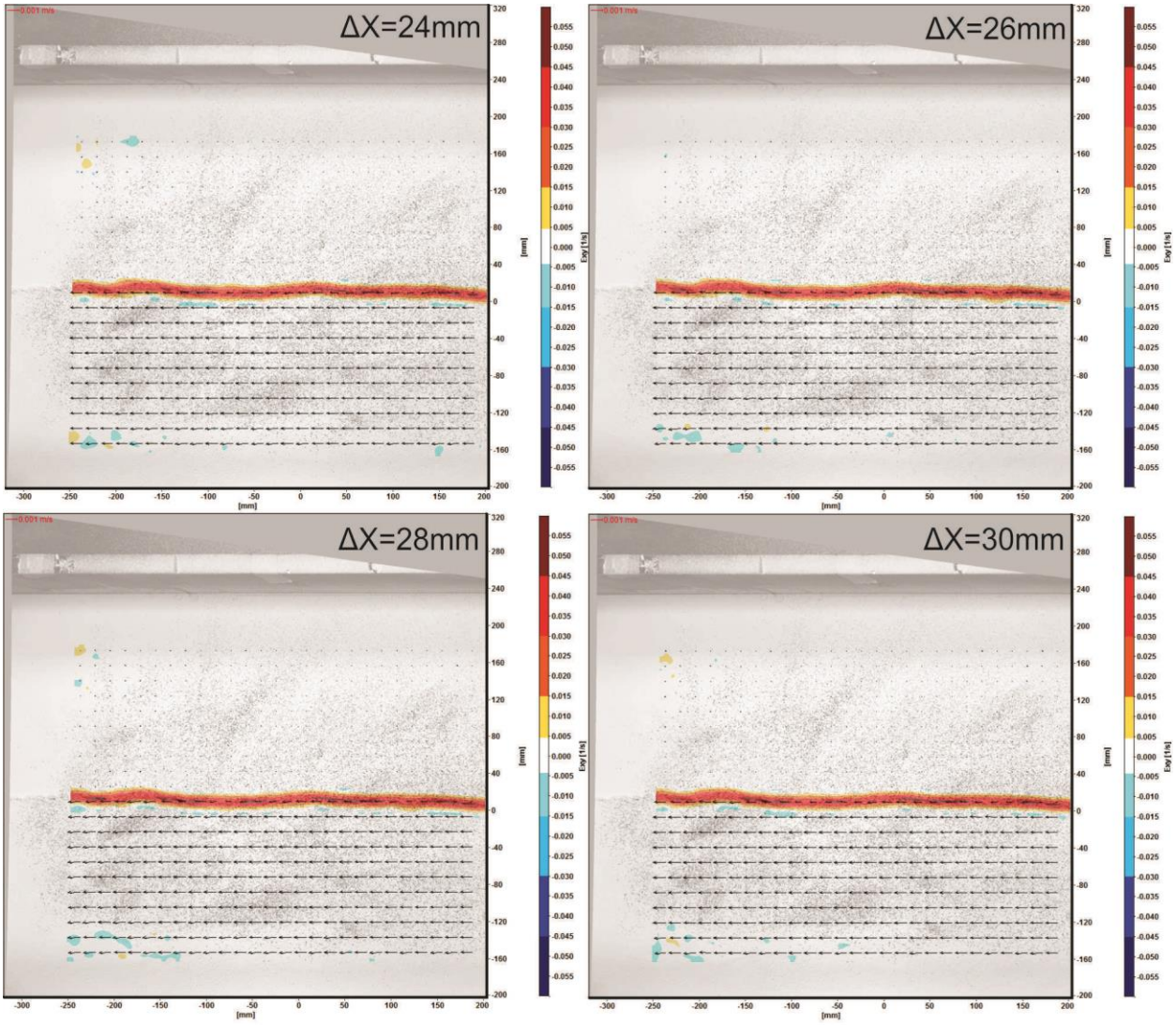

Figure 3.5. TALC_PIV data showing shear strain distribution in 2 mm displacement increments from 0-30 mm. Initially shear strain is distributed widely, then it focuses along oblique Riedel shears before localizing along the Y shear plane. All PIV images are available in Appendix D (data supplement disc).

3.2.1.2 TALC_SED

TALC_SED was designed to test the effects of interseismic sedimentation on surface rupture patterns by displacing the model fault in 5 mm increments and sifting a thin layer of talc onto the model surface while the motor was paused (see section 2.6 for further description). The initial setup was a 2 cm thick layer of talc, and the basement fault was offset at 1 mm/second for

30 mm. The talc layer sifted onto the surface between displacement intervals represents interseismic sedimentation at a fault trace.

As in the TALC experiment, initial Riedel (R) shears appear at 3-5 mm displacement (Figure 3.6). The majority of these early fractures are oblique to the PSZ (115-125°; see Figure 3.7). These were subsequently obscured by the "sedimentation" at 5 mm displacement, but they reappeared within 1-2 mm of motion restarting and began to be linked by lower angle Riedel (R_L) shears at 10 mm displacement. With increasing strain, a much broader range of structures began to develop, at both 50-100° and >150°, as well as some longer structures developing at 10 mm displacement (Figure 3.8). However, even the longest fractures in this experiment (1.5-2.5 cm) are significantly shorter than the longest structures in TALC (2.5-3.5 cm). During the 10-15 mm interval, most displacement occurred on R_L shears, while the higher angle shears took up relatively little displacement.

It should be noted that these low angle shears are not always single extended segments, but are sometimes made up of smaller shears that are slightly oblique to the trend of the overall segment (i.e. "Riedel within Riedel" patterns; Figures 1.6, 1.7). After 15 mm, most displacement continues to occur on R_L and P shears, although some more oblique structures persist (Figure 3.6). The experiment was halted at 30 mm total displacement, when it was approaching a single throughgoing fault zone.

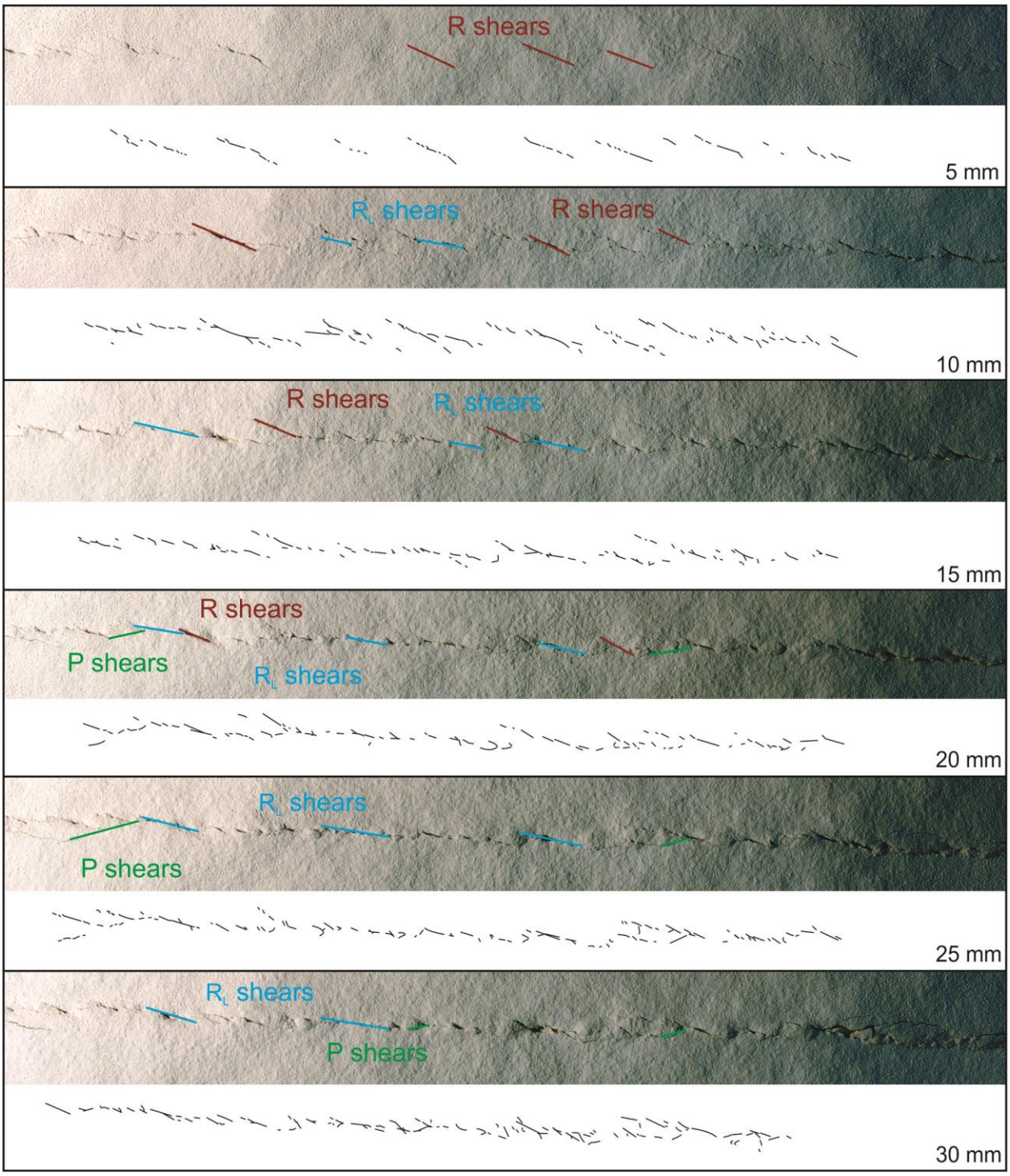

Figure 3.6. TALC_SED images at successive strain increments with corresponding fracture maps. Examples of R, R_L, and P shears are highlighted; Y shears have not developed by the end of the experiment. All experiment images are available in Appendix C (data supplement disc).

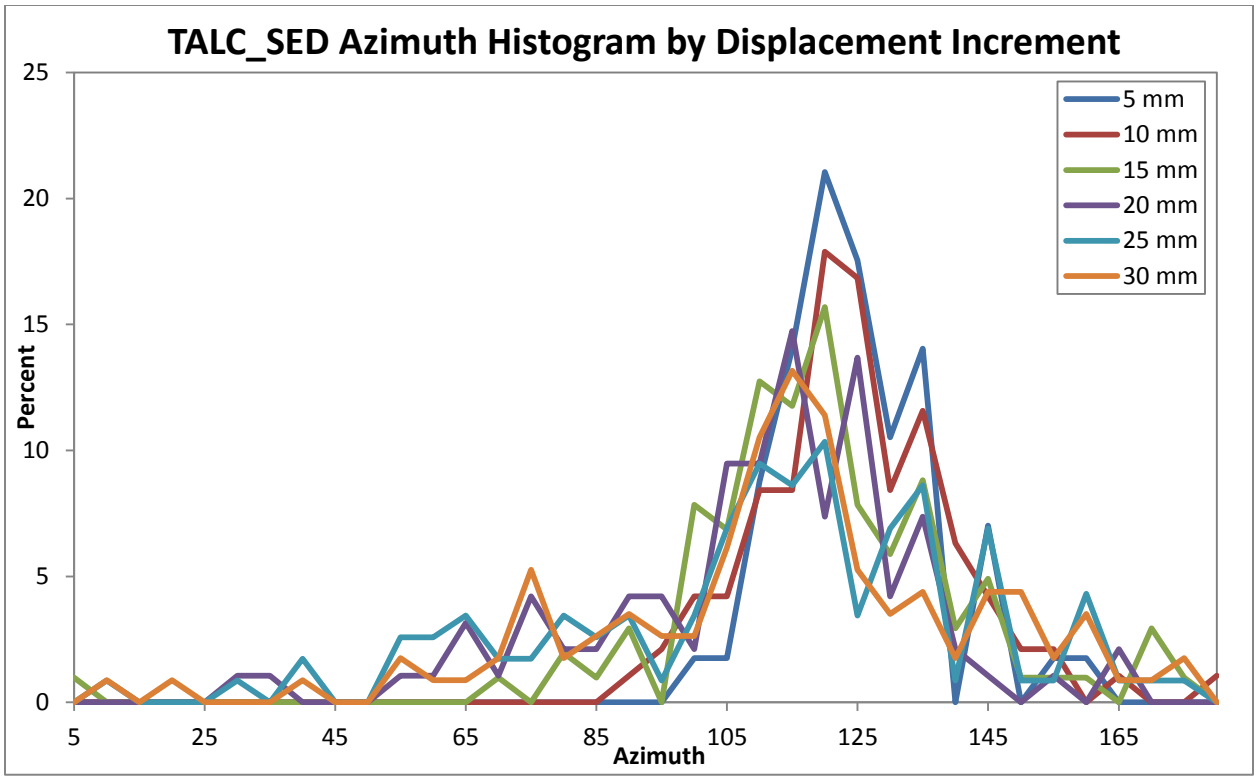

Figure 3.7. Distribution of fracture azimuths in TALC_SED at progressive strain intervals. Initial fractures (5-10 mm) have a noticeably higher percentage of oblique fractures (115-125°) than are present at later strain intervals, where there are more fault-parallel structures.

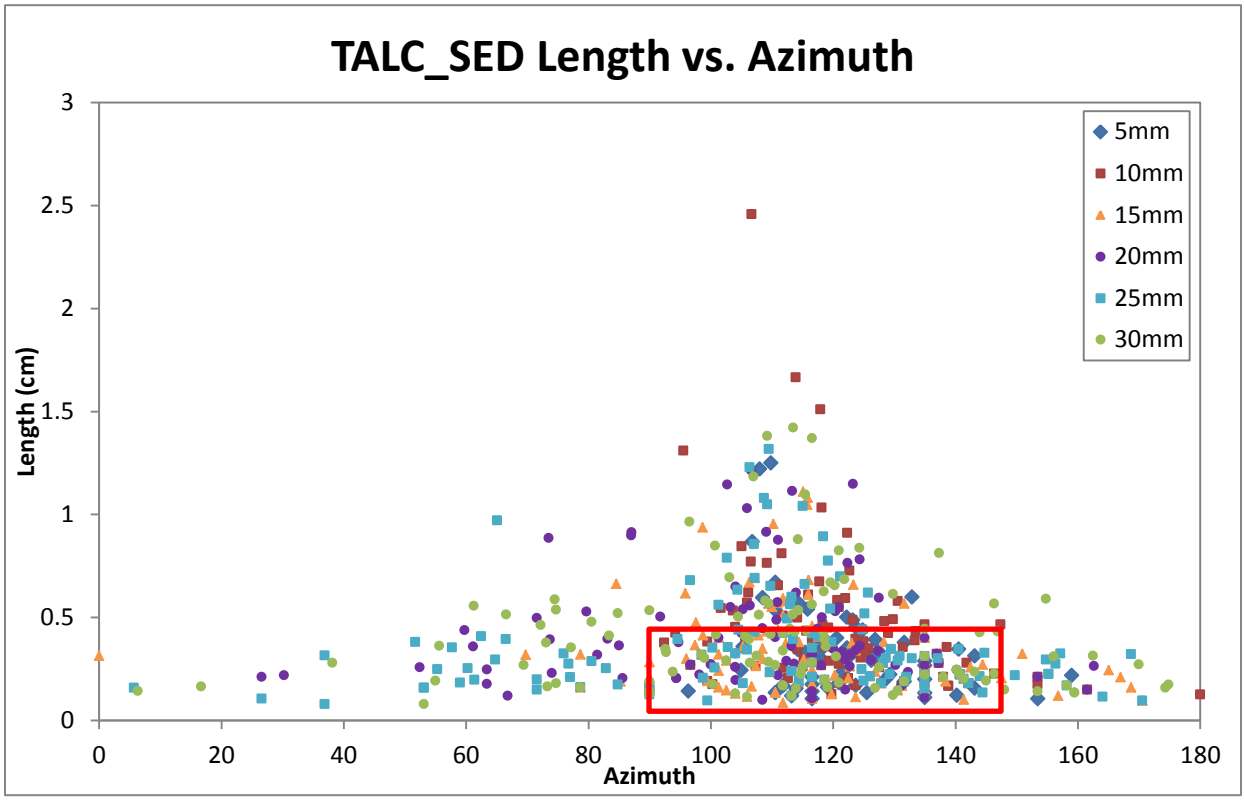

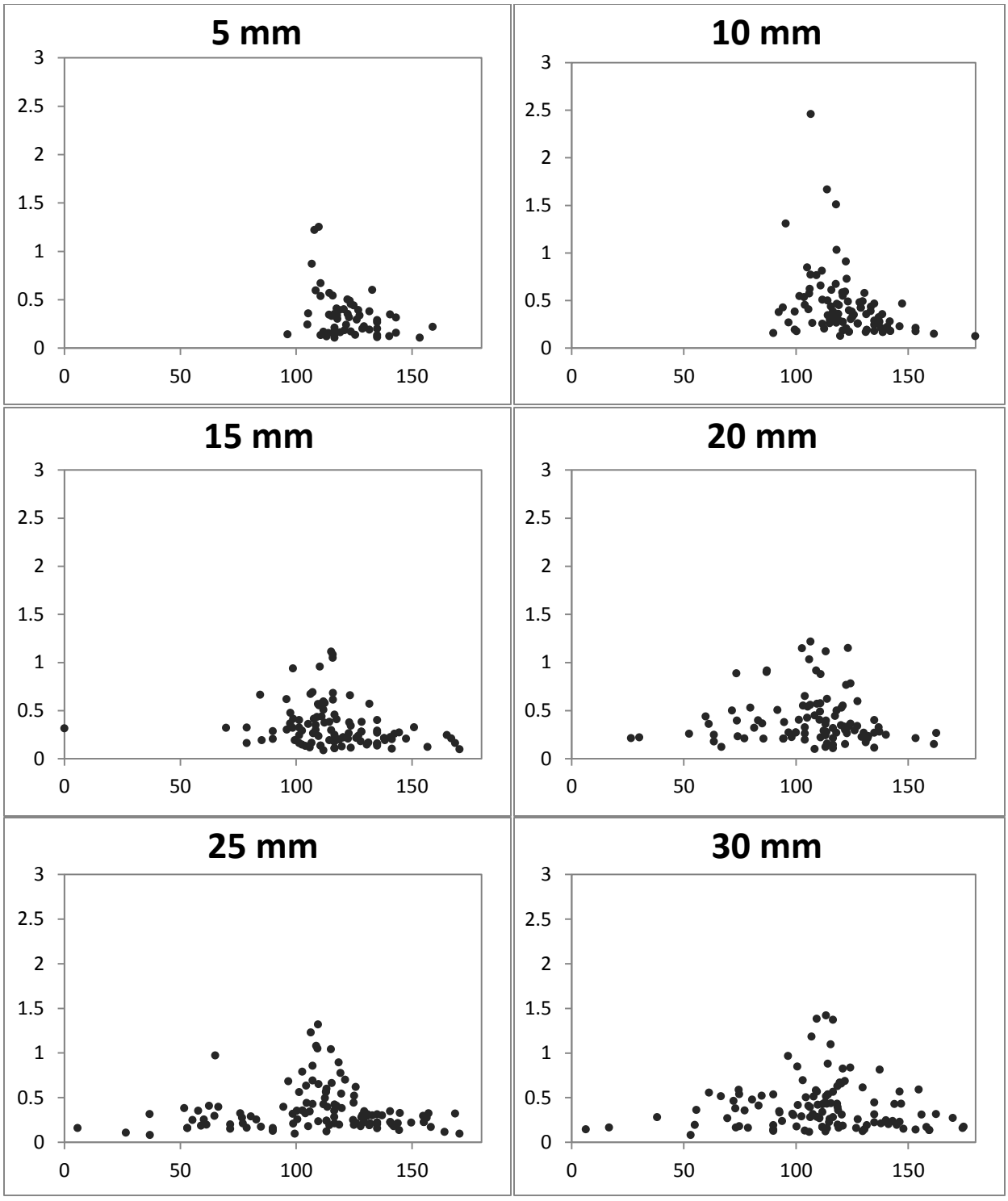

Figure 3.8. TALC_SED fracture length versus azimuth. All displacement increments plotted together (top); individual increments below. Note the development of structures at all azimuths with increasing displacement, while the longest fractures focused between 90 and 130°. The red rectangle in the upper plot highlights the pattern of concentric arcs discussed below.

The plot of length versus azimuth for all strain increments also shows a subtle pattern of concentric arcs, most visible at small lengths in the 100-135° range (highlighted on Figure 3.8), which is generated by the process of tracing the fracture patterns. Each line segment is represented by pixels, so at very short lengths, there are only a few combinations of pixels that can represent the diagonal segments, i.e. x=5, y=2, or x=4, y=3, etc., and therefore only a few specific angles that will be measured. This pattern is also visible in Figure 3.46 in the 80-100° range. The spikes in plots of azimuth distribution at 90° and 135° are also explained by this principle, because they are angles easily represented by small combinations of pixels (e.g. Figure 3.26, 3.38). Essentially, the shorter the segment, the larger the potential error (maximum error is ± ~5°). This should be taken into account when considering short fractures, but the error is minimal for lengths greater than 0.25 cm, and disappears completely for lengths over 0.5 cm. This pattern is present in every plot of length vs. azimuth, but how apparent it is depends on the design of the graph and the conditions of the experiment.

3.2.1.3 TALC_ER

TALC_ER was designed to model interseismic erosion or agricultural activity, by scraping the model surface smooth from right to left before displacement began and at 5 mm intervals afterward (see section 2.6 for further detail). As in TALC and TALC_SED, the initial setup was a 2 cm thick layer of talc, and the model fault was displaced at 1 mm/second for 40 mm total.

The first structures to develop at 3-5 mm displacement are R shears (Figure 3.9). These incipient shears are significantly more oblique than initial R shears in previous experiments, forming at angles greater than 120° (Figure 3.10). There is also a subtle vertical fabric (aligned in

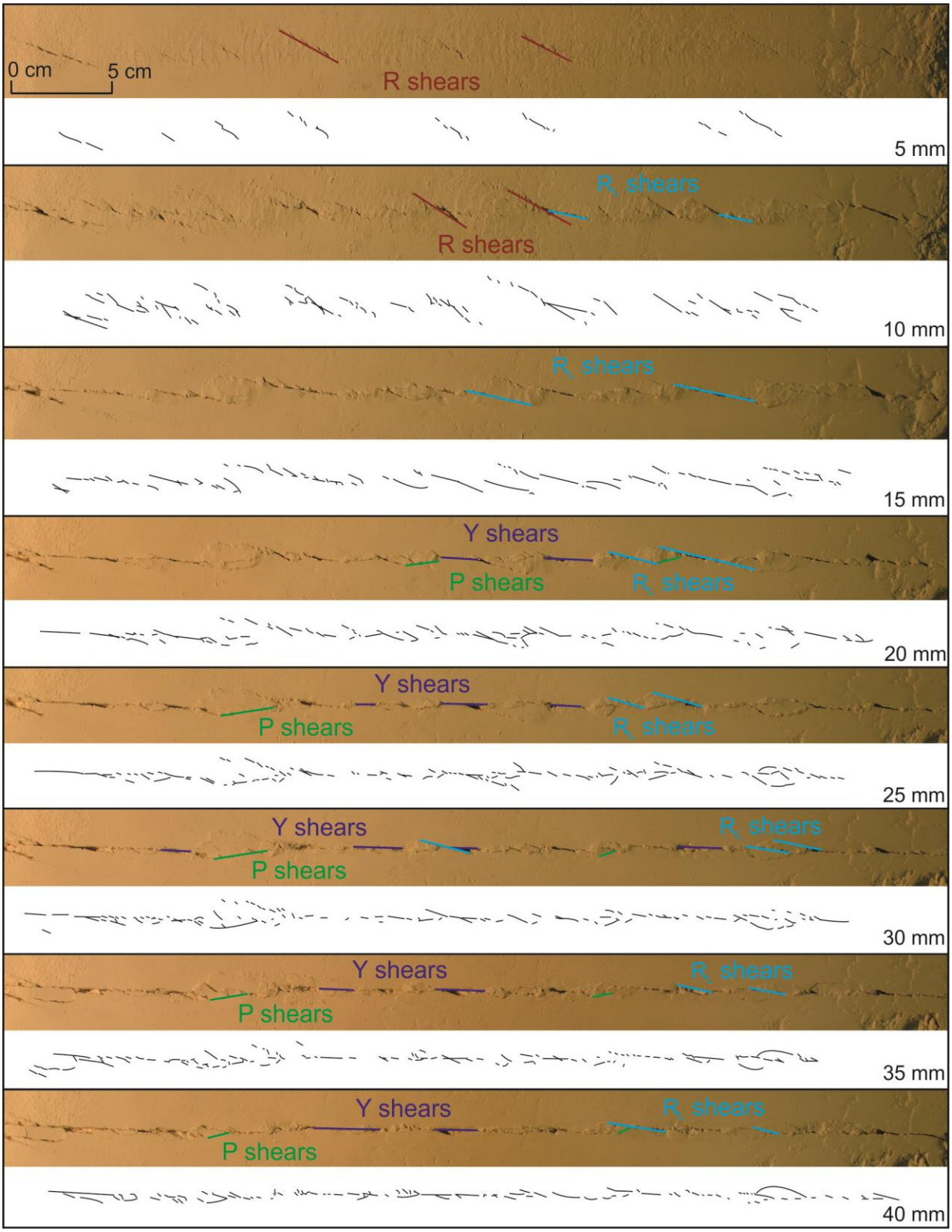

Figure 3.9. TALC_ER images at successive strain increments with corresponding fracture maps. Examples of R, R_L, P, and Y shears are highlighted. Note progression from initial, oblique R shears, to the presence of more fault-parallel structures (R_L, P, and Y shears). All experiment images are available in Appendix C (data supplement disc).

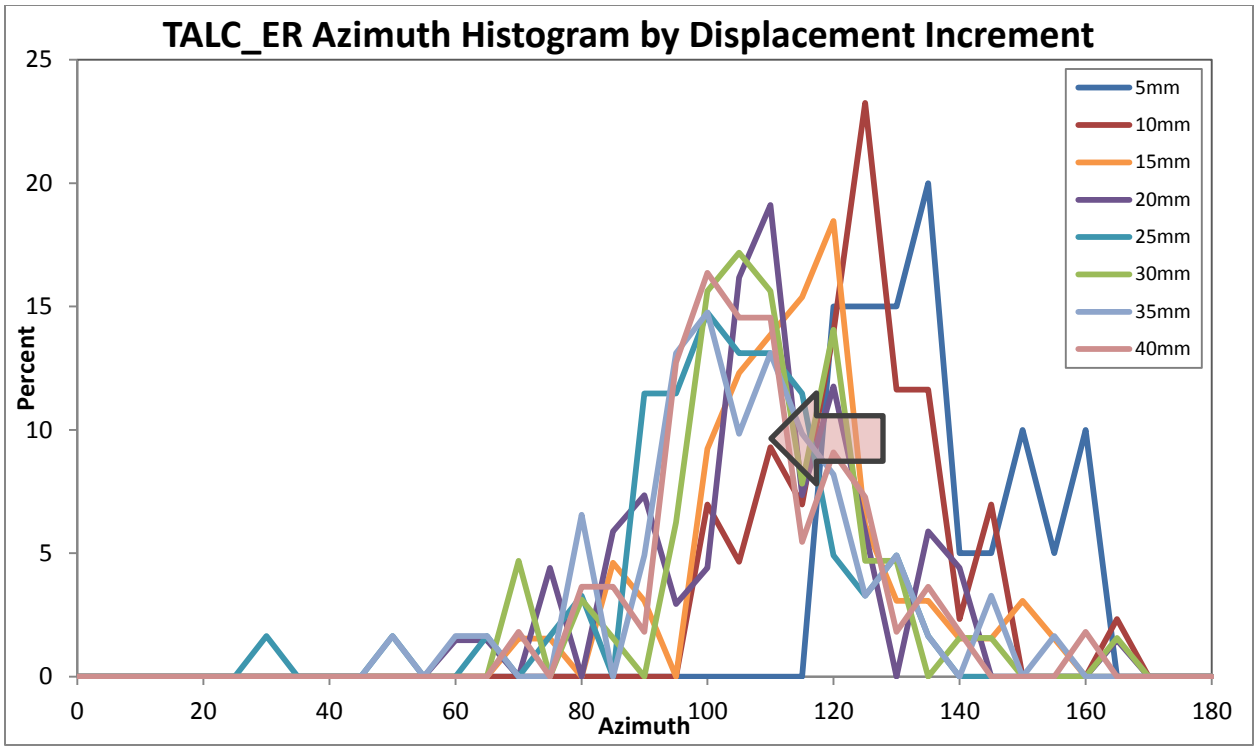

Figure 3.10. Distribution of azimuths in TALC_ER by displacement increment. Arrow indicates general trend from oblique fractures (<120° for structures at 5 mm and 10 mm displacement) to more fault-parallel ones.

the 0°/180° direction) highlighted by progressive deformation. This is likely caused by the process of scraping the surface of the model, which slightly compresses the surface and probably aligns the talc particles so that they are more likely to form fault-perpendicular fractures (see section 4.3.2 for further detail on these surface effects).

With continuing displacement, these initial, oblique R fractures are cross cut by lower angle R_L structures in the 100-120° range, which start to fill in the gaps between initial fractures (Figure 3.9, 10 mm). This transition is easy to see in the plot of azimuth distribution, as well as length versus azimuth, where you can see more fault-parallel structures developing with increasing strain (Figures 3.10, 3.11). By 15 mm displacement, a classic en echelon pattern has developed, made up of R_L shears separated by stepovers and pop-up structures. At 20-25 mm, some P shears have developed as the pop-ups are starting to be cross-cut, and Y shears become

visible as well. As the fault zone develops further (35-40 mm), these fractures begin to coalesce into a single throughgoing fault zone parallel to the PSZ, though some pop-up structures persist.

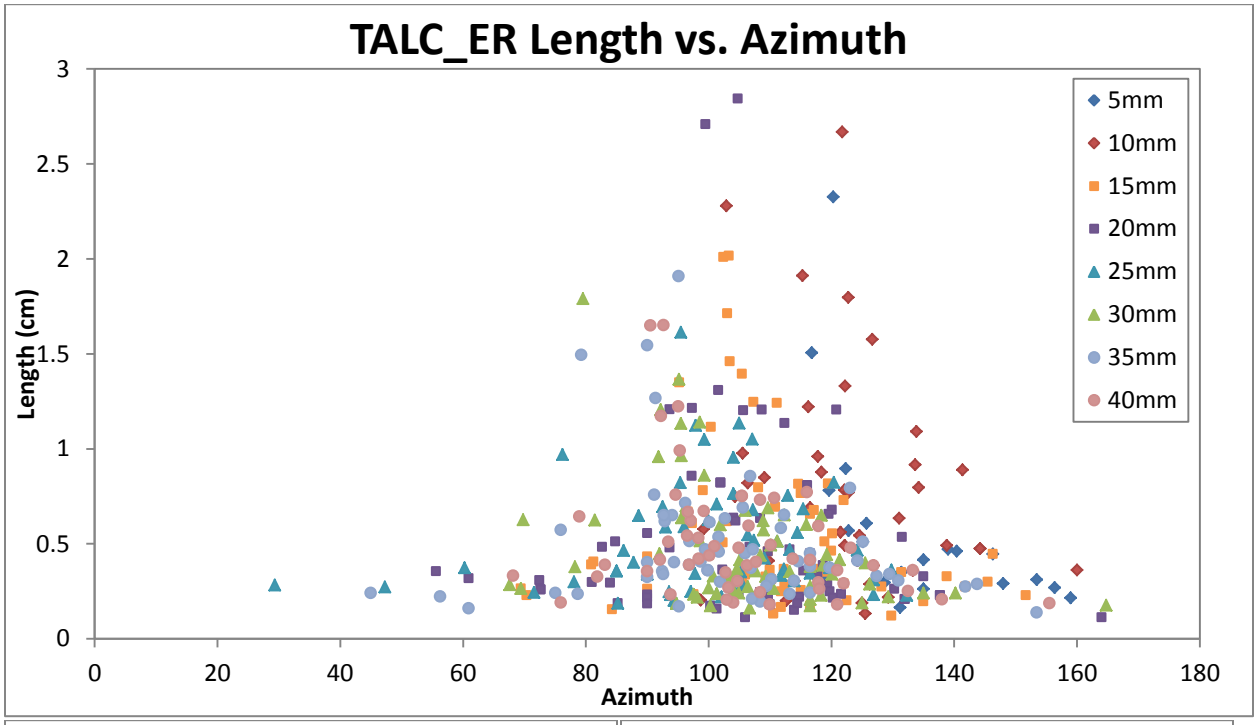

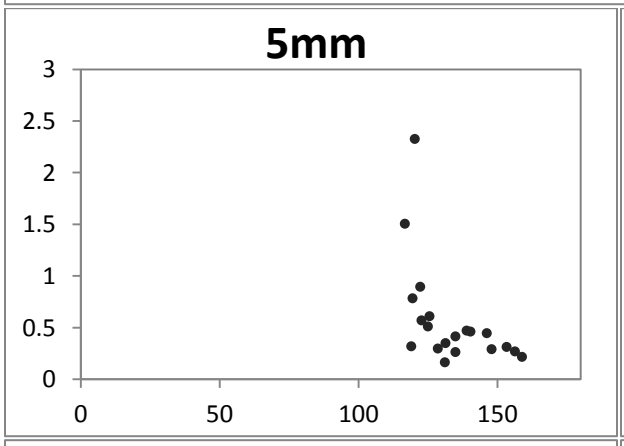

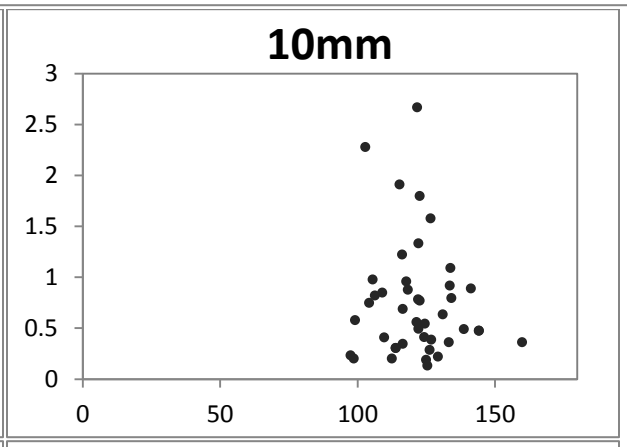

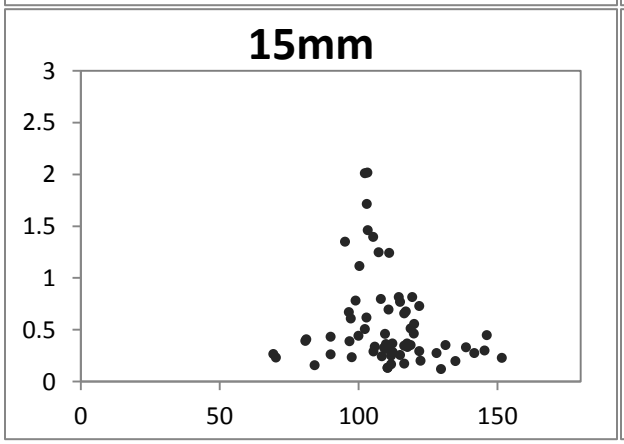

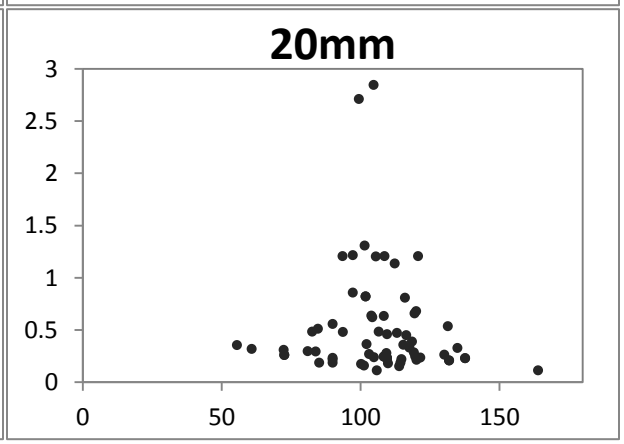

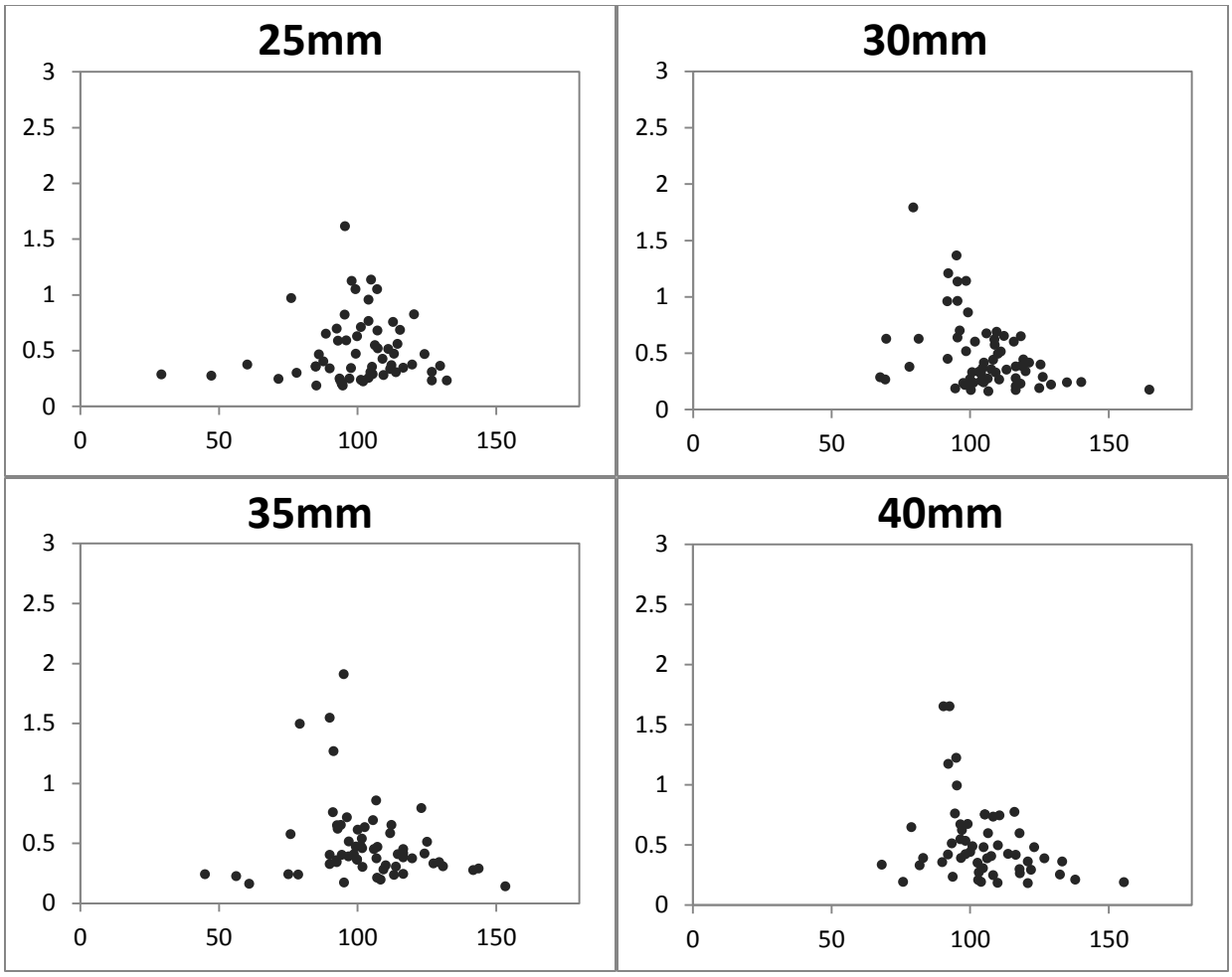

Figure 3.11. TALC_ER: fracture length versus azimuth. All displacement increments (top), individual increments below. This experiment shows a relatively narrow range of azimuths, particularly compared to TALC_SED. The longest structures at earlier strain intervals (5-10 mm) are ~120°, while after further displacement they fall in the 90-100° range (25-40 mm).

The longest structures (>2 cm) all develop between 10 and 20 mm displacement, and they are oriented at 100-120° (Figure 3.11). The structures at 1-2 cm in length, which is still longer than the bulk of the fractures, have a slightly broader range (~90-120°), and are generated during all strain intervals—initially they are ~120° at 5-10 mm displacement, transition to 100-110° at 15-20 mm displacement, and are nearly fault-parallel after 25 mm displacement.

The width of the fracture zone initially increases from the first evidence of surface fracturing (Figure 3.12). Once the more oblique early R shears are cross cut by more fault-

parallel R_L structures at ~10 mm displacement, the fracture zone subsequently narrows through time as deformation localizes along the Y shear plane.

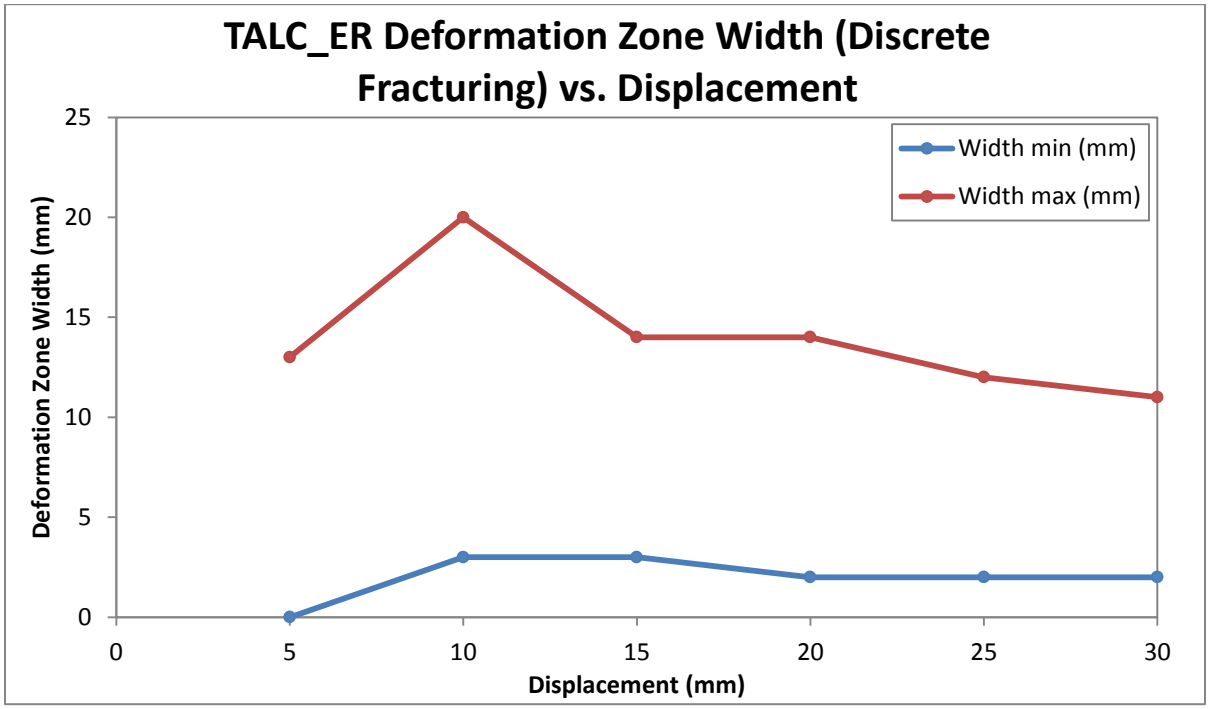

Figure 3.12. Development of TALC_ER discrete fracture zone width (minimum and maximum) with continuing displacement. The minimum width from 10 mm displacement on shows where strain is localized on a single fracture plane, so it remains the same whether the shears are R, R_L, or the eventual Y shear. The maximum width increases with initial R and R_L shear growth, then stabilizes at 15-20 mm when the fault zone is made up of en echelon fractures, then decreases as strain localizes on the Y shear.

3.2.1.4 TALC_SAND and TALC_SAND_PIV

TALC_SAND was designed to test the effects on surface deformation of a cohesive upper layer above a non-cohesive material at depth. This experiment consists of 3.5 cm of sifted fine dry sand with the surface scraped smooth, with 2 cm of talc deposited above the sand (see section 2.6 for further detail). The behaviour of each of these layers individually is known from TALC and TALC_PIV (section 3.2.1.1) and SAND_PIV (section 3.2.1.5), so this experiment can show how the layers interact. The basement fault was displaced at 1 mm/second for 30 mm,

when a throughgoing fault was evident. The experiment was performed twice, once recorded with photography (TALC_SAND), and once with PIV (TALC_SAND_PIV).

R shears first start to appear at 5 mm displacement, but instead of a relatively uniform set of short fractures spaced along the fault zone, as seen in the other experiments, a complex pattern of Riedel shears develops by ~10 mm displacement, with R shears striking at 110-120° and incipient R' structures oriented at 150-160° (see Figure 3.13 for annotated model images; see

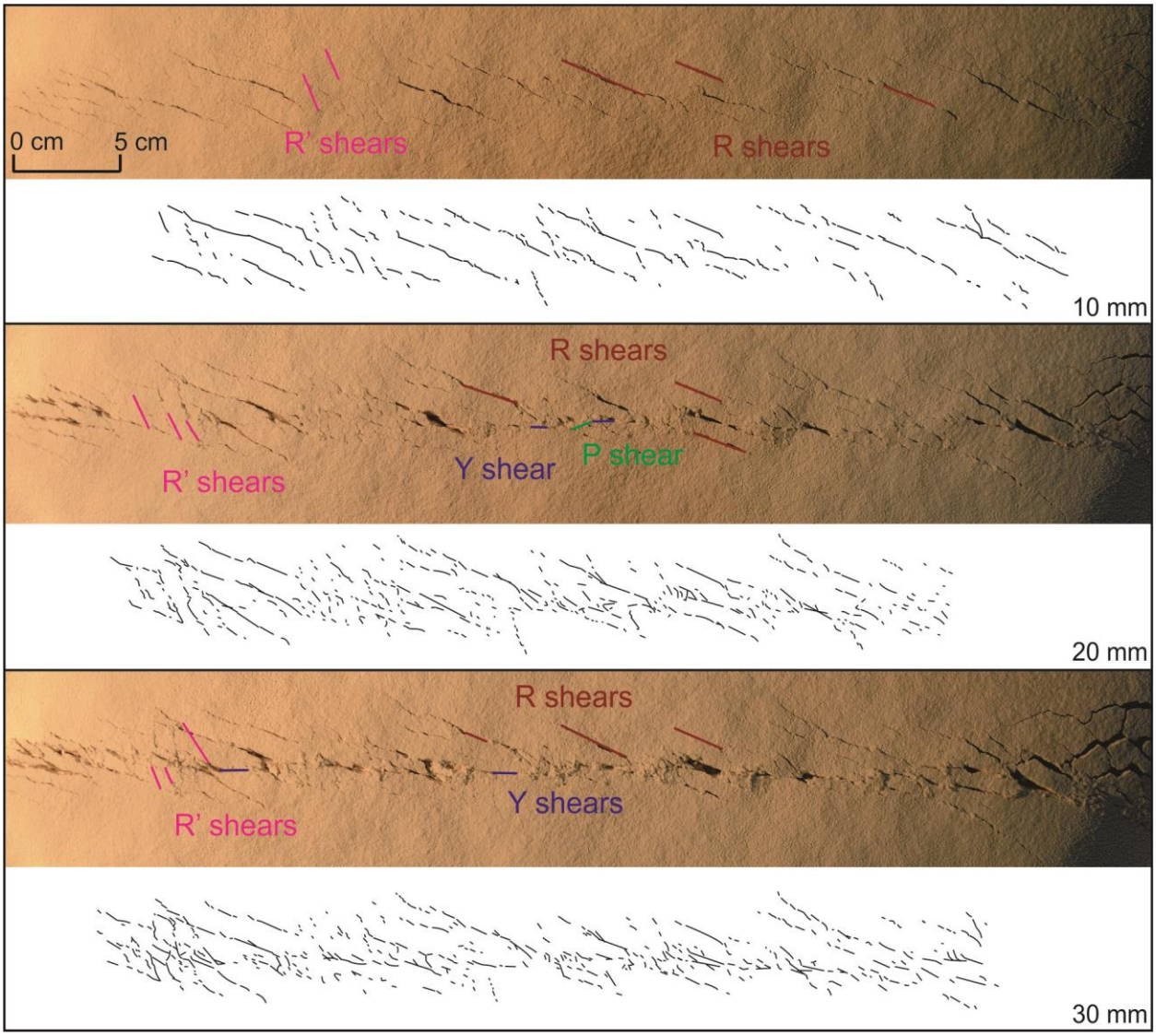

Figure 3.13. TALC_SAND images at successive strain increments with corresponding fracture maps. Examples of R, R', P, and Y shears are traced on the images. Note the presence of antithetic R' shears and the lack of R_L structures, as distinct from the other experiments in this study. All experiment images are available in Appendix C (data supplement disc).

Figure 3.14 for azimuth distribution). It should be noted that R' structures were not observed in any other experiment in this study. R shears remain the dominant structures until they are later cross cut by Y shears. By 15 mm displacement, R' shears are clearly visible, particularly at the left side of the fault zone, striking ~150°. From 15-25 mm displacement, offset continues on the major R shears, while the R' shears are progressively rotated toward the vertical, reaching ~160° before they and the R shears are cross cut by the Y shear (Figure 3.13). The Y shear becomes dominant and throughgoing at ~25 mm displacement, though other inactive structures are still visible (Figure 3.13).

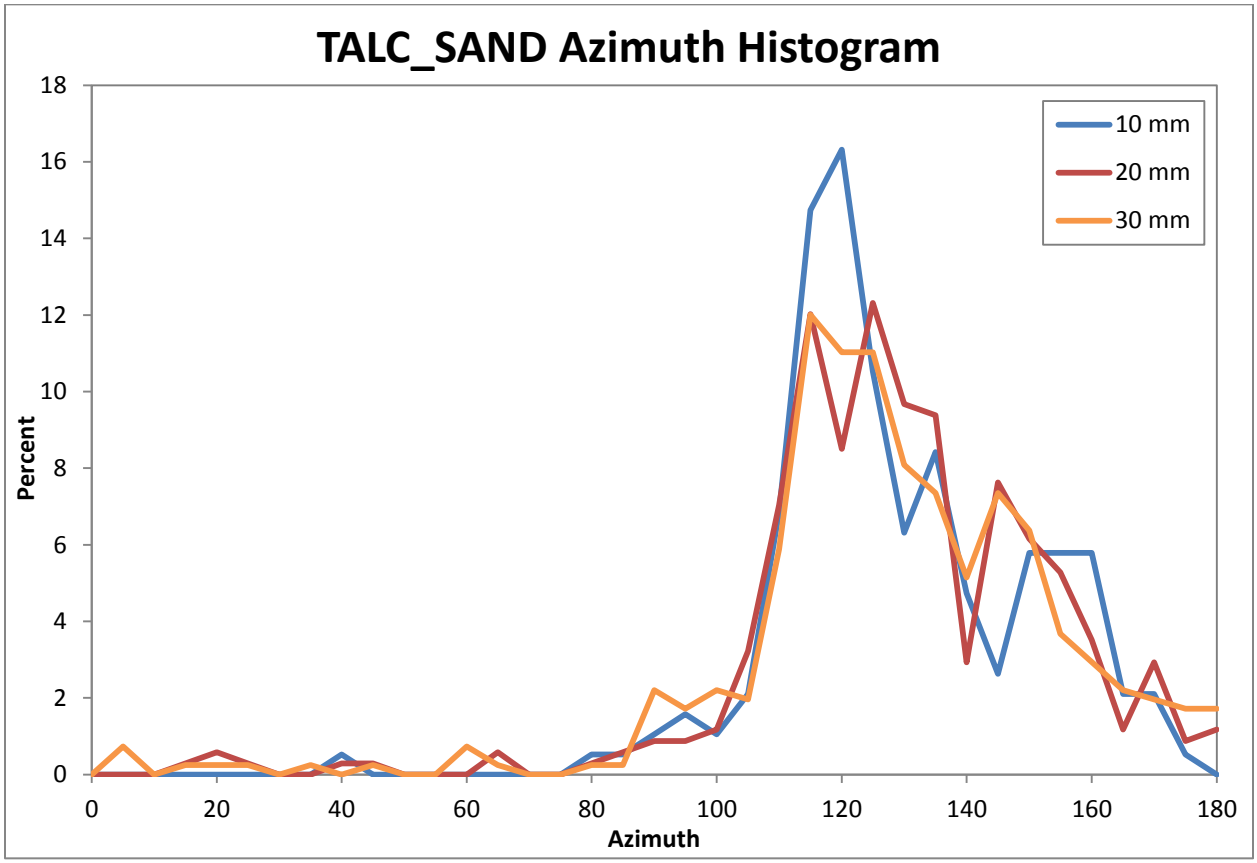

Figure 3.14. Distribution of fracture azimuths in TALC_SAND with ongoing strain. While the early 10 mm structures have a higher percentage of fractures striking 110-120°, the distribution of azimuths stays relatively stable throughout displacement. This is likely due to the persistence of inactive structures, which are mapped at later strain intervals even if they are not being offset at that time.

When fracture length and azimuth are plotted, there is a less marked development with ongoing strain in this model than in TALC, for example. This is partially due to the continued presence of inactive structures on the model surface, unlike in TALC_ER and TALC_SED where only active structures are visible. Likewise, the greatest change in TALC's fractures occur between 5 and 10 mm displacement (Figures 3.2, 3.3), while TALC_SAND was not analysed at 5 mm displacement. Regardless, the bulk of structures are concentrated in the 100-170° range, with the longest fractures (R shears) oriented at 110-120° (Figure 3.15). This is more oblique than the longest fractures in TALC, though they are roughly the same length.

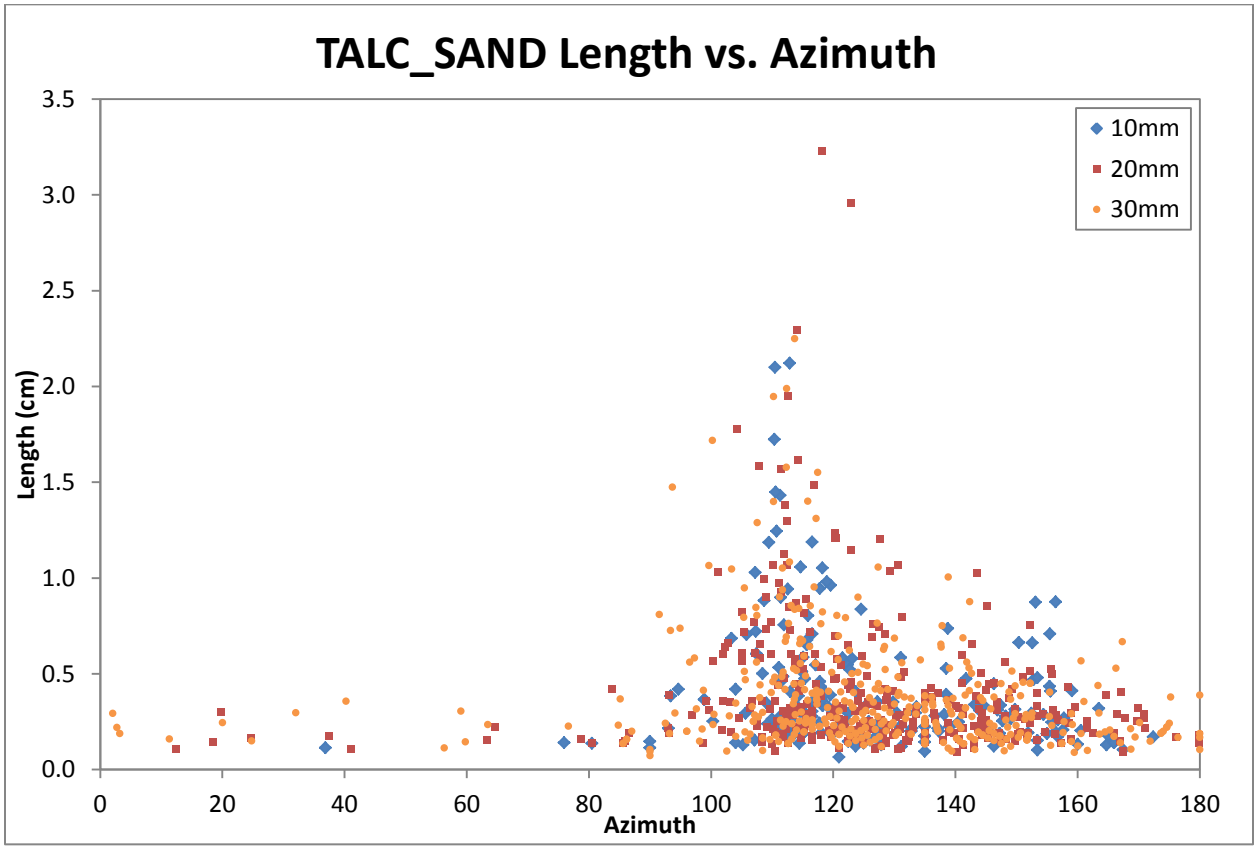

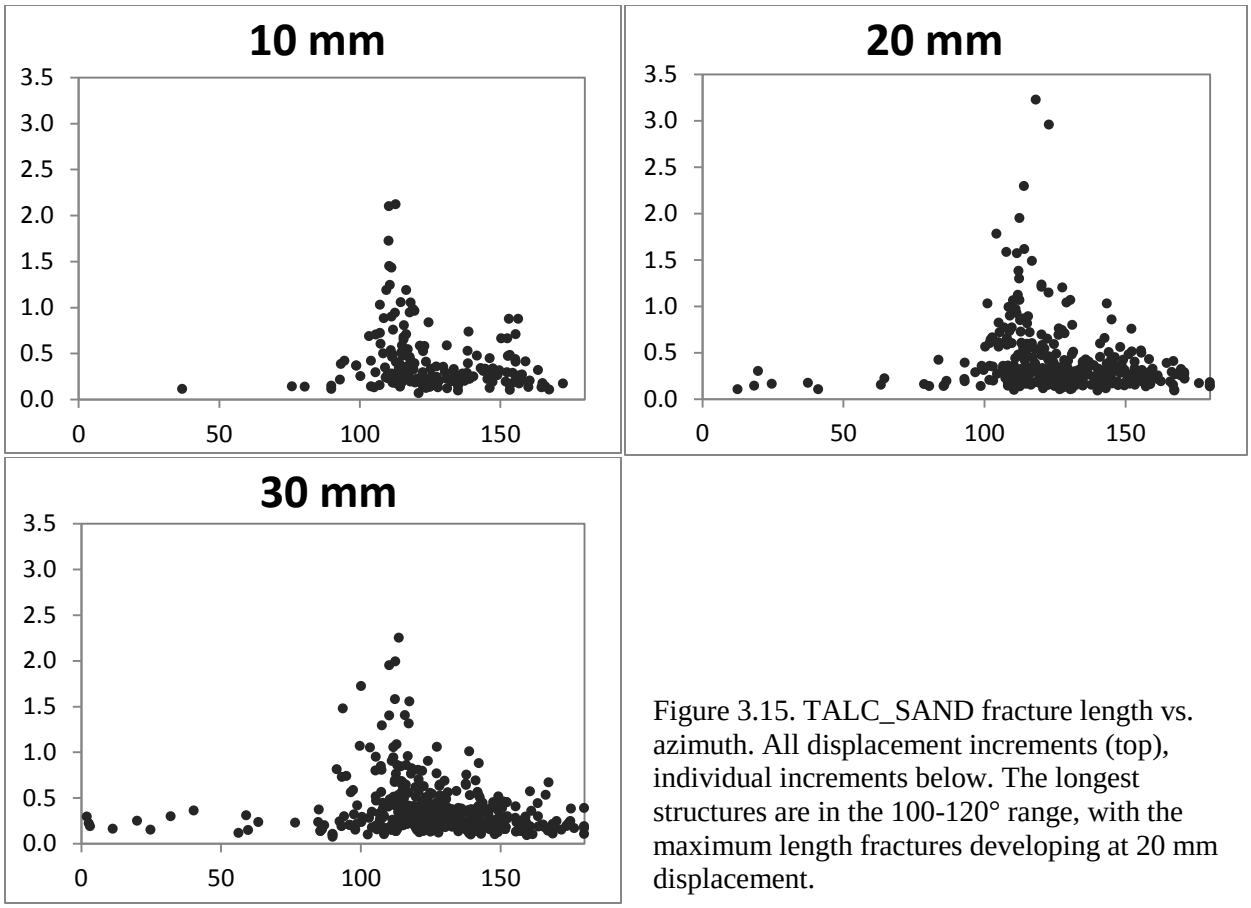

Figure 3.15. TALC_SAND fracture length vs. azimuth. All displacement increments (top), individual increments below. The longest structures are in the 100-120° range, with the maximum length fractures developing at 20 mm displacement.

It is also important to note that the zone of discrete fracturing is significantly wider here (maximum width of ~50 mm; Figure 3.16) than in the other experiments with just a 2 cm thickness of talc (15-20 mm wide; Figures 3.4, 3.12). As in the other experiments, the fracture zone width increases from fracture initiation as the oblique R shears increase in length, before decreasing as deformation localizes along the Y shear (Figure 3.16). However, the width peaks later in this experiment than in the others, at ~14 mm displacement compared to 8-10 mm. This may be because the R shears are so much longer than in other experiments, and therefore they take more time to grow to peak length. There is also some error introduced into the discrete fracture zone measurements, because it is difficult to discern which structures are actively displacing and which are no longer active.

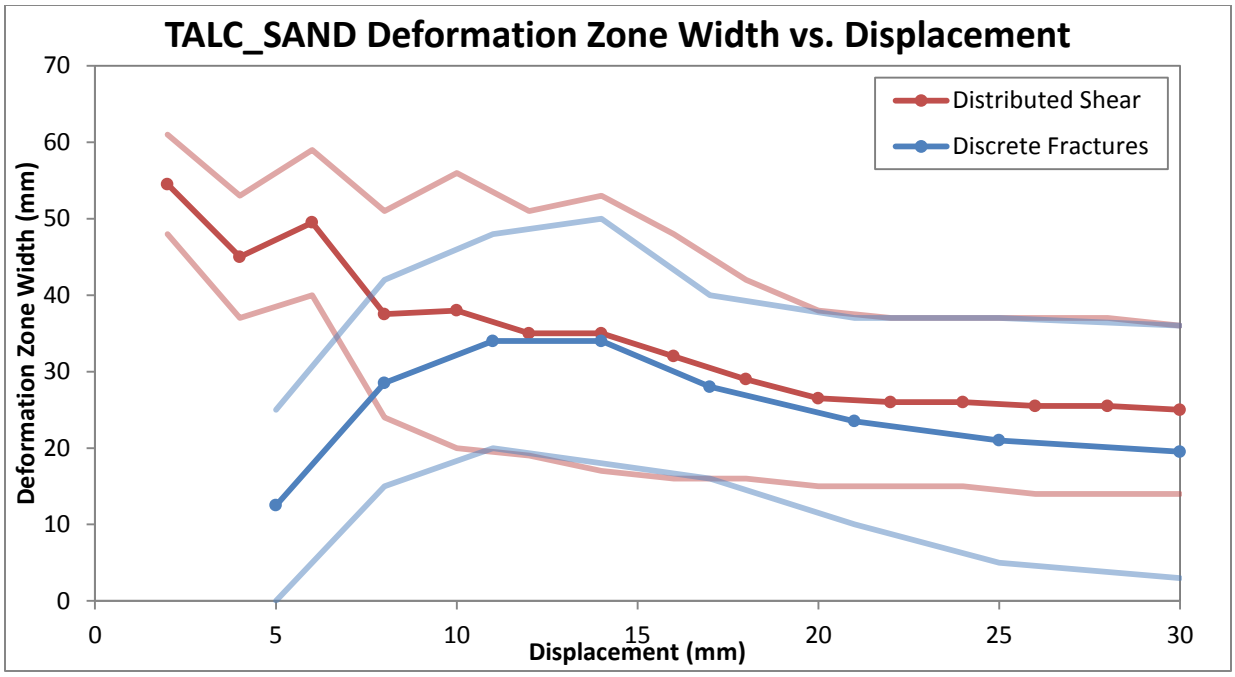

Figure 3.16. Plot showing development of TALC_SAND deformation zone widths (both discrete fracturing and distributed shear) with continuing displacement. The mean width is highlighted, while minimum and maximum values are shown in lighter colours.

The corresponding PIV data, TALC_SAND_PIV, shows a visual representation of the complex pattern of distributed shear in this model, as distinct from the discrete fractures seen in the still photographs. For the first 5 mm of displacement, shear strain is very diffuse and much wider than seen in TALC_PIV, with a maximum width of ~60 mm for the multi-layered model as compared to ~20 mm for just talc (Figure 3.17; 0-4 mm). From 10-15 mm displacement, strain quickly localizes along extended, linear Riedel shears, with a few remaining areas of distributed shear (Figure 3.17; 6-10 mm). During this stage, the maximum width of 50-60 mm represents the widest extent of the R shears, while the minimum of 15-20 mm represents places where shear strain is localized along a single structure. As motion along the fault continues, the maximum width decreases as R shears start to link, though some areas of more distributed strain persist through 30 mm displacement (Figure 3.17; 30 mm). By this time, strain is mostly localized on the Y shear apart. See Figure 3.16 for comparison of distributed shear and discrete fracture zone widths.

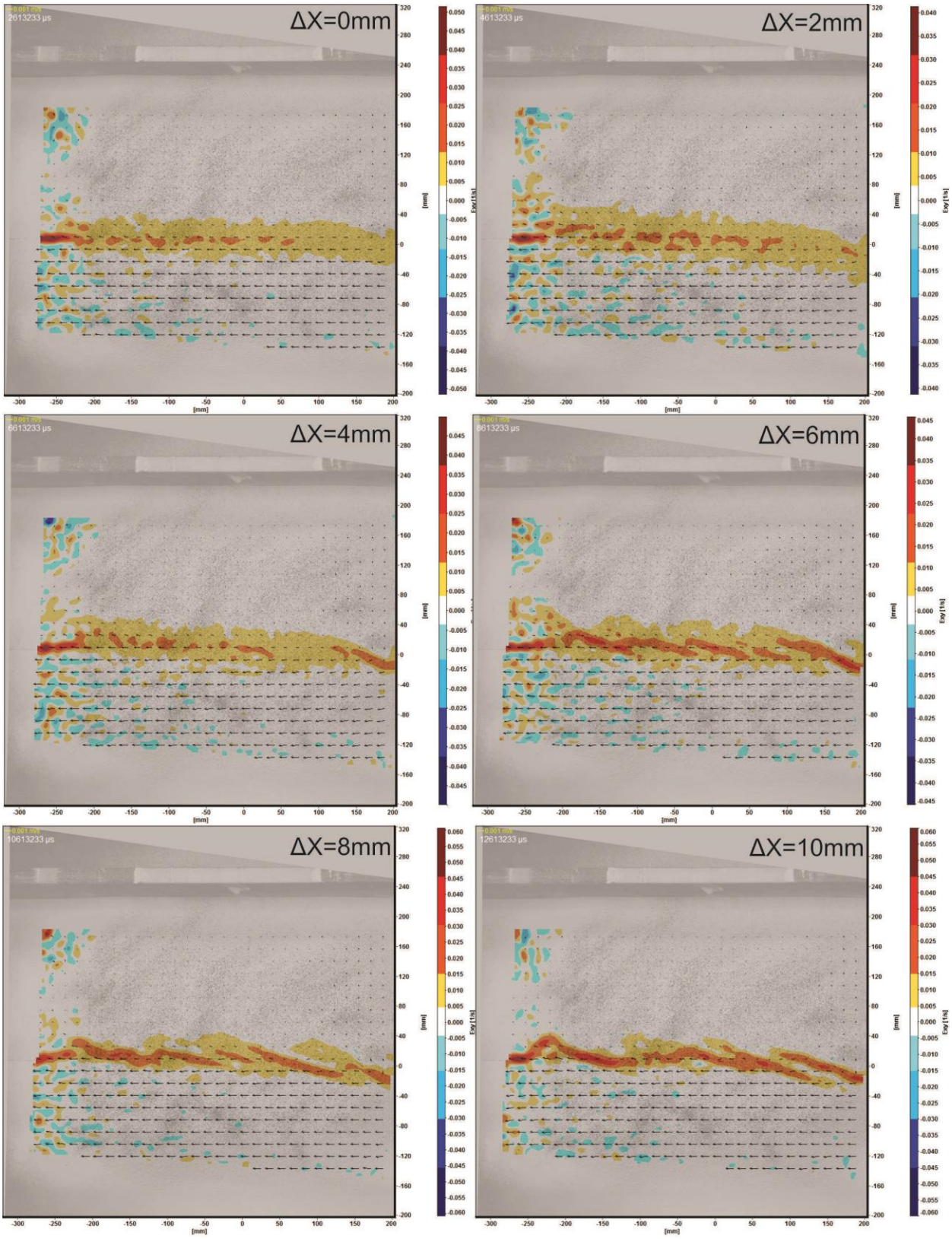
ΔX=0mm
ΔX=2mm
ΔX=4mm
ΔX=6mm
ΔX=8mm
ΔX=10mm
[mm]
Exy [1/s]
Eyy [1/s]

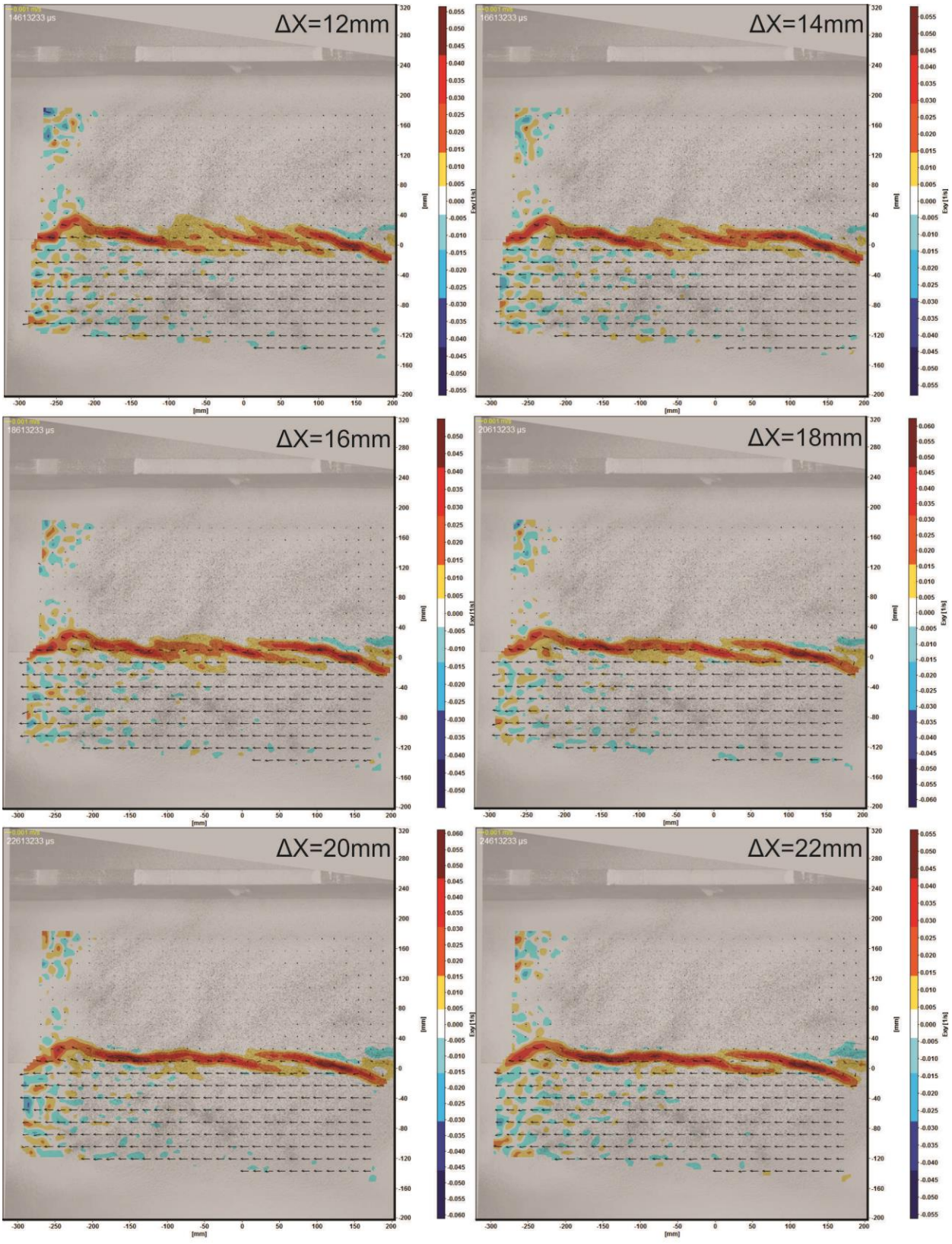
ΔX=12mm
ΔX=14mm
ΔX=16mm
ΔX=18mm
ΔX=20mm
ΔX=22mm

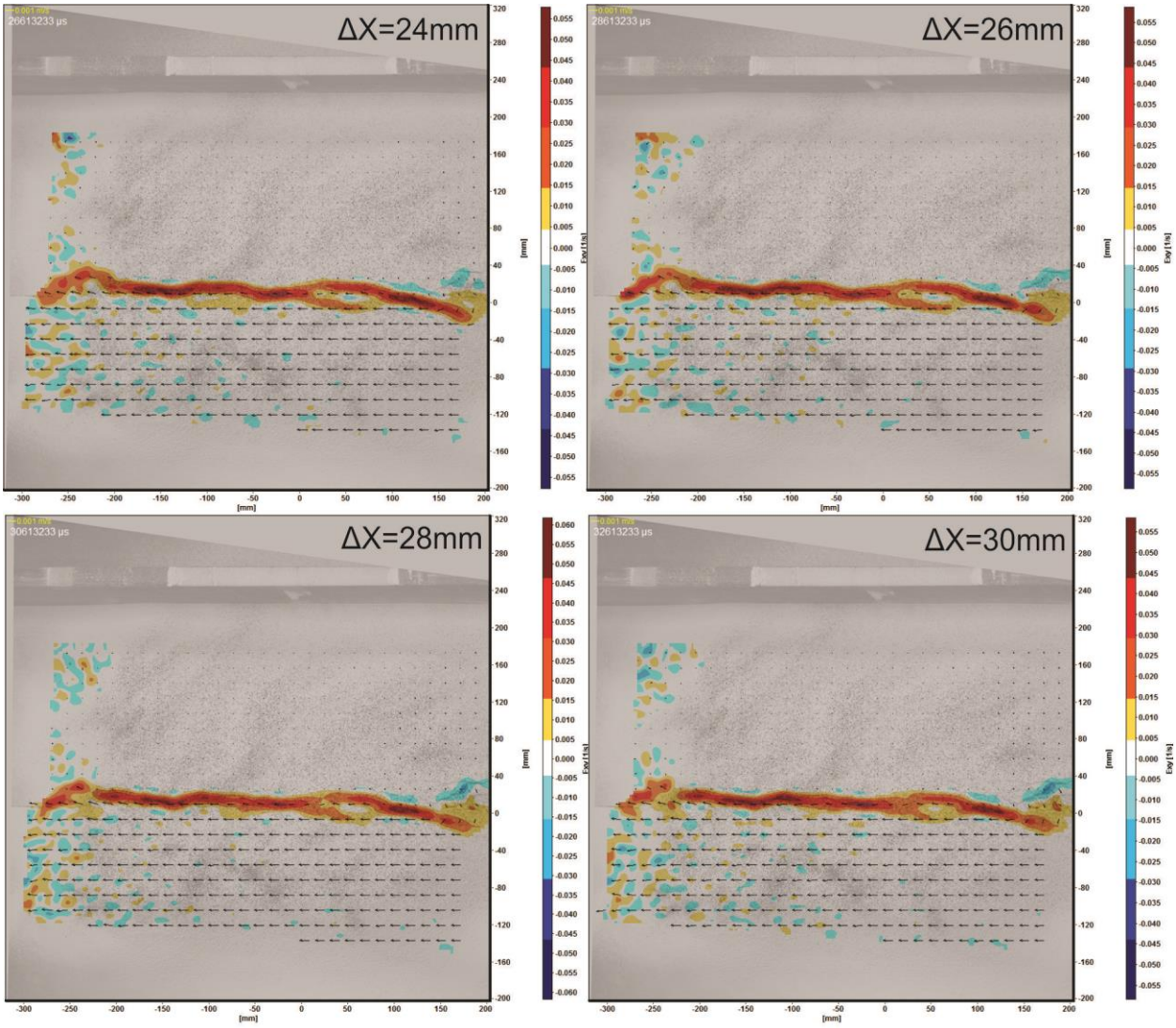

Figure 3.17. TALC_SAND_PIV data, showing shear strain distribution at 2 mm intervals, 0-30 mm. Shear strain gradually localizes on to individual R shears before concentrating along the Y shear. All PIV images are available in Appendix D (data supplement disc).

3.2.1.5 SAND_PIV

SAND_PIV was designed in order to observe the behaviour of the lower sand layer in TALC_SAND individually. The model consists of 3.5 cm of fine sifted sand with the surface scraped smooth before displacement began, identical to the bottom layer of TALC_SAND. The basement fault was offset at 1 mm/second for 50 mm. It was only recorded with PIV, not still

photography. The PIV system does produce images, but it can be difficult to identify detailed surface features because of the dark particles sprinkled on the surface.

Discrete R shears are the only visible surface structures until the Y shear develops, and they are not definitively present until ~15 mm displacement. They may appear earlier, but for the purposes of this study, the conservative estimate is used. At its peak, the width of discrete fracturing is ~10-15mm, significantly smaller than the other models, and it quickly localizes along the Y shear (Figure 3.18).

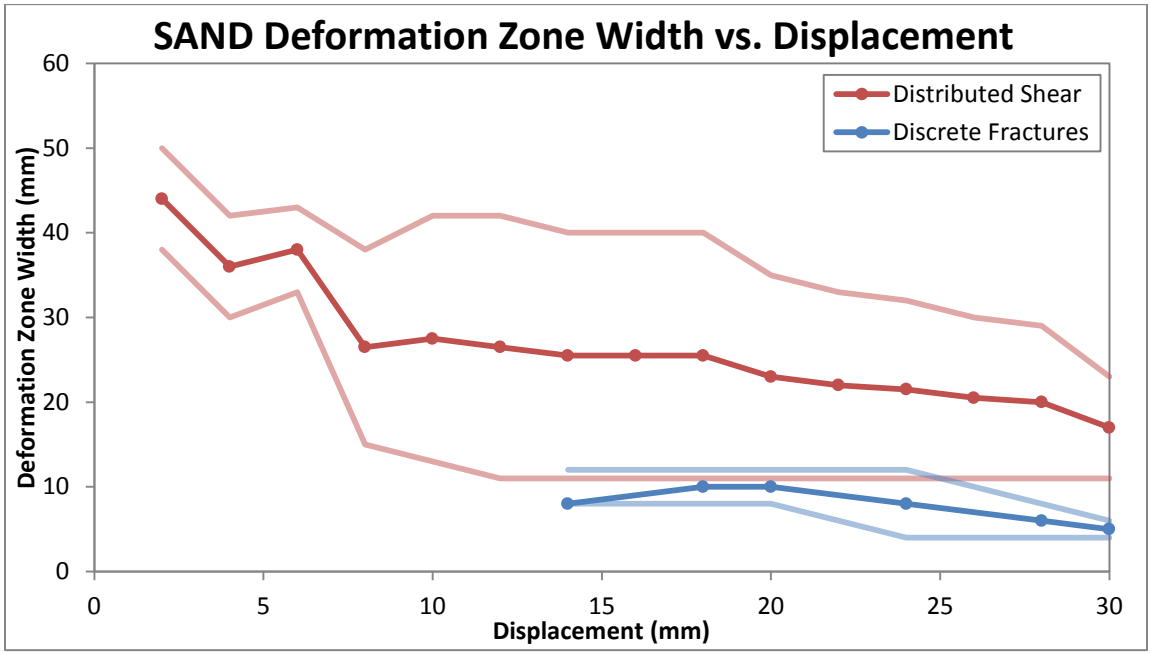

Figure 3.18. Plot showing development of SAND deformation zone widths (both discrete fracturing and distributed shear) with continuing displacement. The mean width is highlighted, while minimum and maximum values are shown in lighter colours. The zone of discrete fracturing is narrow throughout displacement, whereas the distributed shear is initially very wide and does not begin to localize until 20-30 mm displacement.

The fault zone development is much easier to see in the PIV data that shows the distributed shearing (Figure 3.19). While initially wide, deformation localizes along R shears during the first 10 mm of displacement. The shear zone width remains stable, with the maximum width representing areas with persistent, oblique R shears, and the minimum width representing areas where deformation is already localized along a single shear. The mean width decreases

with continued displacement because the maximum width slowly decreases as R shears become inactive (see Figure 3.18 for deformation zone width comparison).

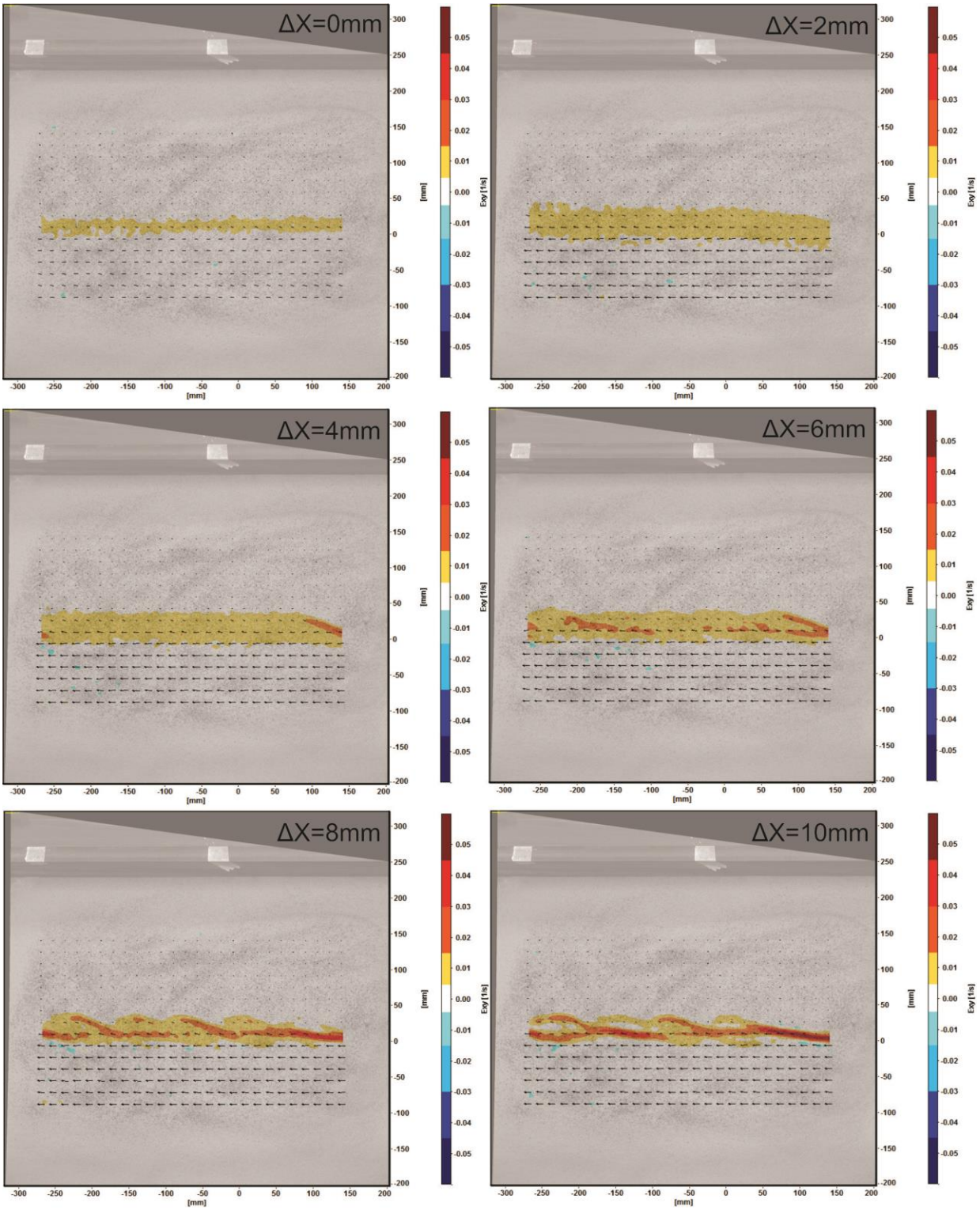

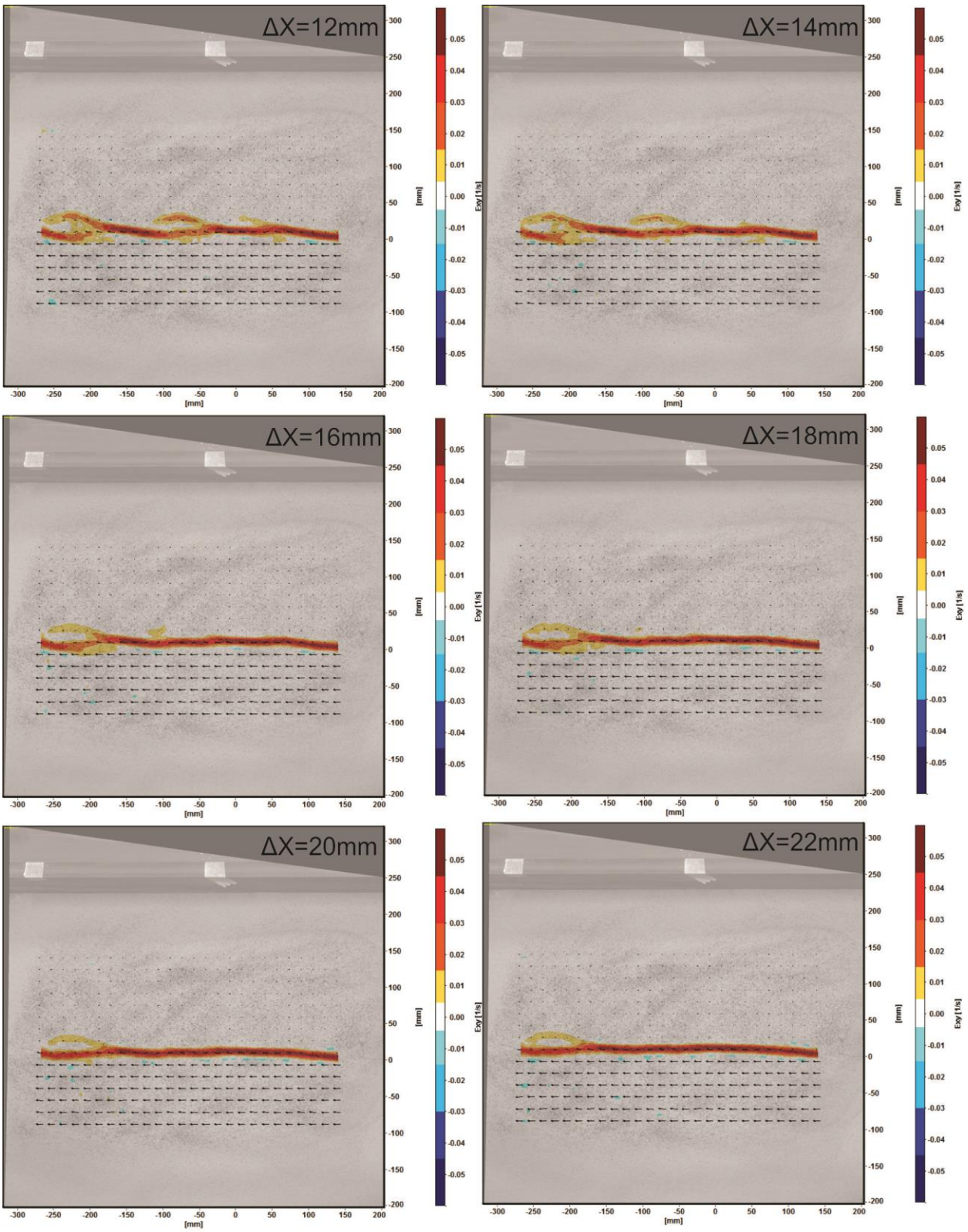
ΔX=12mm
ΔX=14mm
ΔX=16mm
ΔX=18mm
ΔX=20mm
ΔX=22mm
[mm]
Exy[1/s]

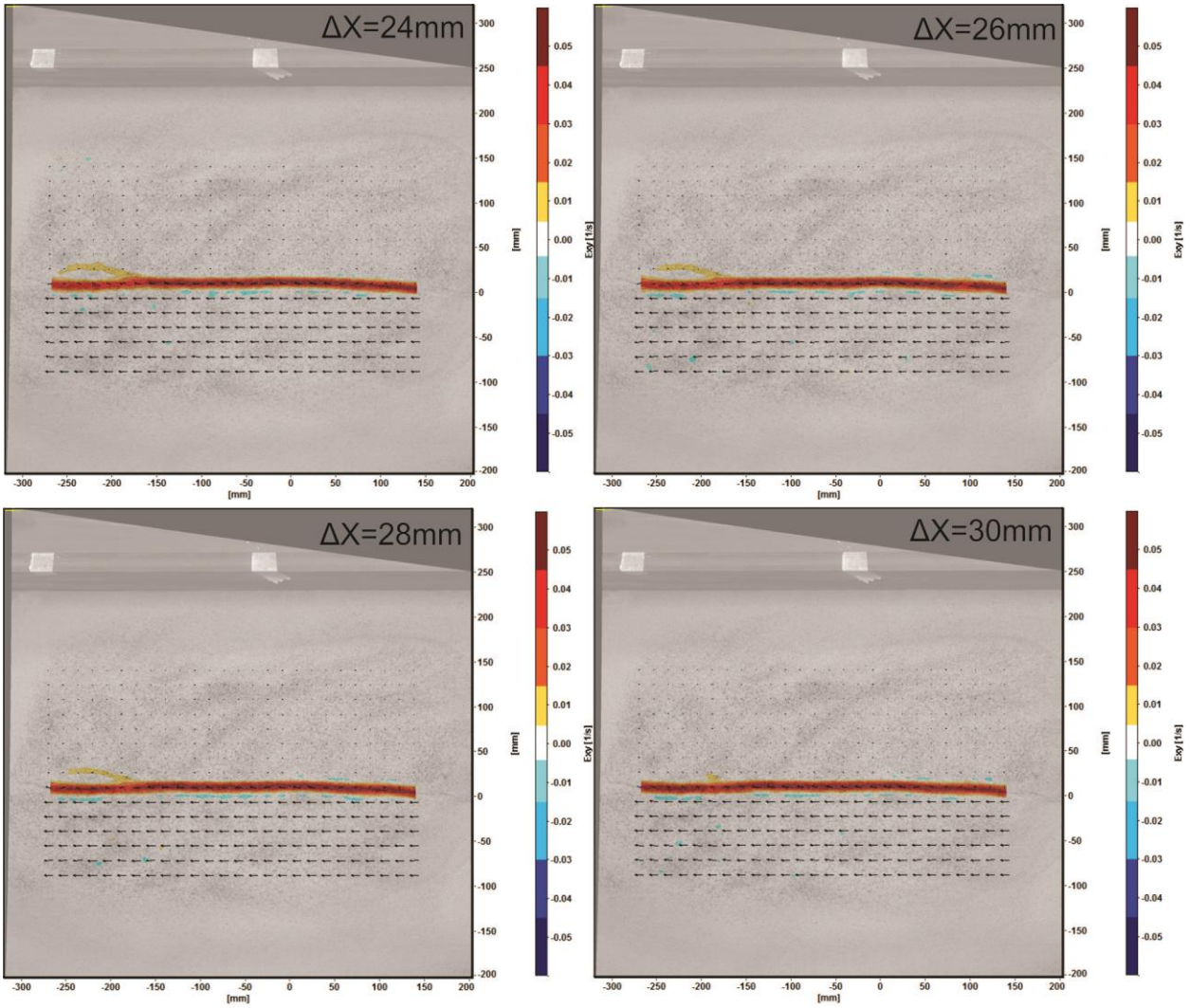

Figure 3.19. SAND_PIV data, showing shear strain distribution at 2 mm intervals, 0-30 mm. All PIV images are available in Appendix D (data supplement disc).

3.2.1.6 General Summary

For the experiments in this study, the general trend is that with ongoing displacement, fracture azimuths become more fault-parallel, while the width of the deformation zone narrows (Figure 3.20). However, there are variations on this ideal scenario due to differences in the setup of each experiment, which can reveal information about the development of each individual fault zone.

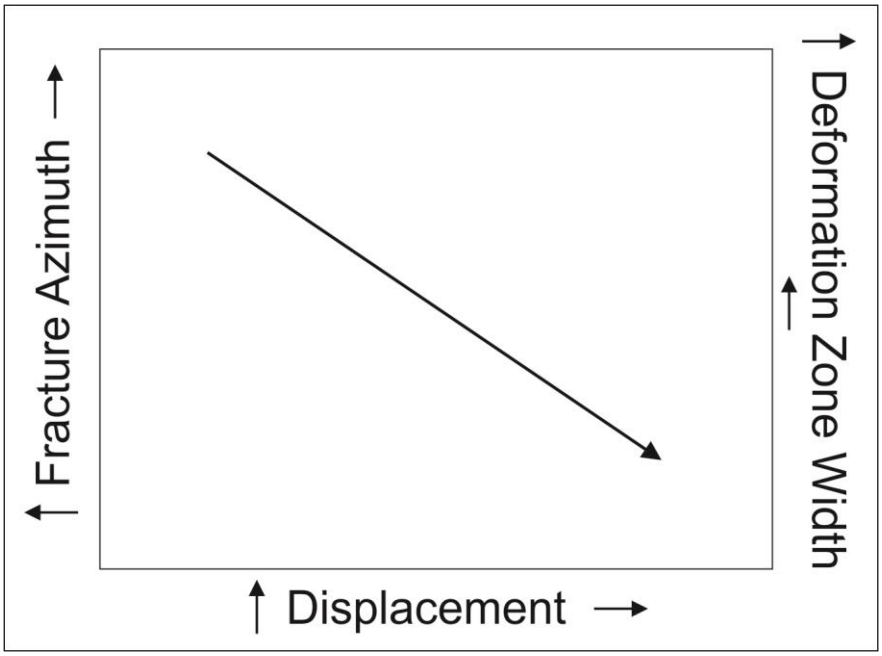

Figure 3.20. Schematic representation of fault zone behaviour with increasing displacement. "Fracture azimuth" here is the angle between a structure and the underlying fault, so that "higher" is more oblique and "lower" is more fault-parallel.

In most experiments, mean azimuth decreases with continuing displacement, as structures transition from oblique Riedel-style shears to more fault-parallel fractures, and eventually form a single throughgoing fault (Figure 3.21). While few other studies have focused specifically on this aspect of fault zone evolution, the general progression from oblique structures to more fault-parallel structures can be frequently observed in analogue experiments (e.g. Schreurs, 1994; Richard et al., 1995; Dauteuil and Mart, 1998).

There is a marked difference between the two models that incorporated interseismic "resurfacing," TALC_SED and TALC_ER, and the two models that retained their inactive structures, TALC and TALC_SAND. The former two have a much more dramatic decrease in azimuth as newer, more fault-parallel structures develop, while the latter two have a relatively stable mean azimuth, even with significant displacement, because inactive structures are still present on the model surface, and are thus continually mapped and measured (Figure 3.21).

Conversely, mean length does not have a common, easily explained behaviour in all four experiments. The initial increases in length in every experiment except TALC_SAND are explained by the formation and growth of R shears, but beyond that, their behaviour diverges. TALC's mean length increases, TALC_ER's decreases, TALC_SAND's remains stable, and TALC_SED's fluctuates significantly (Figure 3.22). This is probably at least partially due to the way that the fractures were mapped, because major R, R' or other structures were often sketched as the smaller, individual structures that make them up (see "Riedel within Riedel" pattern, section 1.3). While this is certainly an accurate way of mapping the fracture patterns, it may not fully represent some aspects of fault zone development; if fractures were mapped more holistically, one would expect the initial increase as observed, then roughly stable lengths as the fault continues to displace, then a second increase in mean length as fault-parallel structures coalesce into a single throughgoing fault.

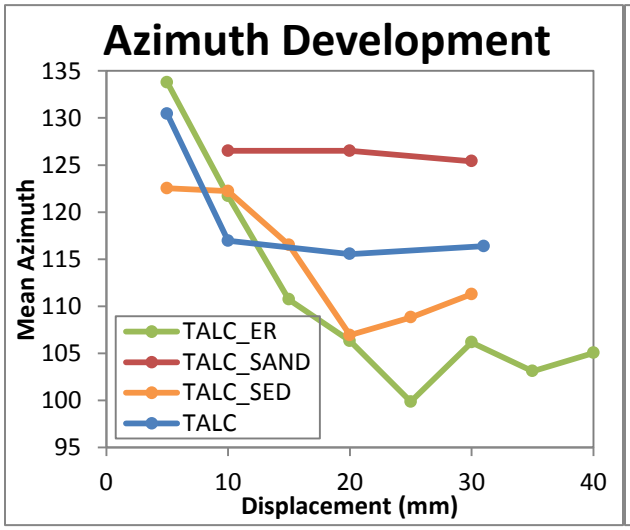

Figure 3.21. Mean azimuth for all experiments by displacement increment. Note decrease from initial oblique R shears to more fault-parallel structures. TALC_SAND and TALC likely show little decrease due to the continued measurement of inactive oblique structures.

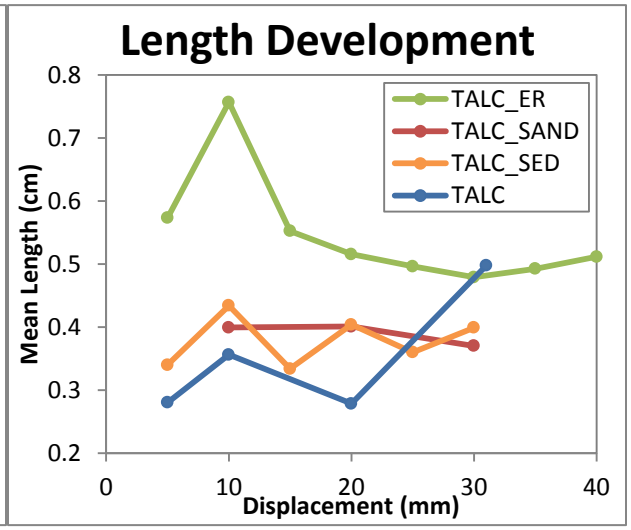

Figure 3.22. Mean length for all experiments by displacement increment. Note initial increase at 5-10 mm, and subsequent decrease or stabilization. Also note TALC's marked increase at 20-30 mm, which could be explained by Y shears linking into a throughgoing fault.

A scaled function was also designed that incorporates both length and azimuth development, such that $F = L \times A$, where the length and azimuth components range between 0 and 1. The "end point" case where L = 1 and A = 1 is a single throughgoing fault the full length of the model (40 cm), that is parallel to the underlying fault (90°). The scaled function would describe this case as 1, and that number would decrease with the presence of structures that were shorter or more oblique to the PSZ. This parameter was calculated for each experiment at several displacement increments, producing the plot in Figure 3.23. It is quite similar to Figure 3.22, but it is possible to see the influence of the azimuth parameter, for example where the TALC_ER sequence is flatter at 5-15 mm displacement in Figure 3.23 than it appears in 3.22 because the mean azimuth is becoming more fault-parallel (Figures 3.21).

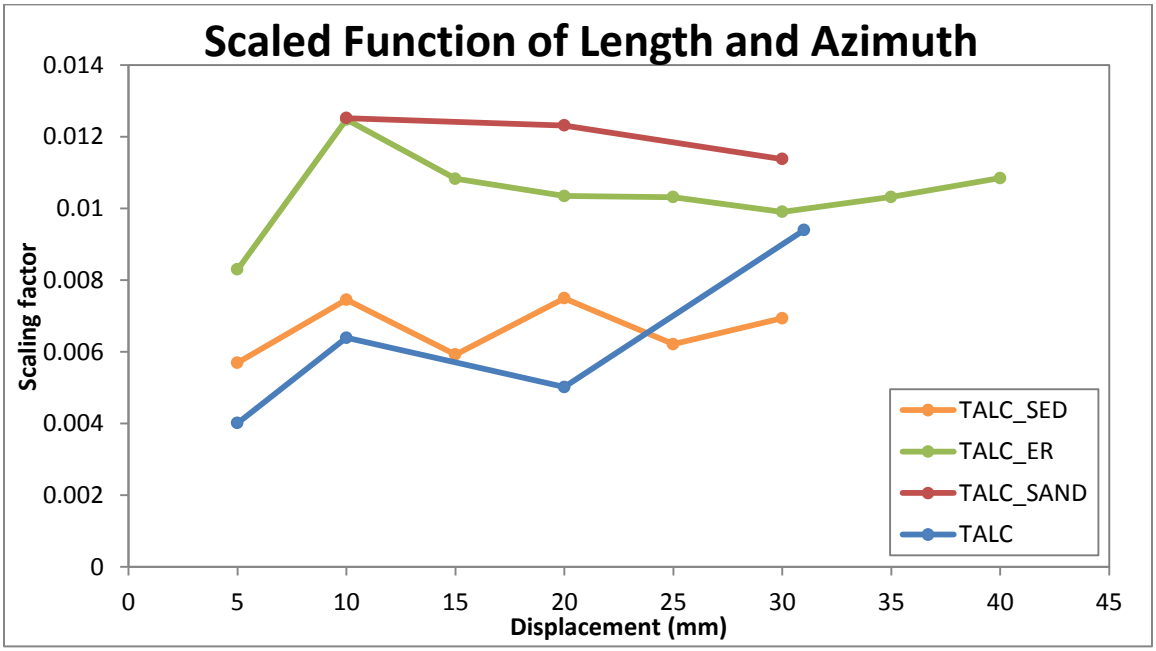

Figure 3.23. Scaled function of length and azimuth for all experiments. It is quite similar to Figure 3.22, with a subtle influence from the values in Figure 3.21.

3.2.2 Greendale Fault Trace

Unlike the analogue experiments, in which the evolution of fault zone fractures is visible through time, the field data from the central Greendale Fault provides a record of deformation at

only a single point in its development. A general description of the fault zone morphology is located in section 1.2.2. At a scale of ~1:7,000, the generally east-west (90°) striking fault zone is made up of subparallel, en echelon segments on the order of 100-1000 meters in length, with pop-up structures in the areas of overlap. However, at a smaller scale of ~1:2500, each of these segments is made up of a complex arrangement of fractures on multiple different scales, from small ~1 m fractures with cm-scale displacements to extended linear segments of >20 m with decimetre to meter-scale displacements.

The morphology of these patterns also varies widely along strike. In places, the fault trace is made up of subparallel linear strands, with small-scale Riedel type structures (Figure 3.24),

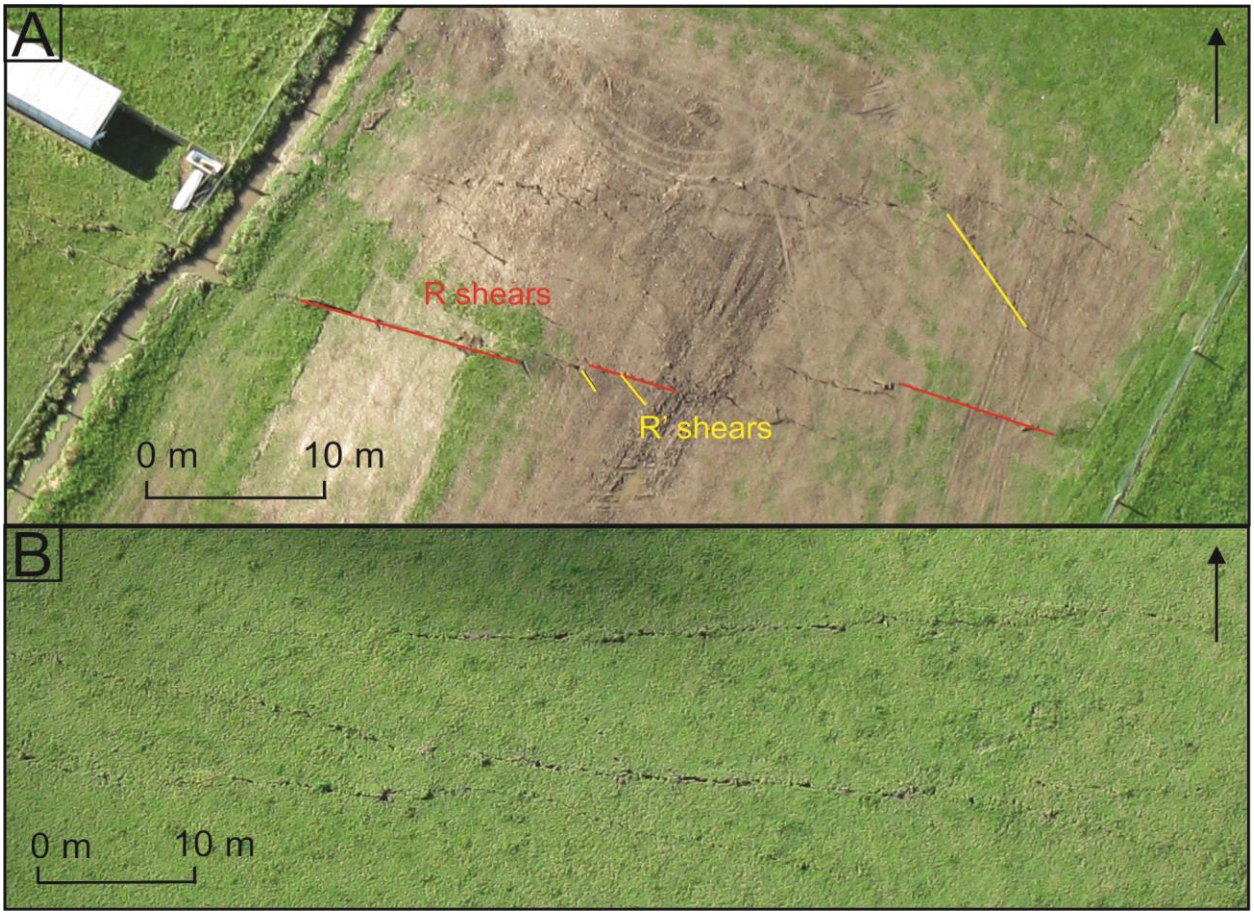

Figure 3.24. Aerial photos of the Greendale Fault trace: A) 1098, B) 1101 (see Figure 1.1 for locations). Note simple fault morphology: A shows dominant R shears and isolated R' shears, while B shows simple, linear fault traces without any complex shear patterns. Arrows indicate North. (Photos courtesy Mark Quigley.)

while elsewhere it is much more complex, with multiple en echelon strands, each consisting of a dense pattern of fractures and shears (Figure 3.25: A, B). Most areas on the fault demonstrate some combination of these morphologies (Figure 3.25: B, C).

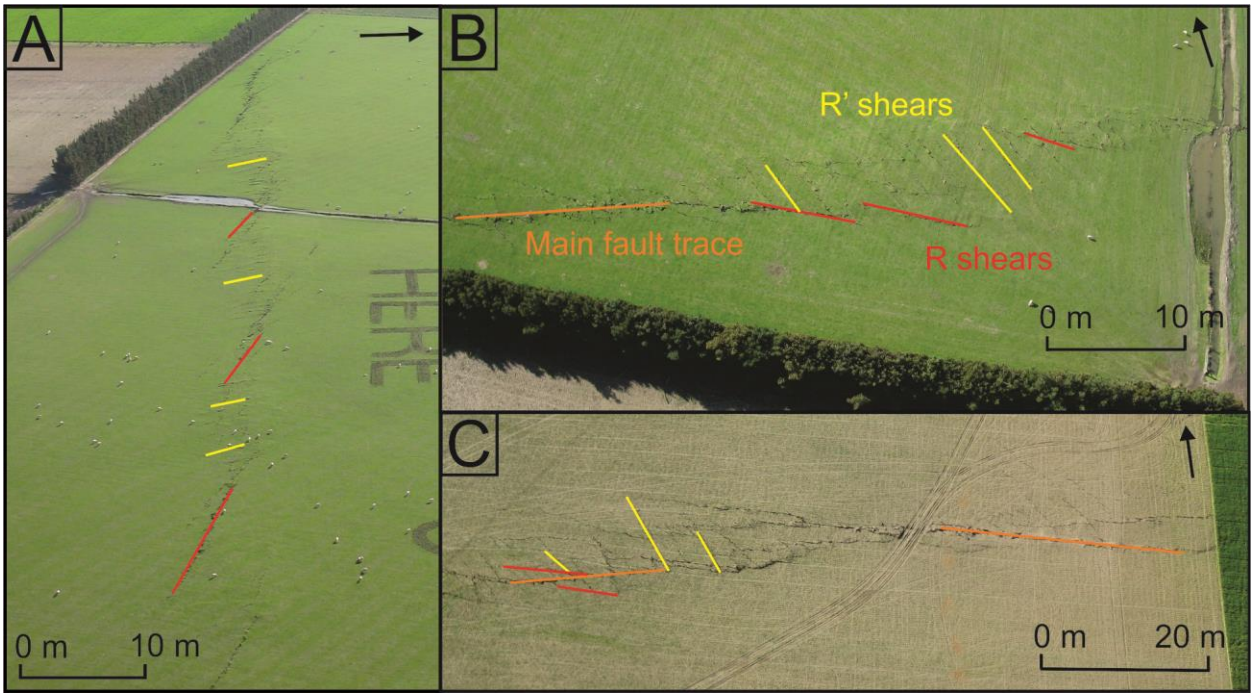

Figure 3.25. Aerial photos of the Greendale Fault trace near Kivers Road: A) 1102, B) 1107, C) 1110 (see Figure 1.1 for locations). Note the left stepping en echelon pattern of A, and the complex pattern of R and R' shears in A and B. B and C both show a combination of Riedel shears and other fractures with more dominant linear fractures parallel to the overall fault trace, as seen in Figure 3.24. Arrows indicate North. (Photos courtesy Mark Quigley.)

The highest percentage of fractures mapped at the Greendale Fault are in the R shear range (105-125°), and there is also a large group of very oblique fractures in the 160-170° range, which are interpreted as R' structures based on their orientation (Figure 3.26). The length versus azimuth plot shows clearly that the longest structures (>50 m) are oriented at 90-130°, while the more oblique R' structures are clustered at shorter lengths, between 0 and 15 m (Figure 3.27). This is what would be expected, based on previous studies of fault zone evolution that show R' shears developing later and linking more dominant R shears, and thus they tend to be shorter (see section 1.3.2 for more detail).

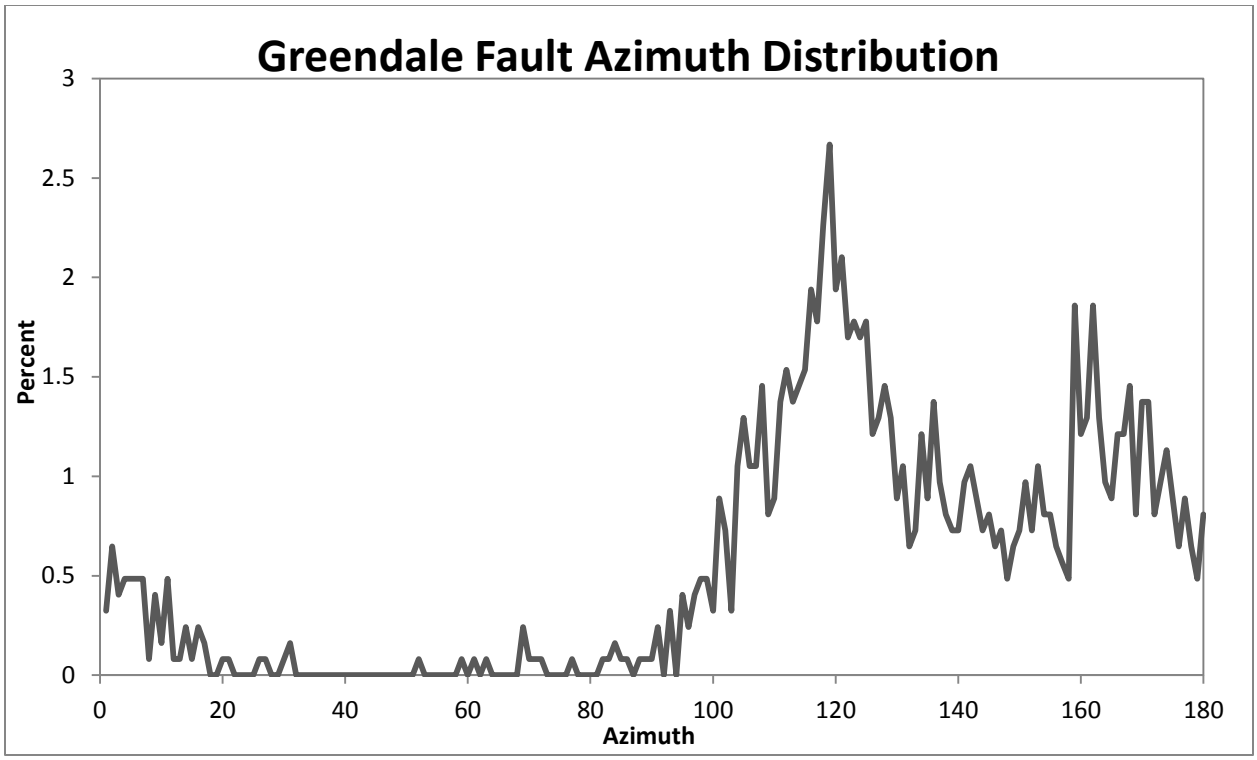

Figure 3.26. Greendale Fault fracture azimuth distribution. The main peak is at Riedel shear orientation (105-125°), and there is a secondary peak at 160-180°, which is interpreted to be R' shears.

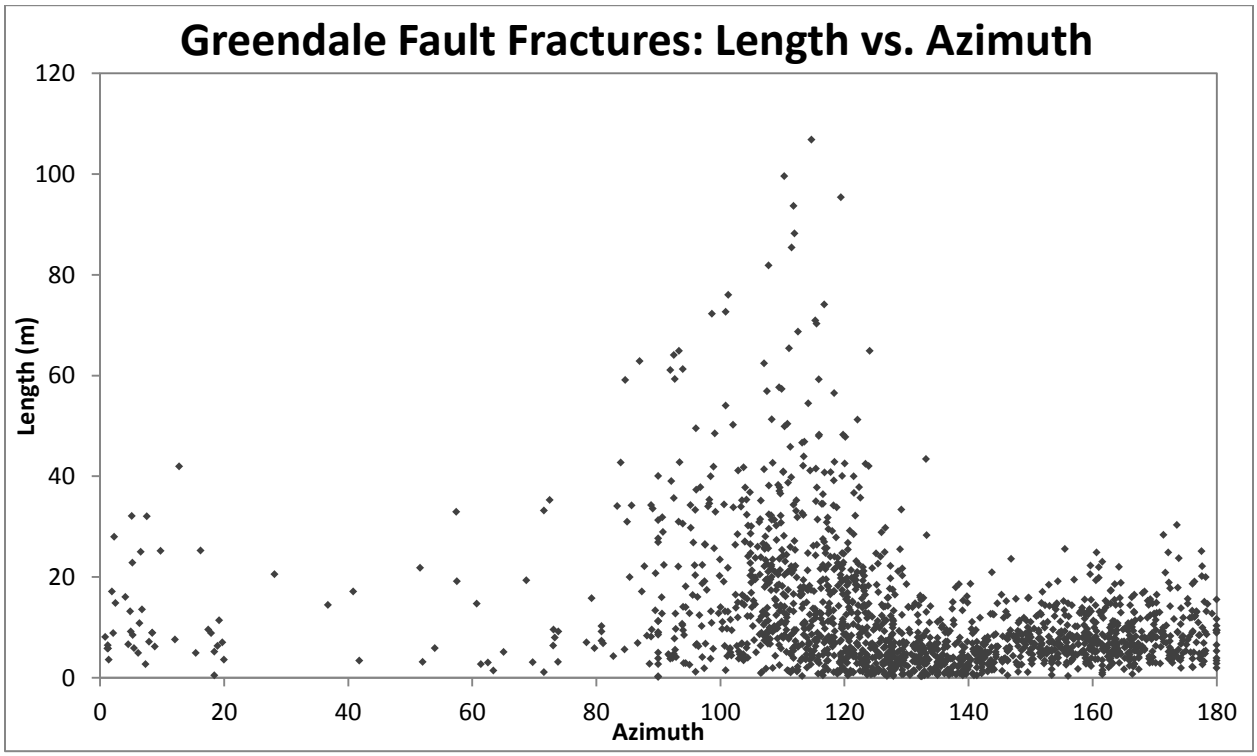

Figure 3.27. Greendale Fault fracture length versus azimuth. The highest density of fractures is at shorter lengths (≤12 m) and oriented at 110-170°. The longest structures are ~90-120°.

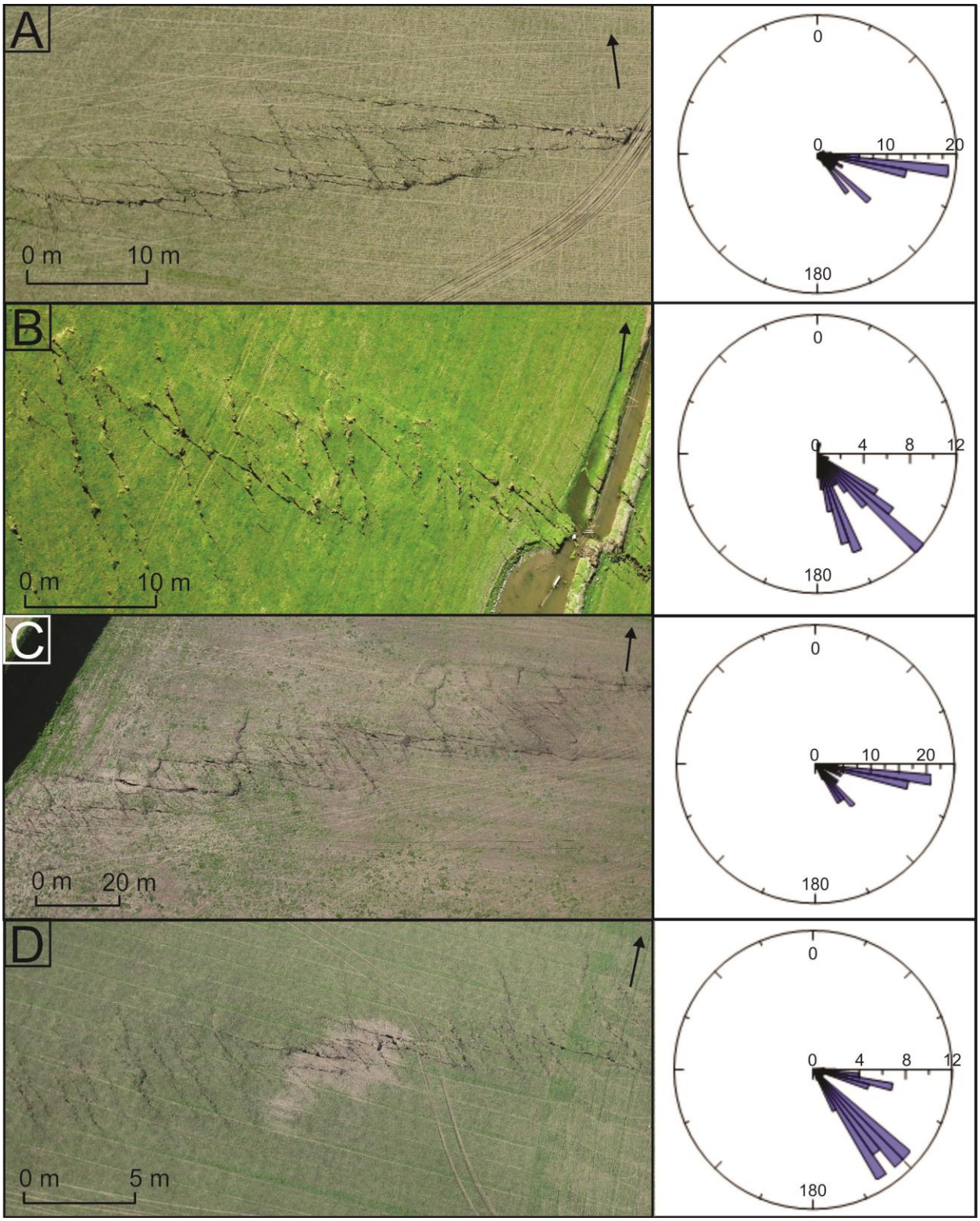

Figure 3.28. Aerial photos of Greendale Fault segments with azimuths plotted. Blue data in rose diagrams show fracture azimuths. Photo numbers as follows: A) 1110, B) 1120, C) 1151, D) 1208 (see Figure 1.1 for locations). Although the surface ruptures have somewhat different appearances, they all have relatively similar fracture orientations, allowing for variation in local fault strike. R shears are dominant in A, B, and C, while R' shears are dominant in D.

Individual fractures were mapped at selected locations using aerial photos of the fault rupture (Figure 3.28; see above). The photos are not exactly orthogonal to the ground surface, which skews the azimuths slightly, but they provide an opportunity to study fracture morphology by mapping the surface deformation in detail at a few locations. Fracture azimuths were measured and plotted by relative frequency, but it was not always possible to reconstruct the exact local fault strike when buildings, roads, or shelterbelts were not present.

3.2.2.1 Stepovers

Stepover features were mapped in detail using the Greendale Fault LiDAR dataset to compare the relationship of fault segment length on either side of the stepover with the width of the stepover itself (Figure 3.29). "Riedel within Riedel" patterns, as described in section 1.3 (Figures 1.6, 1.7, 1.9), are frequently present. These different scale arrays were mapped and measured as two separate datasets, MICRO and MACRO, with each MICRO en echelon array forming a single MACRO segment (Figure 1.6). These two datasets form distinct populations, with the MICRO stepovers clustering at short lengths and widths (50-175 m in length, 15-40 m wide), and the MACRO stepovers more spread out with larger widths and lengths (400-700 m in length, 50-110 m wide; see Figure 3.30).

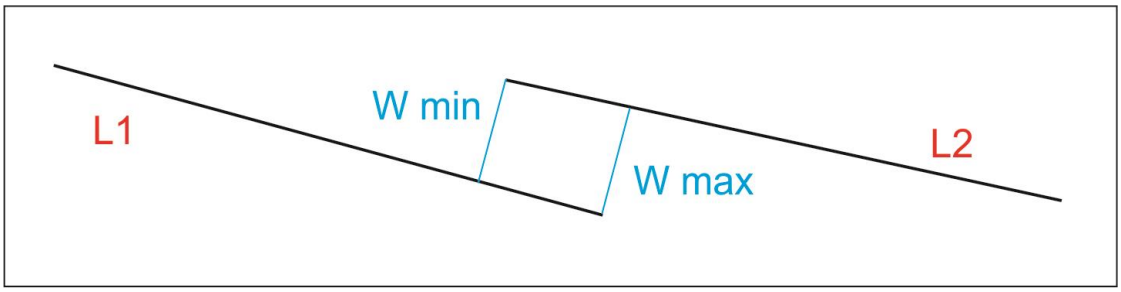

Figure 3.29. Schematic drawing showing how Greendale Fault stepovers were measured.

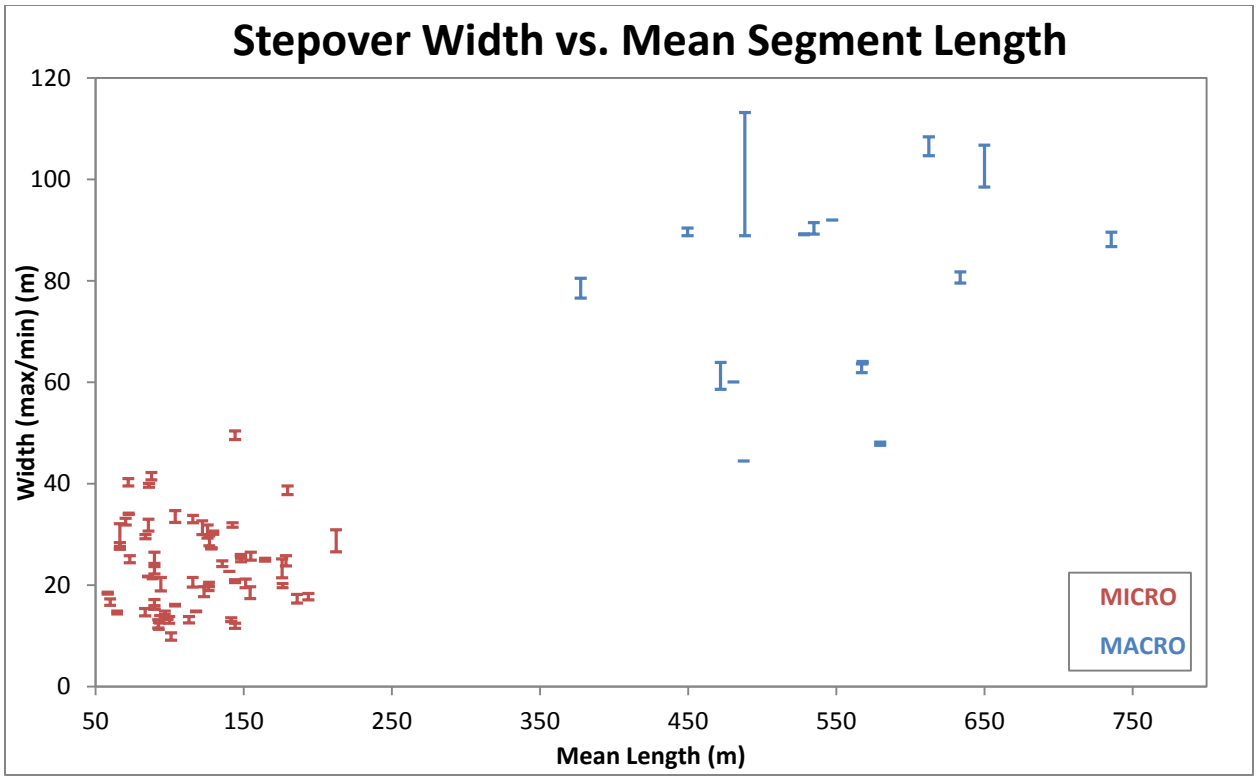

Figure 3.30. Stepover statistics: stepover width versus mean bounding segment length. The MACRO and MICRO stepovers fall into two separate datasets. Length is measured as a mean of the two bounding segments (L_1 and L_2 in Figure 3.29), while both minimum and maximum widths are plotted, measured as shown in Figure 3.29.

3.3 DISCUSSION

3.3.1 Comparisons with Greendale Fault

3.3.1.1 Qualitative Comparisons

There are two separate fault morphologies represented by the experiments in this study, and they represent the Greendale Fault at different scales. This interpretation is supported by clear morphological differences between the two sets of experiments. TALC, TALC_ER, and TALC_SED all have narrow zones of discrete fracturing, with ubiquitous R shears and scattered P or Y shears (Figures 3.1, 3.6, 3.9). These structures form a pattern of subparallel, en echelon fractures, with pop-up structures prominent in TALC_ER and subtle but present in TALC and TALC_SED. These patterns closely resemble the Greendale Fault at a scale of ~1:7,000, where the dominant structures are left-stepping en echelon structures (Figure 3.31). Conversely, TALC_SAND has a wide fracture zone consisting of dominant R shears connected by R' structures (Figure 3.13), which clearly resembles aerial photos of the fault at a smaller scale of ~1:2,500, where complex fracture patterns including R and R' structures are visible (Figure 3.32). The model fault is able to represent multiple scales because it has uniform slip along its

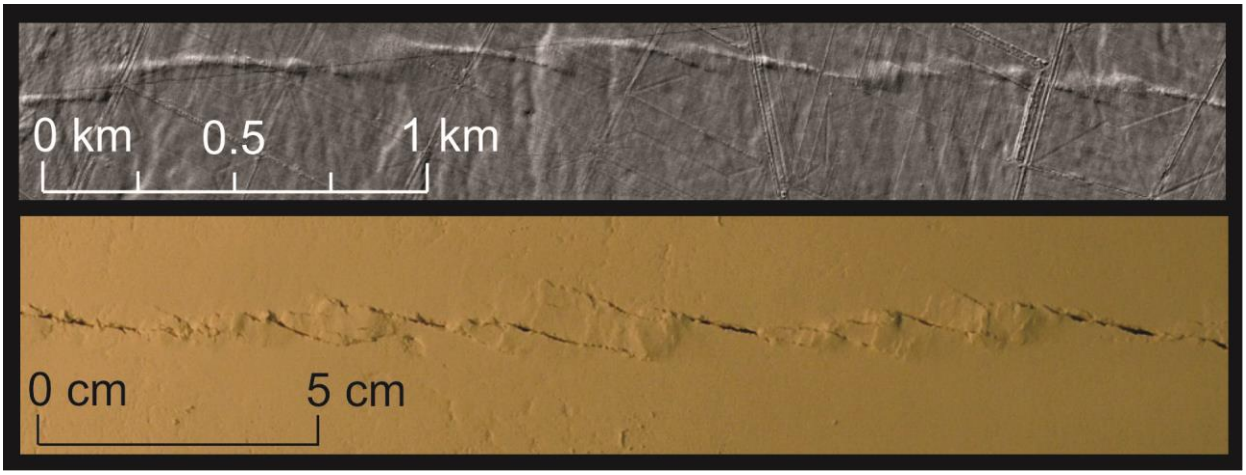

Figure 3.31. Comparison of central Greendale Fault LiDAR data (top) with TALC_ER at 15 mm displacement (below). Note left-stepping en echelon pattern with pop-up structures that is common to both images, as well as structures with similar orientations.

length, apart from edge effects at the model surface. Because a real fault's displacement decreases toward each tip, these experimental faults with uniform slip can model a fault segment of any length. See section 3.3.1.3 for further detail and quantitative comparisons of scaling parameters.

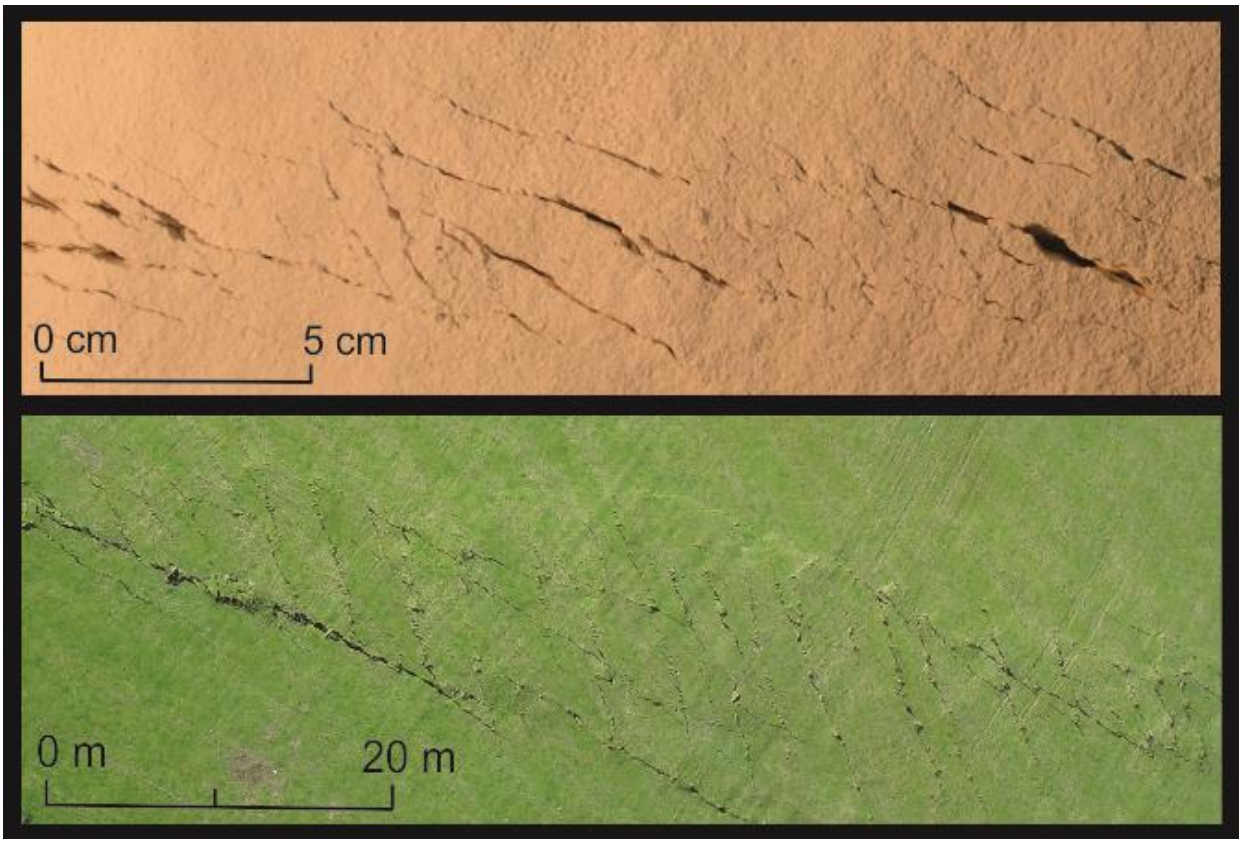

Figure 3.32. Comparison of TALC_SAND at 19 mm displacement (top) with an aerial photo of the central Greendale Fault surface trace (below). Note the similar rupture morphologies, particularly the fracture orientations and the longer R shears being linked by shorter R' shears.

Because TALC_SAND is a multi-layered experiment, it behaves in a fundamentally different manner to the other, single-layer models. Its zone of discrete fracturing is significantly wider than in the single-layer experiments (Figures 3.1, 3.6, 3.9, 3.13; see Figure 3.43 below for direct comparison; see section 3.3.1.3 for quantitative discussion of deformation zone width), which I interpret to be caused by the interaction of the two layers. While the single-layer models deform above a single basement fault, in TALC_SAND the sand layer generates a wide zone of

shear deformation beneath the upper layer of talc, so that the talc is responding to distributed shear rather than a single localized fault plane. This results in a wider, more complex zone of fracturing that includes R' shears, which are not found in any of the single-layer models (see section 3.3.1.3 for further discussion). As noted by other authors, R' shears are most common in materials undergoing distributed shear deformation (e.g. Hoeppener et al., 1969; Freund, 1974; Schreurs, 1994; An and Sammis, 1996).

This may be an appropriate analogue for the Canterbury Plains gravels at the Greendale Fault, where a lightly cemented surface layer is deforming above less cohesive gravels at depth. These lower gravels would behave as the sand does in the model, producing a distributed shear zone, above which the more cohesive surface gravels produce a complex pattern of surface deformation, including R' shears (Figure 3.32).

Conversely, the deformation in the single-layer models TALC and TALC_SED is generated by the single, planar "basement fault". This is a more reasonable analogue for the Greendale Fault at a much larger scale, where it branches from a more confined fault plane at depth, and surface effects are not the most important control on morphology (see section 3.3.1.4 for a quantitative discussion of these depths). Likewise, R' shears are not present at this scale in the models or at the Greendale Fault (Figure 3.31).

The behaviour of TALC_ER is influenced by both of these styles of deformation. It has the same thickness of talc as TALC and TALC_SED, and is also deforming above the single fault in the base of the model. However, the process of scraping the surface smooth at the start and at 5 mm intervals compresses the surface slightly. This creates a more brittle crust on the surface deforming over the shear zone beneath it, in a similar manner to the multilayer TALC_SAND model. Also, under compression, talc's internal angle of friction increases

(section 2.4), which may explain the slightly more oblique angle of initial Riedel shears in TALC_ER (see sections 3.3.2.1, 4.3.2 for further detail).

TALC_ER, and to some extent TALC_SED, are particularly interesting because of the element of "resurfacing" that they share—by erasing surface evidence of previous deformation at 5 mm intervals, the only structures that appear during displacement are ones that are active at that time. Therefore rather than measuring the results of cumulative deformation, as in TALC and TALC_SAND, only the actively deforming fractures are mapped and measured. This is more likely what would be observed on an active fault in the field—depending, of course, on the recurrence interval of the fault and the local sedimentation/erosion rate—so it provides an opportunity to consider fault development and how to best study paleoruptures (see Chapter 4 for detailed discussion).

The fault zones generated in these experiments are highly intricate, with multiple types of shears that develop and link with increasing strain, but they are generated by displacement on a single, planar, "basement" fault. While there are certainly complications at the Greendale Fault beyond this ideal model (e.g. multiple faults at depth with different magnitudes and directions of slip, variations in slip gradients along those faults, rupture directionality and dynamics, etc.), these experiments demonstrate that it is possible to generate surface complexity from a simple, planar structure undergoing uniform slip.

3.3.1.2 Quantitative Comparisons

The qualitative comparisons described above are supported by quantitative measurements of fault zone deformation. As mentioned previously, the length and azimuth of each fault segment was measured and recorded to generate the following plots. The experimental data and

the Greendale Fault data were compared using plots of length versus azimuth (Figures 3.33-37, 3.46), as well as histograms showing the relative distributions of azimuths (Figures 3.38, 39).

In a plot of cumulative length versus azimuth that includes all of the experimental and field data, the longer fractures in every dataset are in the 90-130° range, with the very longest structures striking 100-120° (Figure 3.33). The majority of structures strike between 100° and 170° and are relatively short. The Greendale Fault has more fractures that are oblique to the overall fault strike (~90°), with a significant population from 90-180°, as well as 0-20°, whereas the experimental data are more fault-parallel, with most structures falling between ~80-165°.

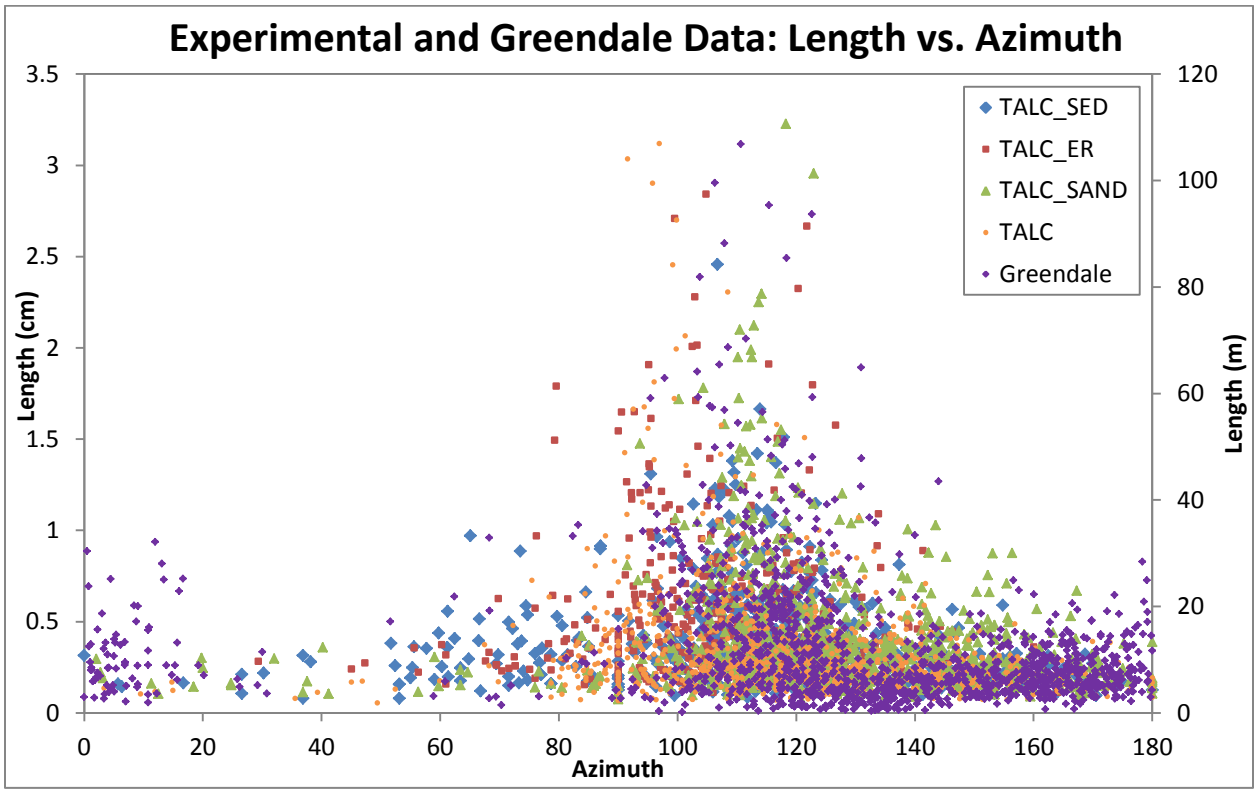

Figure 3.33. Length vs. Azimuth comparison for TALC, TALC_SAND, TALC_SED, TALC_ER, and the Greendale Fault. The longest structures in all experiments overlap in the 100-120° range. Note comparative lack of Greendale Fault structures at 20-80°, and lack of experimental structures ≥160°.

Length versus azimuth plots can also be used to compare the experiments at different strain intervals to find the best match with the Greendale Fault data (Figures 3.34-3.36). In this

study, the plots have only been compared qualitatively, visually noting areas where data points are denser or scarcer, and comparing the spatial overlap between datasets. Further statistical analysis has not been performed, but the datasets could be quantitatively tested for how similar they are using techniques designed for fingerprint matching, which also determines the similarity of a set of points mapped in two dimensions (e.g. Jain et al., 1997; Duta et al., 2002).

As expected, initial fractures are cross cut by more fault-parallel structures with continuing displacement, and a few long structures develop in the 90-120° range. The closest overlap between the models and the field data is a point between 10 and 20 mm displacement. In the 10 mm plot, there is good overlap among the longest structures, but there are moderate-length experimental structures at 130-160° that are not present in the field data, and conversely, there are field structures at 0-20° that are not present in the experimental data (Figure 3.34). In the 20 mm plot, the longest structures seem to be a better match in terms of their azimuth range, and the experiments have developed some fractures in the 0-30° range (Figure 3.35). However, the experiments also have a population of structures oriented at 30-100° that is significantly greater than the relative population of Greendale structures in that azimuthal range. By 30 mm displacement, the experiments have developed too many fault-parallel structures (80-100°) to be a reasonable analogue for the field data (Figure 3.36). Only TALC_ER and TALC_SED were measured at 15 mm displacement, but they display a close match with the Greendale Fault data at this point (Figure 3.37).

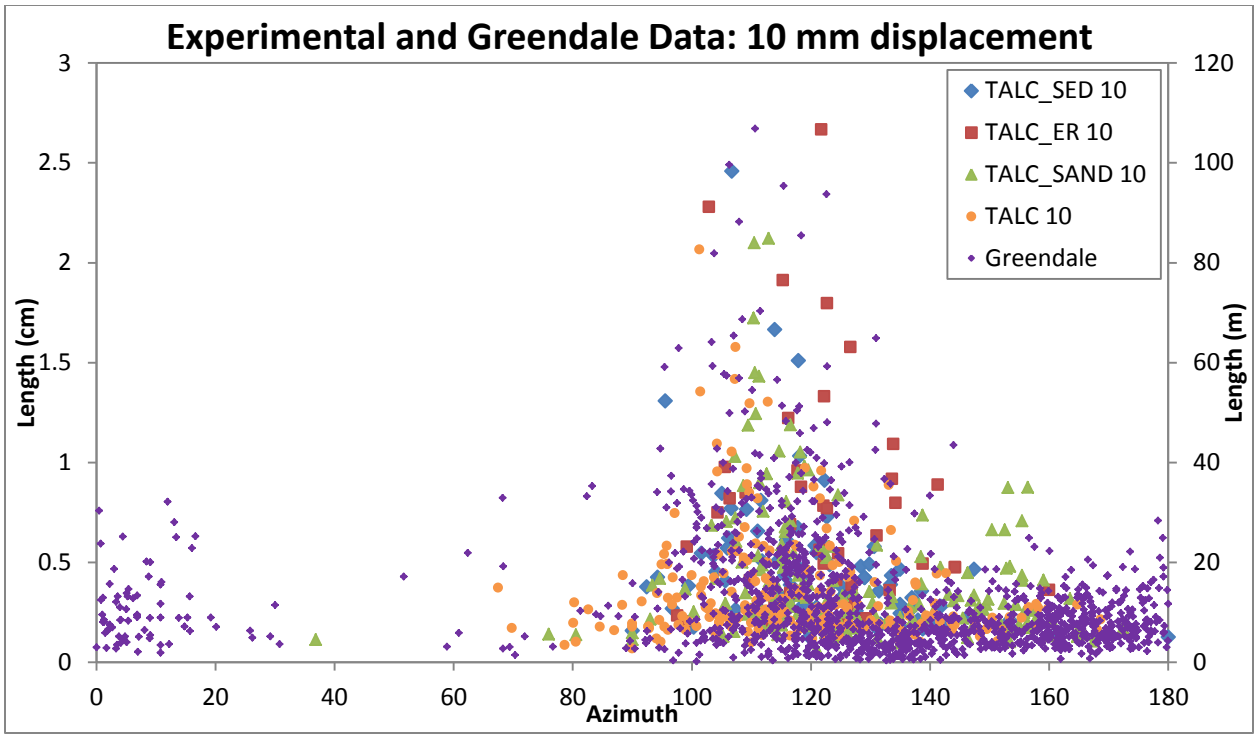

Figure 3.34. Model data at 10 mm displacement with Greendale Fault data. The populations of longer structures (≥1 cm) are very similar throughout the datasets, but the field data has a much higher density of structures ≥160° and at 0-20°.

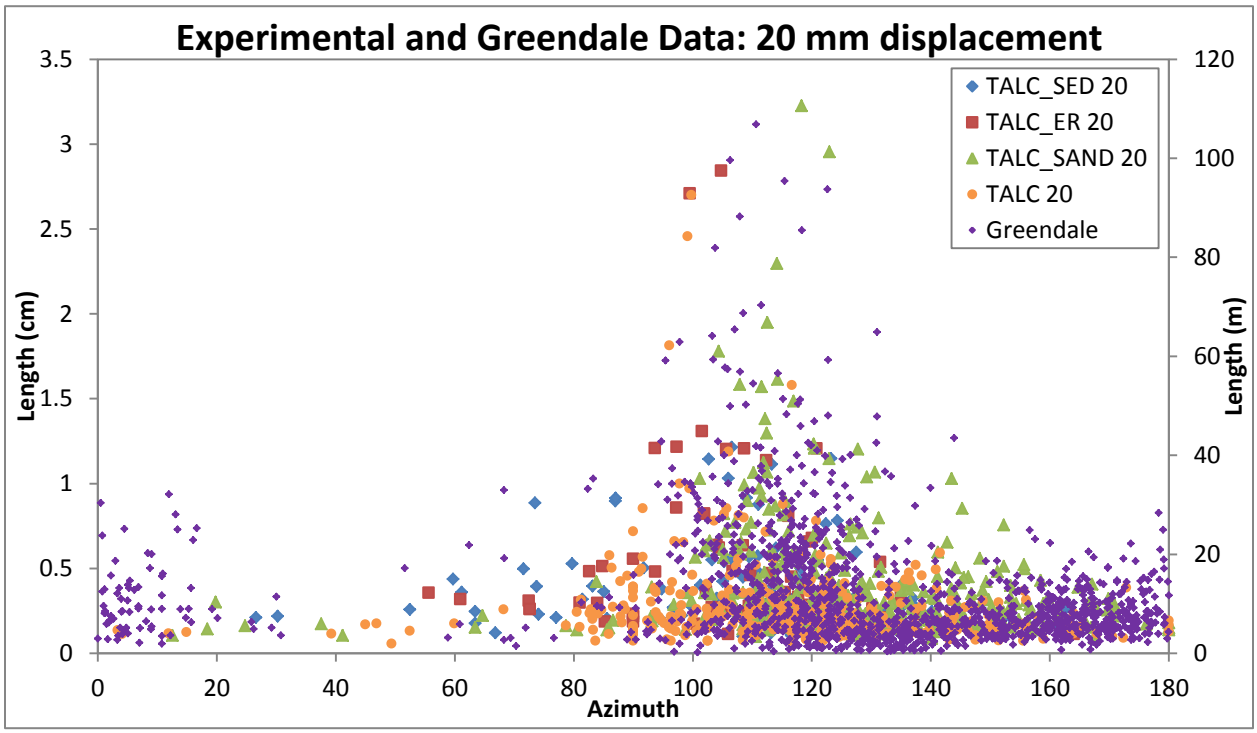

Figure 3.35. Model data at 20 mm displacement with Greendale Fault data. The longest structures are again similar throughout all datasets, and at this strain interval, the experiments have developed some structures where they were previously lacking (e.g. 160-180°, 0-20°). However, the experimental data also now show a small population ~60-90°, where there are very few field data points.

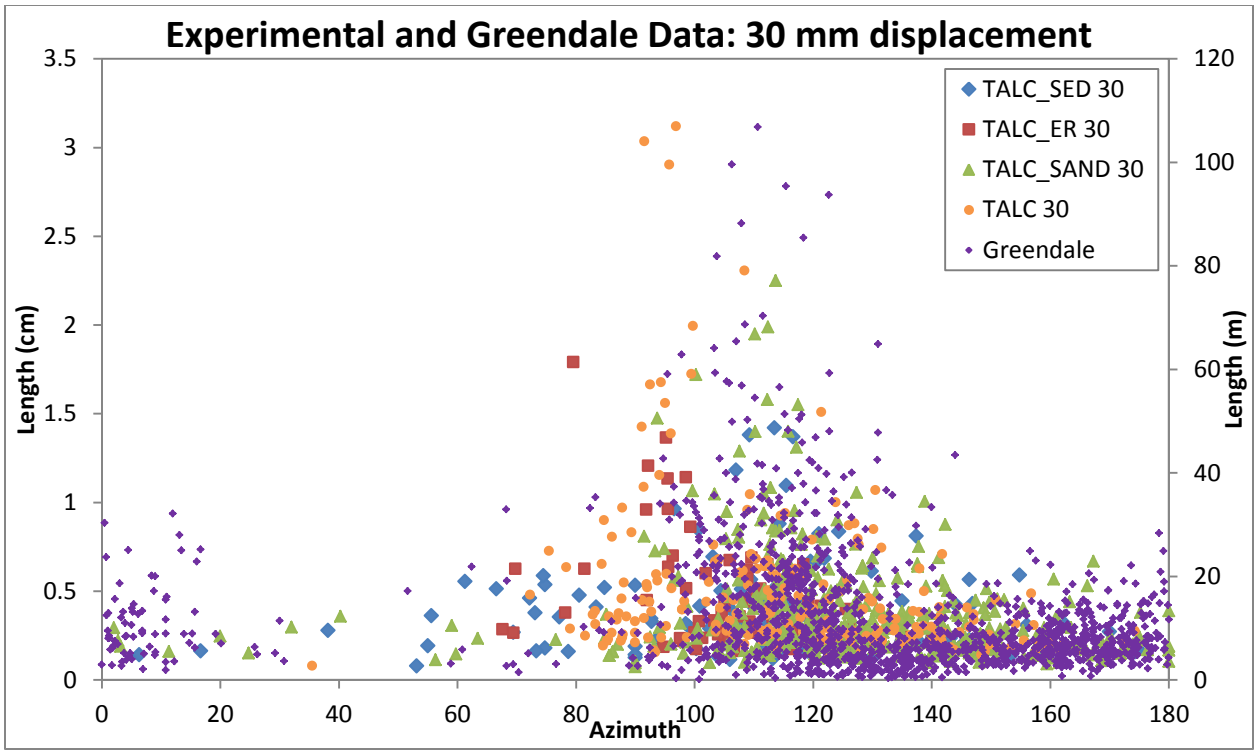

Figure 3.36. Model data at 30 mm displacement with Greendale Fault data. There is good overlap here between all datasets at 100-180°, but the experimental datasets have developed a significant population at 50-90° that is not present in the field data.

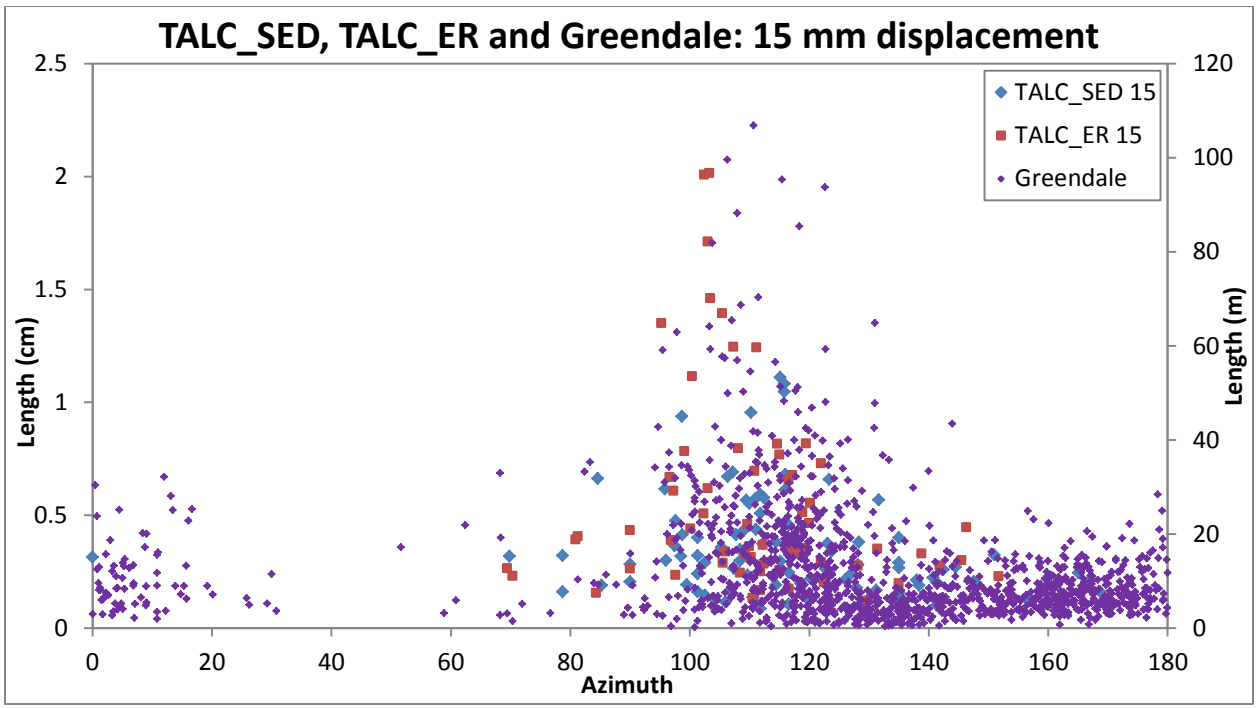

Figure 3.37. TALC_SED and TALC_ER at 15 mm displacement compared with Greendale Fault data. All the datasets have their longest structures at 100-120°, although TALC_SED's longest structures are relatively shorter than those of the other datasets. There is good overlap in the spatial distribution of points from all three datasets, particularly in the 80-150° azimuth range.

Another way to compare the field and model data is to consider the relative frequency of fracture azimuths, which shows a close match between all five datasets (Figure 3.38). They all show a main peak in the 100-120° Riedel shear range, with azimuth frequencies decreasing in both directions from that peak. The largest discrepancy between the field and experimental data is the Greendale Fault's significant proportion of highly oblique fractures at 160-180°, which continues at 0-15°. Likewise, TALC_ER has a higher proportion of fractures in the 90-110° range than the other datasets.

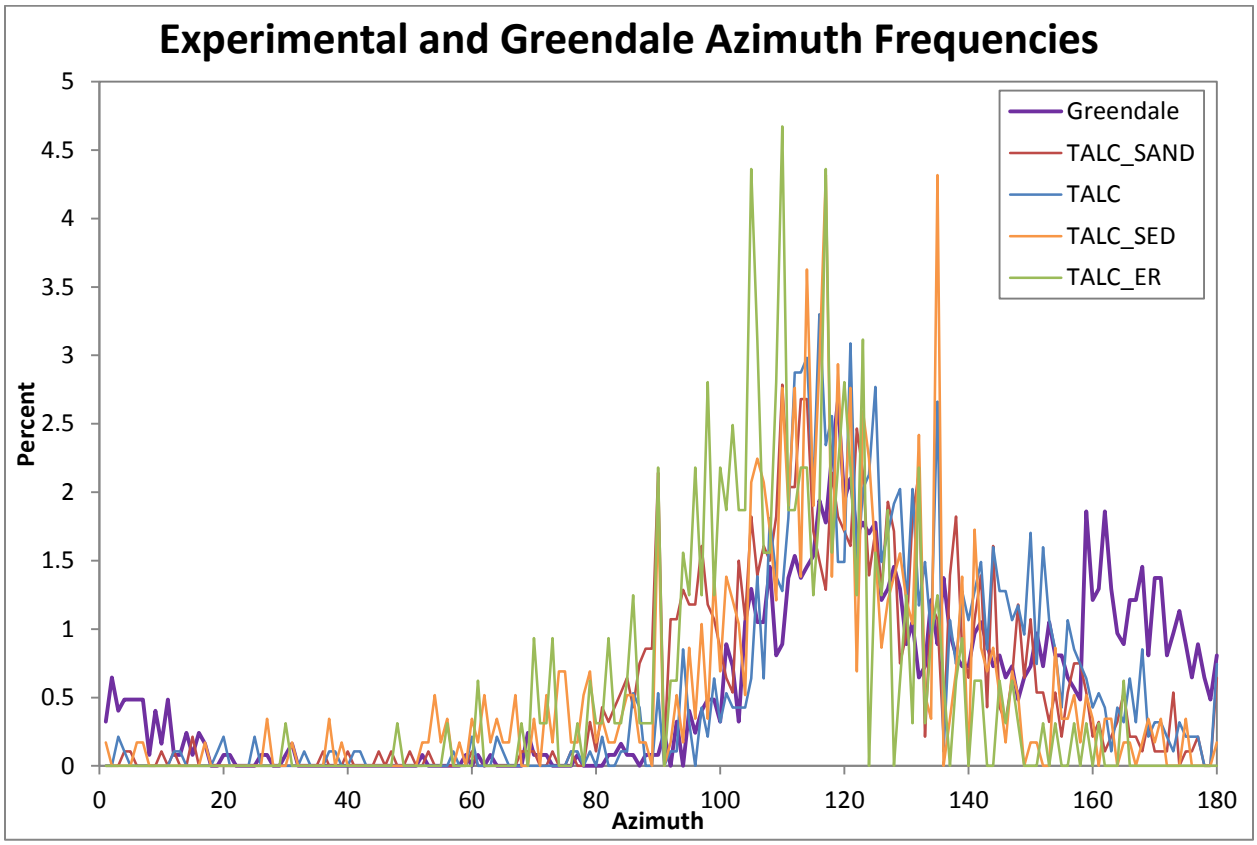

Figure 3.38. Relative frequency of fracture azimuths in Greendale Fault data as compared with model data (0-30 mm displacement). The experiments fit the field data best in the 90-140° range, with the partial exception of TALC_ER, and the largest discrepancy is the higher frequency of Greendale Fault fractures at 160-180° and 0-10°. The peak at 135° is an artefact.

The length vs. azimuth plots (Figures 3.34-3.37) suggest that the models at 15 mm displacement are the best estimate of the field deformation, and of the experiments measured at 15 mm, TALC_ER has the closest azimuth distribution (Figure 3.38). In particular, the sum of the azimuth distributions at 10 and 15 mm is a very good estimate of the Greendale Fault main fracture peak, aside from the more oblique fractures that are not present in the models (Figure 3.39).

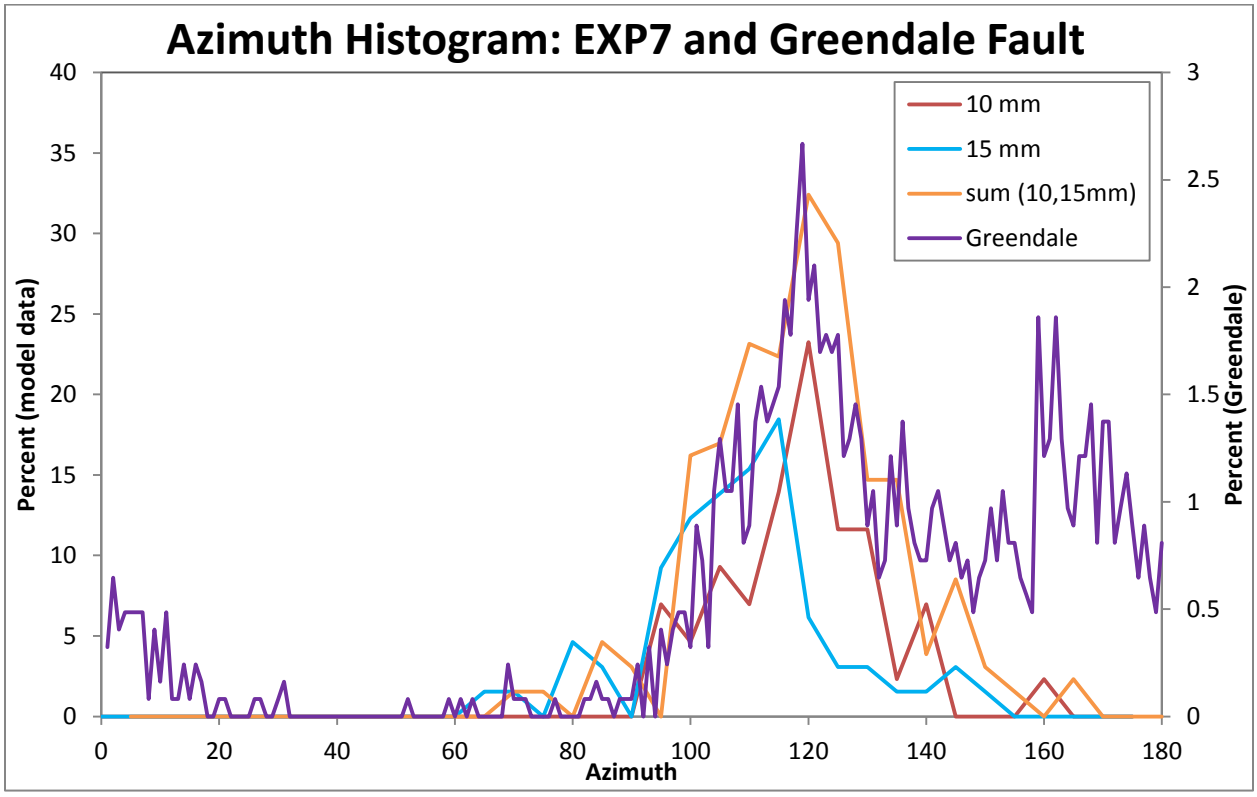

Figure 3.39. Azimuth distribution of Greendale Fault data compared with TALC_ER data (10 and 15 mm intervals, and the sum of the two). The sum of the azimuths in TALC_ER at 10 and 15 mm are a very close match with the field data in the 20-140° range.

The highly oblique structures (160-180°) present in the Greendale Fault data (Figure 3.38) are mainly R' shears based on their orientation, and the majority of them are very short (≤10 m; Figure 3.33). These small-scale structures are measurable because it is possible to view the digital dataset at very large or small scales and map the fractures present in both. However,

the resolution of the model photographs does not allow for fracture mapping at this level of detail—the scale at which these would have been generated in TALC, TALC_ER, and TALC_SED is too small to have been measured. R' shears are present in TALC_SAND, but the scale of that experiment is more than an order of magnitude smaller and cannot approximate the morphology of the central Greendale Fault as a whole.

3.3.1.3 Deformation Zone Width

Still photographs of the experiments record the development of discrete fracture patterns, while the PIV data shows distributed shear strain, providing an opportunity to consider the relationship between these deformation styles as well as the factors that control them.

The data for distributed shear demonstrates that the width of early deformation is directly proportional to the thickness of material above the basement fault (Figure 3.40). The experiments are TALC, SAND, and TALC_SAND, which shows that this relationship holds true for different materials as well as for single- and multi-layer experiments. The width of discrete fracturing has a slight correlation with overburden thickness, but not as strong as the correlation with distributed strain (Figure 3.41). This implies that regardless of material properties , the width of distributed shear is controlled by material thickness, as noted by other authors (e.g. Naylor et al., 1986; Atmaoui et al., 2005), while the width of discrete fracturing is influenced by other factors.

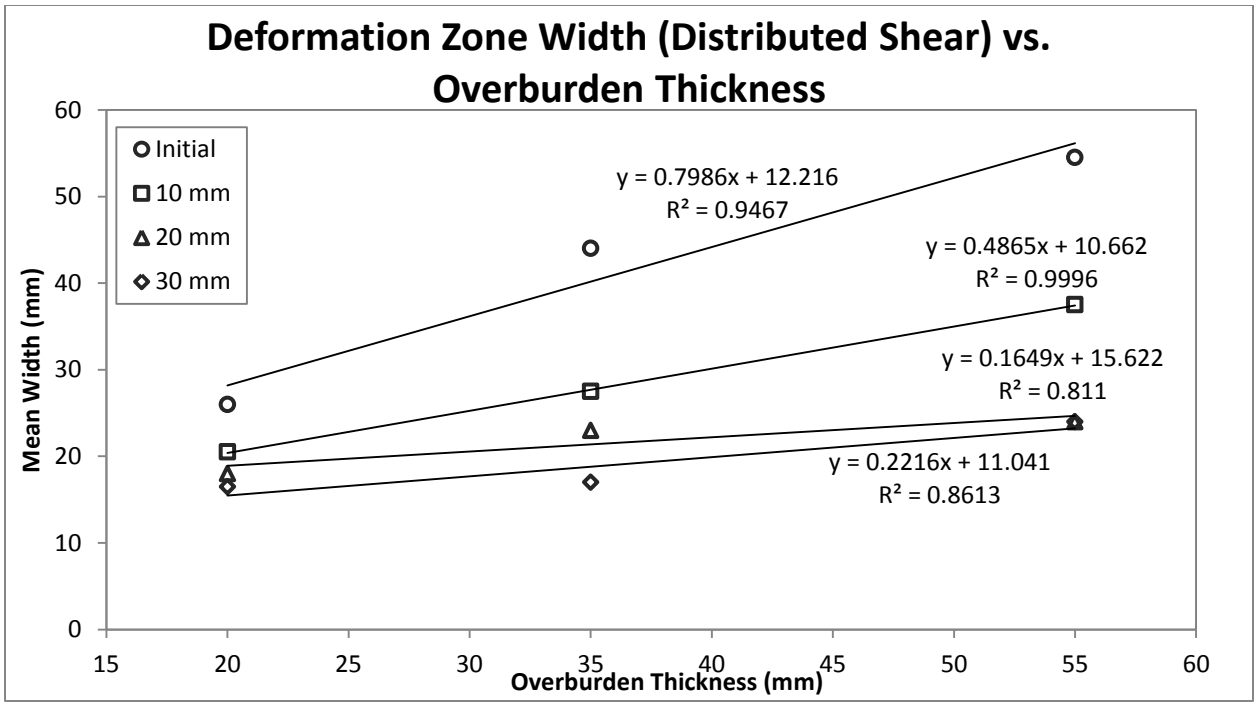

Figure 3.40. Mean width of distributed shear vs. overburden thickness plotted for TALC (20 mm thickness), SAND (35 mm thickness), and TALC_SAND (55 mm thickness) at different strain increments. Width and depth are closely correlated throughout displacement, although the closest fits are at earlier strain intervals.

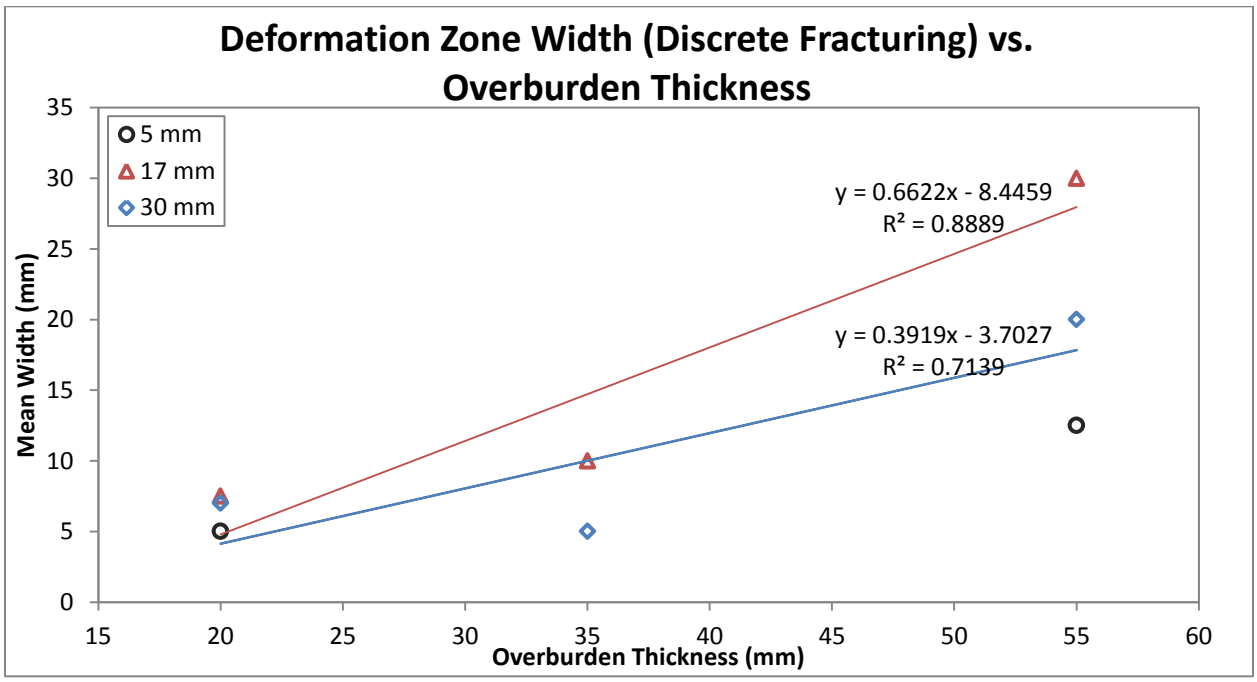

Figure 3.41. Mean width of discrete fracturing vs. overburden thickness for TALC (20 mm thickness), SAND (35 mm thickness), and TALC_SAND (55 mm thickness) at different strain increments. There may be a loose correlation for the 17 and 30 mm intervals, but it is not as strong as the correlation between the width of distributed strain and the overburden thickness. Trendlines are colour coded based on the series they belong to: red for 17 mm displacement and blue for 30 mm displacement. (Note: there is no data point for SAND at 5 mm because discrete fractures had not yet appeared.)

The development of each deformation zone width (discrete fracturing and distributed shear) was plotted with respect to displacement. The distributed shear strain is initially very diffuse and then narrows quickly, during the first few mm of displacement, then widens as oblique fractures start to grow and lengthen at 4-6 mm displacement (Figure 3.42). Maximum values are measured where the most highly oblique structures (R shears) persist, and they remain stable or gradually decrease while oblique fractures develop and are active, then they decrease as displacement concentrates on the Y shear. Minimum values, measured where deformation is localized on a single shear, quickly drop to a stable level (10-30 mm displacement).

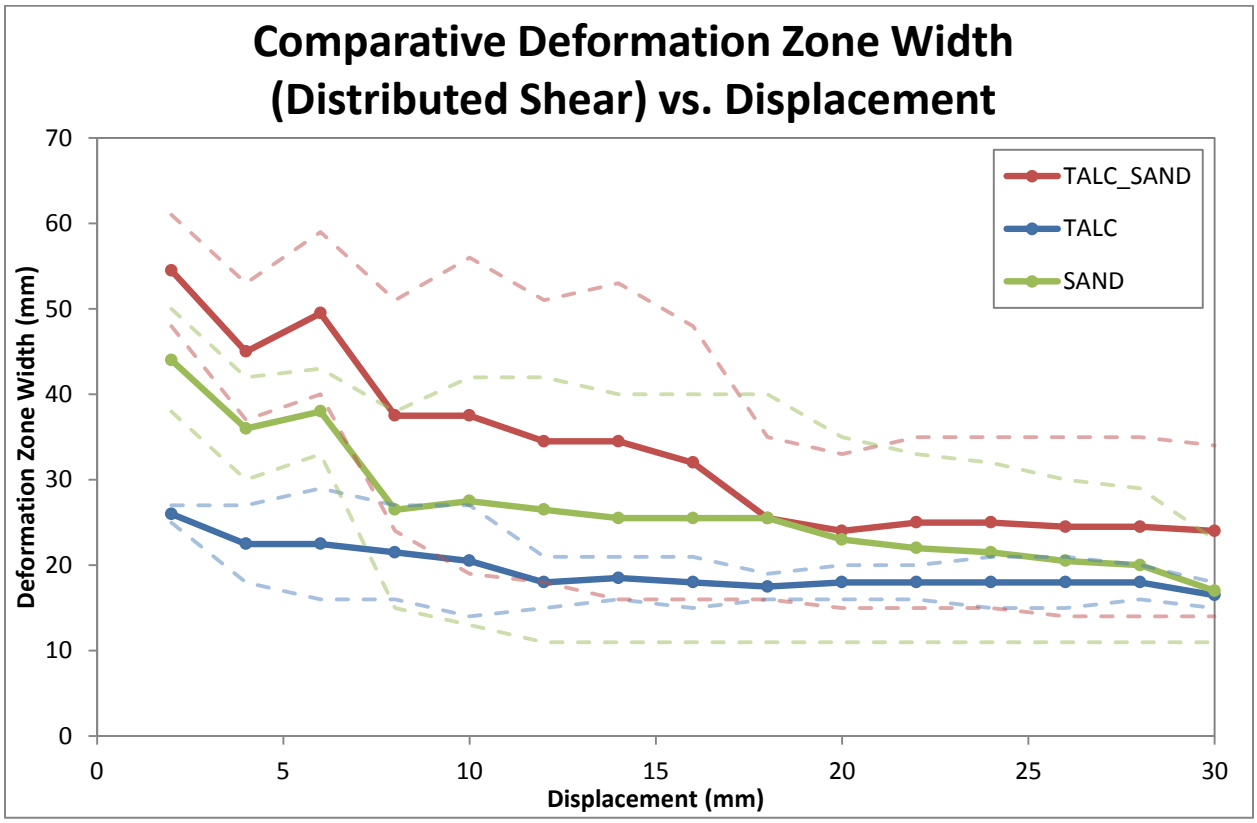

Figure 3.42. Width of zone of distributed shearing with ongoing displacement for TALC, SAND, and TALC_SAND. Mean values highlighted, with maximum and minimum values shown as dashed lines. The minimum values show where deformation is quickly localized on a single shear, while the behaviour or the maximum values are more complex.

Discrete fractures are not visible until ~5 mm displacement, when the fracture zone width begins to increase as the oblique R shears develop (Figure 3.43). For TALC and SAND, it increases very slightly, while for TALC_SAND, it increases dramatically. There is no SAND data until ~15 mm displacement because the PIV images make it difficult to identify discrete shears, so they were not measured until they were undoubtedly present. After ~8 mm displacement in TALC and TALC_SAND, the maximum values remain high due to the presence of inactive fractures, while the minimum values decrease, which shows localization on the Y shear.

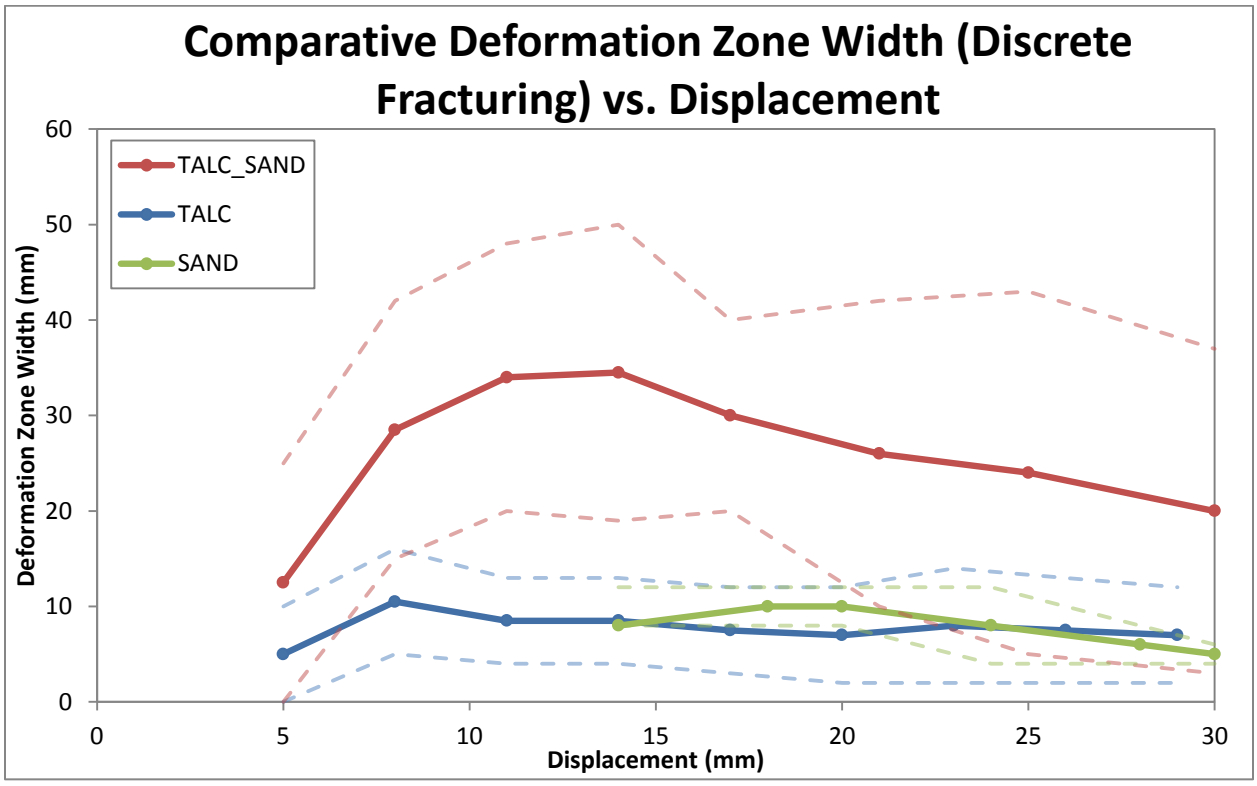

Figure 3.43. Width of discrete fracturing zone with ongoing displacement for TALC, SAND, and TALC_SAND. Mean values highlighted, with maximum and minimum values shown as dashed lines.

As discussed in section 3.3.1.1, the single-layer models behave differently than the multilayer model because they are being deformed by a single basement fault, as opposed to the

multilayer model in which the top layer is deforming over a distributed shear zone generated in the bottom sand layer. Regardless of cohesiveness, the single-layer models had narrow zones of discrete fracturing that were ~40% as wide as the total zone of distributed shear. However, the multilayer model had a wide, complex pattern of discrete fracturing, which approached the same width as the zone of distributed shear (Figure 3.44).

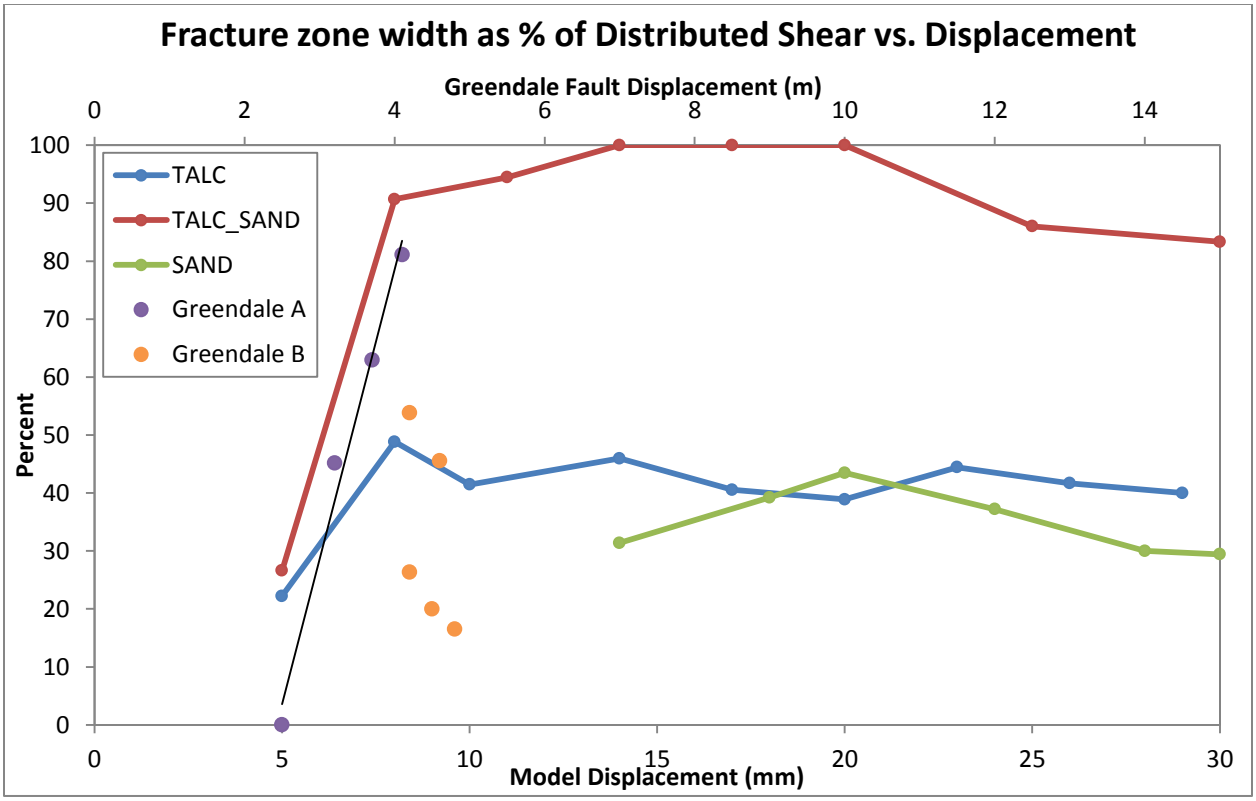

Figure 3.44. Discrete fracturing zone width as a percentage of the distributed shear zone width, with ongoing strain. The Greendale Fault data are plotted as a function of the displacement at the site where the deformation zones were measured. The trendline is fit to Greendale set A, which shows similar behaviour to the initial stages of TALC_SAND. Greendale set B is a series of measurements with higher displacement that diverge from that initial trend. The field and experimental displacements are scaled according to Table 3.1.

The distributed shear data from the Greendale Fault rupture come from the initial field mapping done by the University of Canterbury and GNS teams (Quigley et al., 2010; Van Dissen et al., 2011), while the discrete fracture zone widths are measured using the digital datasets produced from the LiDAR mapping (see section 2.7 for details). These are plotted as a function

of the displacement at the location where they were measured, which can be considered as an analogue to the increasing displacement in the experiments. At these initial stages of displacement and fracture growth, the field data matches TALC_SAND's behaviour very closely. However, after this initial steady increase, the discrete fracture zone at higher displacements along the Greendale Fault is significantly narrower. This may be explained by displacement focusing onto a few major structures at high displacements, or by heterogeneities present in the field.

Since the TALC and SAND models are the same thicknesses as the corresponding layers in TALC_SAND, it is possible to directly compare how the multi-layered model deforms with how TALC and SAND behave individually. TALC and SAND's fracture and shear zones have a given width at each model's surface (the maximum values at 11 mm displacement are used in this case; see Figures 3.42, 3.43). Deformation branches out from the basement fault, so the deformation zones can be thought of as triangles, where the bottom angle is characteristic of the material (Figure 3.45). Based on these angles, it is possible to model how the deformation in the upper layer of TALC_SAND is related to the lower layer. The closest approximation is where the talc layer is being deformed by the distributed shear zone of the sand beneath it (Figure 3.45B). This is a slight overestimate of TALC_SAND's surface deformation, which may be because the talc is not greatly affected by the very low shear strain at the edges of the SAND shear deformation zone, so the outer edge of the distributed shear zone is slightly narrower than how it is shown. Alternatively, perhaps because the sand behaves slightly differently with the added layer of talc on its surface because it is confined at its upper surface, or because the weight of the talc layer compresses it slightly. Another possibility is that the boundary of the shear zone is not strictly linear, as assumed here, which could explain the slight mismatch between the

observed shear zone widths in TALC_SAND and those predicted by the model in Figure 3.45B (e.g. Schrank et al., 2008).

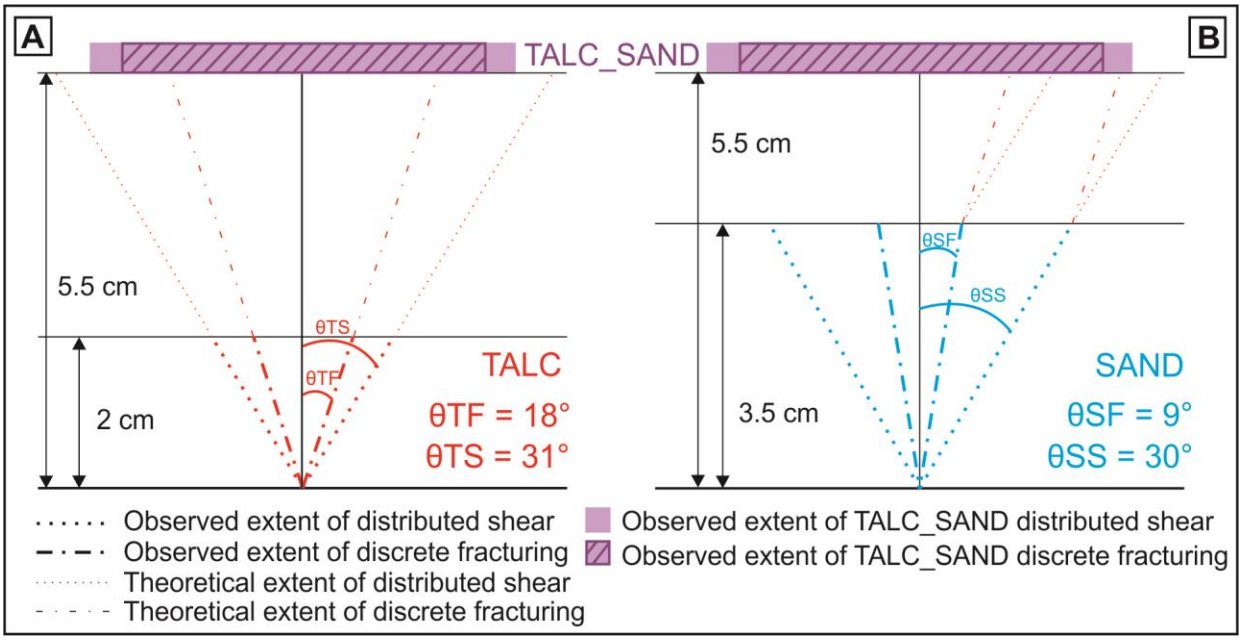

Figure 3.45. Schematic representations of model deformation in cross section. Deformation zones are idealized as straight lines from the basement fault to the model's surface. The zones of discrete fracturing and distributed shear are shown as they were observed at the surface of A) TALC and B) SAND, with the deformation from TALC_SAND noted at the upper surface of both A and B. The angles at which they stem from the basement fault are noted. A compares the observed surface deformation in TALC_SAND with the theoretical distribution of surface deformation in a model with the same thickness as TALC_SAND (5.5 cm) based on θ_{TF} and θ_{TS}; the distributed shear zone is much wider, while the discrete fracturing is much narrower. B compares the observed surface deformation of TALC_SAND with the modelled combination of the SAND and TALC experiments: the talc deforms at angles θ_{TF} and θ_{TS} from the furthest extent of the discrete fracture zone and from the extent of the distributed shear zone. The latter is a much closer match with the observed deformation in TALC_SAND because both the distributed shear zone is wide enough, and the discrete fracture zone is much wider than could be generated by the same thickness of only talc or sand.

3.3.1.4 Scaling

This experiment is scaled according to the parameters described by Hubbert, 1937 (section 2.5). Beyond these basic relationships between density, length, cohesion, etc., multiple different length dimensions of the fault zones can be measured and scaled in a useful way. As discussed above (section 3.3.1.1), TALC_SAND models the fault zone at a smaller scale than TALC, TALC_ER and TALC_SED, which is made possible by uniform slip on the model fault.

Qualitatively, TALC_SAND models the fault at a scale of tens to hundreds of meters, where complex fracture patterns including R and R' shears are visible, while the other experiments model the fault at a scale of hundreds to thousands of meters, where the dominant morphology is that of left-stepping en echelon segments. This section will more quantitatively explore those scaling relationships.

Several parameters are considered here to scale the Greendale Fault surface trace with the experimental faults: the width of the deformation zone (specifically, the zone of discrete surface fractures), the length of the fault segment being modelled, the average fracture length, and the depth at which the structures branch from a more confined fault plane. The specific structures considered for these scaling relationships are the dominant ones at each scale: R and R' shears for Table 3.1, and larger en echelon segments for Table 3.2 (see Figures 3.31, 3.32 for visual comparisons of the Greendale Fault with the experiments).

	Fracture Zone Width	Length	Avg. R Length	Avg. R' Length	Displacement	Branching Depth
TALC_SAND	0.05	0.4	0.06	0.03	0.01	0.055
Greendale	35	200	30	12	5	27.5
Scaling factor	700	500	500	400	500	500

Table 3.1. TALC_SAND and Greendale Fault scaling relationships. All units are meters.

	Fracture Zone Width	Length	Avg. Fracture Length	Branching Depth
TALC, TALC_ER, TALC_SED	0.015	0.4	0.04	0.02
Greendale	100	2667	400	133
Greendale	6667	6667	10000	6667

Table 3.2. TALC, TALC_ER, TALC_SED, and Greendale Fault scaling relationships. All units are meters.

It may seem intuitive to scale the depth of granular material in these experiments with the thickness of Quaternary sediments at the Greendale Fault. However, scaling this quantity the

same way as other parameters gives a "depth" for the Greendale Fault that is much shallower than the depth to bedrock, which is known to be 750±250 m in the region of the fault (Jongens et al., 2012). Instead, this depth corresponds to the branching depth, the point at which Riedel shears and other structures splay from a single, more localized fault plane (Figure 1.8). In the experiments, all structures branch from the basement fault, so this depth is simply the thickness of granular material. The larger, hundred meter-scale structures being modelled by the experiments in Table 3.2 have a deeper branching depth than the ones in TALC_SAND (Table 3.1), so subsidiary R and R' structures could branch off of those. See section 3.3.3 for further discussion of branching depths.

3.3.2 Effects of interseismic sedimentation and erosion

3.3.2.1 Experimental Data

TALC_SED and TALC_ER were both designed to test the influence of interseismic effects on the development of surface rupture patterns, with the former considering interseismic sedimentation and the latter interseismic erosion. As suspected, they were relatively similar to TALC, the "baseline" model; regardless of surface effects, the structures should continue to develop the same way at depth, and previously fractured planes would remain the path of least resistance.

The majority of fractures from TALC_ER and TALC_SED fall between 90° and 130°, which includes a significant population of short fractures (<1 cm), and a few long fractures up to 3 cm in length (Figure 3.46). While the length versus azimuth plot shows a similar range of fractures for all three experiments, there is a higher density of TALC_ER and TALC_SED structures at lower azimuths (50-80°), and a higher density of TALC structures at higher azimuths (140-180°; Figure 3.46). These discrepancies are likely due to the resurfacing element

of TALC_ER and TALC_SED, where initial, more oblique structures would be erased when they are no longer active. Conversely, TALC gives a measurement of cumulative deformation, so an early-forming, oblique structure would continue to be measured repeatedly even after it becomes inactive.

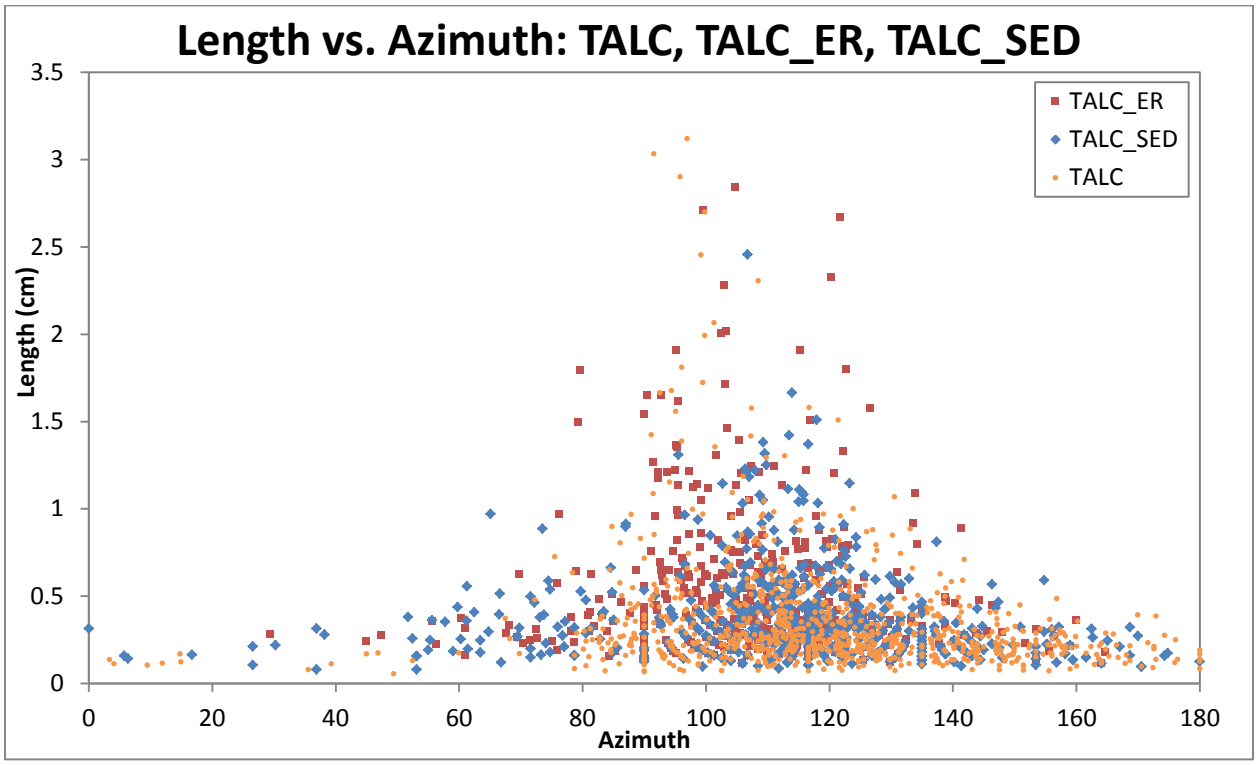

Figure 3.46. Comparison of fracture length vs. azimuth for TALC, TALC_ER, and TALC_SED. Highest density of fractures is in the 100-130° azimuth range at short lengths, whereas the longest structures fall between 90 and 120°.

Another contrast between the models is that TALC_SED developed fewer long fractures than TALC or TALC_ER (Figure 3.46). If this was a general phenomenon caused by erasing the surface deformation every 5 mm, the same pattern should be evident in TALC_ER, which it is not. Instead, the element unique to TALC_SED is sedimentation. While TALC_SED may have developed the same extended structures at depth as the other experiments, perhaps they were unable to propagate through the layer of new sediment to the surface along their full length during the short intervals of displacement (5 mm) between sedimentation events. Essentially, the

fracture propagation could not keep pace with the sedimentation. The scraping of the surface in TALC_ER does not cause the same effect; although the surface is "reset", the resurfacing process in this case only erases the deformation in a very thin layer, rather than adding material, so it is more easily ruptured during the subsequent 5 mm of displacement.

However, scraping the model surface in TALC_ER may affect deformation in other ways. In particular, TALC_ER develops more very oblique structures at higher lengths (≥120°, ≥0.5 cm) that are not present in other experiments (Figure 3.46). The process of smoothing the surface compresses the talc slightly, and shear wagon tests showed that talc's angle of internal friction (φ) increases with compaction (section 2.4). The angle of Riedel shear formation is dependent on φ, so this explains the presence of more oblique fractures in TALC_ER, particularly at early strain intervals when the surface is relatively unfractured. As a side note, Figure 3.38 seems to show a higher population of more fault-parallel structures, but this is because TALC_ER is measured from 0-40 mm displacement, while other experiments stop at 30 mm. The higher proportion of measurements at later displacements, when more structures are fault-parallel, skews the graph in this direction, despite the significant presence of oblique structures earlier in model development.

3.3.2.2 Application to Active Faults

Paleoseismology is critical to understanding how faults have behaved in the past and how they might in the future, which is key for land use planning and hazard assessment purposes. This study examines factors that could affect how faults develop through multiple ruptures, such as interseismic activity at the fault surface, which would influence how they appear in the paleoseismic record.

It is widely recognized that mature, fast-slipping faults consistently reactivate the same rupture plane (e.g. the San Andreas Fault, the Alpine Fault, the Wellington Fault), but the detailed mapping of the Greendale Fault surface rupture raises the question of whether faults with complex surface rupture patterns will reactivate the same structures in future events, and if so, how frequently will they be reactivated, and which specific structures will be reactivated? In particular, I considered how interseismic activity affects fault morphology from rupture to rupture, or whether the changing rupture morphology as the fault matures could be a more important control on which fractures are reactivated (e.g. Figure 3.9). The question of interseismic activity is addressed here, while further examination of fracture reactivation is found in Chapter 4.

Once a fault has matured past its initial stages of fracture formation and development, the trend observed in these experiments is for the deformation zone to narrow through time. The dominant morphology initially is R and R' shears oblique to the fault zone, which are then cross-cut by subparallel R_L structures, and eventually deformation localizes on the Y shear plane. It is important to note that these are not the same structures simply rotating toward the PSZ—rather, they are cross-cut by later generations of fractures. The progression of the deformation zone narrowing with time is visible both in the time lapse photographs of the faults' development that show discrete fractures, and particularly in the PIV images that show the distribution of shear strain (Figures 3.42, 3.43; section 3.3.1.3). Common sense suggests that a previously-ruptured plane would be the path of least resistance and thus the easiest pattern for subsequent ruptures to follow, separate from the evolution of structures from oblique to fault-parallel. However, I wanted to test if this hypothesis held true despite different interseismic effects.

One caveat that should be noted is that the experiments are based on a single basement fault that remains consistent from rupture to rupture. The Greendale Fault has many possible complications beyond this ideal case, particularly variable rupture length and magnitude, and the involvement of multiple subsurface faults (Beaven et al., 2010; Holden et al., 2011; Elliott et al., 2012). These factors and others, like variations in recurrence interval, increased or decreased interseismic annealing, and rupture directionality could alter the surface position or morphology of a future rupture.

For example, cohesiveness and surface cementation are major factors in determining surface rupture morphology (section 3.3.1.3), and increased interseismic annealing at depth, or surface cementation or pedogenesis during a long recurrence interval would significantly increase the cohesiveness of the ground surface. This would likely result in a rupture with a wider, more complex fault zone with more discrete fractures than a similar rupture with minimal interseismic cementation.

Scraping the surface of TALC_ER between displacement intervals could be a reasonable analogue for a fault with moderate interseismic cementation or pedogenesis, while TALC_SED or even TALC could show the development of a fault where these processes are not a major factor. But despite these complications, the experiments provide a useful foundation with which to make reasonable predictions about the behaviour of recently active faults.

My models show that, as suspected, regardless of interseismic activity at the surface—sedimentation, erosion, agricultural or other human activity, etc.—the surface deformation zone narrows with time after initial fracture growth (Figures 3.42, 3.43). These results will hold different interest for different groups: scientists will want to know if the same fault strands are reactivated in multiple events, and how past deformation would show up in a paleoseismic trench

(see Chapter 4). Conversely, for land use planning purposes, local variation within a fault zone several hundred meters in width is of little concern, while understanding broader characteristics of fault behaviour is much more important. Villamor et al. (2011) designed a "fault avoidance zone" around the Greendale Fault based on a 1 km buffer zone around the farthest extent of the 2010 surface deformation; the results of this study confirm that a previously mapped rupture should give a maximum extent for surface deformation in future events, and that future earthquakes will likely produce a narrower surface deformation zone. (See section 4.3.4 for a more detailed discussion of fault zone development with time.)

3.3.3 Stepovers

The Greendale Fault stepovers have two strikingly different populations, each with their own ranges for segment length and stepover width (Figure 3.30), that together manifest as a classic "Riedel within Riedel" pattern (Figures 1.6, 1.7). Some of the experimental fault zones show this type of double en echelon fracturing, particularly the middle stages of TALC_ER and TALC_SED (Figures 3.1, 3.9). The "Riedel within Riedel" morphology that is characteristic of the Greendale Fault is not as widespread in the experiments, but it is present at small scales (Figure 3.47). Perhaps the element of resurfacing in these models—scraping the surface in TALC_ER and adding talc to the surface of TALC_SED—creates a separate layer from which these secondary Riedels are branching, which is absent in the other experiments.

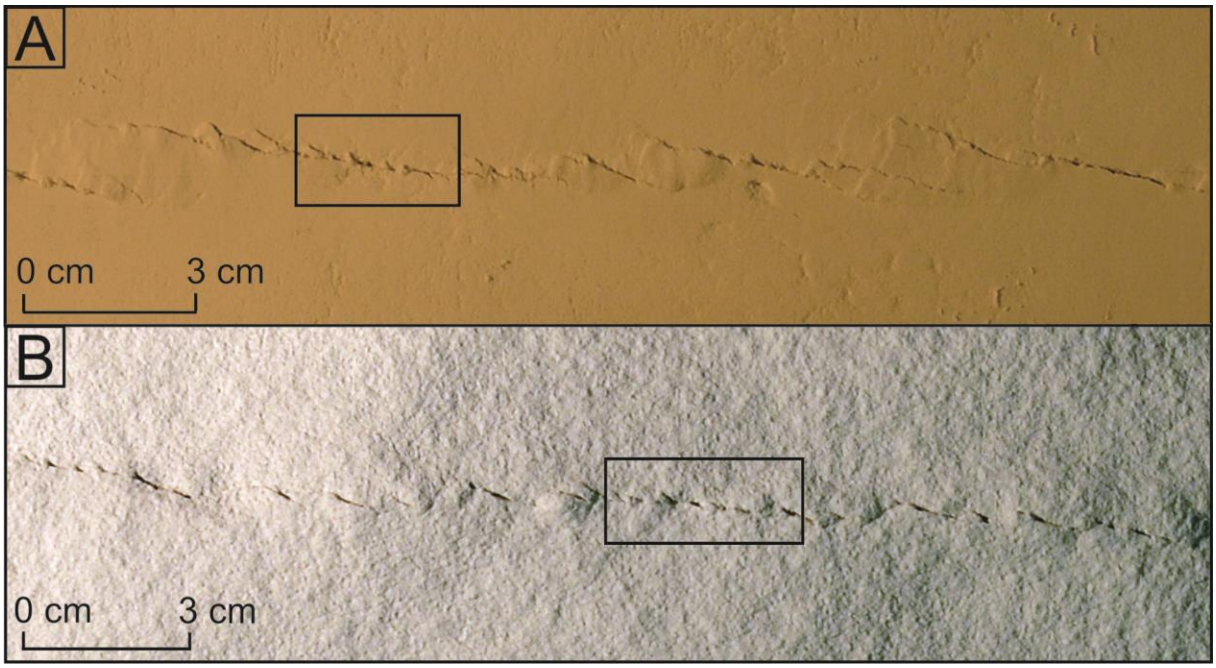

Figure 3.47. “Riedel within Riedel” patterns highlighted in analogue models: A) TALC_ER, B) TALC_SED.

At the Greendale Fault, segments at either scale of the double en echelon pattern are Riedel shears branching from a more confined fault plane at depth (Figure 1.8), so the two separate populations may be related to two separate branching depths. A similar phenomenon has been observed on the Wairarapa Fault, where kinematic-volumetric analysis quantified branching depths for two separate populations of stepover widths, with one of those depths coinciding with a stratigraphic boundary (Carne and Little, 2012). Potentially, each MACRO segment of the Greendale Fault branches off the main throughgoing fault at depth, and then these structures may subsequently branch into the smaller MICRO segments closer to the surface.

This hypothesis is supported by the alignment of the MICRO structures along the MACRO structures, as well as by volumetric calculations on stepovers and related pop-ups in a similar geologic environment that suggest that the larger scale, higher-displacement structures that generate pop-ups tend to be deeply rooted in the subsurface (Carne and Little, 2012). As interpreted at the Wairarapa Fault, there may be some stratigraphic control on one or both of

these branching depths, such as a change in lithology or material properties of the Pliocene or Quaternary gravels. Conversely, smaller-scale R, R', and T fractures that are spread across the fault zone may die out in the upper few meters of gravels. At the Greendale Fault, short (1-10 m), low-displacement R and R' shears only extend to depths of 0.5-2 m (Hornblow et al., 2012), which implies that these small-scale surface fractures are a relatively shallow process.

Scaling relationships for my analogue experiments provide branching depths for two different scales of structures at the Greendale Fault, one at 28 m and one at 133 m (Tables 3.1, 3.2). While the "Type A" and "Type B" structures and stepovers in Carne and Little (2012)'s work are ~3 times larger than the MACRO and MICRO sets highlighted in Figure 3.30, their volumetric analysis produced comparable branching depths of <20 m and 100-260 m.

Analogue experiments with only talc (TALC, TALC_ER, and TALC_SED) all show some evidence of pop-up structures, but they are absent from experiments that involve sand (TALC_SAND, SAND). Each experiment is displaced in the same way, so the behaviour differences can be attributed to the properties of the respective materials. I suggest that the non-cohesive sand dissipates any vertical topography that might be generated during deformation, while the cohesive talc clearly transmits that motion to the model surface, producing the pop-ups. Therefore a more accurate analogue for the Greendale Fault might be a multilayer model similar to TALC_SAND, but with a slightly more cohesive base layer that will transmit vertical motion while still producing the zone of distributed shear that generates the fracture patterns characteristic of TALC_SAND.

3.4 CONCLUSION

Analogue models, using cohesive and non-cohesive granular materials, have successfully simulated aspects of the surface deformation from the 2010 Darfield earthquake at different scales, based on visual comparisons of the respective fault zones as well as quantitative comparison of the distributions of fracture length and azimuth. Overburden thickness was found to be a main control on the initial width of distributed shearing, which subsequently narrows with increasing displacement. The relationship between this zone of distributed shear and the width of discrete fracturing is mainly controlled by how deformation is distributed in the subsurface, which is related to the cohesiveness of the material(s) involved. The best analogue for the Greendale Fault is a cohesive layer deforming over a zone of distributed shear in a less cohesive layer.

Interseismic effects such as sedimentation and erosion were found to affect the morphology of fractures visible at the surface, but the fault zones followed the same pattern of localization as other experiments. Stepover structures at the Greendale Fault were measured in detail and found to fall into two distinct sets based on their scale. These two groups are likely determined by the depth at which they branch from a single fault plane, which in turn may be stratigraphically controlled. Alternatively, these branching depths could be affected by variations in the gravel properties with depth, which is not included in our experiments.

These results demonstrate that cohesive powders can be used to effectively model the behaviour of strike-slip faults in granular materials at the hundred- to thousand-meter scale, and that the combination of cohesive and non-cohesive materials can represent granular materials that are cemented at the surface and more loosely consolidated at depth. These experiments also have implications for paleoseismology and land use assessment: regardless of interseismic

surface effects, a fault zone should narrow with increasing displacement, so a previously mapped surface rupture should approximate the maximum area of surface deformation in subsequent earthquakes.

4. APPLICATIONS OF ANALOGUE MODELLING TO PALEOSEISMOLOGY

4.1 Introduction

This chapter focuses on the relevance of analogue models for paleoseismic studies of active faults in young granular materials, which can produce diffuse, complex surface ruptures instead of a single throughgoing trace, particularly when the ground surface has not seen large amounts of displacement (e.g. Philip and Meghraoui, 1983; Quigley et al., 2012; see section 1.1). In such cases, the results of analogue modelling studies can augment our understanding of the behaviour and development of these faults through time. This study looks at which fractures are more likely to be reactivated at different increments during increasing strain, how fault morphology evolves with increasing displacement, and what structures would be more or less likely to appear in a paleoseismic trench. These results help to constrain better trenching sites, more accurately estimate previous displacement, improve our interpretation of trench exposures, and better predict the behaviour of future ruptures.

4.2 Data and Results

TALC_ER consists of a 2 cm thick layer of talc scraped smooth at 5 mm intervals to model interseismic erosion or agricultural activity. Each 5 mm increment shows a "snapshot" of structures active during that interval. The fracture pattern was traced at each step, generating eight sequential fracture maps (Figure 4.1).

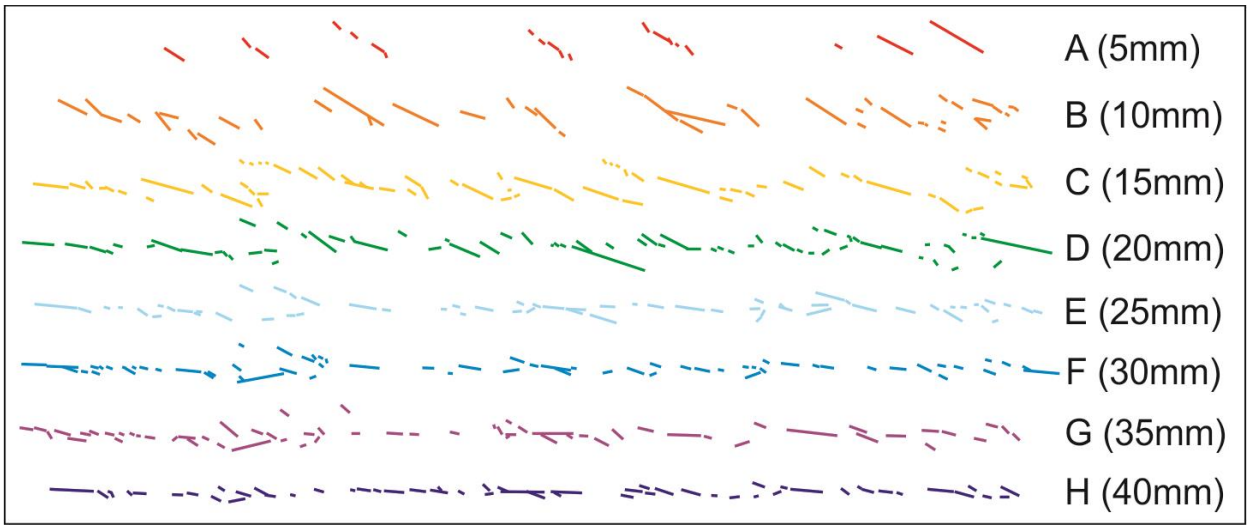

Figure 4.1. Active deformation mapped at 5 mm intervals. Initial fractures (A, B) are oblique to the PSZ, and are later cross-cut by more fault-parallel structures (C-F) until the Y shear becomes the dominant structure (G, H).

Every structure visible in the still photographs of the experiments was mapped, with a minimum fracture length of ~1.5 mm based on the limits of the drawing program, and all eight deformation maps were then superimposed to reveal where fractures were reactivated during multiple ruptures (Figures 4.2, 4.3). See sections 2.6 and 3.2 for more detailed description of TALC_ER setup and development. The 5 mm intervals were chosen to show the fault's development in the highest resolution possible, within practical limitations, but that increment may not be representative of coseismic displacements on many faults. For example, the 2010 Greendale Fault rupture (maximum horizontal displacement = 5.2±0.2 m; Quigley et al., 2012) corresponds to 15 mm of model displacement, based on qualitative and quantitative comparisons

of rupture morphology (Figures 3.31, 3.39). The fault surface was unruptured prior to September 2010, so the 2010 rupture accounts for all 15 mm of model displacement (Hornblow et al., 2012). Other, slow-slipping faults could correspond to very small increments, i.e. 5 mm, whereas fast-slipping faults could be as much as 30-40 mm (see section 4.3.1 for further discussion of relationship between experimental and field displacements).

Tracing the incremental deformation and superimposing all eight steps made it possible to identify areas where the same fractures were reactivated multiple times—locations where it would be ideal to locate a paleoseismic trench (Figure 4.2). A reactivated fracture was defined as one where at least one subsequent fracture followed the same path within a distance of 0.5 mm and within an angle of 10°, and overlapping for a length of at least 1.5 mm.

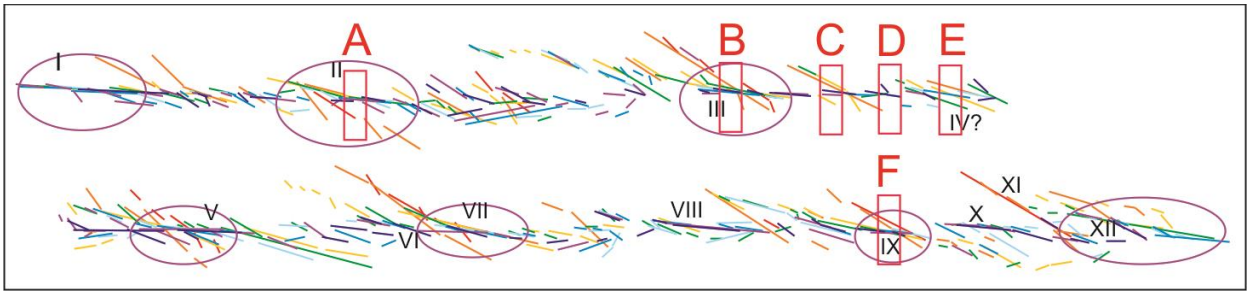

Figure 4.2 Active structures superimposed upon one another, highlighting structures that are reactivated repeatedly. Major reactivation areas are circled and numbered (I-XII). Schematic trench locations (Figure 4.6) noted and labelled in red (A-F). Note presence of initial (generation A, coloured red; Figure 4.1) fractures at major reactivation areas (circled).

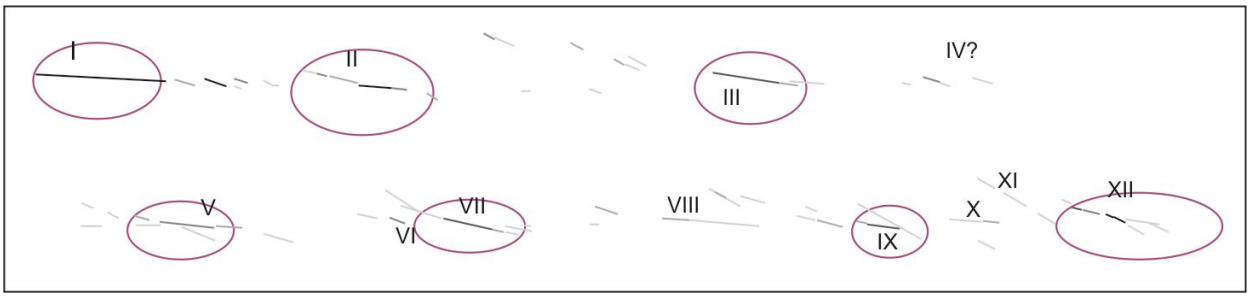

Figure 4.3. Map of reactivated structures only, with darker shades showing structures that have been reactivated more frequently. Reactivated structures are generally oriented slightly oblique to the PSZ, and encompass fractures of diverse lengths. There are many gaps along the fault zone with no reactivated structures, and few individual structures have been reactivated more than 4-5 times.

Intermediate and late stage fractures (C through H, Figure 4.1) were reactivated most frequently, at angles of 90-120° (Figures 4.2, 4.4) and most of the reactivation areas are relatively short (<7 mm). Fractures from generations A and B have similar morphologies (Figure 4.1) and often overlap with one another (Figure 4.2). However, the majority of these fractures are highly oblique to the PSZ (≥120°), so they are cross-cut by later generations of more fault-parallel structures, instead of being reactivated. Interestingly, the major reactivation areas (circled in Figures 4.2, 4.3) frequently correspond to the locations of these initial structures (e.g. Figure 4.2, areas II, III, V, VII, IX). Perhaps these early fractures weaken the material in the areas where they develop, so that subsequent fractures are more likely to recur in the same regions.

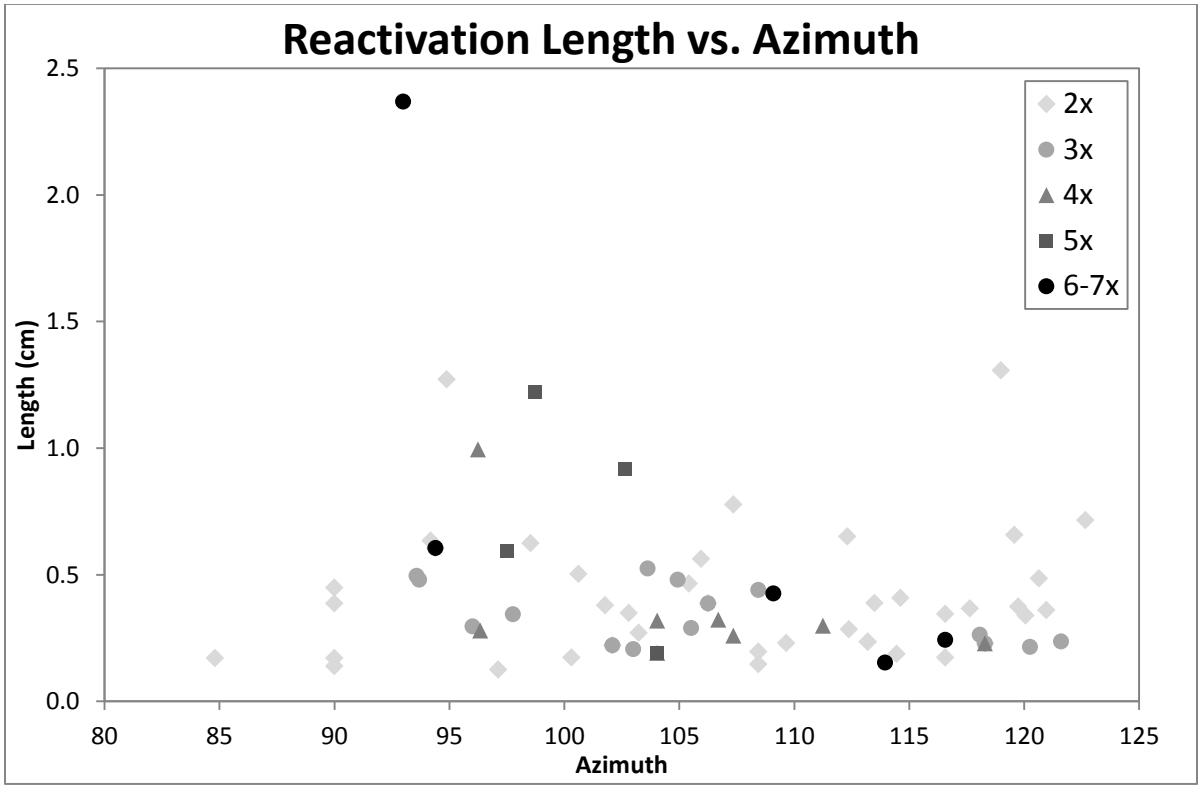

Figure 4.4: Length versus azimuth of reactivated fracture segments (see Figure 4.5 for comparison with all fractures). The majority of fractures fall between 95-120°, with a wide range of lengths. Few structures are reactivated more than 4 times out of the 8 total "ruptures".

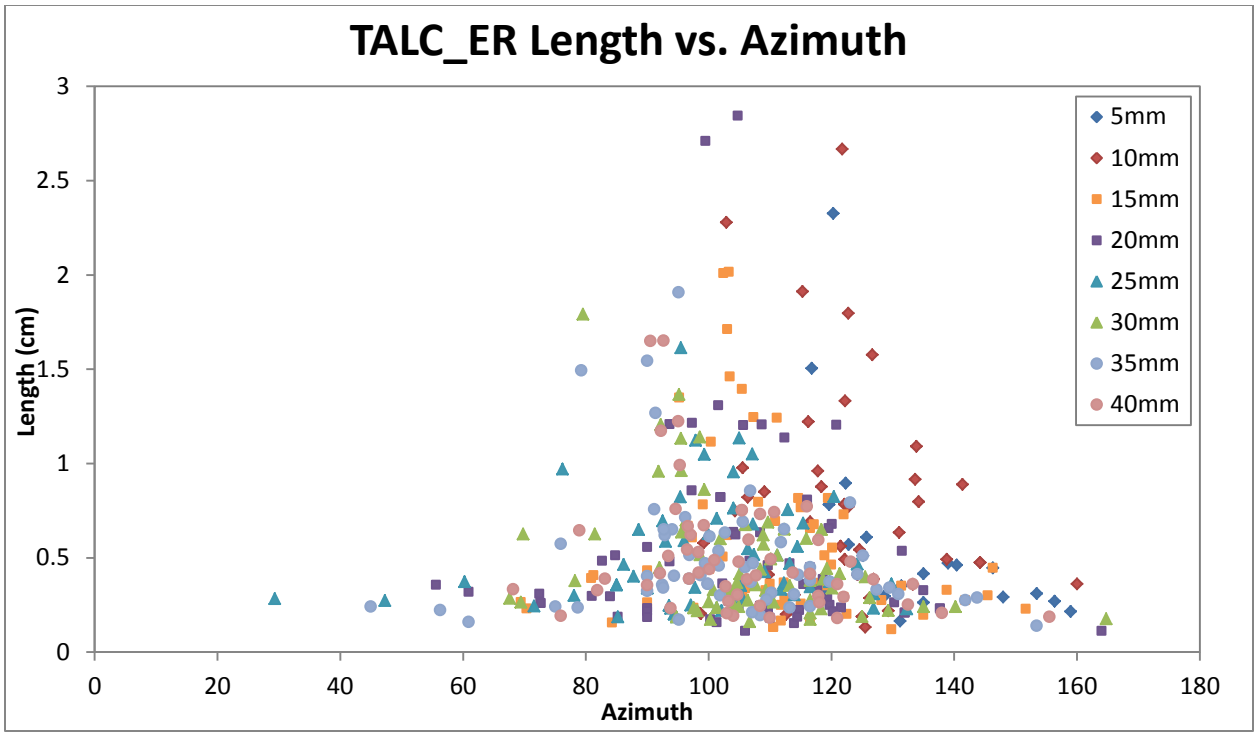

Figure 4.5. TALC_ER length versus azimuth: all strain increments. The distribution of the reactivated areas in Figure 4.4 closely matches the distribution of all fractures in TALC_ER. The highest density of structures is found at lengths ≤1 cm and azimuths 90-120°, and the longest structures are also found in that same azimuth range.

Throughout eight total "ruptures", no single structure was active in every single rupture, and only a small percentage (1.1%) were reactivated 6 or 7 times. Of 437 total fractures generated, only 73 were reactivated 2 or more times (~16% of structures). Likewise, the reactivation areas are not evenly spaced along the fault zone—there are several segments of 1-1.5 cm along strike without a single reactivated structure (Figure 4.3). This distribution suggests that placing a trench in what might seem to be a well-established fault zone may not accurately represent the rupture history of the fault.

Essentially, there is significant along-strike variation in the number of ruptures that would be observed in a trench, as well as in the local configuration of those structures. Figure 4.6 shows a series of potential trenches across the TALC_ER experimental fault, all of which would produce very different rupture histories for the fault.

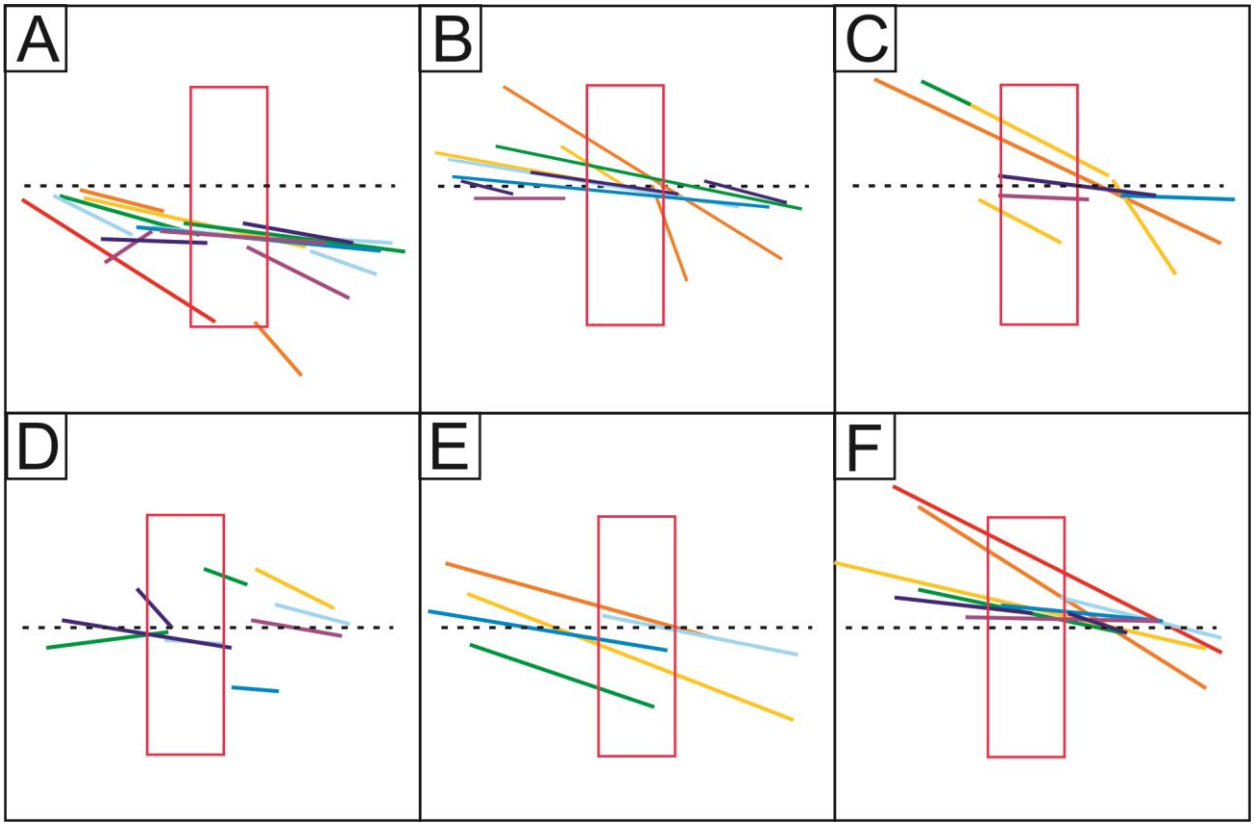

Figure 4.6. Schematic trenches placed along the TALC_ER model fault zone (see Figure 4.2 for locations along strike). Black dotted line shows location of underlying fault. Note the major differences between each trench location: different events are represented, with structures intersecting at different angles. A) One structure has been reactivated in nearly every fault rupture, but it is not centered along the Y shear, so it could be misidentified or missed completely depending on the size of the trench. B) Nearly all events are represented here, but complex cross-cutting relationships could make it difficult to reconstruct an accurate rupture history from this exposure. C) These structures are in a relatively simple configuration with two early, oblique shears and two later, more fault-parallel structures. However, these only represent half the total events on the fault. They happen to be the two most recent events and two quite early events, which would produce an unrealistically long recurrence interval estimate. D) This is one of the least representative trench placements, showing only the most recent event and one (or possibly two, depending on the trench dimensions) previous rupture, with no evidence of earlier activity. E) Evidence for five ruptures is present in this trench, although it is distributed among four separate structures. It could be very difficult to tell these events apart, depending on the sedimentation rate and recurrence interval, and the availability of datable material. F) This trench is as close to an ideal case as one could expect to see, with early oblique structures and a single, nearly fault-parallel, reactivated structure that encompasses most ruptures.

This group of schematic trenches highlights the inherent challenges of paleoseismic studies on faults of this type, with rapidly changing and developing surface morphology. Two major difficulties stand out: 1) multiple cross-cutting faults can form in a single event (see Table

4.1 for types of shears active at each displacement interval), leading to an overestimate of the number of paleoearthquakes (e.g. Figure 4.6B, generation B fractures (orange); Figure 4.6C generation H fractures (dark purple)). 2) Not every rupture will be represented in a typical trench, which would lead to an underestimate of paleoearthquake activity. Of the six trenches in Figure 4.6, only half (A, B, and F) represent all or nearly all of the events that have occurred on the model fault. Additionally, subsequent deformation will not always reactivate the same structure: the maximum number of events occurring on a single structure is five, in trenches A and B. This would add to difficulties in distinguishing which structures belong to the same events and which belong to sequential events.

Displacement	Types of shears present
5 mm	R
10 mm	R, R_L
15 mm	Mostly R_L, a few P, (some very low angle R_Ls, approaching Y shear?)
20 mm	R_L, few P, few Y
25 mm	Y, very low-angle R_L, few P
30 mm	Dominantly Y, scattered R_L and P
35 mm	Dominantly Y, scattered R_L, very few P
40 mm	Dominantly Y, scattered R_L

Table 4.1. List of different types of shears present at each 5 mm increment of displacement. Shears at different azimuths are active simultaneously and could cross-cut one other, making interpretation in a paleoseismic trench difficult.

4.3 Discussion

4.3.1 Reactivated Structures: Analogue and Field Examples

In the experimental fault zone, the most frequently reactivated structures are R_L shears and Y shears (90-120°; Figures 4.3, 4.4). It is unsurprising that R_L shears are so commonly reactivated, because they make up the largest proportion of total fractures (Figure 4.5). Conversely, Y shears are few in number because they are not active until relatively late in fault development, and initial, more oblique R shears were cross cut, rather than being reactivated multiple times over. It was somewhat unexpected that length is not a more important factor. Longer structures were anticipated to be frequently reactivated, whether they are long because of repeated offset or because they are at a structurally preferred orientation. Instead, it seems that due to the wide range of azimuths and different types of structures that appear during the model's displacement (i.e. R, R_L, P, Y), it is rare to have extended segments where fractures all occur at a single angle.

It should be noted that this study is specific to faults rupturing through moderately cohesive granular materials that have not seen extensive faulting. On a fault of this style, the Y shear is rarely the structure that has recorded the highest number of events; depending on the maturity of the fault, it may not even be present. With continued fault activity, surface deformation will become more localized along the Y shear plane, and Y shears will become the dominant structures in the surface trace. However, those are not the structures that carry the most information about paleoearthquakes in the early stages of rupture development. Instead, paleoseismologists need to target R_L shears, which can be identified by their strike relative to the PSZ, because they carry the most information about past earthquakes until a major throughgoing Y shear has developed.

The result that R_L shears are the most commonly reactivated structure from rupture to rupture is confirmed by field data from a trench at the Greendale Fault near Highfield Road, which was excavated across multiple Riedel shears active in the 2010 event (Figure 4.7). In that most recent rupture, the three shears noted in Figure 4.7 had 0.65, 0.8, and 0.7 m (listed north to south) of dextral offset (Hornblow et al., 2012). Preliminary results suggest that another 0.55 m of dextral displacement occurred on the northernmost shear in an earlier, as yet undated earthquake (Hornblow et al., 2012); Figure 4.8). While it is unlikely that every shear was reactivated, this field evidence demonstrates that Riedel shears can be active in multiple ruptures, depending on the coseismic displacement on the fault.

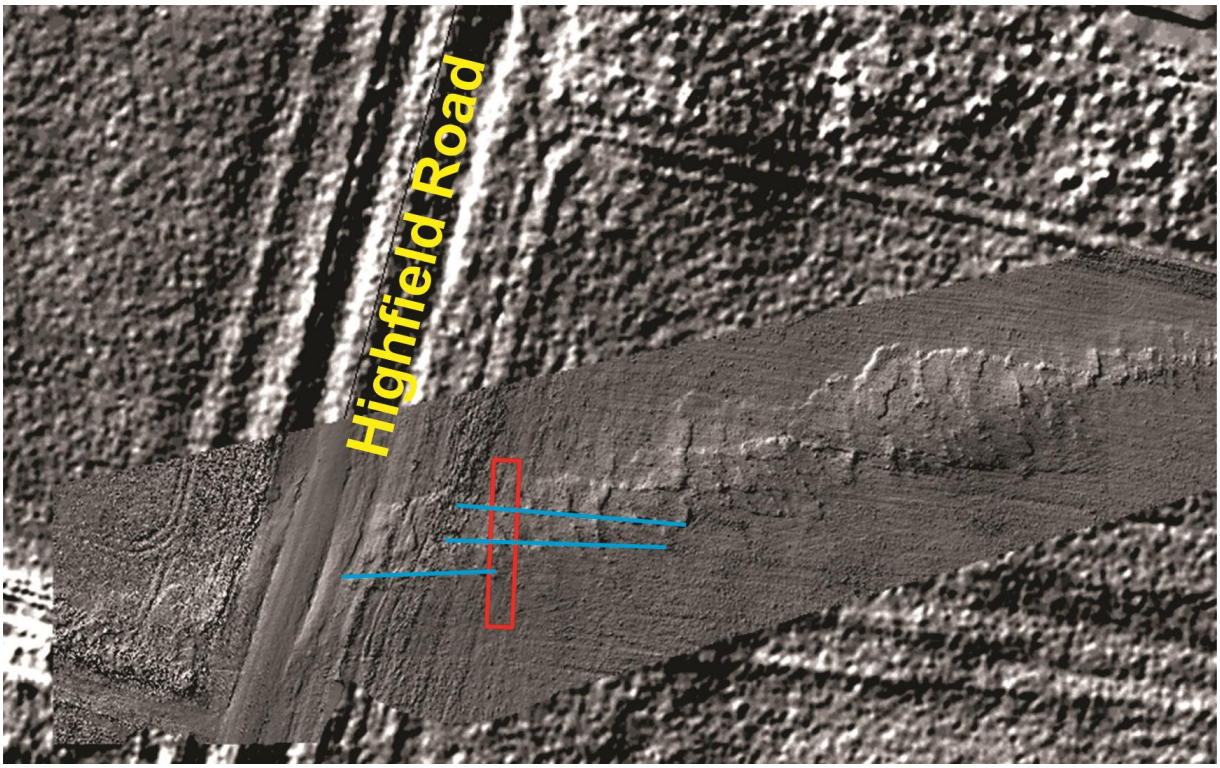

Figure 4.7. Terrestrial laser scan image overlaying a LiDAR image of the September 2010 Greendale Fault rupture near Highfield Road. Red rectangle shows September 2012 trench location, while blue lines highlight Riedel shears active in 2010 rupture. (After Hornblow et al., 2012.) Laser scan data collection and processing by Garth Archibald, GNS.

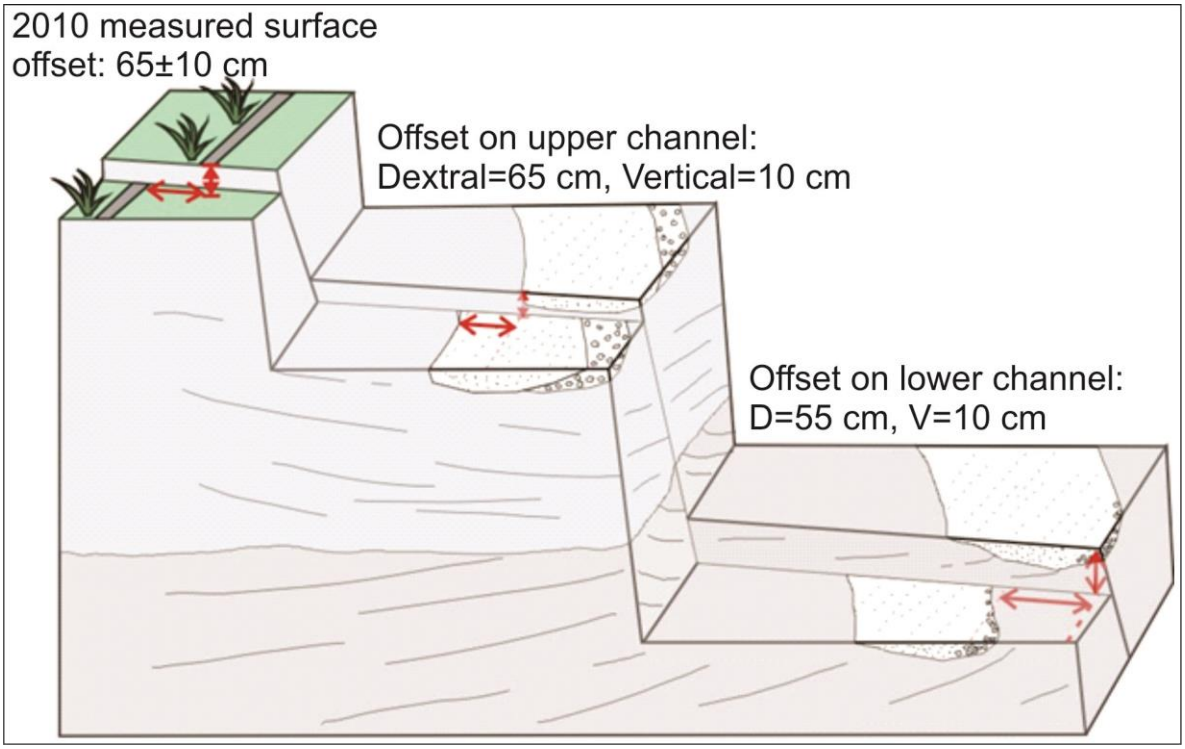

Figure 4.8. Schematic drawing showing the distribution of offset through two earthquakes on the northern Riedel shear visible in the Greendale Fault trench (Figure 4.7). (After Hornblow et al., 2012.)

As discussed in section 4.2, we must also consider how the 5 mm displacement intervals in the experiment scale with coseismic displacements on active faults. The 2010 Greendale Fault rupture (peak lateral slip = 5.2 ± 0.2 m; Quigley et al., 2012) corresponds to model displacement from 0 to 15 mm, so if characteristic ruptures are assumed, and the ground surface remains static, then the morphology of the next rupture should be predicted by TALC_ER at 30 mm displacement. Considering only the 15 and 30 mm fractures (although some additional structures may develop during rupture as well), the same areas of major reactivation are still active (circled in Figure 4.9). Therefore R and R_L shears at 90-120° remain the best structures to target in paleoseismic studies (see Figure 4.10 for schematic trenches). See section 4.3.4 for further discussion.

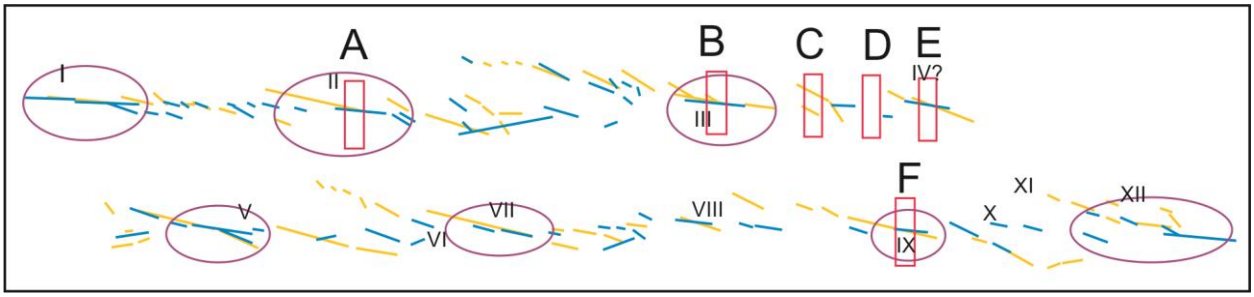

Figure 4.9. TALC_ER deformation at only 15 mm (yellow) and 30 mm (blue) intervals, which shows the potential overlap areas between the 2010 Greendale Fault rupture and the next event on that fault.

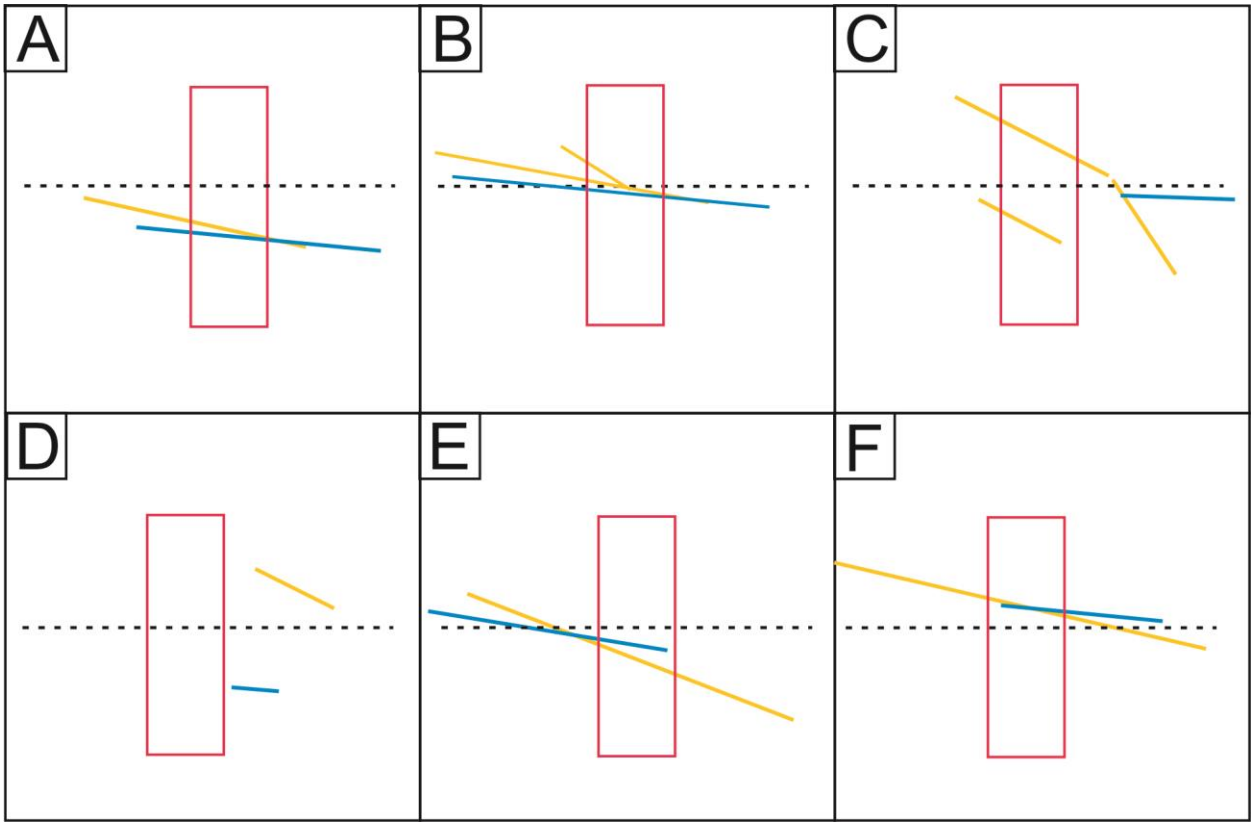

Figure 4.10. The same schematic trench locations as Figure 4.6, with only 15 mm and 30 mm structures. Despite the difference in overall morphology and number of structures from Figure 4.6, structures at Riedel shear orientations are frequently reactivated (e.g. A, B, F, and to some extent E).

A different scenario is represented by the 1986 Marryat Creek, Australia earthquake, which occurred on a very slow-slipping intraplate fault, producing a maximum coseismic lateral displacement of 0.6 m and maximum total offset of 0.8 m (McCue, 1990; Machette et al., 1993). Coseismic slip of this magnitude would correspond to ≤5 mm of model displacement, so one

might expect a complex surface rupture morphology (as shown by the increments in Figure 4.1), particularly in previously unfaulted material. This progression is confirmed by evidence from trenches that show a 10-15 m wide zone of altered and fractured granite with fault gouge along formerly active fault planes, although only a few planes near the principal slip zone were reactivated in the 1986 rupture (Machette et al., 1993). This gradual fault zone development with very small coseismic displacements would produce complex paleoseismic records that could be difficult to interpret (e.g. similar to the schematic trenches depicted in Figure 4.6).

Alternatively, the Alpine Fault is a very fast-slipping plate boundary fault, with a dextral slip rate of 23±2 mm/yr, corresponding to coseismic displacements of 8-9 m (Sutherland et al., 2006). Even in places where the fault is rupturing through young granular materials (e.g. fan surfaces, outwash plains) that overlie its established trace in bedrock, this amount of slip would likely correspond to ≥30 mm of model displacement, enough to localize on the Y shear plane within a single rupture. Trenches on this type of fault would reveal large slip events that are relatively concentrated around the Y plane, which is reasonably straightforward to interpret.

Another complication on smaller faults like Marryat Creek or the Greendale Fault is that peak displacements are only found at the central portion of the fault trace, while slip decreases toward the fault tips. At the Greendale Fault, for example, slip near the fault tips is 1-2 m (Van Dissen et al., 2011), which would correspond to ~5 mm of model displacement. These amounts of slip in both the model and in the field produce minimal surface fracturing and mostly distributed shear (Figure 3.9; Van Dissen et al., 2011; Quigley et al., 2012), which would be very difficult to detect in paleoseismic trenches. If this is a characteristic amount of slip for these parts of the fault, it should develop there as described by the 5 mm intervals in the model (Figure 4.1).

4.3.2 Effects of Surface Cementation

The unusually high angle of the initial R fractures in TALC_ER (<120°) may be related to the process by which the surface of the talc was scraped smooth (see section 3.3.2.1). It compressed the surface slightly, increasing the angle of internal friction (φ), creating a more cohesive "crust" on the surface of the model. Therefore the first fractures to form in this brittle crust were at more oblique angles, as Riedel shears in right lateral environments form at an angle of φ/2 clockwise from the PSZ. However, after the initial crust was fractured during the first 5-10 mm of displacement, later Riedel shears formed at more typical angles (100-110°). The "resurfacing" did not seem to simulate any interseismic cementation of the fault zone, as shears after the initial oblique structures were considerably more fault-parallel; if scraping the surface actually returned the surface to its original state, the shears should have remained at oblique angles.

This is an unusual effect, but it could serve as a useful analogue for granular materials that are cemented at the surface and then ruptured, as observed on the Canterbury Plains. At least the upper seven meters of gravels were weakly cemented ~200 m from the Greendale Fault (section 1.2.2), and during excavation of a trench across the fault, the recently ruptured gravels may have initially been lightly cemented, but they had been weakened by the network of recent fractures. Likewise, gravels below the upper 1-2 m were even less indurated, likely due to previous fracturing. These conditions match the experimental scenario where a brittle surface was ruptured repeatedly, resulting in a much less cohesive zone around the fault. However, it is difficult to quantify the extent to which these recently disturbed gravels might re-cement due to pedogenic processes before the next rupture.

4.3.3 Relationship of Rupture Morphology to Fault Zone Development

TALC_ER traces surface deformation in small increments of strain, providing a high resolution picture of the fault zone as it develops, which can be compared with the Greendale Fault surface rupture. The closest morphological match is the 15 mm step, with its extended, linear, low-angle Riedel shears, with pop-up structures in the stepover areas (see section 3.3.1.1 for visual comparisons). Quantitative comparisons of the azimuth distributions show that the Greendale Fault deformation is best represented by the combined 10 mm and 15 mm intervals (Figure 3.39).

This concept of matching fault morphology to a specific stage in the overall development of a fault zone is applicable to any surface rupture, not just the Greendale Fault. Given a rupture map, recent scarp, or known fault zone, the sequence of fault zone development described here and in Chapter 3 can be used to look backward, guiding where to search for paleoruptures, or forward, predicting the most likely path of future ruptures. There are many factors at play that are idealized in this model, including the maturity of the fault, the maturity of the surface, and the geometry of the fault at depth, but this model of fault development should be widely applicable as a general case.

4.3.4 Implications for Paleoseismology

This experiment can inform our understanding of paleoseismic structures in trenches, as well as our understanding of the number and magnitude of events that may go unobserved by trenching studies. As mentioned previously, lower-angle Riedel (R_L) shears are the structures most likely to be reactivated in subsequent ruptures. However, more oblique Riedel (R) shears generated by the first stages of displacement appear sporadically along the fault zone (Figure

4.1), and a trench placed without knowledge of previous ruptures might not intersect them. Interestingly, the zones with the highest density of reactivated structures tend to be located near these initial R shears (Figure 4.2), so identifying these in a trench would suggest that that location would provide an especially complete rupture history.

Another difficulty is that the diffuse shear deformation that accommodated so much of the displacement at the Greendale Fault frequently extended for >100 m perpendicular to fault strike and was only detectable due to the abundance of previously linear markers that could be measured across the fault (Quigley et al., 2012). This type of deformation would be challenging to detect in a trenching study, and difficult to distinguish from naturally meandering stream channels, for example.

This component of distributed shear would also complicate efforts to measure accurate displacements in order to estimate a paleoearthquake magnitude. Likewise, the displacement taken up on discrete shears is frequently distributed among several different structures, all of which may not be visible within a single trench. For example, at one of the Highfield Road paddocks, the total lateral displacement is 4.8 m, part of which is taken up by 0.6-0.8 m displacements on three parallel Riedel shears (section 4.3.1), and the other component of which is taken up on smaller subsidiary fractures and/or by more distributed deformation. Underestimating total displacement would lead to an underestimate of the earthquake magnitude generated by a fault.

This study also indicates that cross-cutting relationships in trenches need to be particularly carefully considered. Generally, one structure cross-cutting another in a trench would be seen as evidence of multiple ruptures. However, this model shows that multiple types of shears with different characteristic angles (i.e. R and R_L, R_L and Y, etc.) can be active during a

single rupture and could cross-cut one another either at the surface or at depth, as well as potentially offsetting each other if they are active at different times during a single rupture (Figure 4.11; Table 4.1). Interpreting these as two separate events would result in an overestimate of the number of ruptures on a fault.

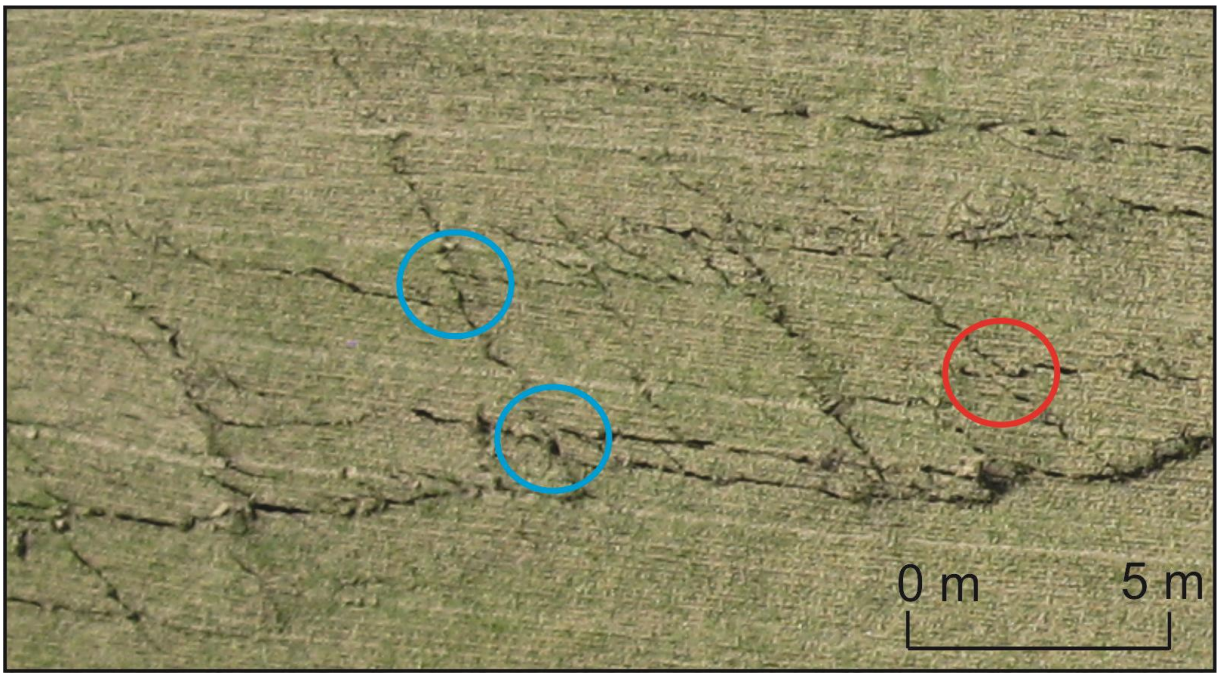

Figure 4.11. Aerial photograph of Greendale Fault rupture segment, showing synthetic R shears apparently offsetting antithetic R' shears (denoted by red circle) and vice versa (blue circle). These types of fracture interactions would be difficult to interpret in a paleoseismic trench.

However, considering the schematic trenches across the experimental fault zone (Figure 4.6), it seems likely that more total events would be overlooked because fractures produced by that rupture do not intersect a trench site. This would produce an overall underestimate of number of ruptures, slip rate, and recurrence interval. In fact, no single structure is reactivated in all eight "ruptures" on the model fault. It may be possible to find a trench site that intersects all of them, albeit on multiple structures, but it would be a very small segment of the overall length of the fault trace. A more robust way to ensure an accurate rupture history is to trench at several sites, increasing the probability of intersecting structures from all recent ruptures.

Excavating multiple trenches is also critical because of the high variability among shorter structures in the fault zone. While some have been reactivated in almost every event, others with similar lengths and orientations have been active in only a single rupture. Trenching more sites gives a much higher probability of finding these key structures that record several events.

It should be noted that these results are also influenced by the way coseismic displacements scale with the 5 mm "ruptures" in the model. The morphology at the Greendale Fault segments with peak slip (~5 m) match 15 mm of model displacement best, while lower slip segments nearer the fault tips (1-2 m of slip) are more likely to correspond to the 5 mm displacement intervals in the model. This means that after 2 events, for example, the central portion of the fault will have more localized, higher-displacement structures (Figure 4.9), while the ends of the fault will have barely developed discrete fractures. This highlights the challenges in recognizing the full extent of paleoruptures—surface rupture length is a key parameter used to estimate M_W from paleoseismic evidence, so underestimating rupture length would significantly underestimate the potential rupture magnitude.

Overall, this model suggests that a single trenching study is likely to significantly underestimate the number of ruptures that a fault has seen, as well as their magnitudes, due to the scarcity of frequently reactivated structures and the complex distribution of surface deformation. Some complications would lead to overestimates of the number of events, such as the problem of cross-cutting relationships described above. However, this possibility does not outweigh the factors that tend toward underestimating the number and magnitude of paleoruptures.

4.4 Conclusion

This chapter focuses on how analogue modelling studies can be used to guide paleoseismic studies on faults in granular materials, and how they can help to interpret observations in trenches. I have summarized this work as a list of recommendations for paleoseismologists attempting to establish the rupture history of faults like these.

1. During the early stages of a surface rupture, lower angle Riedel (R_L) shears (~90-120°) are the structures most likely to be reactivated during multiple earthquakes, regardless of fracture length. This evolves with fault zone activity until the Y shear eventually becomes the structure that carries the most information about paleoruptures.
2. Cross-cutting structures in trenches are not necessarily evidence of multiple ruptures, because depending on coseismic slip, multiple types of shears at different azimuths can be active during a single event.
3. Fault zones tend to localize with continuing displacement, as a throughgoing fault develops. Early ruptures will have a wide deformation zone, while later ruptures will successively narrow with time.
    a. Earlier structures tend to be more oblique to the underlying fault trace (≥120°), whereas later structures tend toward fault-parallel (90-100°).
4. The appearance of a fault in the paleoseismic record is heavily dependent on the characteristic coseismic displacements on that fault. Trenches on a fault with high coseismic slip (e.g. the Alpine Fault or the Wellington Fault) will be much more straightforward to interpret than a fault with very low coseismic slip (e.g. the Greendale Fault or the Marryat Creek Fault).

5. Areas with the most reactivated structures in the experiments tend to occur at or near the locations of initial, oblique R fractures.
6. As a whole, trench observations on a fault of this type are likely to significantly underestimate the number of past ruptures, their total displacement, and their magnitude. This can be mitigated by trenching at multiple locations on a single fault, as well as by estimating the proportion of displacement not represented (i.e. that is taken up by distributed deformation), because it must be taken into account when assessing the future hazard posed by a fault.

5. CONCLUSION AND FUTURE WORK

This study has successfully used cohesive and non-cohesive materials to model the surface deformation patterns produced by strike-slip faulting in Quaternary gravels with pedogenesis. Complex rupture morphologies similar to those of the Greendale Fault (including en echelon fractures, R, R', P, and T structures, and pop-up structures) were generated with a simple, linear fault at depth. The fault zones initiated with oblique fractures that were subsequently cross-cut by more fault-parallel structures, which eventually linked into a single, throughgoing fault zone. These rupture patterns demonstrate that surface complexity can be produced independent of fault geometry at depth, slip gradients, or other complications.

This work also examines the relationship between distributed shear strain and discrete surface fracturing. The width of the former is controlled mainly by the thickness of overburden above the basement fault, while the latter is controlled by the nature and behaviour of the overburden. The experiments with a single layer of material (either cohesive or noncohesive) all had a narrow zone of fracturing relative to the zone of distributed shear, while the multi-layered model (cohesive talc over noncohesive sand) produced a wide, complex zone of fracturing, including R' shears, which did not appear in any other model. I suggest that this is a product of the sand generating a wide, distributed shear zone beneath the talc, which is different than the other experiments which deform above a single fault plane in the base of the model. Stepover structures were also measured in detail at the Greendale Fault. These fall into distinct datasets with two different scales, which may be defined by stratigraphic controls on their branching depths.

These results also have several key implications for paleoseismic studies on strike-slip faults in young granular materials. Initial, highly oblique shears tend to be cross-cut by more fault-parallel structures early in fault development, and it is these lower angle Riedel (R_L) shears, regardless of length, that are the fractures most frequently reactivated in successive ruptures. It is critical to identify and target those structures in trenching studies, and this result is confirmed by field studies at the Greendale Fault. It is also important to note that the Y shear is *not* representative of a fault's history in its early stages of development, as it does not develop until the fault has already seen significant displacement. Overall, only a small proportion of total fractures is reactivated (~16%), so it is unlikely that any single trench would produce an accurate estimate of the total number of ruptures on a fault. This is particularly important for faults with very low coseismic displacements; faults with higher characteristic coseismic slip are more straightforward to interpret. Another difficulty is that displacement is often divided among multiple fractures, as well as being taken up by distributed deformation, so it is highly likely that trenching studies would underestimate the number, displacement, and magnitude of paleoruptures on a fault, as well as the hazard of a future rupture.

There is certainly scope for expanding on the work undertaken in this thesis, both further interpreting experiments previously performed as well as constructing more sophisticated models. It would be worthwhile to further constrain the variables involved, such as by testing different thicknesses of materials above the basement in a more systematic way. Preliminary tests gave some evidence about these processes, but this simple question would merit further examination. Different materials could also be investigated, such as clay or other cohesive powders. In particular, it would be useful to identify the active structures in the experiments as they develop, rather than continually measuring persistent but inactive fractures. Likewise, there

is more information still to be gathered about the Greendale Fault surface rupture that would complement the hypotheses tested in these models.

This study has addressed some basic questions, but more detailed experiments would surely provide more specific information about different types of fault zones. For example, creating a more precise model of the Canterbury Plains stratigraphy, including more rigid volcanic layers, might give a more accurate picture of how subsurface geology affected surface deformation at the Greendale Fault. It would also be worthwhile to develop a method for modelling the effects of multiple faults rupturing at depth, since that is one of the factors that likely contributed to the complexity of the Greendale surface rupture. Three-dimensional observation of these models has also been considered, and would greatly increase our understanding of the processes involved in this type of faulting.

REFERENCES

Adam, J., Urai, J. L., Wieneke, B., Oncken, O., Pfeiffer, K., Kukowski, N., Lohrmann, J., Hoth, S., Van der Zee, W., and Schmatz, J., 2005, Shear localisation and strain distribution during tectonic faulting—new insights from granular-flow experiments and high-resolution optical image correlation techniques: Journal of Structural Geology, v. 27, no. 2, p. 283-301.

An, L.-J., and Sammis, C., 1996, Development of strike-slip faults: shear experiments in granular materials and clay using a new technique: Journal of Structural Geology, v. 18, p. 1061-1077.

Angelier, J., and Bergerat, F., 2002, Behaviour of a rupture of the 21 June 2000 earthquake in South Iceland as revealed in an asphalted car park: Journal of Structural Geology, v. 24, p. 1925-1936.

Atmaoui, N., Kukowski, N., Stöckhert, B., König, D, 2006, Initiation and development of pull-apart basins with Riedel shear mechanism: insight from scaled clay experiments: International Journal of Earth Science, v. 95, p. 225-238.

Barrell, D.J.A., Litchfield, N.J., Townsend, D.B., Quigley, M., Van Dissen, R.J., Cosgrove, R., Cox, S.C., Furlong, K., Villamor, P., Begg., J.G., Hemmings-Sykes, S., Jongens, R., Mackenzie, H., Noble, D., Stahl, T., Bilderback, E., Duffy, B., Henham, H., Klahn, A., Lang, E.M.W., Moody, L., Nicol, R., Pedley, K., and Smith, A., 2011, Strike-slip ground-surface rupture (Greendale Fault) associated with the 4 September 2010 Darfield earthquake, Canterbury, New Zealand: Quarterly Journal of Engineering Geology and Hydrogeology, v. 44, p. 283-291.

Beavan, J., Samsonov, S., Motagh, M., Wallace, L., Ellis, S., and Palmer, N., 2010, The Darfield (Canterbury) earthquake: geodetic observations and preliminary source model: Bulletin of the New Zealand Society for Earthquake Engineering, v. 43, p. 228-235.

Berberian, M., and Walker, R., 2010, The Rudbar M_W 7.3 earthquake of 1990 June 20; seismotectonics, coseismic and geomorphic displacements, and historic earthquakes of the western 'High-Alborz', Iran: Geophysical Journal International, v. 182, p. 1577-1602.

Bjarnason, I.Th., Cowie, P.A., Anders, M.H., Seeber, L., Scholz, C.H., 1993, The 1912 Iceland Earthquake rupture: growth and development of a nascent transform system: Bulletin of the Seismological Society of America, v. 83, p. 416–435.

Boutelier, D., Schrank, C., Cruden, A., 2008, Power-law viscous materials for analogue experiments: New data on the rheology of highly-filled silicone polymers: Journal of Structural Geology, v. 30, p. 341-353.

Brown, L., and Weeber, J., 1994, Hydrogeological implications of geology at the boundary of Banks Peninsula volcanic rock aquifers and Canterbury Plains fluvial gravel aquifers: New Zealand Journal of Geology and Geophysics, v. 37, p. 181-193.

Carne, R.C., and Little, T.A., 2012, Geometry and scale of fault segmentation and deformational bulging along an active oblique-slip fault (Wairarapa fault, New Zealand): Geological Society of America Bulletin, v. 124, no. 7/8, p. 1365-1381.

Clifton, A., and Einarsson,P., 2005, Styles of surface rupture accompanying the June 17 and 21, 2000 earthquakes in the South Iceland Seismic Zone: Tectonophysics, v. 396, p. 141-159.

Cloos, H., 1928, Experimente zur inneren Tektonik: Centralbl Mineral Pal, v. 5, p. 609-621

Dauteuil, O., and Mart, Y., 1998, Analogue modeling of faulting pattern, ductile deformation, and vertical motion in strike-slip fault zones: Tectonics, v. 17, p. 303-310.

Davy, B., Stagpoole, V., Barker, D., and Yu, J., 2012, Subsurface structure of the Canterbury region interpreted from gravity and aeromagnetic data: New Zealand Journal of Geology and Geophysics, v. 55, no. 3, p. 185-191.

Deramond, J., Sirieys, P., and Soula, J.C., 1983, Mécanismes de deformation de l'écorce terrestre: structures et anisotropies induites *in* 5th International Congress on Rock Mechanics, Melbourne, F 89-93.

Dorn, C., Green, A.G., Jongens, R., Carpentier, S., Kaiser, A.E., Campbell, F., Horstmeyer, H., Campbell, J., Finnemore, M., and Pettinga, J., 2010, High-resolution seismic images of potentially seismogenic structures beneath the northwest Canterbury Plains, New Zealand: Journal of Geophysical Research, v. 115, B11303, p. 1-19.

Dresen, G., 1991, Stress distribution and the orientation of Riedel shears: Tectonophysics, v. 188, p. 239-247.

Duffy, B., Quigley, M.C., Barrell, D.J.A., Van Dissen, R., Stahl, T., Leprince, S., McInnes, C., Bilderback, E., 2012, Fault kinematics and surface deformation across a releasing bend during the 2010 M_W 7.1 Darfield, New Zealand, earthquake revealed by differential LiDAR and cadastral surveying: Geological Society of America Bulletin, doi: 10.1130/B30753.1.

Duman, T., Emre, O., Dogan, A., and Ozalp, S., 2005, Step-over and bend structures along the 1999 Duzce earthquake surface rupture, North Anatolian Fault, Turkey: Bulletin of the Seismological Society of America, v. 95, p. 1250-1262.

Duta, N., Jain, A.K., Mardia, K.V., 2002, Matching of palmprints: Pattern Recognition Letters, v. 23, p. 477-485.

Erdlac, R. J., Jr., and Anderson, T. H., 1982, The Chixoy-Polochic fault and its associated fractures in western Guatemala: Geological Society of America Bulletin, v. 93, p. 57-67.

Fakher, A., Cheshomi, A., Khamechiyan, M., 2007, The addition of geotechnical properties to a geological classification of coarse-grained alluvium in a pediment zone: Quarterly Journal of Engineering Geology and Hydrology, v. 40, p. 163-174.

Forsyth, P., Barrell, D., and Jongens, R., 2008, Geology of the Christchurch Area: Institute of Geological and Nuclear Sciences 1:250,000 Geological Map 16.

Freund, R., 1974, Kinematics of transform and transcurrent faults: Tectonophysics, v. 21, p. 93-134.

Ghisetti, F.C., and Sibson, R.H., 2012, Compressional reactivation of E-W inherited normal faults in the area of the 2010-2011 Canterbury earthquake sequence: New Zealand Journal of Geology and Geophysics, v. 55, no. 3, p. 177-184.

Haeussler, P.J., Schwartz, D.P., Dawson, T.E., Stenner, H.D., Lienkaemper, J.J., Sherrod, B., Cinti, F.R., Montone, P., Craw, P.A., Crone, A.J., Personius, S.F., 2004, Surface rupture and slip distribution in of the Denali and Totschunda faults in the 3 November 2002 M 7.9 earthquake, Alaska: Bulletin of the Seismological Society of America, v. 94, no. 6B, p. S23-S52.

Hessami, K., Tabassi, H., Okumura, K., Abbassi, M.R., Azuma, T., 2005, Surface deformation and the fault responsible for the 2003 Bam, Iran, earthquake: Earthquake Spectra, v. 21, n. S1, p. S113-S123.

Hoeppener, R., Kalthoff, E., and Schrader, P, 1969, Zur physikalischen Tektonik: Bruchbildung bei verschiedenen affnen Deformationen im Experiment: Geologische Rundsrhau, v. 59, p. 179-193

Holden, C., Beavan, J., Fry, B., Reyners, M., Ristau, J., Van Dissen, R., and Villamor, P., 2011, Preliminary source model of the Mw 7.1 Darfield earthquake from geological, geodetic and seismic data *in* Proceedings of the Ninth Pacific Conference on Earthquake Engineering, Auckland, New Zealand, April 2011, paper no. 164.

Holland, M., Urai, J.L., Martel, S., 2006, The internal structure of fault zones in basaltic sequences: Earth and Planetary Science Letters, v. 248, p. 286-300.

Hornblow, S., Quigley, M.C., Nicol, A., Van Dissen, R., Sasnett, P., Newton, K., and Barrell, D., 2012, Recent rupture history of the Greendale Fault, Canterbury, integrating paleoseismic trenching and geophysical techniques *in* Proceedings, Geological Society of New Zealand Annual Meeting, Hamilton, New Zealand.

Horsefield, W.T., 1977, An experimental approach to basement-controlled faulting: Geologie en Mijnbouw, v. 56, p. 363-370.

Hubbert, M.K., 1937, Theory of scale models as applied to study of geological structures: Geological Society of America Bulletin, v. 48, p. 1459-1520.

—, 1951, Mechanical basis for certain geological structures: Geological Society of America Bulletin, v. 62, p. 355-372.

Jain, A., Hong, L., Bolle, R., 1997, On-line fingerprint verification: IEEE Transactions on Pattern Analysis and Machine Intelligence, v. 19, no. 4, p. 302-314.

Jongens, R., Barrell, D.J.A., Campbell, J.K., Pettinga, J.R., 2012, Faulting and folding beneath the Canterbury Plains identified prior to the 2010 emergence of the Greendale Fault: New Zealand Journal of Geology and Geophysics, v. 55, i. 3, p. 169-176.

Keller, E. A., Bonkowski, M. S., Korsch, R. J., and Shlemon, R. J., 1982, Tectonic geomorphology of the San Andreas fault zone in the southern Indio Hills, Coachella Valley, California: Geological Society of America Bulletin, v. 93, p. 46-56.

Li, C-Y., Pang, J-Z., Zhang, Z-Q., 2012, Characteristics, geometry, and segmentation of the surface rupture associated with the 14 April 2010 Yushu earthquake, Eastern Tibet, China: Bulletin of the Seismological Society of America, v. 102, no. 4, p. 1618-1638.

Lin, A., Fu, B., Guo, J., Zeng, Q., Dang, G., He, W., and Zhao, Y., 2002, Co-seismic strike-slip and rupture length produced by the 2001 Ms 8.1 Central Kunlun earthquake: Science, v. 296, p. 2015-7.

Lin, A., and Nishikawa, M., 2011, Riedel shear structures in the co-seismic surface rupture zone produced by the 2001 Mw 7.8 Kunlun earthquake, northern Tibetan Plateau: Journal of Structural Geology, v. 33, p. 1302-1311.

Little, T.A., Van Dissen, R., Rieser, U., Smith, E.G.C., and Langridge, R.M., 2010, Coseismic strike slip at a point during the last four earthquakes on the Wellington fault near Wellington, New Zealand: Journal of Geophysical Research, v. 115, B05403, doi:10.1029/2009JB006589.

Lohrmann, J., Kukowski, N., Adam, J., and Oncken, O., 2003, The impact of analogue material properties on the geometry, kinematics, and dynamics of convergent sand wedges: Journal of Structural Geology, v. 25, p. 1691-1711.

Machette, M. N., Crone, A.J., and Bowman, J.R., 1993, Geologic investigations of the 1986 Marryat Creek, Australia, earthquake: Implications for paleoseismicity in stable continental regions: US Geological Survey Bulletin 2032-B.

McClay, K., and Bonora, M., 2001, Analog models of restraining stepovers in strike-slip fault systems: AAPG Bulletin, v. 85, p. 233-260.

McClay, K., and Dooley, T., 1995, Analogue models of pull-apart basins: Geology, v. 23, no. 9, p. 711-714.

McCue, K., 1990, Australia's large earthquakes and recent fault scarps: Journal of Structural Geology, v. 12, no. 5/6, p. 761-766.

Morgenstern, N.R., and Tchalenko, J.S., 1967, Microscopic shear zones in kaolin subjected to direct shear: Geotechnique, v. 17, p. 309-328.

Naylor, M., Mandl, G., and Sijpesteijn, C., 1986, Fault geometries in basement-induced wrench faulting under different initial stress states: Journal of Structural Geology, v. 8, no. 7, p. 737-752.

Norris, R.J. and Cooper, A.F., 2000, Late Quaternary slip rates and slip partitioning on the Alpine Fault, New Zealand: Journal of Structural Geology, v. 23, p. 507-520.

Oskin, M.E., Arrowsmith, J.R., Hinojosa-Corona, A., Elliott, A.J., Fletcher, J.M., Fielding, E.J., Gold, P.O., Gonzalez Garcia, J.J., Hudnut, K.W., Liu-Zeng, J., Teran, O.J., 2012, Near-field deformation from the El Mayor-Cucapah earthquake revealed by differential LIDAR: Science, v. 335, p. 702-705.

Pettinga, J., Yetton, M., Van Dissen, R., and Downes, G., 2001, Earthquake source identification and characterisation for the Canterbury region, South Island, New Zealand: Bulletin of the New Zealand Society for Earthquake Engineering, v. 34, p. 282-317.

Philip, H., and Meghraoui, M., 1983, Structural analysis and interpretation of the surface deformations from the El Asnam earthquake of October 10, 1980: Tectonics, v. 2, no. 1, p. 17-49.

Quigley, M., Van Dissen, R., Litchfield, N., Villamor, P., Duffy, B., Barrell, D., Furlong, K., Stahl, T., Bilderback, E., and Noble, D., 2012, Surface rupture during the 2010 Mw 7.1 Darfield (Canterbury) earthquake: Implications for fault rupture dynamics and seismic-hazard analysis: Geology, v. 40, p. 55-58.

Quigley, M., Villamor, P., Furlong, K., Beavan, J., Van Dissen, R., Litchfield, N., Stahl, T., Duffy, B., Bilderback, E., Noble, D., Barrell, D., Jongens, R., Cox, S., 2010, Previously unknown fault shakes New Zealand's South Island: Eos, v. 91, no. 49, p. 469-488.

Rahe, B., Ferrill, D.A., Morris, A.P., 1998, Physical analog modeling of pull-apart basin evolution: Tectonophysics, v. 285, p. 21-40.

Richard, P., Naylor, M.A., Koopman, A., 1995, Experimental models of strike-slip tectonics: Petroleum Geoscience, v. 1, p. 71-80.

Richard, P., 1991, Experiments on faulting in a two-layer cover sequence overlying a reactivated basement fault with oblique-slip: Journal of Structural Geology, v. 13, p. 459-469.

Richard, P., Mocquet, B., and Cobbold, P., 1991, Experiments on simultaneous faulting and folding above a basement wrench fault: Tectonophysics, v. 188, p. 133-141.

Riedel, W., 1929, Zur mechanik geologischer Brucherscheinungen: Zentralblatt Mineral Geol Paläont, B:354–368.

Rossi, D., and Storti, F., 2003, New artificial granular materials for analogue laboratory experiments: aluminium and siliceous microspheres: Journal of Structural Geology, v. 25, p. 1893-1899.

Rybicki, K.R., and Yamashita, T., 1998, Faulting in vertically inhomogenous media and its geophysical implications: Geophysical Research Letters, v. 25, p. 2893-2896.

Schellart, W., 2000, Shear test results for cohesion and friction coefficients for different granular materials: scaling implications for their usage in analogue modelling: Tectonophysics, v. 324, p. 1-16.

Schrank, C.E., Boutelier, D.A., Cruden, A.R., 2008, The analogue shear zone: From rheology to associated geometry: Journal of Structural Geology, v. 30, p. 177-193.

Schrank, C.E., and Cruden, A.R., 2010, Compaction control of topography and fault network structure along strike-slip faults in sedimentary basins: Journal of Structural Geology, vs. 32, p. 184-191.

Schreurs, G., 1994, Experiments on strike-slip faulting and block rotation: Geology, v. 22, p. 567-570.

Sibson, R.H., Ghisetti, F.C., and Crookbain, R.A., 2012, 'Andersonian' wrench faulting in a regional stress field during the 2010-2011 Canterbury, New Zealand, earthquake sequence. In: *Faulting, Fracturing and Igneous Intrusion in the Earth's Crust*, ed. D. Healy, R.W.H. Butler, Z.K. Shipton, and R.H. Sibson, *Geological Society, London, Special Publication* 367, 7-18.

Sibson, R.H., Ghisetti, F.C., and Ristau, J., 2011, Stress control of an evolving strike-slip fault system during the 2010-2011 Canterbury, New Zealand, earthquake sequence: Seismological Research Letters, v. 82, p. 824-832.

Sieh, K.E., and Jahns, R.H., 1984, Holocene activity of the San Andreas fault at Wallace Creek, California: Geological Society of America Bulletin, v. 95, p. 883-896.

Sieh, K.E., Stuiver, M., and Brillinger, D., 1989, A more precise chronology of earthquakes produced by the San Andreas Fault in Southern California: Journal of Geophysical Research, v. 94, no. B1, p. 603-623.

Soula, J.C., Bessiere, G., and Herail, G., 1988, Simple-shear experiments on basement-cover sequences with a comparison to the Bierzo basin, NW Spain: Bulletin of the Geological Institution of the University of Uppsala, v. 14, p. 163-179.

Soula, J.C., 1984, Genèse de bassins sédimentaires en régime de cisaillement transcurrent: modèles expérimentaux et exemples géologiques: Bulletin de la Société Belge de Géologie, v. 93, p. 83-104.

Sutherland, R., Berryman, K., Norris, R., 2006, Quaternary slip rate and geomorphology of the Alpine Fault: Implications for kinematics and seismic hazard in Southwest New Zealand: Geological Society of America Bulletin, v. 118, no. 3/4, p. 464-474.

Sylvester, A.G., 1988, Strike-slip faults: GSA Bulletin, v. 100, p. 1666-1703.

Tchalenko, J., 1968, The evolution of kink-bands and the development of compression textures in sheared clays: Tectonophysics, v. 6, p. 159-174.

—, 1970, Similarities between shear zones of different magnitudes: GSA Bulletin, v. 81, p. 1625-1640.

Tchalenko, J., and Ambraseys, N., 1970, Structural analysis of the Dasht-e Bayaz (Iran) earthquake fractures: GSA Bulletin, v. 81, p. 41-60.

Ueta, K., Tani, K., Kato, T., 2000, Computerized X-ray tomography analysis of three dimensional fault geometries in basement-induced wrench faulting: Engineering Geology, v. 56, p. 197-210.

Van Dissen, R., Barrell, D.J.A., Litchfield, N., Villamor, P., Quigley, M.C., King, A., Furlong, K., Begg, J., Townsend, D., Mackenzie, H., Stahl, T., Noble, D., Duffy, B., Bilderback, E., Claridge, J., Klahn, A., Jongens, R., Cox, S., Langridge, R., Ries, W., Dhakal, R., Smith, A., Hornblow, S., Nicol, R., Pedley, K., Henham, H., Hunter, R., Zajac, A., Mote, T., 2011, Surface rupture displacement on the Greendale Fault during the M_W 7.1 Darfield (Canterbury) earthquake, New Zealand, and its impact on man-made structures, *in* Proceedings of the Ninth Pacific Conference on Earthquake Engineering, Auckland, New Zealand, April 2011, paper no. 186.

Van Gent, H.W., Holland, M., Urai, J.L., Loosveld, R., 2010, Evolution of fault zones in carbonates with mechanical stratigraphy – Insights from scale models using layered cohesive powder: Journal of Structural Geology, v. 32, p. 1375-1391.

Van Gent, H.W., 2005, Scaled analogue models of normal faulting in brittle lithologies [MSc thesis]: Utrecht University, 143 p.

Villamor, P., Barrell, D., Litchfield, N., Van Dissen, R., Hornblow, S., and Levick, S., 2011, Greendale Fault investigation of surface rupture characteristics for fault avoidance zonation, *GNS Science Consultancy Report* 2011-121. 58 p.

Wesnousky, S.G., Displacement and geometrical characteristics of earthquake surface ruptures: Issues and implications for seismic-hazard analysis and the process of earthquake rupture: Bulletin of the Seismological Society of America, v. 98, no. 4, p. 1609-1632.

Wilcox, R.E., Harding, T., and Seely, D., 1973, Basic wrench tectonics: AAPG Bulletin, v. 57, p. 74-96.

Yetton, M.D., 1998, Progress in understanding the paleoseismicity of the central and northern Alpine Fault, Westland, New Zealand: New Zealand Journal of Geology and Geophysics, v. 41, p. 475-483.

APPENDICES

Appendix A: Macro Stepover Experiments

The macro stepover group referred to in section 2.6 (Table 2.3) was generated by placing a rectangular plate roughly half the length of the shear table on the base of the model at the bottom right corner, slightly overlapping the basement fault, creating a right lateral, left stepover like the ones characteristic at the Greendale Fault (Figure A.1)**.** Two different stepover widths were tested: 1.5 cm and 3 cm. The talc layer was 2 cm thick, and the underlying fault was displaced at 1 mm/second, as in the other experiments. Initial Riedel shears develop quickly, and a pop-up structure grows with increasing displacement (Figure A.2, A.3). Some splay faults grow outside the pop-up while the main fault segments start to become throughgoing. STEP1.5 shows many structures beginning to cross-cut the main pop-up structure, while STEP3 developed fewer of these, likely because of the larger stepover width.

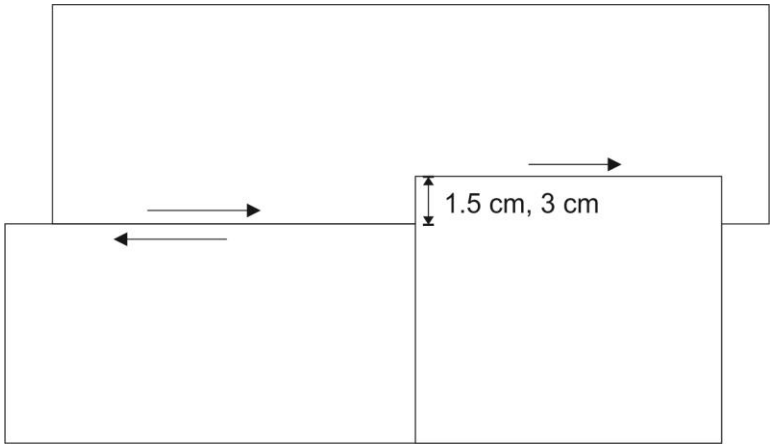

Figure A.1. Schematic plan view of the shear table being offset with a plate in the bottom right corner generating a left stepover. The stepover widths tested were 1.5 and 3 cm.

However, when viewed in sequence, these experiments do not seem to realistically model the behaviour of pop-up structures seen in the field. While the overall morphology is similar, the faults do not interact in ways that they might in nature. For example, the model stepover was induced by generating two separate, parallel faults, while in the field, the two faults probably branch from a single structure at depth (Figure 1.8). Likewise, regardless of geometry at depth, the slip on both surface faults should decrease as they approach the pop-up structure, which does not occur on the experimental faults. There was also some asymmetry in how the stepovers

developed, because the left-moving plate and the material above it generated a small "snowplow" effect in the stepover area. Due to these and other discrepancies, detailed analysis was not performed on these models.

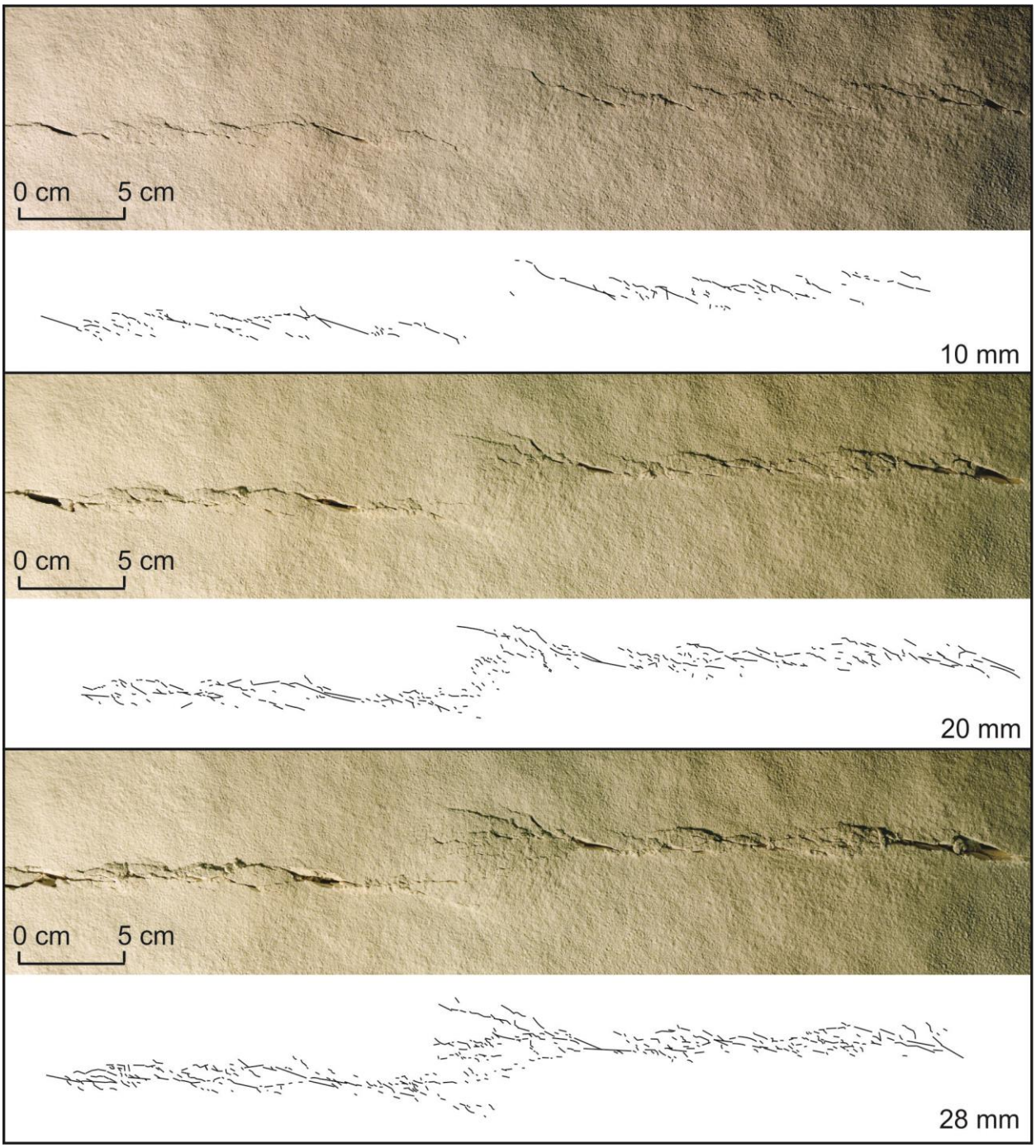

Figure A.2. STEP1.5 at successive displacement intervals, with fracture maps shown below each image. All experiment images are available in Appendix C.

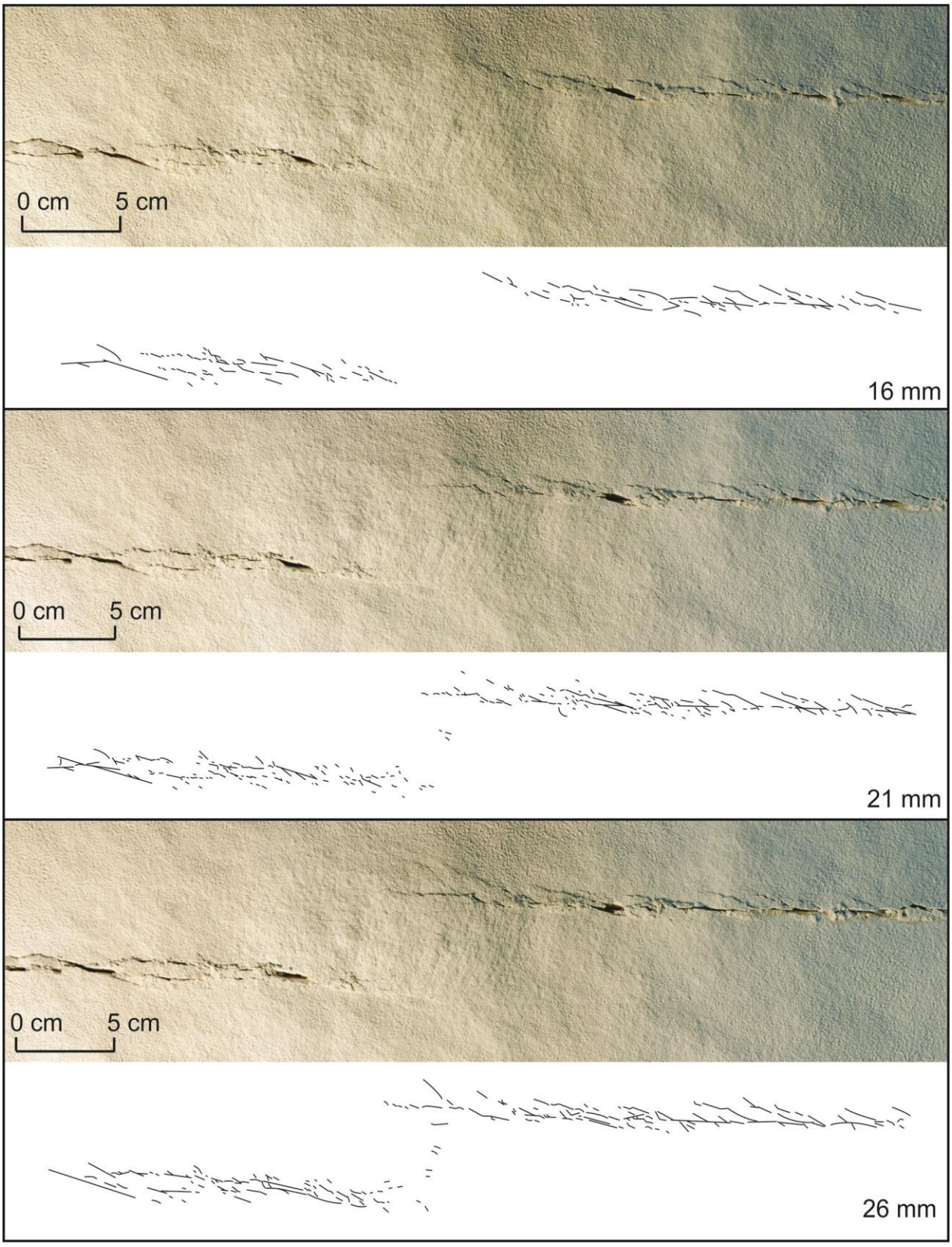

Figure A.3. STEP3 at successive displacement intervals, with fracture maps shown below each image. All experiment images are available in Appendix C.

Appendix B: Shear Wagon Data

Shear wagon tests were performed to constrain the material properties of the talc powder and fine sand used in the analogue experiments. Each plot shows the force required to move the shear wagon with ongoing displacement.

Experiments with Fine Sand

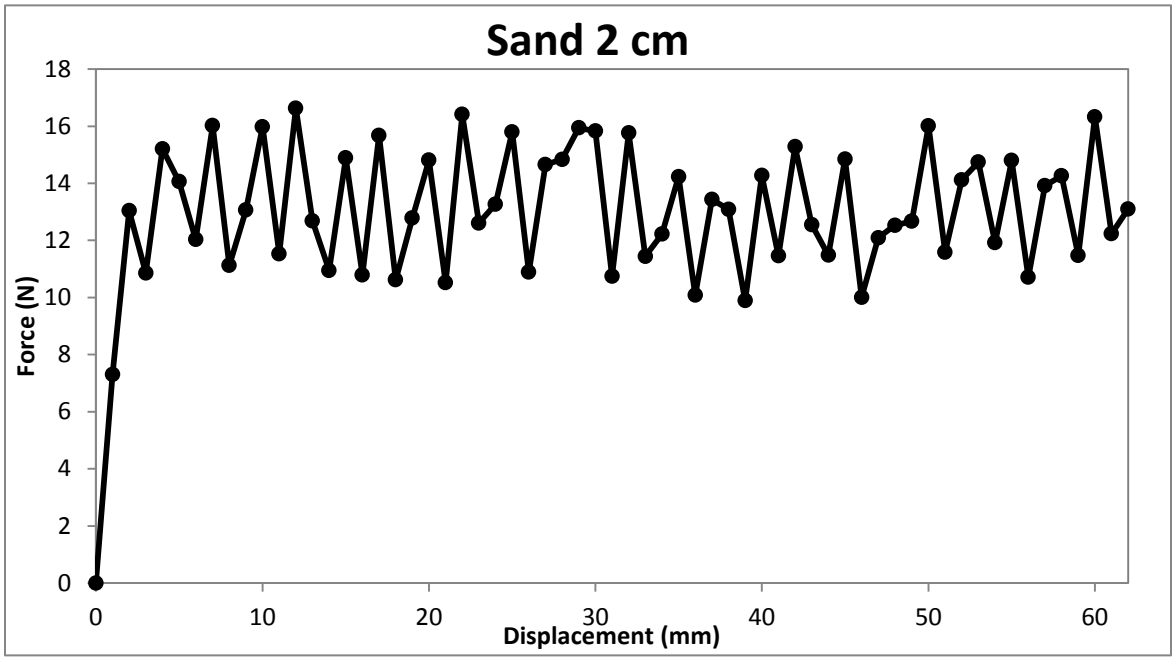

Figure B.1. Shear wagon data for fine sand (2 cm thick).

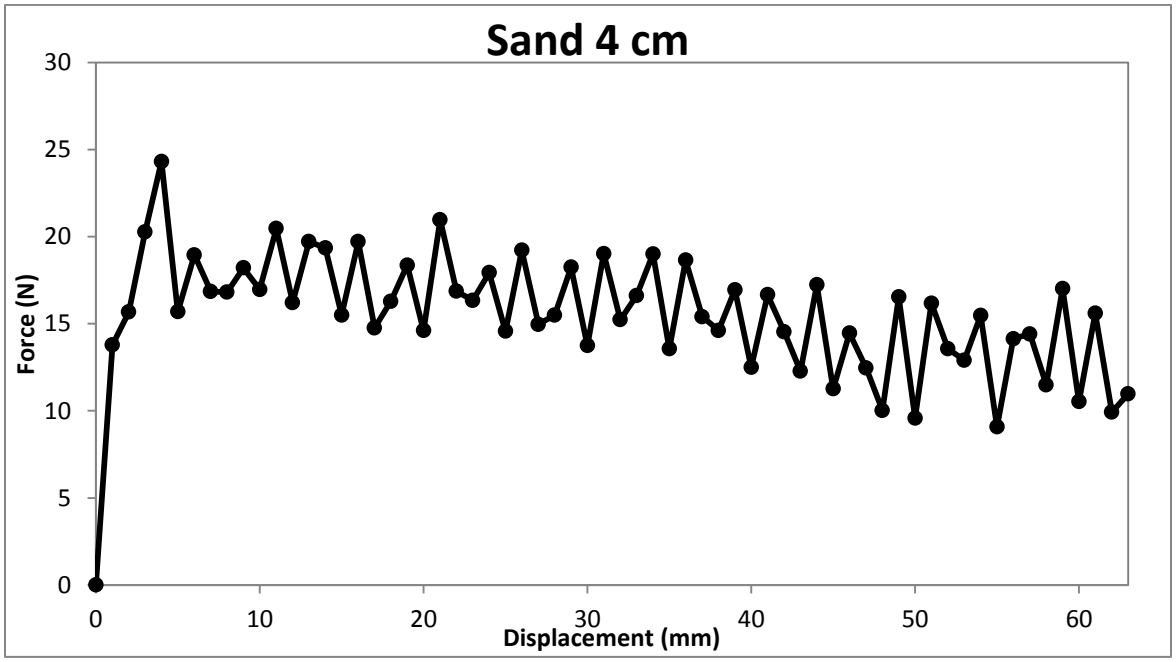

Figure B.2. Shear wagon data for fine sand (4 cm thick).

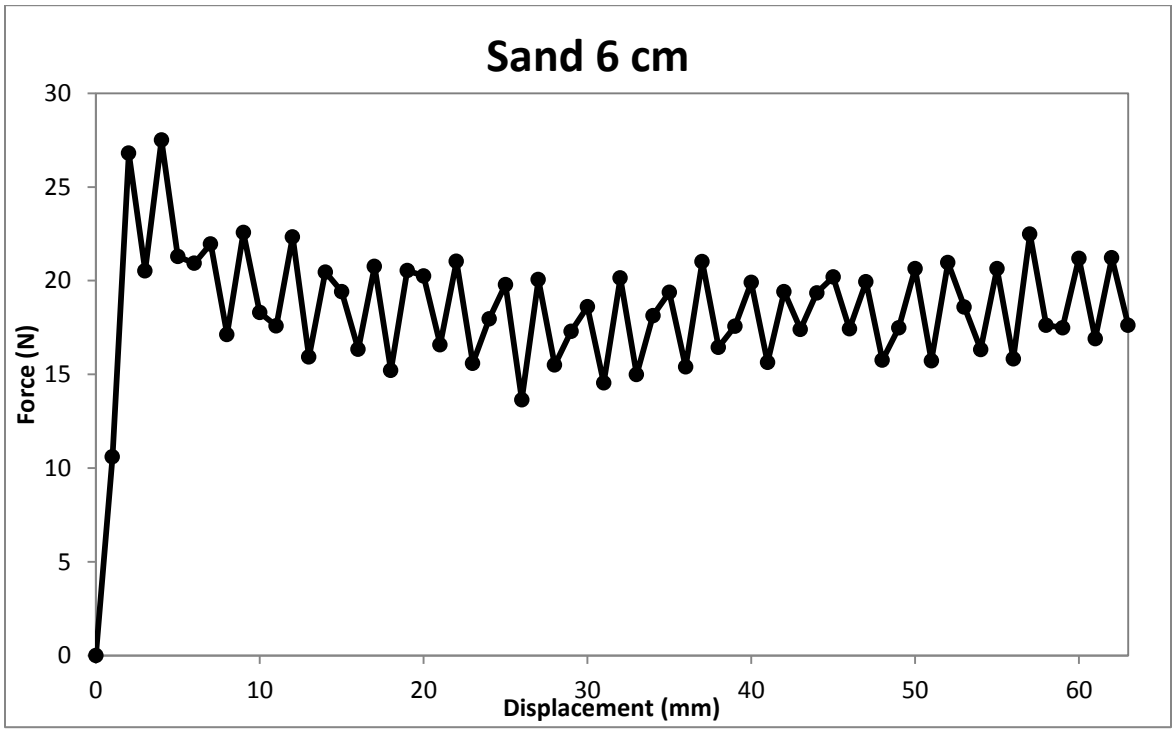

Figure B.3. Shear wagon data for fine sand (6 cm thick).

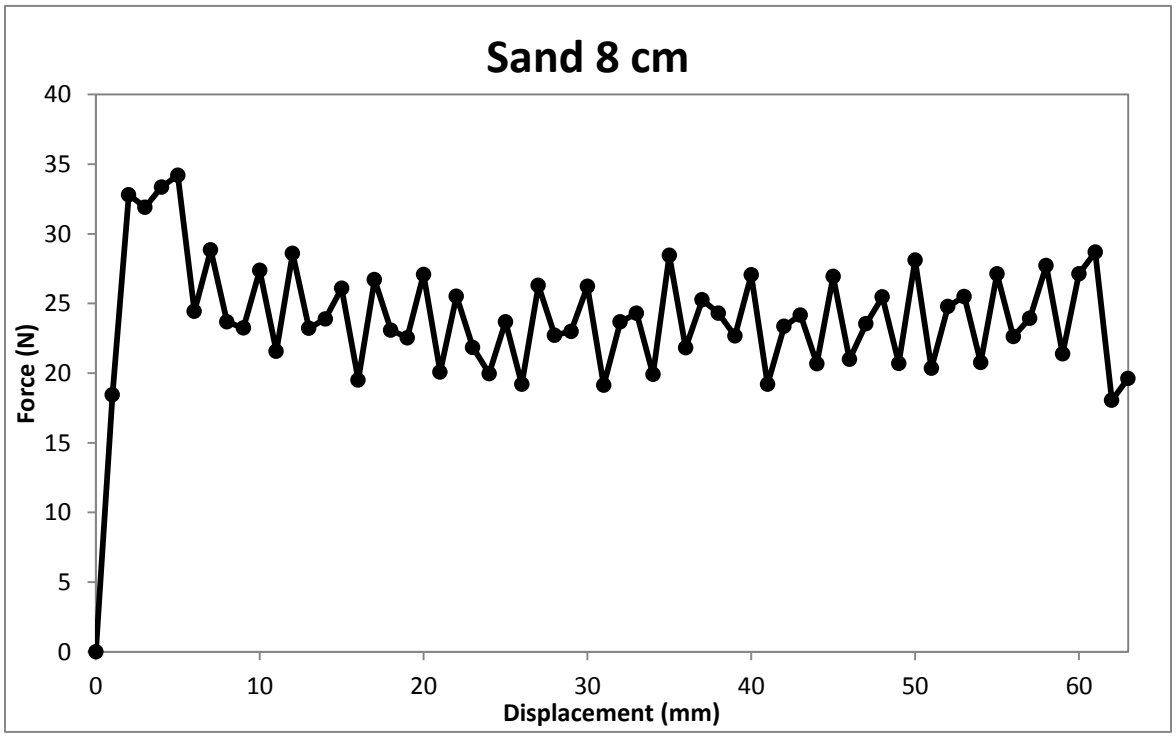

Figure B.4. Shear wagon data for fine sand (8 cm thick).

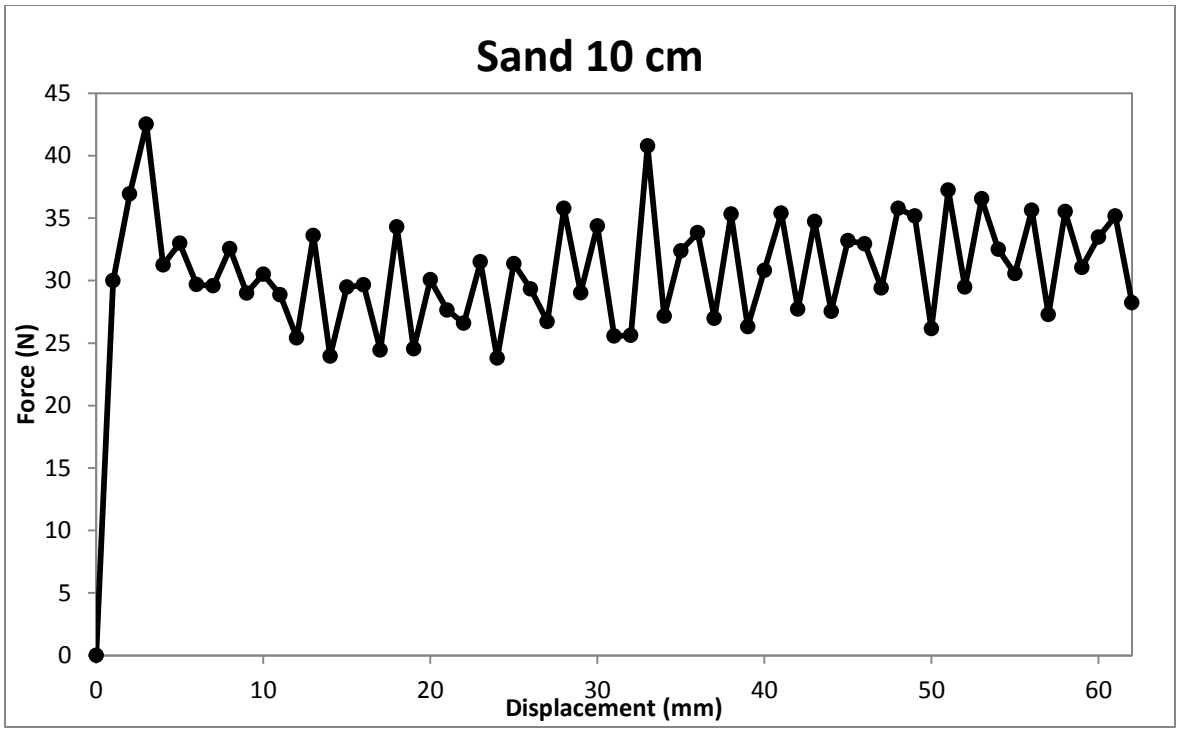

Figure B.5. Shear wagon data for fine sand (10 cm thick).

Experiments with Talc

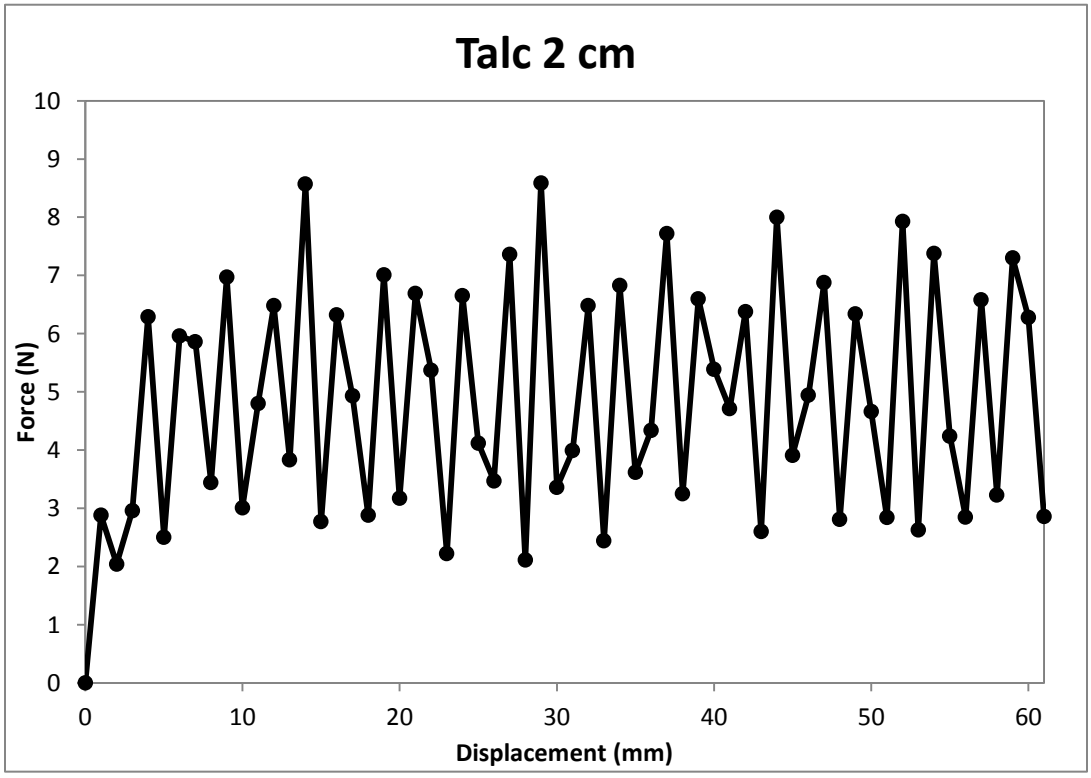

Figure B.6. Shear wagon data for talc (2 cm thick).

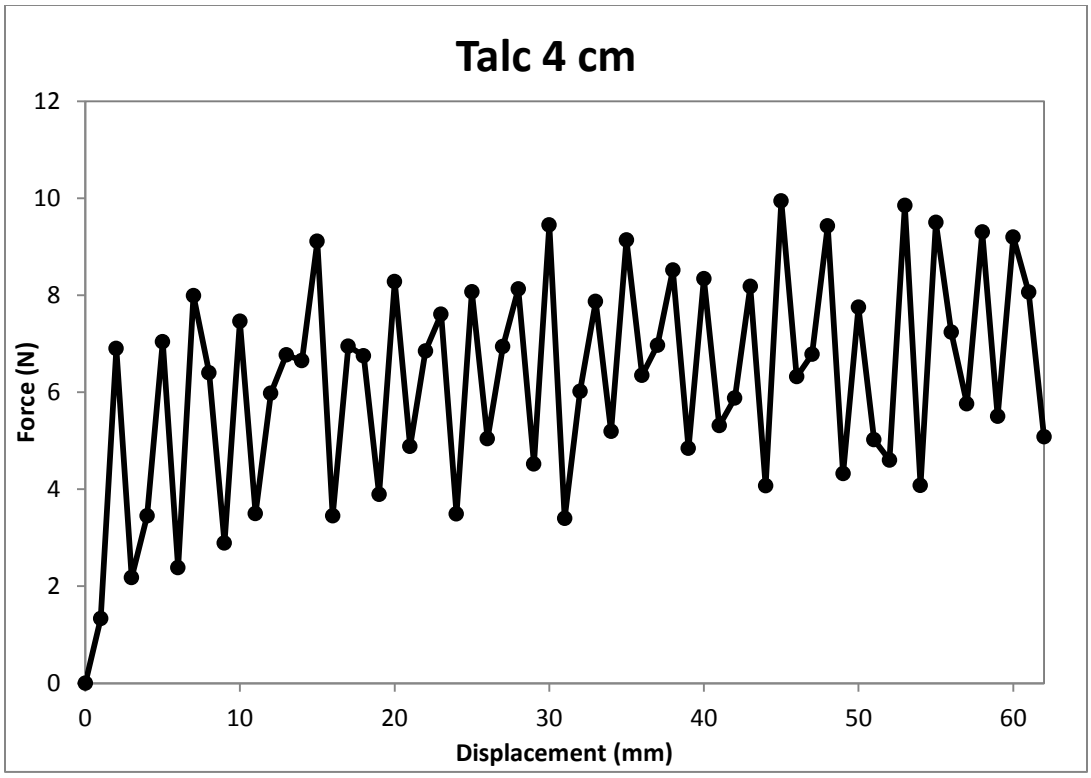

Figure B.7. Shear wagon data for talc (4 cm thick).

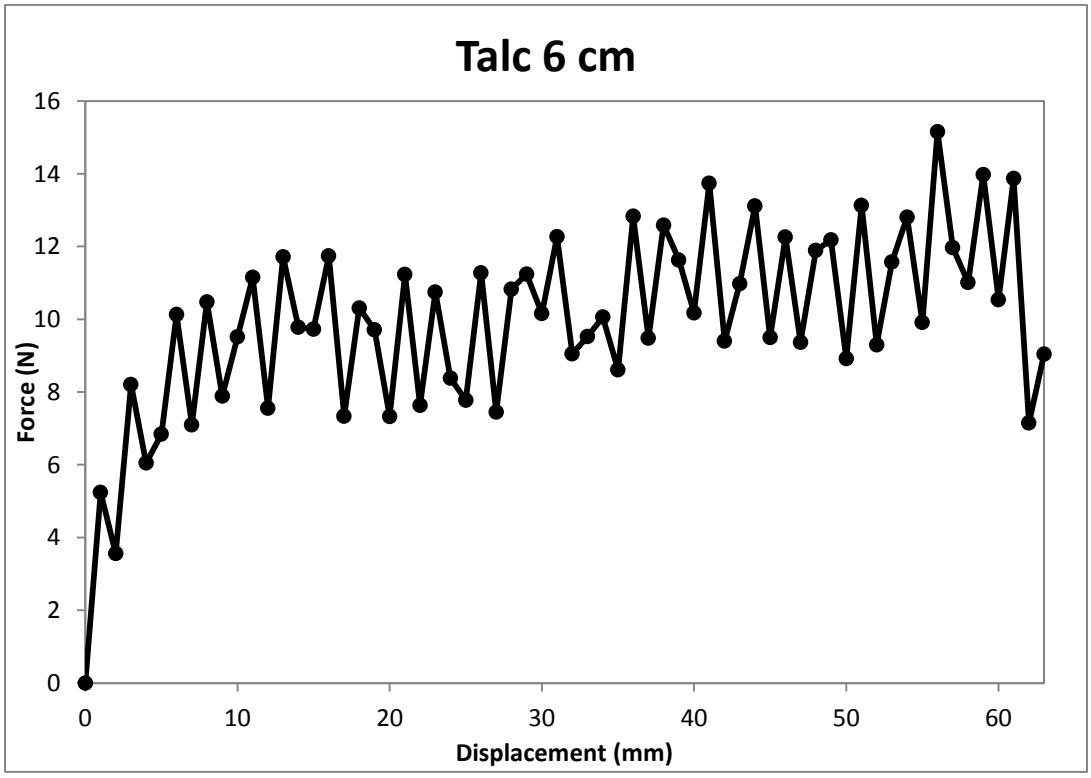

Figure B.8. Shear wagon data for talc (6 cm thick).

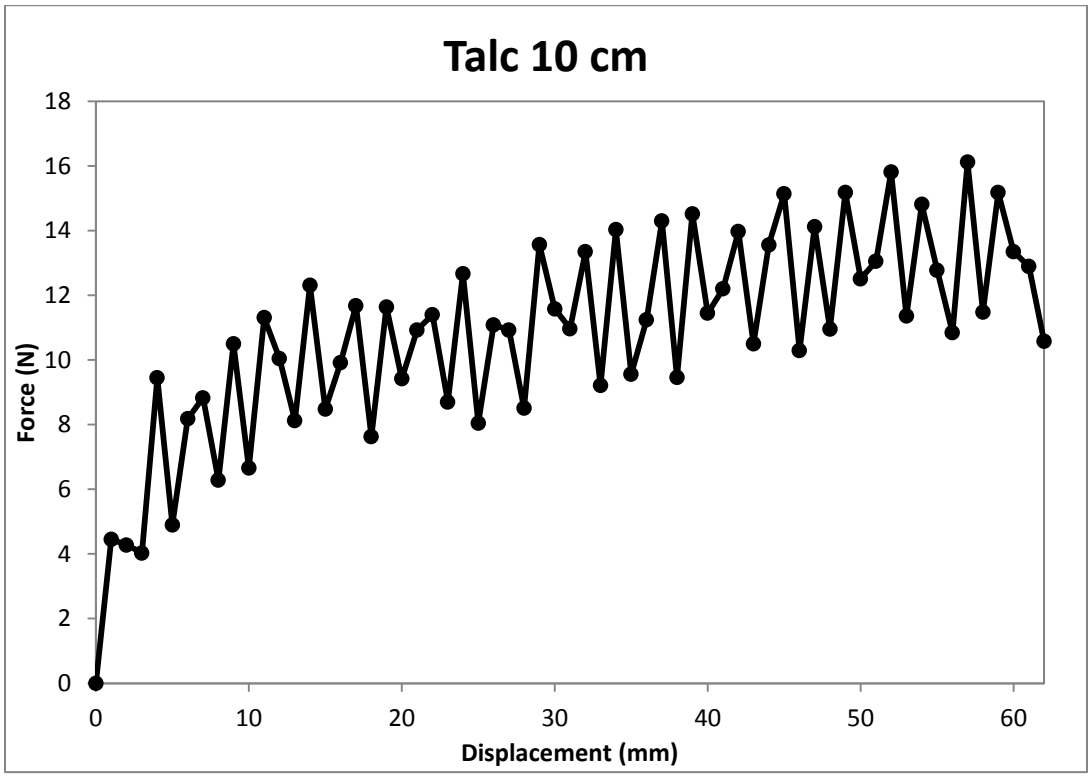

Figure B.9. Shear wagon data for talc (10 cm thick).

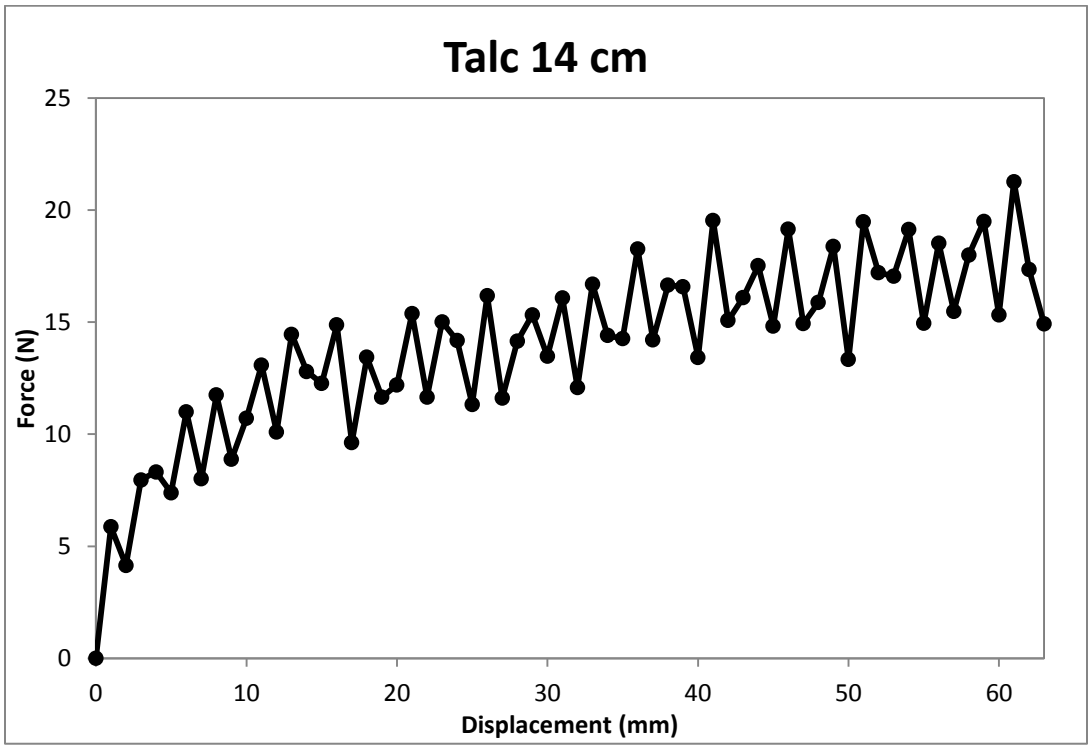

Figure B.10. Shear wagon data for talc (14 cm thick).

Appendix C: Analogue Model Photographs

Each analogue experiment was recorded with high-resolution photography. The model fault was displaced at 1 mm/second, so the camera was set to record one image per second, and thus one image per 1 mm of displacement. A fault with the camera occasionally resulted in a decrease of this rate to one image every ~2.5 seconds, but the fault's rate of displacement does not change.

Original photos are located in folder titled "Uncropped," and cropped photographs are in folder titled "Cropped". The four experiments that the thesis focuses on are included (TALC, TALC_SED, TALC_ER, and TALC_SAND), as well as the macro stepover experiments discussed in Appendix A (STEP_1.5, and STEP_3).

See data supplement discs for photographs, available from University of Canterbury libraries.

Appendix D: PIV Images

PIV images showing the development of shear strain with ongoing displacement are included for each experiment. The rate at which the photos were taken was set at 5 Hz (5 images per second), but at times this decreased to ~4 Hz. The timestamp on each image can be used to confirm the rate at which they were taken.

Warmer colours indicate more concentrated shear strain, while yellow and orange areas denote more diffuse strain. The three experiments with PIV data that are analysed in the thesis are included here (TALC_PIV, TALC_SAND_PIV, and SAND_PIV).

See data supplement discs for images, available from University of Canterbury libraries.